

Originaldokument gespeichert auf dem Dokumentenserver der Universität Basel  
**edoc.unibas.ch**



Dieses Werk ist unter dem Vertrag „Creative Commons Namensnennung-Keine kommerzielle Nutzung-Keine Bearbeitung 3.0 Schweiz“ (CC BY-NC-ND 3.0 CH) lizenziert.  
Die vollständige Lizenz kann unter  
**[creativecommons.org/licenses/by-nc-nd/3.0/ch/](https://creativecommons.org/licenses/by-nc-nd/3.0/ch/)**  
eingesehen werden.

# From Ligand-Stabilized Gold Nanoparticles to Hybrid Organic-Inorganic Superstructures

**Inauguraldissertation**

zur

Erlangung der Würde eines Doktors der Philosophie

vorgelegt der

Philosophisch-Naturwissenschaftlichen Fakultät

der Universität Basel



von

**Jens Peter Hermes**  
aus Syke, Deutschland

Basel 2014

Genehmigt von der Philosophisch-Naturwissenschaftlichen Fakultät auf  
Antrag von

Prof. Dr. Marcel Mayor

Prof. Dr. Thomas Pfohl

Prof. Dr. Ulrich Simon

Basel, den 18.09.2012

Prof. Dr. Jörg Schibler (Dekan)





*allen meinen Verwandten*



## Acknowledgements

I like to thank my supervisor Professor Dr. Marcel Mayor. Marcel, I thank you for giving me the opportunity to work on this fascinating topic, your support throughout my studies and also for the challenges as opportunities for growth. I enjoyed our conversations, and I feel honored for having worked with you.

I thank Professor Dr. Ulrich Simon for co-refereeing this thesis.

I am grateful to Professor Dr. Thomas Pfohl for co-refereeing this thesis and for the fruitful collaboration and nice discussions. A special thanks goes to Raphael Urbani for performing and interpreting the SAXS measurements.

I am also very thankful to Damien Thompson for the fruitful collaboration and discussions, and for proofreading parts of this thesis.

I thank Philipp Ringler for supplying TEM grids and other TEM hardware. His constant support helped improving our TEM measurement techniques.

My special thanks goes to Kiril Tishinov, Tom Eaton and Dr. Loïc Le Pleux for proof-reading the thesis.

I would like to thank the golden boys and girls Dr. Torsten Peterle, Fabian Sander, Dr. Carla Cioffi and Ulrike Fluch for the nice team spirit. Especially, I thank Fabian Sander for the awesome teamwork and interesting discussions, and not only on chemical issues.

I also thank all past and present members of the Mayor group for the nice atmosphere not only for working but also for living and thriving. I dedicate a special thanks to Lab 8, in particular the Northern district.

The atmosphere was great within the whole department and I thank all past and present coworkers for the nice time during work and beyond that.

I am very grateful for all the support within the department: I thank Ewald Schönhofer for helping with the TGA investigation and Dr. Heinz Nadig for performing FAB and EI mass measurements. Werner Kirsch and Sylvie Mittelheiser are acknowledged for performing the elemental analysis. The Werkstatt Team, Roy Lips and Markus Hauri helped in many circumstances by solving problems and by repairing or even developing new devices. The endless support of our secretary staff Brigitte Howald, Marina Mambelli-Johnson and Beatrice Erismann is also gratefully acknowledged.

I am grateful for the financial support from the European Union through the FUNMOL project and the Swiss National Science Foundation.

I extend my special gratitude to my whole family and relatives for their support, positive energy and love. MuM, besonders deine Unterstützung und Liebe waren und sind ein wichtiger Grundstein in allen Lebenslagen.

Last but not least, a big THANKS to all my friends, (team)mates, brothers and sisters who enriched my life on a daily basis, shared happiness and gave support throughout tough times.





The aim of the present PhD thesis was the controlled formation of stable small gold nanoparticle and their tailored functionalization. These functional nanoparticles were designed for their further assembly to organic-inorganic hybrid superstructures.

## Outline

The present cumulative PhD thesis consists of the following parts:

In the **Introduction** the research field of gold nanoparticles is presented with a focus on their stabilization using multidentate thioether macromolecules, in particular dendrimers. The second focus will be on the controlled functionalization of gold nanoparticles with one or two binding sides, which will be submitted as review for publication in ..

Within **Concept and Strategy** the goals of the research project are introduced and the concepts and outputs of the resulting publications are presented.

The **Publications** are accumulated with their respective Supporting Information, in the order in which they were prepared:

*From Ligand-stabilized Gold Nanoparticles to Hybrid Organic-Inorganic Superstructures*, Jens Peter Hermes, Fabian Sander, Torsten Peterle and Marcel Mayor,\* *CHIMIA* **2011**, 65, 219–222.

*Direct Control of the Spatial Arrangement of Gold Nanoparticles in Organic–Inorganic Hybrid Superstructures*, Jens Peter Hermes, Fabian Sander, Torsten Peterle, Carla Cioffi, Philipp Ringler, Thomas Pfohl and Marcel Mayor,\* *Small* **2011**, 7, 920-929.

*Gold Nanoparticles Stabilized by Thioether Dendrimers*, Jens Peter Hermes, Fabian Sander, Torsten Peterle, Raphael Urbani, Thomas Pfohl, Damien Thompson and Marcel Mayor,\* *Chem. Eur. J.* **2011**, 17, 13473–13481.

*Scanning the Potential Energy Surface for Synthesis of Dendrimer-Wrapped Gold Clusters: Design Rules for True Single-Molecule Nanostructures*, Damien Thompson,\* Jens Peter Hermes, Aidan Quinn and Marcel Mayor, *ACS Nano* **2012**, 6, 3007–3017.

*Monofunctionalized Gold Nanoparticles stabilized by a Single Dendrimer form Dumbbell Structures upon Homo-coupling*, Jens Peter Hermes, Fabian Sander, Ulrike Fluch, Torsten Peterle, Damien Thompson, Raphael Urbani, Thomas Pfohl and Marcel Mayor,\* *J. Am. Chem. Soc.* **2012**, 134, 14674-14677.

*Controlled Formation of Bi- and Monofunctionalized Gold Nanoparticles*, Jens Peter Hermes and Marcel Mayor,\* manuscript prepared for submission.

Finally, within **Conclusion and Outlook** the main results are briefly summarized and further potential research is proposed.



## Table of Contents

<b>1</b>	<b>Introduction</b> .....	<b>1</b>
1.1	Gold Nanoparticles.....	1
1.2	Towards Applications.....	2
1.3	Gold Nanoparticle Formation and Stabilization.....	3
1.4	Controlled Functionalization of Gold Nanoparticles .....	7
1.5	Assembly of Nanoparticles to Form Hybrid Superstructures.....	15
1.6	References.....	17
<b>2</b>	<b>Concept and Strategy</b> .....	<b>21</b>
2.1	Previous Work.....	21
2.2	Goals and Results.....	22
2.3	References.....	25
<b>3</b>	<b>Publications</b> .....	<b>26</b>
3.1	<i>CHIMIA</i> <b>2011</b> , 65, 219–222.....	27
3.2	<i>Small</i> <b>2011</b> , 7, 920-929. ....	31
3.2.1	Supporting Information of <i>Small</i> <b>2011</b> .....	41
3.3	<i>Chem. Eur. J.</i> <b>2011</b> , 17, 13473–13481.....	65
3.3.1	Supporting Information of <i>Chem. Eur. J.</i> <b>2011</b> .....	75
3.4	<i>ACS Nano</i> <b>2012</b> , 6, 3007–3017 .....	95
3.4.1	Supporting Information of <i>ACS Nano</i> <b>2012</b> .....	107
3.5	<i>J. Am. Chem. Soc.</i> <b>2012</b> , accepted.....	123
3.5.1	Supporting Information of <i>J. Am. Chem. Soc.</i> <b>2012</b> .....	127
3.6	Review Article prepared for submission .....	143
<b>4</b>	<b>Conclusion and Outlook</b> .....	<b>159</b>



# 1 Introduction

## 1.1 Gold Nanoparticles

Gold nanoparticles (Au NPs) are attracting renewed interest due to their usefulness in chemistry, electronics, catalysis and medicine.<sup>[1–3]</sup> However, the formation and utilization of Au NPs dates back far before their current vogue, with dying of glass by freshly precipitated colloidal gold solutions already known in late Greco-Roman times.<sup>[4]</sup> A famous example is the 4<sup>th</sup> Century Lycurgus cup, which appears red when lit from behind and green when lit from the front, as light is absorbed and scattered by nanoparticles of a gold–silver alloy. In 1857, Faraday was the first to connect the color with the size of Au NPs and was the first to investigate their deliberate synthesis.<sup>[5]</sup> The next milestone was the formation and analysis of citrate-stabilized NPs by Turkevich et al. in 1951.<sup>[6]</sup> More recent breakthroughs demonstrated ultrahigh precision in the formation of passivated Au NPs.<sup>[7–10]</sup> Schmid et al. presented the gold cluster  $\text{Au}_{55}(\text{PPh}_3)\text{Cl}_6$ ,<sup>[7]</sup> which has become known as the ‘Schmid-cluster’, having stimulated the areas of quantum electronics<sup>[8]</sup> and labeling.<sup>[11]</sup> Brust et al. introduced a two-phase protocol that allowed aqueous tetrachloroauric(III) acid ( $\text{HAuCl}_4$ ) to be transferred into the organic phase (toluene) using tetraoctylammonium bromide (TOAB). The gold salt was then reduced with aqueous sodium borohydride in the presence of an alkanethiol yielding stable Au NPs with diameters below 3 nm and narrow size distributions.<sup>[9]</sup>

Since then the number of studies dedicated to Au NPs increased significantly over the past two decades, exploiting the unmatched stability of Au NPs among metal nanoparticles. They also show fascinating size and shape dependent properties<sup>[12]</sup> and have various applications. They are used as plasmonic devices, for example as a plasmonic ruler to measure the distance between two NPs attached to linkers of unknown length.<sup>[13,14]</sup> Extended research is conducted on Au NPs in nanoelectronics<sup>[2,15]</sup> such as information storages devices.<sup>[16]</sup> As Au NPs of different sizes are easily visualized by electron microscopy they are the label of choice for visualizing and investigating bio- and macromolecules.<sup>[17–20]</sup> Au NPs also have numerous current and future applications as sensors<sup>[21–23]</sup> and as catalysts.<sup>[24,25]</sup> More background information is available within extended review articles<sup>[1,2,26]</sup> and in a special issue of *Chem. Soc. Rev.* entitled “Gold - Chemistry, Materials and Catalysis”.

## 1.2 Towards Applications

The size dependent physical and optical properties (quantum size effect) are maybe the most interesting properties and are in the focus of various investigations. The ability to obtain different colored solutions of Au NPs by altering the size of the NP is due to the surface plasmon resonance of the NP. The conduction electrons on the NP's surface oscillate collectively by the interaction with the electromagnetic field of the incoming light. The light thereby creates polarized charges on the surface like a dipole and with this also a restoring force that tries to compensate it. This force has a unique resonance frequency to match the oscillation of electrons within the nanoparticle.

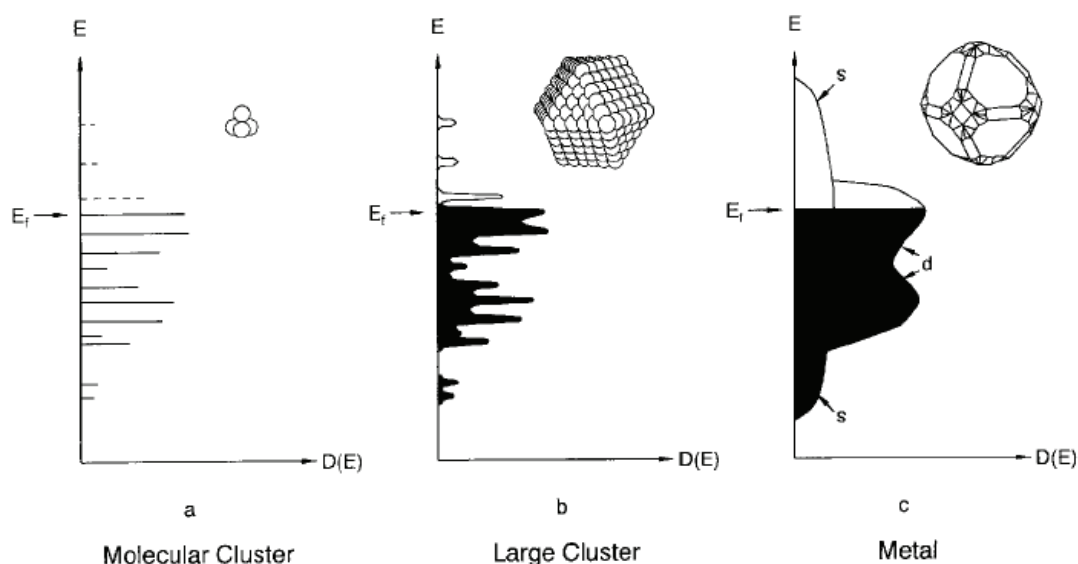


Figure 1. Formation of a metallic band structure. On the way from a molecule a) via nanosized clusters b) the quasi delocalization of valence electrons increases until the bulk state c) is reached.  $E_F$ =Fermi energy,  $D$  = Density of states. From Reference [27]

Another size dependent property of Au NPs is their electronic behavior. Electronic properties depend on the distribution of states and their occupation with electrons. Figure 1a shows the well-known situation in a molecule with discrete energy levels, also called molecular orbitals. The other extremity is the bulk material (Figure 1c) where no molecular behavior is expected and energy bands are present instead of discrete levels. The research field of nanoparticles lies between these two extremes (Figure 1b). The transitions are continuous and no sharp boundary can be distinguished. However, the smaller the nanoparticle then more defined energy levels will be present. Our research will be conducted between molecular and large

clusters. The term 'cluster' is used within this thesis to describe nanoparticles with a defined and unique structure and 'nanoparticle' will be used for assemblies with certain dispersity. People also utilize the terms 'nanocrystal' or 'colloid' but they will not be used within this thesis.

As mentioned above, Au NPs have a broad variety of current and future applications. One very important application is their use in home pregnancy tests where NPs are coated with a certain antibody and their coagulation occurs if the specific antigen is present in the urine, triggering a plasmonic response that can be detected by the naked eye as the clumps of coagulated NPs are trapped in a filter.<sup>[28]</sup> If the specific antigen is not present the NPs will remain separated and the coloring of the filter will not occur. In order for this pregnancy test to work certain conditions need to be fulfilled (see also Figure 5 in Chapter 1.4). 1) The NPs need to be formed in a certain size and they need to be stable. 2) The surface of the NP needs to be functionalized with the antibody and 3) the specific antigen must be present. These operations are vital for most applications of Au NPs and various possibilities for each step will be described in the following sections in more detail.

### **1.3 Gold Nanoparticle Formation and Stabilization**

In order to use the size-dependent properties of Au NPs ideally monodisperse NPs are envisaged. However, the preparations of NPs often lead to certain size distributions and require purification techniques to reduce the dispersity obtained.

The basic principle to form Au NPs is to reduce  $\text{Au}^{3+}$ -ions in the presence of a stabilizing ligand. In the case of the citrate-stabilized Au NPs introduced by Turkevich<sup>[6]</sup> citrate is used as both a reducing and stabilizing agent. Nowadays this approach is mostly used if a loose ligand shell is desired for example for further ligand exchange.<sup>[29]</sup> Other ligands are phosphines<sup>[7,30]</sup>, amines<sup>[31]</sup> and thiolates. Thiolates are the most intensively investigated ligands since Brust et al.<sup>[9]</sup> introduced their NP preparation protocol. Since then sodium borohydride is mostly used as the reducing agent, especially if one aims at Au NPs with a size of 1 - 3 nm. Sardar and Shumaker-Barry recently introduced a mild protocol for the synthesis of Au NPs with a higher tolerance for functional groups.<sup>[32]</sup> They used borabicyclo-[3.3.1]nonane (9-BBN) as their reducing agent and performed the reaction just in organic media.



Terminal thiols are used because they form a strongly bound ligand shell on the NPs' surface. In crystal structures of gold clusters the sulfur was even found to be embedded in the outer gold layer as so called staples.<sup>[33,34]</sup> The use of terminal thiols has one major drawback. As many thiols are needed to stabilize one NP there might be also many functionalities upon introduction of functional groups (see next section). Within this thesis a different approach will be presented by using macromolecular multidentate thioether ligands, as this should reduce the number of ligands and thus the number of functionalities. Thioethers are found to bind less strong than thiols<sup>[35]</sup> but they have the ability to bind in a cooperative manner and still stabilize Au NPs sufficiently.<sup>[36]</sup>

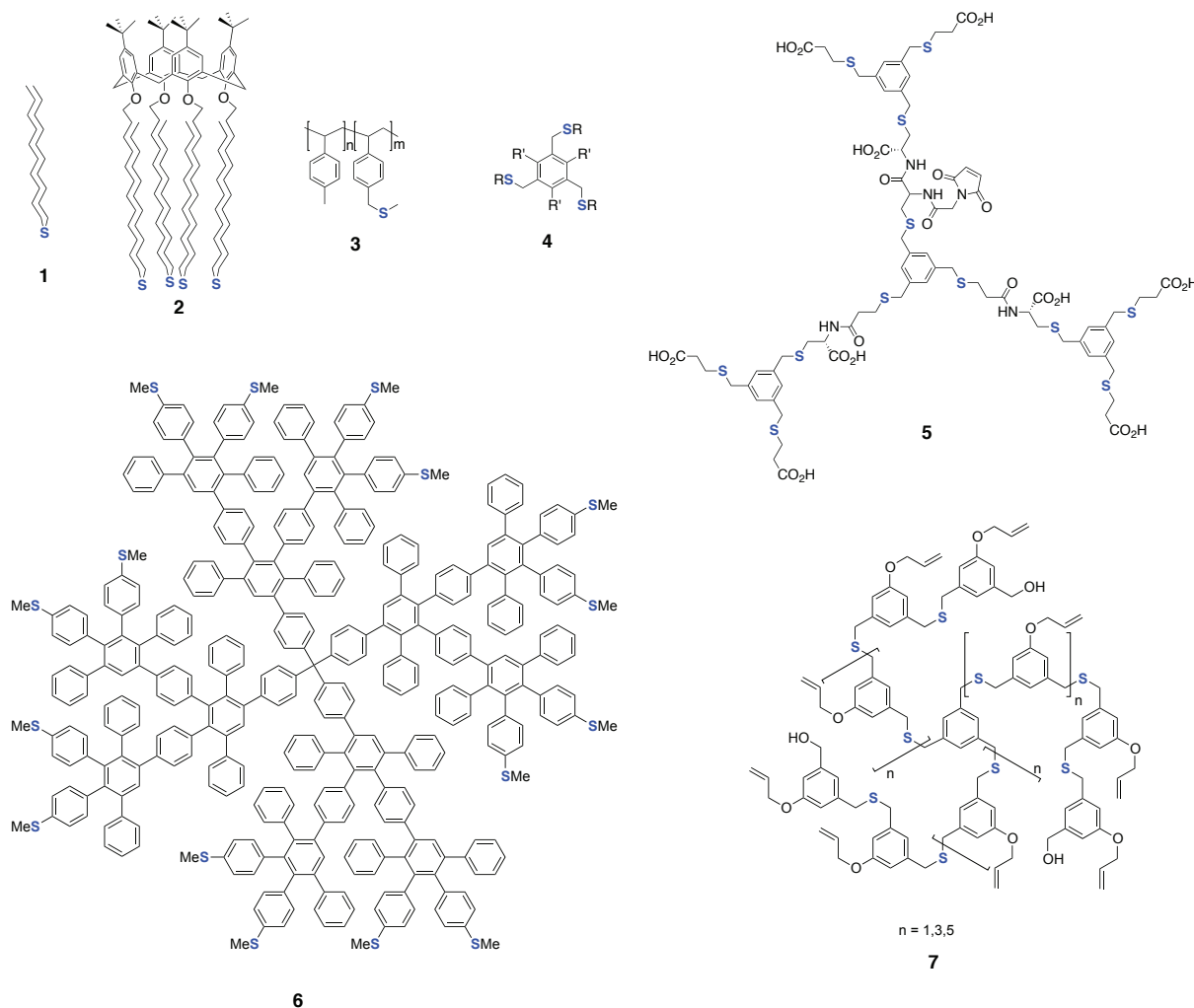


Figure 2. Thioether ligands **1,2**,<sup>[37]</sup> **3**,<sup>[38]</sup> **4**,<sup>[39]</sup> **5**,<sup>[40]</sup> **6**<sup>[41]</sup> and **7**<sup>[42]</sup> of different structures and denticities used for the stabilization of Au NPs. Thioether moieties are highlighted in blue.

In 2001 Reinhoudt and coworkers presented the utilization of thioethers as stabilizers for Au NPs.<sup>[37]</sup> Several thioether ligands were synthesized and used as stabilizing

ligands during the Brust synthesis. Besides the mono- and tetradentate ligands **1** and **2** (Figure 2) other thioether molecules were investigated. Their work already showed the importance of the cooperative stabilization of thioethers as the NP stability increased with the thioether denticity. Huang et al. used thioether polymer **3** as polydentate ligand and obtained stable NPs of varying sizes, depending on the NP-polymer ratio.<sup>[38]</sup> Other polymeric ligands were also presented to stabilize Au NPs.<sup>[43,44]</sup> However, these polymers were mono- and tridentate concerning thioether moieties indicating that their stabilizing ability probably depended on the polymer backbone and other functional groups present. The drawback of polymers is their large dispersity in molecular size. Variation in ligand size might lead to differences in stabilizing properties and thus difficulties in tailoring NP properties.

In 2001 Kiedrowski and coworkers presented the successful stabilization of a the Au<sub>55</sub> Schmid-cluster with four tridentate benzylic thioether ligands.<sup>[39]</sup> The ligands were based on the 1,3,5-trimethylbenzene structure **4** and substituted the twelve phosphine ligands around the cluster by a phase transfer reaction into a buffered aqueous solution. Follow-up research published in 2006 presented the fusion of four tridentate ligands to form the dodecadentate ligand **5** able to solely stabilize the Au cluster.<sup>[40]</sup> This approach of using pure macromolecular dendritic ligands introduced a more controlled approach to forming and functionalizing Au NPs.

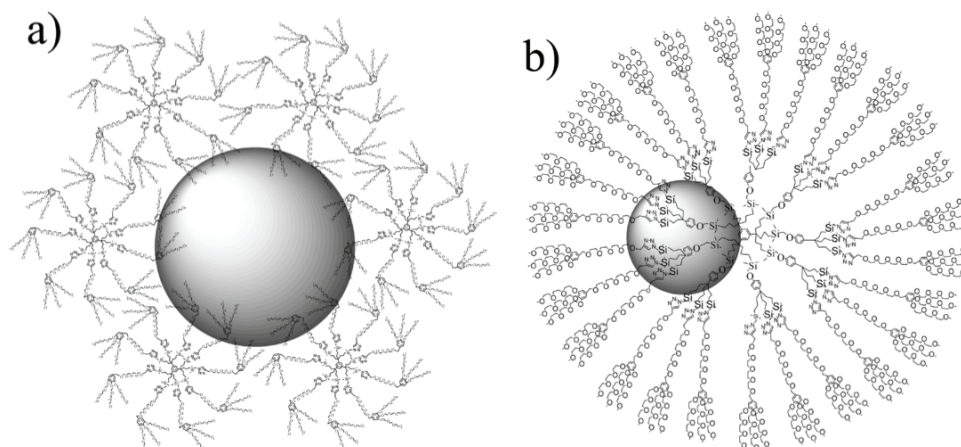


Figure 3. a) Large dendrimer stabilized NPs are formed with lower generations of dendrimers while b) higher generations produce dendrimer encapsulated NPs with smaller diameters, adapted from Reference [45].

Crooks and coworkers and Esumi and coworkers presented the first examples of macromolecules to encapsulate and stabilize metal NPs.<sup>[46,47]</sup> They used different dendrimer generations based on poly(amidoamine) (PAMAM) and poly(propylene

imine) (PPI) structures as macromolecular stabilizers. Besides that poly(ethylene glycol) (PEG) dendrimers containing triazole rings were also able to form stable Au NPs (Figure 3).<sup>[45]</sup> Within these studies it was found that lower dendrimer generations form NPs with larger diameters (Figure 3a). It was proposed that these NPs are dendrimer stabilized while higher generations form dendrimer encapsulated NPs with smaller diameters (Figure 3b).<sup>[45,47]</sup>

Thioether based dendrimers as the stabilizing ligand were also presented and the molecular structures vary from stiff arylidic sulfides<sup>[41]</sup> to highly flexible benzylic thioether dendrimers.<sup>[42]</sup> These dendrimers were present during the NPs synthesis following the Brust-Schiffrin protocol and the latter showed better stability and monodispersity. The results are difficult to compare as Hosokawa's star shaped molecules **7** contained thioethers throughout the whole structure and additional ether moieties<sup>[42]</sup> while the stiff polyphenylene dendrimer **6** of Taubert et al. just had terminal thioethers and a huge aromatic core whose stabilizing abilities are unknown.<sup>[41]</sup> Besides the thioether flexibilities Vögtle and De Cola also compared dendrimers with a different extent of the branching of thioether moieties.<sup>[48]</sup> They were able to conclude that higher generations lead to increased stabilities and that the stabilizing capability of the branches is also vital. Interestingly most of their NPs still contained the phase transfer agent TOAB so probably the dendrimers did not stabilize the NP sufficiently.<sup>[48]</sup> Bergamini et al. used a dodecadentate persulfurated coronene to form stable and monodisperse NPs by disproportionation of Au<sup>+</sup>.<sup>[49]</sup> In 2009 Peterle et al. of our research group used linear thioether oligomers to stabilize Au NPs.<sup>[50]</sup> Bi-, tetra-, hexa- and octadentate thioether ligands were synthesized (Figure 4) and the latter showed the highest NP stability and smallest dispersity. The benzylic thioethers gave the flexibility and *tert*-butyl functionalized benzenes as bridges gave a sufficiently large ligand shell to ensure long-term stability.<sup>[50]</sup> This study nicely supports the overall conclusions we draw for using thioether-based ligands: denticity, thioether flexibility and extent of the ligand shell increase the stability and monodispersity of Au NPs.

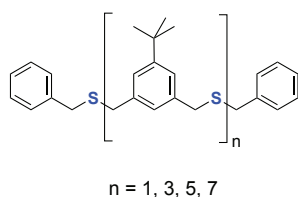


Figure 4. Molecular structure of linear thioether ligands used to stabilize Au NPs.<sup>[50]</sup>

## 1.4 Controlled Functionalization of Gold Nanoparticles

There are various ways to functionalize and assemble Au NPs and different approaches can be chosen. One can either i) form unfunctionalized NPs (Figure 1a) or NPs bearing many functionalities (Figure 1c) and use linker molecules and experimental conditions that favor formation of discrete NP architectures (Figure 5a,c) or ii) one can try to control the number of functional groups on the NP surface for the subsequent assembly (Figure 5b, green arrow in green box). Examples of the first approach may be found in the studies of Dadosh et al. and Brousseau III et al., who formed NP dimers of citrate-stabilized NP using a carefully chosen ratio of unfunctional NPs to dithiol linker molecules (Figure 5a).<sup>[51,52]</sup> Simon and coworkers used an excess of multifunctional NPs to click them to a DNA template and obtained ordered chain-like architectures.<sup>[53]</sup> There are many other examples that utilize similar approaches and some are presented in recent reviews that show the richness of NP assemblies.<sup>[54–58]</sup> Within the present thesis we focus on the controlled functionalization (green arrow in Figure 5b) of Au NPs with one or two functional group on the NP surface for their further assembly without an additional linker.

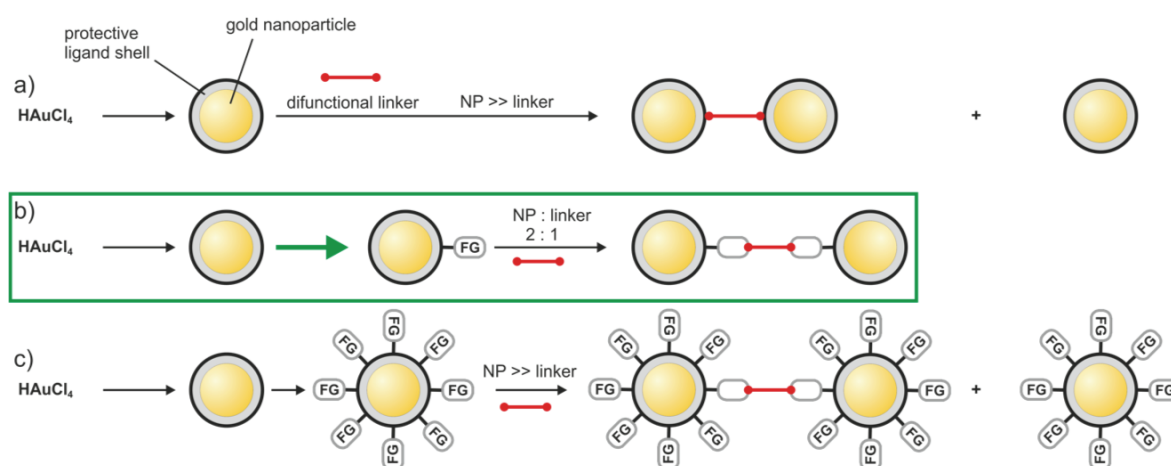


Figure 5. Different concepts for the functionalization of Au NPs and their assembly into multimeric structures (taking dimers as an illustrative example). The individual NPs are formed by reducing  $\text{HAuCl}_4$  and then stabilized with a protective ligand shell. a) Dimers may be formed using a well-chosen ratio of unfunctional NPs and difunctional linkers, although monomers remain the major product. b) NPs are monofunctionalized (FG = functional group) and then covalently fused to form mostly dimers. c) NPs are multifunctionalized and linked in an excess of NPs (as in route (a) above), yielding a mixture of dimers and monomeric structures. Experiments performed via route (a) or (c) using lower excesses of NP relative to linker produce multi-linker bearing NPs and so high-n multimer assemblies.<sup>[29,59]</sup>

There are various approaches to introduce functionalities onto a NP surface. One way is to form NPs stabilized by weak ligands like citrate or amines first. Afterwards the ligand is replaced by a stronger-binding alkanethiol molecule<sup>[60]</sup> followed by exchange with a functional thiol, e.g. OPE-dithiol.<sup>[29]</sup> This approach is very convenient if many functional groups are envisaged or if the concentration of linker molecules used for the subsequent NP assembly may be controlled. It is also possible to exchange the weak ligand with a mixture of functional and unfunctional thiols at the same time for an increased control over the number of functionalities on the NP surface. Stoddart and coworkers used a molar ratio of 3000:1 of alkanethiol and functional thiol to obtain mono-functionalized NPs in a large excess of nonfunctionalized NPs.<sup>[61]</sup> The subsequent assembly of dimers and trimers was achieved without removing the unfunctional NPs.

Controlled assemblies are needed for applications in labeling and medical diagnostics, and are the key remaining bottleneck for the development of reproducible nanoelectronics components based on NP superstructures, such as dimers, chains and 3D architectures. A very promising route to controlled assembly (Figure 1b) requires simply pure samples of monofunctionalized NPs. To our knowledge only a few review articles focus on the controlled functionalization of Au NPs.<sup>[57,58,62–64]</sup> One way to obtain NPs with a controlled low number of functionalities is by separating NPs using chromatography. The first report of monovalent Au NPs was presented in the 1980s where a undecagold cluster ( $\text{Au}_{11}$ ) was stabilized by seven phosphine ligands, with just one of the phosphines carrying a functionality (Figure 6a).<sup>[65,66]</sup> The clusters were purified by repeated ion-exchange chromatography and their monofunctionality was inferred from photometry and their chemical behavior. Monovalent undecagold (0.8 nm diameter) was then further labeled with an antibody by Hainfeld.<sup>[30]</sup> The unlabeled NPs were removed by ion-exchange chromatography and the presence of mono-labeled NPs was confirmed by electron microscopy. This approach was later extended to synthesize a monovalent 1.4 nm gold cluster that is commercially available since 1992 as Nanogold by Nanoprobes (Figure 6b).<sup>[11]</sup> Therefore we will not present Au NP assemblies using these commercial NPs.

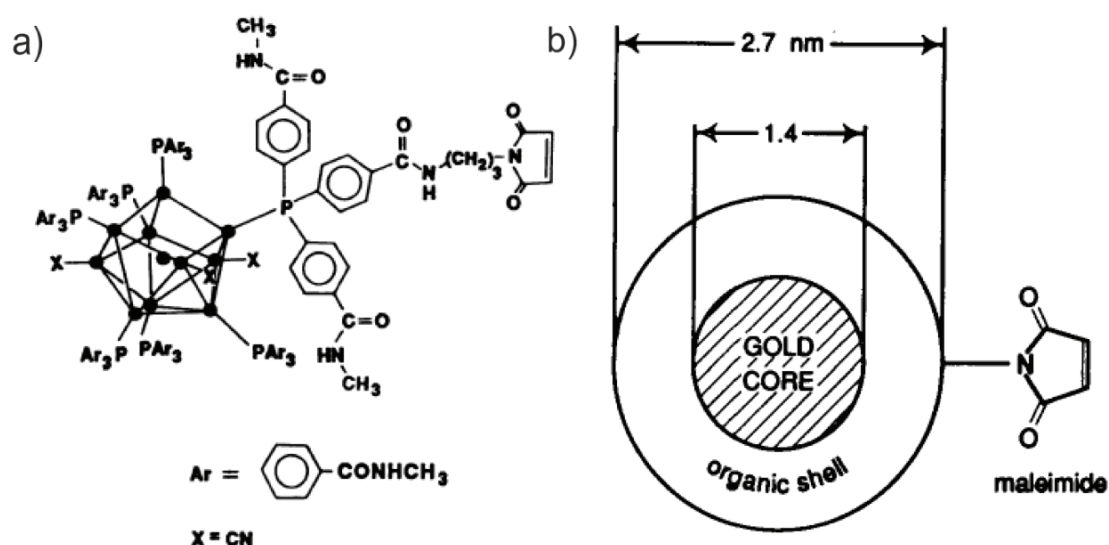


Figure 6. a) The proposed molecular structure of monofunctionalized undecagold (0.8 nm diameter), from Reference [30]; b) schematic drawing of commercially available monofunctionalized gold cluster called Nanogold, from Reference [11].

Au NPs functionalized with different amounts of DNA strands were successfully separated by gel electrophoresis (Figure 7a).<sup>[67]</sup> Mono- to penta-functionalized NPs were isolated by Alivisatos and coworkers with DNA strands consisting of at least 100 base pairs. The pure mono-DNA-labeled NPs were later covalently dimerized by enzyme ligation supported by a reversible duplex formation with a template DNA<sup>[68]</sup> in a neat combination of covalent chemistry plus non-covalent self-assembly. In earlier studies the same group had already used gel electrophoresis to isolate NP dimers and trimers.<sup>[69]</sup> Monofunctional NPs purified by gel electrophoresis were also used to form cyclic hexameric structures<sup>[70]</sup> and highly ordered two-dimensional NP arrays on DNA tiles.<sup>[71–73]</sup> NPs with multiple functionalities were also used to form 2D arrays resulting in more defects and lesser control of the final assembly.<sup>[74]</sup>

The long DNA strands used for the purification have a drawback: they require higher efforts and costs for their production and can also be an obstacle for the tailored NP assembly. Aldaye and Sleiman, and Ohya and coworkers, were able to reduce the size of the DNA marker by a reversible elongation with a second DNA strand and isolated the mono-DNA-labeled NPs by gel electrophoresis (Figure 7b).<sup>[75,76]</sup> After removal of the elongation strands the NPs were assembled into 1D- and 2D-architectures, such as chains, triangles and squares. NPs with two DNA markers were also isolated by gel electrophoresis and used to build up trimers with two monofunctionalized NPs.<sup>[68,76]</sup> If these trimeric structures were connected by single

stranded DNA, two complementary trimers were synthesized and hybridized to form hexameric structures.<sup>[68]</sup> Most superstructures aligned in linear structures reflecting the steric benefit of binding the two functionalities on opposite sides of the NP. Suzuki and coworkers preassembled two single stranded DNA markers to a template in order to attach two functional units to the NP surface at the same time in close proximity.<sup>[77]</sup> They subsequently attached two smaller functional NPs to the bifunctional NPs and obtained triangular architectures clearly showing the close proximity of the two initial DNA labels.

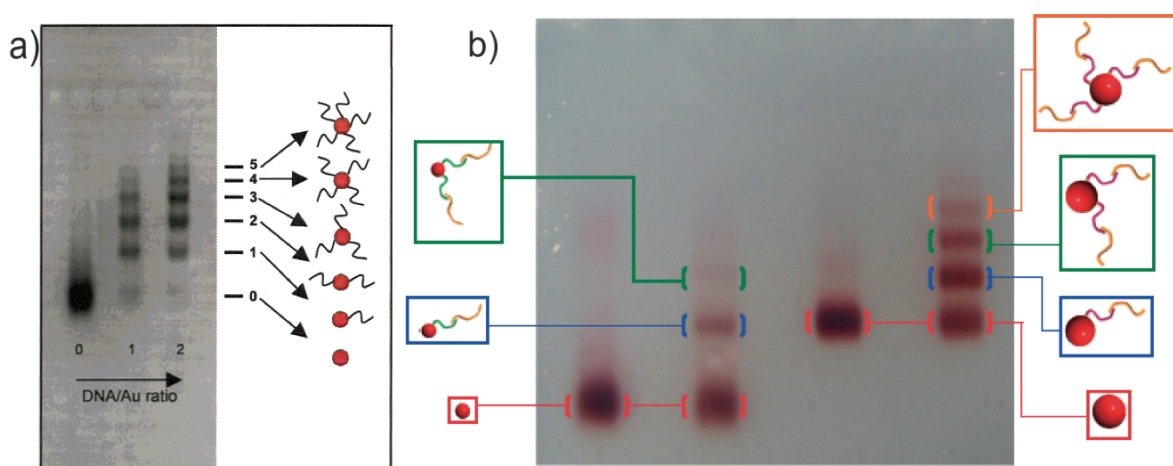


Figure 7. Successful separation of Au NPs bearing different numbers of DNA strands: a) at least 100 base pairs are required in order to achieve sufficient separation, from Reference [67]; b) shorter DNA markers are used by reversibly extending to a double strand for the purification, from Reference [76].

Immobilized metal ion affinity chromatography (IMAC) was used to purify mono-peptide labeled NPs.<sup>[78]</sup> Coordinating a peptide tag to an immobilized metal ion enabled the separation of functional and unfunctional NPs. In this case, a sequence of six histidines was used as a tag (His<sub>6</sub>-tag) and Nickel(II) as the immobilized metal ion. This Nickel-mediated NP-protein binding was introduced earlier by Hainfeld and coworkers.<sup>[62,79]</sup> After forming the Nickel-His-tag complexes in a chromatography column the unfunctional NPs were washed off and the mono-labeled NPs were eluted with imidazole (Figure 8a). However, in order to obtain only mono-functionalized Au NPs the concentration of peptide marker had to be very low (10fold excess of NPs) so that the NPs bear either one or no functionality leading to a low yield of monofunctional NPs. The same approach was chosen to synthesize Au NPs with the Nickel(II) complex<sup>[80]</sup> on their surface in order to bind these labeled NP to His<sub>6</sub>-tag functionalized proteins<sup>[80]</sup> and nanofibres.<sup>[81]</sup> Leung and coworkers were able

to remove unfunctional NPs with a similar protocol (Figure 8b).<sup>[82]</sup> A mixture of monofunctionalized and unfunctionalized Au NPs was separated using crownether functionalized magnetic particles that noncovalently bound the NP functional group, a protonated secondary amine. The unfunctionalized NPs were washed away with dichloromethane, while the amines of the functional NPs were deprotonated, allowing the functional NPs to be separated from the magnetic particles by applying an external magnetic field.

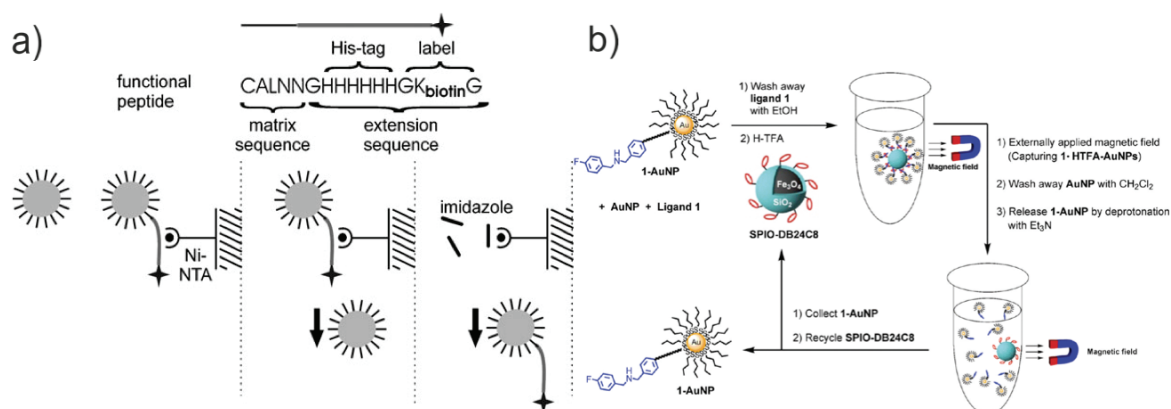


Figure 8. Concept used to separate a mixture of NPs having either one or no functional group attached to their surface. Functionalized NP were selectively trapped in a column (left) or on magnetic particles (right), while unfunctional NPs were removed. Finally pure samples of monofunctionalized NPs were released and collected, from References [78,82].

All attempts presented so far require expensive and time-consuming purification steps. Reactions on solid supports provide an alternative route to obtain monofunctional NPs without the need for chromatographic purification. A polymer resin was functionalized with an alkyl chain bearing a terminal thiol, which was allowed to undergo exchange with the surface of an alkanethiol stabilized Au NP (Figure 9a). Unreacted NPs were washed off before the cleavage from the resin was performed under acidic conditions and monofunctional NPs with a diameter of around 2.8 nm were obtained.<sup>[83]</sup> This research published by Huo and coworkers was the first example of asymmetric functionalization, which means that just one part of the NP surface is functionalized while the rest of the surface is blocked. Shortly after that Sung et al. published a similar example<sup>[84]</sup> and within both studies the monofunctionalized NPs were assembled to dimeric structures with TEM investigations clearly confirming their identity.<sup>[83,84]</sup> The usefulness of solid supports was further improved by introducing noncovalent attachment to the polymer resins (Figure 9b) permitting the use of milder, less acidic conditions for the cleavage.<sup>[85]</sup>



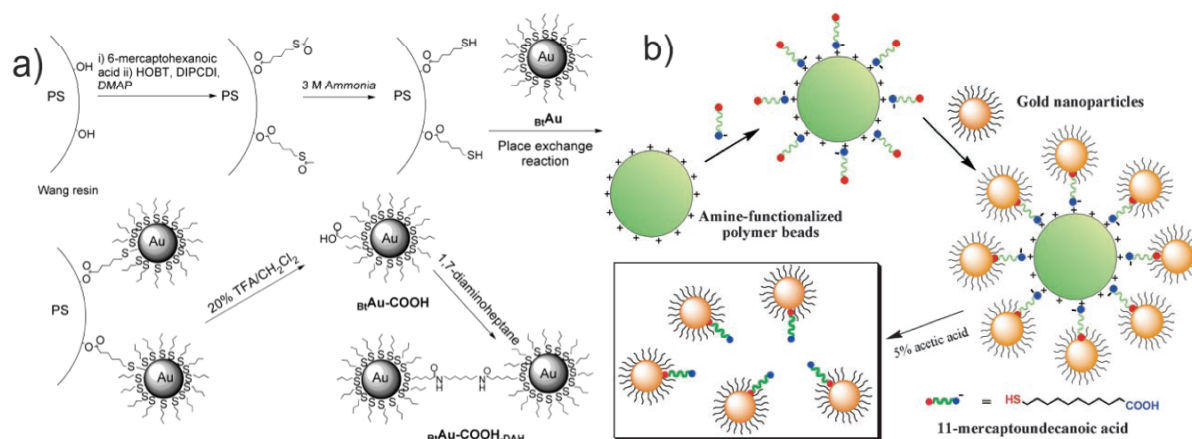


Figure 9. Schematic of the stepwise formation of monofunctionalized Au NPs using molecular exchange with a polymer resin: a) the alkanethiol is covalently attached to the resin, from Reference[83]; b) the alkanethiol is immobilized on the polymer beads using noncovalent interaction, from Reference [85].

Shumaker-Parry and coworkers used a glass surface as solid support for the asymmetric functionalization of Au NPs with a diameter of 41 nm.<sup>[86]</sup> This allowed the introduction of different functionalities upon removal from the glass surface. A drawback of this technique was the presence of an unknown number of functional ligands. However, this unknown number seemed to be low and concentrated to just one area of the surface. These NPs, each bearing either a carboxylic acid or an amine, were coupled with each other to form mostly dimers and therefore could be described as quasi monofunctionalized.<sup>[86]</sup> This means that the NPs behave in monofunctional nature although multiple functionalities are present. The versatility of this protocol was later proven using smaller 18 nm diameter NPs and other binding motifs for the formation of dimeric structures, while the stabilization was improved by using trivalent thiols.<sup>[87]</sup> Mirkin and coworkers used SiO<sub>2</sub> particles (much larger than the Au NPs) as a basis for this asymmetric functionalization.<sup>[88]</sup> Au NPs stabilized with multiple DNA strands were hybridized onto the SiO<sub>2</sub> particle and the free DNA strands were blocked. After tailored melting of the first duplex quasi monofunctionalized Au NPs were obtained and successfully assembled around a larger multifunctionalized NP to obtain a satellite structure (Figure 10a).<sup>[88]</sup> This concept was further improved by Li et al. who obtained truly mono-DNA-functionalized Au NPs.<sup>[89]</sup> They also used relatively large SiO<sub>2</sub> particles and introduced a bulky DNA functionality after removal from the solid support to block the attachment of a second functionality (Figure 10b). In general, the utilization of solid supports is an elegant way for controlled functionalization of Au NPs. One drawback

is that an excess of NPs is required in order to favor monofunctionalization, which leads to lower yields. While there are several examples of the solid support approach for DNA or peptide labeled NPs, our impression is that commercial 'Nanogold' and NPs purified by gel electrophoresis are the two most common approaches to obtain monofunctionalized NPs in aqueous media. As the controlled functionalization in aqueous solvents was studied to a greater extent, solid supports seem to be more convenient for nonpolar organic media. Therefore, the following examples will mostly focus on controlled functionalization in organic solvents.

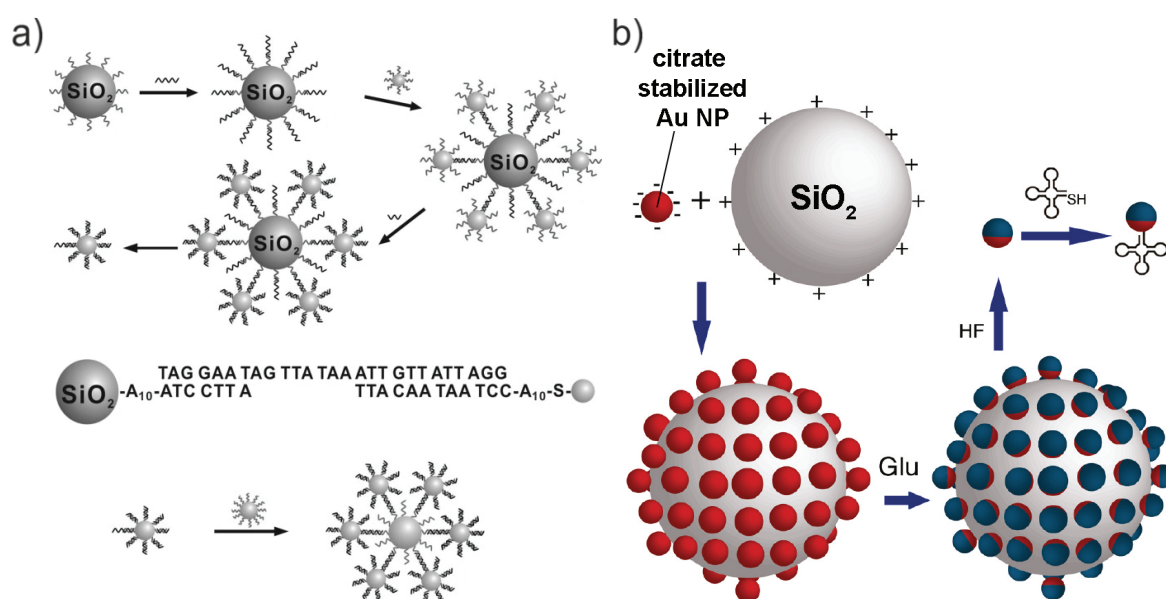
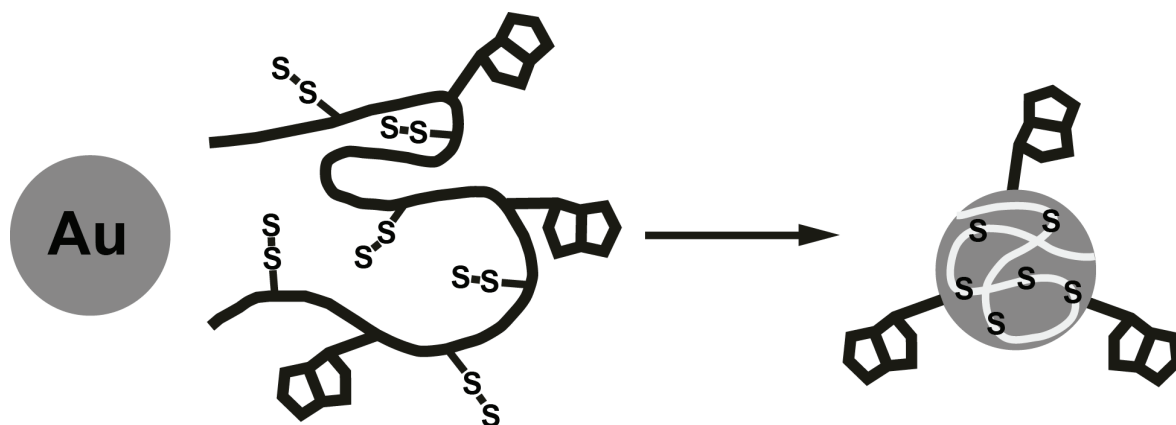


Figure 10. The concept of asymmetric functionalization to obtain a) quasi-monofunctionalized and b) truly monofunctionalized Au NPs. Initially Au NPs are bound to a larger  $\text{SiO}_2$  particle and their free surface is blocked against further functionalization. Upon cleavage from the larger particle either quasi-monofunctionalized NPs are obtained with just a small surface area available for functionalization. If the functional group of choice is relatively large monofunctionalized Au NPs are obtained; adapted from References [88,89].

Ligand polymerization on the NP surface was another successful attempt to synthesize monofunctional NPs.<sup>[90]</sup> 4-Vinylthiophenol was used as a stabilizing ligand for Au NPs (diameter between 2 nm and 5 nm) and was polymerized on the NP surface. A controlled free radical polymerization was performed under high dilution conditions and with small amounts of starter molecules that contained a carboxylic acid group. This led to the introduction of just one carboxylic acid group on the NP surface. The NPs were dimerized and attached onto polypeptide chains, confirming the monofunctionalization.

The approaches described so far mostly produced NPs bearing one functionality while unfunctional ligands are still present on the NP surface. All approaches needed further purification steps or additional reactions of the initial NP in order to obtain monofunctional NPs. On the other hand, a macromolecular stabilizing ligand able to cover the entire or most of the NP surface could provide a more efficient route to monofunctional NPs. This concept was first reported in 2004 by Wilson and coworkers.<sup>[91]</sup> They prepared dextran polymers that contained many disulfide bonds and were big enough to enwrap an entire Au NP, 15 nm in diameter. On average, one NP was stabilized by one polymer molecule (Scheme 1). To our knowledge this was the first report of a one-to-one ratio of NP and stabilizing ligand. While in this case the polymer carried several functionalities, a new concept was introduced towards mono-functionalization.

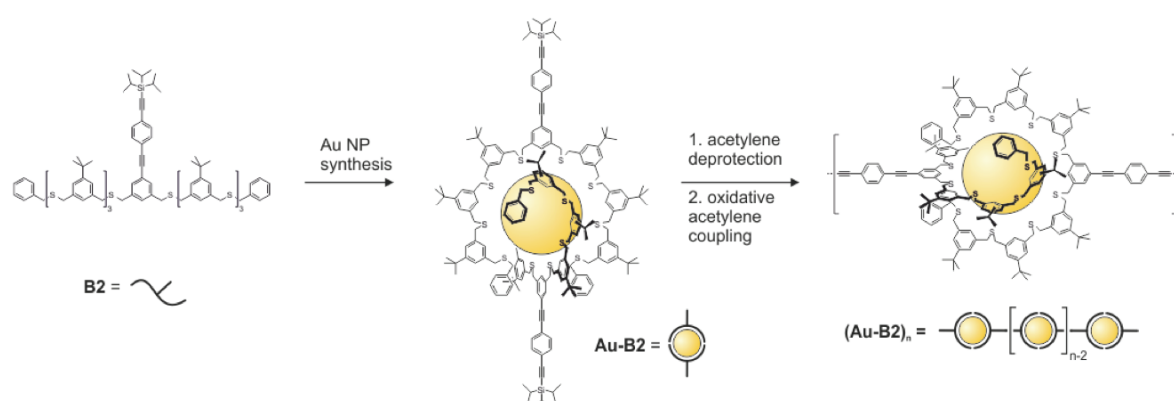


Scheme 1. The concept of enwrapping of a 15 nm gold nanoparticle with a single polymer molecule, adapted from Reference [91].

The dodecadentate ligand **5** introduced by Kiedrowski and coworkers (Figure 2), which was able to solely stabilize one Au<sub>55</sub> Schmid-cluster also carried a functionality leading to the successful formation of a monofunctional Au clusters.<sup>[40]</sup> The gold clusters were attached to a single stranded DNA of interest for performing temperature dependent studies on the DNA duplex formation.<sup>[40]</sup> This DNA melting was performed in order to study the thermostability of the label.

The concept of introducing the desired functionality into a macromolecular ligand was also used by Peterle et al. in our research group.<sup>[92]</sup> Benzylic thioethers were assembled as linear oligomers to form octadentate ligands. The thioether ligand was functionalized with an oligo phenylene ethynylene (OPE) rod already present before the Au NP formation (Scheme 2). Functional Au NPs were directly obtained and closer investigation showed that the Au NPs are on average bifunctional, carrying

two terminal protected acetylenes. These acetylenes were used to covalently assemble the NP monomers to NP superstructures by an oxidative homocoupling protocol.<sup>[92,93]</sup> Divalent NPs were also formed by Stellacci and coworkers.<sup>[94]</sup> They selectively functionalized Au NPs by ligand exchange. This place exchange was found to be favored at diametrically opposed positions due to polar defects occurring when a curved NP surface is coated with an ordered monolayer. The divalent NPs were used to form 1D-chains with different NP distances depending on the diamine linker used for the assembly.<sup>[94]</sup>



Scheme 2. Concept of using pre-functionalized macromolecular ligands to introduce the desired functionality already within the NP formation, adapted from Reference [93].

## 1.5 Assembly of Nanoparticles to Form Hybrid Superstructures

We will shortly present various approaches used for the formation of NP architectures. The possibilities to assemble Au NPs are as broad as the various chemical or physical interactions we can imagine. As mentioned earlier, well orientated NP assemblies can be obtained by using DNA,<sup>[53,70,74,88,95–98]</sup> acetylene homocoupling<sup>[92]</sup>, amide formation,<sup>[83,84,90]</sup> click-chemistry<sup>[99]</sup>, and dithiol linkers.<sup>[10,29,51,52,100–105]</sup> Other examples of the covalent assembly of Au NPs are Diels-Alder reactions,<sup>[106,107]</sup> oxidative homocouplings of thiophene and pyrrole,<sup>[108]</sup> and the light triggered reaction of *o*-nitrobenzylalcohol with benzylamine.<sup>[109]</sup> Assemblies can also be achieved with non-covalent linkages including host-guest interactions,<sup>[61,110]</sup> hydrogen bonding,<sup>[111–113]</sup> coordinate bonds,<sup>[114]</sup>  $\pi$ - $\pi$ <sup>[115]</sup> and charge-transfer<sup>[116]</sup> interactions. Figure 11 depicts some of the concepts used for the assembly of Au NPs.

In order to achieve controlled assemblies of NPs such as dumbbells, chains and 2D-networks it is important to either control the number of functionalities on the NP

surface or control the NP linker ratio (see previous section). Within the present thesis we aim for Au NPs bearing a controlled low number of functionalities for their further assembly.

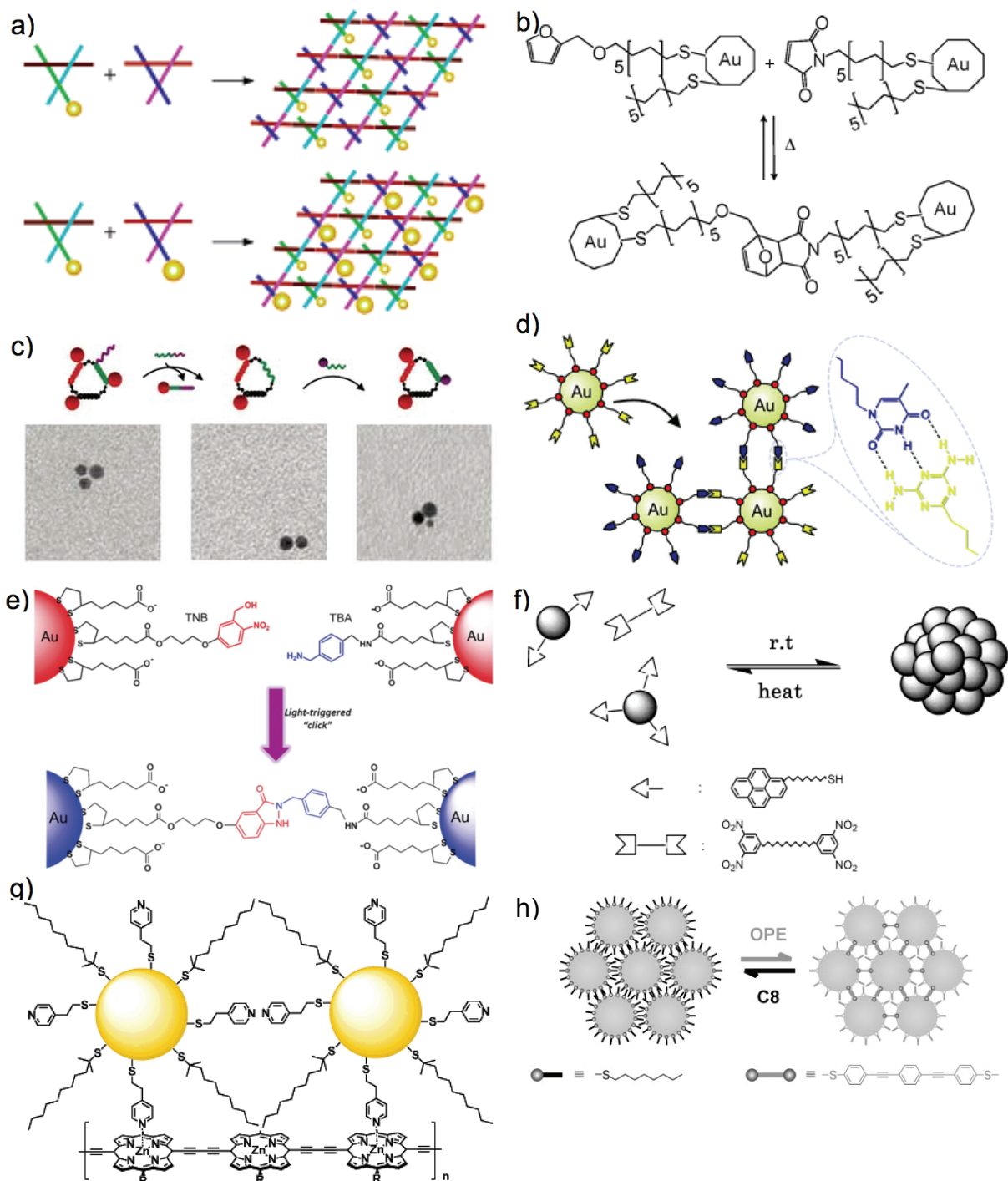


Figure 11. Various concepts for the assembly of Au NPs. NP superstructures are formed by a) DNA tiles (adapted from [71]), b) reversible Diels-Alder reactions (adapted from [106]), c) DNA templates (from [75]), d) hydrogen-bonding (from [113]), e) light triggered indazolone formation (from [109]), f)  $\pi$ -stacking of electron-rich and electron-poor aromatic moieties (from [116]), g) coordinate bonds (from [114]) and h) dithiol linkers (from [29]).

## 1.6 References

- [1] M.-C. Daniel, D. Astruc, *Chem. Rev.* **2004**, *104*, 293–346.
- [2] M. Homberger, U. Simon, *Phil. Trans. R. Soc. A* **2010**, *368*, 1405–1453.
- [3] R. Sardar, A. M. Funston, P. Mulvaney, R. W. Murray, *Langmuir* **2009**, *25*, 13840–13851.
- [4] H. Goesmann, C. Feldmann, *Angew. Chem. Int. Ed.* **2010**, *49*, 1362–1395.
- [5] M. Faraday, *Phil. Trans. R. Soc. Lond.* **1857**, *147*, 145–181.
- [6] J. Turkevich, P. C. Stevenson, J. Hillier, *Discuss. Faraday Soc.* **1951**, *11*, 55.
- [7] G. Schmid, R. Pfeil, R. Boese, F. Bändermann, S. Meyer, G. H. M. Calis, J. W. A. van der Velden, *Chem. Ber.* **1981**, *114*, 3634–3642.
- [8] G. Schmid, *Chem. Rev.* **1992**, *92*, 1709–1727.
- [9] M. Brust, M. Walker, D. Bethell, D. J. Schiffrin, R. Whyman, *J. Chem. Soc., Chem. Commun.* **1994**, 801–802.
- [10] M. Brust, D. J. Schiffrin, D. Bethell, C. J. Kiely, *Adv. Mater.* **1995**, *7*, 795–797.
- [11] J. F. Hainfeld, F. R. Furuya, *J Histochem Cytochem* **1992**, *40*, 177–184.
- [12] H. Häkkinen, *Chem. Soc. Rev.* **2008**, *37*, 1847–1859.
- [13] J. M. Romo-Herrera, R. A. Alvarez-Puebla, L. M. Liz-Marzán, *Nanoscale* **2011**, *3*, 1304.
- [14] P. K. Jain, M. A. El-Sayed, *Chem. Phys. Lett.* **2010**, *487*, 153–164.
- [15] G. Schmid, *Chem. Soc. Rev.* **2008**, *37*, 1909–1930.
- [16] S.-J. Kim, J.-S. Lee, *Nano Lett.* **2010**, *10*, 2884–2890.
- [17] I. Willner, B. Willner, *Nano Lett.* **2010**, *10*, 3805–3815.
- [18] R. D. Powell, J. F. Hainfeld, *Micron* **2011**, *42*, 163–174.
- [19] J. I. Cutler, E. Auyeung, C. A. Mirkin, *J. Am. Chem. Soc.* **2012**, *134*, 1376–1391.
- [20] L. Dykman, N. Khlebtsov, *Chem. Soc. Rev.* **2012**, *41*, 2256.
- [21] R. Wilson, *Chem. Soc. Rev.* **2008**, *37*, 2028–2045.
- [22] Z. Wang, Y. Lu, *J. Mater. Chem.* **2009**, *19*, 1788.
- [23] X. Zhang, Q. Guo, D. Cui, *Sensors* **2009**, *9*, 1033–1053.
- [24] C. Della Pina, E. Falletta, L. Prati, M. Rossi, *Chem. Soc. Rev.* **2008**, *37*, 2077–2095.
- [25] A. Corma, H. Garcia, *Chem. Soc. Rev.* **2008**, *37*, 2096–2126.
- [26] R. A. Sperling, W. J. Parak, *Phil. Trans. R. Soc. A* **2010**, *368*, 1333–1383.
- [27] G. Schmid, *Adv. Eng. Mater.* **2001**, *3*, 737–743.
- [28] L. B. Bangs, *Pure Appl. Chem.* **1996**, *68*, 1873–1879.
- [29] J. Liao, L. Bernard, M. Langer, C. Schönenberger, M. Calame, *Adv. Mater.* **2006**, *18*, 2444–2447.
- [30] J. F. Hainfeld, *Science* **1987**, *236*, 450–453.
- [31] M. Karg, N. Schelero, C. Oppel, M. Gradzielski, T. Hellweg, R. von Klitzing, *Chem. Eur. J.* **2011**, *17*, 4648–4654.
- [32] R. Sardar, J. S. Shumaker-Parry, *Chem. Mater.* **2009**, *21*, 1167–1169.
- [33] P. D. Jadzinsky, G. Calero, C. J. Ackerson, D. A. Bushnell, R. D. Kornberg, *Science* **2007**, *318*, 430–433.
- [34] M. W. Heaven, A. Dass, P. S. White, K. M. Holt, R. W. Murray, *J. Am. Chem. Soc.* **2008**, *130*, 3754–3755.
- [35] F. Sander, T. Peterle, N. Ballav, F. von Wrochem, M. Zharnikov, M. Mayor, *J. Phys. Chem. C* **2010**, *114*, 4118–4125.
- [36] D. Thompson, J. P. Hermes, A. J. Quinn, M. Mayor, *ACS Nano* **2012**, *6*, 3007–3017.

- [37] X.-M. Li, M. R. de Jong, K. Inoue, S. Shinkai, J. Huskens, D. N. Reinhoudt, *J. Mater. Chem.* **2001**, *11*, 1919–1923.
- [38] H.-M. Huang, C.-Y. Chang, I.-C. Liu, H.-C. Tsai, M.-K. Lai, R. C.-C. Tsiang, *J. Polym. Sci. A Polym. Chem.* **2005**, *43*, 4710–4720.
- [39] W. M. Pankau, G. von Kiedrowski, K. Verbist, *Chem. Commun.* **2001**, 519–520.
- [40] W. M. Pankau, S. Mönninghoff, G. von Kiedrowski, *Angew. Chem. Int. Ed.* **2006**, *45*, 1889–1891.
- [41] A. Taubert, U.-M. Wiesler, K. Müllen, *J. Mater. Chem.* **2003**, *13*, 1090–1093.
- [42] Y. Hosokawa, S. Maki, T. Nagata, *Bull. Chem. Soc. Jpn.* **2005**, *78*, 1773–1782.
- [43] I. Hussain, S. Graham, Z. Wang, B. Tan, D. C. Sherrington, S. P. Rannard, A. I. Cooper, M. Brust, *J. Am. Chem. Soc.* **2005**, *127*, 16398–16399.
- [44] D. Wan, Q. Fu, J. Huang, *J. Appl. Polym. Sci.* **2006**, *101*, 509–514.
- [45] E. Boisselier, A. K. Diallo, L. Salmon, C. Ornelas, J. Ruiz, D. Astruc, *J. Am. Chem. Soc.* **2010**, *132*, 2729–2742.
- [46] R. M. Crooks, M. Zhao, L. Sun, V. Chechik, L. K. Yeung, *Acc. Chem. Res.* **2001**, *34*, 181–190.
- [47] K. Esumi, A. Kameo, A. Suzuki, K. Torigoe, *Colloids Surf. A* **2001**, *189*, 155–161.
- [48] A. D'Aléo, R. M. Williams, F. Osswald, P. Edamana, U. Hahn, J. van Heyst, F. D. Tichelaar, F. Vögtle, L. De Cola, *Adv. Funct. Mater.* **2004**, *14*, 1167–1177.
- [49] G. Bergamini, P. Ceroni, V. Balzani, M. Gingras, J.-M. Raimundo, V. Morandi, P. G. Merli, *Chem. Commun.* **2007**, 4167.
- [50] T. Peterle, A. Leifert, J. Timper, A. Sologubenko, U. Simon, M. Mayor, *Chem. Commun.* **2008**, 3438–3440.
- [51] L. C. Brousseau III, J. P. Novak, S. M. Marinakos, D. L. Feldheim, *Adv. Mater.* **1999**, *11*, 447–449.
- [52] T. Dadosh, Y. Gordin, R. Krahné, I. Khivrich, D. Mahalu, V. Frydman, J. Sperling, A. Yacoby, I. Bar-Joseph, *Nature* **2005**, *436*, 677–680.
- [53] M. Fischler, A. Sologubenko, J. Mayer, G. Clever, G. Burley, J. Gierlich, T. Carell, U. Simon, *Chem. Commun.* **2008**, 169–171.
- [54] F. Westerlund, T. Bjørnholm, *Curr. Opin. Colloid In.* **2009**, *14*, 126–134.
- [55] C. L. Choi, A. P. Alivisatos, *Annu. Rev. Phys. Chem.* **2010**, *61*, 369–389.
- [56] M. Grzelczak, J. Vermant, E. M. Furst, L. M. Liz-Marzán, *ACS Nano* **2010**, *4*, 3591–3605.
- [57] C. P. Shaw, D. G. Fernig, R. Lévy, *J. Mater. Chem.* **2011**, *21*, 12181.
- [58] T. Zhang, Z. Yang, D. Liu, *Nanoscale* **2011**, *3*, 4015.
- [59] M. Sikora, P. Szymczak, D. Thompson, M. Cieplak, *Nanotechnology* **2011**, *22*, 445601.
- [60] H. Häkkinen, *Nat. Chem.* **2012**, *4*, 443–455.
- [61] M. A. Olson, A. Coskun, R. Klajn, L. Fang, S. K. Dey, K. P. Browne, B. A. Grzybowski, J. F. Stoddart, *Nano Lett.* **2009**, *9*, 3185–3190.
- [62] J. F. Hainfeld, R. D. Powell, *J. Histochem. Cytochem* **2000**, *48*, 471–480.
- [63] Q. Huo, J. G. Worden, *J Nanopart Res* **2006**, *9*, 1013–1025.
- [64] Zou Jianhua, Dai Qiu, Guda Ramakrishna, Liu Xiong, Worden James G., Goodson Theodore, Huo Qun, in *Nanoparticles: Synthesis, Stabilization, Passivation, and Functionalization*, American Chemical Society, **2008**, pp. 31–40.
- [65] J. E. Reardon, P. A. Frey, *Biochemistry* **1984**, *23*, 3849–3856.
- [66] D. Safer, L. Bolinger, J. S. Leigh Jr., *J. Inorg. Biochem.* **1986**, *26*, 77–91.

- [67] D. Zanchet, C. M. Micheel, W. J. Parak, D. Gerion, A. P. Alivisatos, *Nano Lett.* **2001**, *1*, 32–35.
- [68] S. A. Claridge, A. J. Mastroianni, Y. B. Au, H. W. Liang, C. M. Micheel, J. M. J. Fréchet, A. P. Alivisatos, *J. Am. Chem. Soc.* **2008**, *130*, 9598–9605.
- [69] C. J. Loweth, W. B. Caldwell, X. Peng, A. P. Alivisatos, P. G. Schultz, *Angew. Chem. Int. Ed.* **1999**, *38*, 1808–1812.
- [70] F. A. Aldaye, H. F. Sleiman, *Angew. Chem. Int. Ed.* **2006**, *45*, 2204–2209.
- [71] J. Zheng, P. E. Constantinou, C. Micheel, A. P. Alivisatos, R. A. Kiehl, N. C. Seeman, *Nano Lett.* **2006**, *6*, 1502–1504.
- [72] J. Sharma, R. Chhabra, Y. Liu, Y. Ke, H. Yan, *Angew. Chem. Int. Ed.* **2006**, *45*, 730–735.
- [73] J. Sharma, R. Chhabra, C. S. Andersen, K. V. Gothelf, H. Yan, Y. Liu, *J. Am. Chem. Soc.* **2008**, *130*, 7820–7821.
- [74] J. D. Le, Y. Pinto, N. C. Seeman, K. Musier-Forsyth, T. A. Taton, R. A. Kiehl, *Nano Lett.* **2004**, *4*, 2343–2347.
- [75] F. A. Aldaye, H. F. Sleiman, *J. Am. Chem. Soc.* **2007**, *129*, 4130–4131.
- [76] T. Tamaki, N. Miyoshi, T. Uehara, Y. Ohya, *Chemistry Letters* **2010**, *39*, 1084–1085.
- [77] K. Suzuki, K. Hosokawa, M. Maeda, *J. Am. Chem. Soc.* **2009**, *131*, 7518–7519.
- [78] R. Lévy, Z. Wang, L. Duchesne, R. C. Doty, A. I. Cooper, M. Brust, D. G. Fernig, *ChemBioChem* **2006**, *7*, 592–594.
- [79] J. F. Hainfeld, W. Liu, C. M. R. Halsey, P. Freimuth, R. D. Powell, *J. Struct. Biol.* **1999**, *127*, 185–198.
- [80] L. Duchesne, D. Gentili, M. Comes-Franchini, D. G. Fernig, *Langmuir* **2008**, *24*, 13572–13580.
- [81] M. Bruning, L. Kreplak, S. Leopoldseder, S. A. Müller, P. Ringler, L. Duchesne, D. G. Fernig, A. Engel, Z. Ucurum-Fotiadis, O. Mayans, *Nano Lett.* **2010**, *10*, 4533–4537.
- [82] C.-P. Chak, S. Xuan, P. M. Mendes, J. C. Yu, C. H. K. Cheng, K. C.-F. Leung, *ACS Nano* **2009**, *3*, 2129–2138.
- [83] J. G. Worden, A. W. Shaffer, Q. Huo, *Chem. Commun.* **2004**, 518–519.
- [84] K.-M. Sung, D. W. Mosley, B. R. Peelle, S. Zhang, J. M. Jacobson, *J. Am. Chem. Soc.* **2004**, *126*, 5064–5065.
- [85] X. Liu, J. G. Worden, Q. Dai, J. Zou, J. Wang, Q. Huo, *Small* **2006**, *2*, 1126–1129.
- [86] R. Sardar, T. B. Heap, J. S. Shumaker-Parry, *J. Am. Chem. Soc.* **2007**, *129*, 5356–5357.
- [87] A. Hofmann, P. Schmiel, B. Stein, C. Graf, *Langmuir* **2011**, *27*, 15165–15175.
- [88] F. Huo, A. K. R. Lytton-Jean, C. A. Mirkin, *Adv. Mater.* **2006**, *18*, 2304–2306.
- [89] Z. Li, E. Cheng, W. Huang, T. Zhang, Z. Yang, D. Liu, Z. Tang, *J. Am. Chem. Soc.* **2011**, *133*, 15284–15287.
- [90] C. Krüger, S. Agarwal, A. Greiner, *J. Am. Chem. Soc.* **2008**, *130*, 2710–2711.
- [91] R. Wilson, Y. Chen, J. Aveyard, *Chem. Commun.* **2004**, 1156.
- [92] T. Peterle, P. Ringler, M. Mayor, *Adv. Funct. Mater.* **2009**, *19*, 3497–3506.
- [93] J. P. Hermes, F. Sander, T. Peterle, C. Cioffi, P. Ringler, T. Pfohl, M. Mayor, *Small* **2011**, *7*, 920–929.
- [94] G. A. DeVries, M. Brunnbauer, Y. Hu, A. M. Jackson, B. Long, B. T. Neltner, O. Uzun, B. H. Wunsch, F. Stellacci, *Science* **2007**, *315*, 358–361.
- [95] Z. Deng, Y. Tian, S.-H. Lee, A. E. Ribbe, C. Mao, *Angew. Chem. Int. Ed.* **2005**, *44*, 3582–3585.



- [96] S. E. Stanca, R. Eritja, D. Fitzmaurice, *Faraday Discuss.* **2006**, *131*, 155–165.
- [97] J. H. Lee, D. P. Wernette, M. V. Yigit, J. Liu, Z. Wang, Y. Lu, *Angew. Chem. Int. Ed.* **2007**, *46*, 9006–9010.
- [98] M. H. S. Shyr, D. P. Wernette, P. Wiltzius, Y. Lu, P. V. Braun, *J. Am. Chem. Soc.* **2008**, *130*, 8234–8240.
- [99] R. Voggu, P. Suguna, S. Chandrasekaran, C. N. R. Rao, *Chem. Phys. Lett.* **2007**, *443*, 118–121.
- [100] R. P. Andres, J. D. Bielefeld, J. I. Henderson, D. B. Janes, V. R. Kolagunta, C. P. Kubiak, W. J. Mahoney, R. G. Osifchin, *Science* **1996**, *273*, 1690–1693.
- [101] V. Torma, O. Vidoni, U. Simon, G. Schmid, *Eur. J. Inorg. Chem.* **2003**, 1121–1127.
- [102] R. Klajn, T. P. Gray, P. J. Wesson, B. D. Myers, V. P. Dravid, S. K. Smoukov, B. A. Grzybowski, *Adv. Funct. Mater.* **2008**, *18*, 2763–2769.
- [103] L. Bernard, Y. Kamdzhilov, M. Calame, S. J. van der Molen, J. Liao, C. Schönenberger, *J. Phys. Chem. C* **2007**, *111*, 18445–18450.
- [104] J. Liao, M. A. Mangold, S. Grunder, M. Mayor, C. Schönenberger, M. Calame, *New J. Phys.* **2008**, *10*, 065019.
- [105] H. Yan, S. I. Lim, Y.-J. Zhang, Q. Chen, D. Mott, W.-T. Wu, D.-L. An, S. Zhou, C.-J. Zhong, *Chem. Commun.* **2010**, *46*, 2218–2220.
- [106] J. Zhu, A. J. Kell, M. S. Workentin, *Org. Lett.* **2006**, *8*, 4993–4996.
- [107] X. Liu, H. Liu, W. Zhou, H. Zheng, X. Yin, Y. Li, Y. Guo, M. Zhu, C. Ouyang, D. Zhu, A. Xia, *Langmuir* **2010**, *26*, 3179–3185.
- [108] G. Zotti, B. Vercelli, A. Berlin, *Chem. Mater.* **2008**, *20*, 397–412.
- [109] J. Lai, Y. Xu, X. Mu, X. Wu, C. Li, J. Zheng, C. Wu, J. Chen, Y. Zhao, *Chem. Commun.* **2011**, *47*, 3822.
- [110] R. Klajn, M. A. Olson, P. J. Wesson, L. Fang, A. Coskun, A. Trabolsi, S. Soh, J. F. Stoddart, B. A. Grzybowski, *Nat. Chem.* **2009**, *1*, 733–738.
- [111] A. K. Boal, F. Ilhan, J. E. DeRouchey, T. Thurn-Albrecht, T. P. Russell, V. M. Rotello, *Nature* **2000**, *404*, 746–748.
- [112] S. Fullam, H. Rensmo, S. N. Rao, D. Fitzmaurice, *Chem. Mater.* **2002**, *14*, 3643–3650.
- [113] C. R. van den Brom, P. Rudolf, T. T. M. Palstra, B. Hessen, *Chem. Commun.* **2007**, 4922–4924.
- [114] H. Ozawa, M. Kawao, H. Tanaka, T. Ogawa, *Langmuir* **2007**, *23*, 6365–6371.
- [115] M. Kanehara, E. Kodzuka, T. Teranishi, *J. Am. Chem. Soc.* **2006**, *128*, 13084–13094.
- [116] K. Naka, H. Itoh, Y. Chujo, *Langmuir* **2003**, *19*, 5496–5501.

## 2 Concept and Strategy

### 2.1 Previous Work

In 2008 and 2009 our research group introduced a new concept for the stabilization and functionalization of Au NPs.<sup>[1,2]</sup> By using macromolecular octadentate thioether ligands (Figure 12a) stable NPs with 1 nm diameter were obtained. The thioether moieties in the benzylic position provided sufficient flexibility needed to enwrap the curved NP surface. The *tert*-butyl functionalized benzene bridges ensured the NP stability by forming a protective ligand shell. The ligands were further functionalized in their center with a protected acetylene on an oligo phenylene ethynylene (OPE) rod. In the presence of these functional ligands Au NPs were formed following the Brust-Schiffrin-method<sup>[3]</sup> where they were directly functionalized in their periphery. Therefore, the two steps required for the formation and the subsequent functionalization of Au NPs (compare Figure 5) were combined in one (long green arrow in Figure 12b). As a result, Au NPs carrying two functional groups on their periphery were obtained. After deprotection, the free acetylenes were used to form NP oligomers by oxidative homocoupling. The investigation of the interparticle spacings of coupled NPs revealed distances shorter than expected. These studies were reviewed within the first paper of this thesis, published in *CHIMIA*.<sup>[4]</sup>

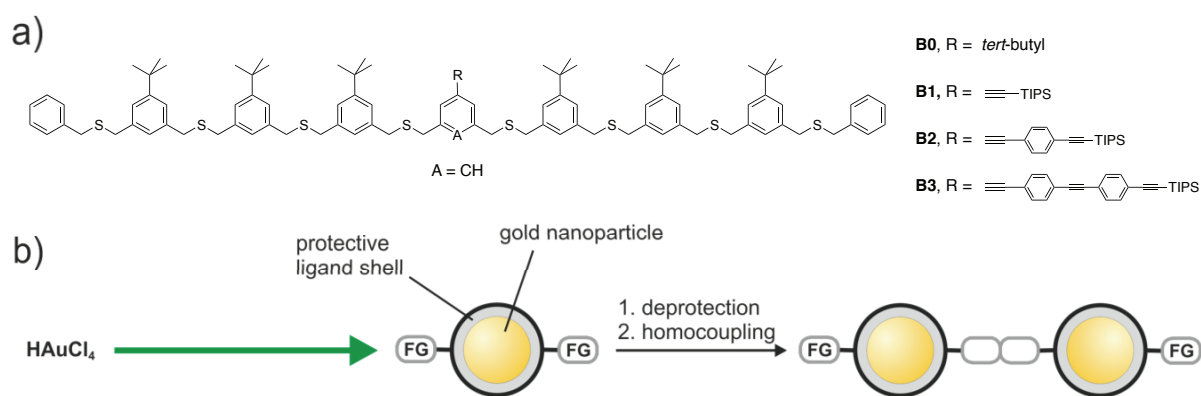


Figure 12. a) Octadentate thioether ligands that were used for the formation and functionalization of Au NPs, A = anchor point of functionality. b) The concept introduced by Peterle et al. to directly form functional Au NPs by reduction of Au<sup>3+</sup>. The long green arrow represents NP formation and functionalization achieved in one step, FG = functional group.

## 2.2 Goals and Results

The goal of the present thesis was to investigate two outputs of the work of Peterle et al. in more detail: 1) the interparticle distance should be investigated and extended in order to increase the control of NP architectures and 2) the monofunctionalization of Au NPs was envisaged (Figure 13). The monofunctionality is desired for applications as labels and for NP dumbbells, which might find use as architectures in molecular electronics.

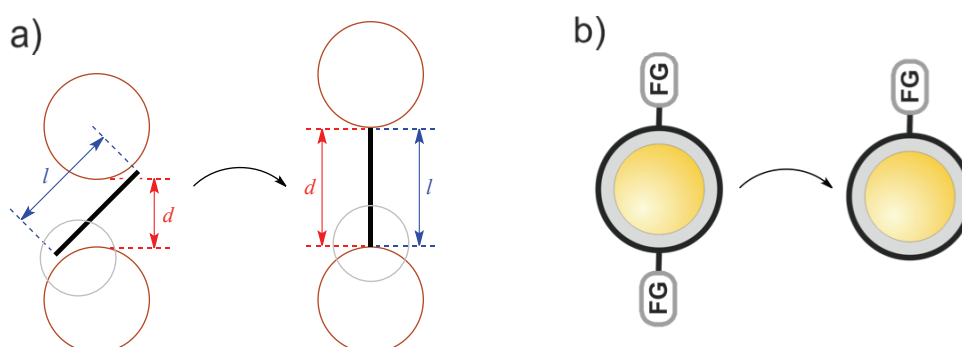


Figure 13. The two main goals of this thesis: a) to control the distance of NP oligomers and b) to form monofunctionalized Au NPs, FG = functional group.

The first goal was approached by investigating the anchor point of the functional OPE rod on the NP surface (Figure 14a,b). Initially the OPE rod was attached on a central benzene ring (Figure 12a). We proposed that the steric repulsion of the benzene's central hydrogen led to a tilted arrangement on the surface and thus a reduced interparticle distance (Figure 14a). A new series of octadentate thioether ligands was synthesized with an anchor group based on pyridine and Au NPs were formed in their presence. Pyridine was chosen as the anchor group because no hydrogen is present in the ligand structure and the nitrogen's lonepair could coordinate to the gold surface. This coordination should lead to perpendicular arrangement on the NP surface (Figure 14b). NPs were formed in the presence of the old and new octadentate ligand series and functionalized NPs were obtained, which had similar size distributions around 1.1 nm diameter. The NPs were again coupled to form organic-inorganic hybrid superstructures. Measurements of the interparticle spacing of NP oligomers revealed that the single atom substitution in the ligand design was able to extend the NP distance by forming a perpendicular arrangement on the NP surface. This work was published in *SMALL* and the respective table of contents (TOC) graphic is depicted on Figure 14c.<sup>[5]</sup>

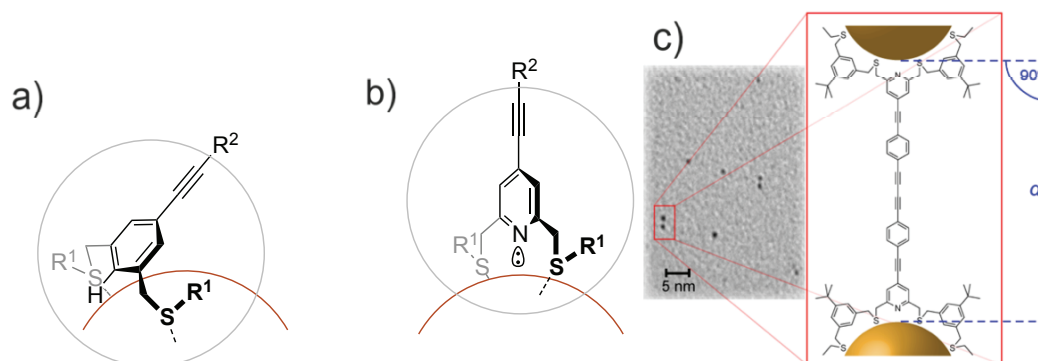


Figure 14. a),b) The proposed arrangement of the functional anchors on the NP surface. c) Table of contents (TOC) graphic of the studies published in *SMALL*.

The second goal was approached by a new ligand design. Dendritic thioether ligands were desired target compounds, as their successful utilization as stabilizing ligands for Au NPs was already shown by other research groups (see Introduction Chapter 1.3). With the knowledge of the linear thioether ligands and the background of previous studies two different types of unfunctional dendrimers were synthesized. Both were multidentate structures with flexible thioether moieties and 1,3,5-trisubstituted benzenes as branching units. Instead of ball-shaped dendrimers we chose to synthesize just one hemisphere for two reasons: i) the ligand should form dendrimer stabilized NPs rather than dendrimer encapsulated NPs (see Figure 3) and ii) the ligands center should be able to carry a functional group. The dendritic branching units were diluted in order to favor longer arms over a three-dimensional space filling. This should enable the dendrimers to enwrap the curved surface of Au NPs. We found that one class of dendritic ligands did not supply a sufficiently large protective shell leading to aggregation and precipitation of Au NPs. The second series was able to stabilize NPs with a narrow size distribution (Figure 15). The *tert*-butyl functionalized benzene bridges between the branching units were vital for the formation of stable NPs due to the larger protective ligand shell they formed. The number of dendritic ligands required to stabilize one Au NP was investigated. In analogy to the linear octadentate ligands the first generation dendrimers (eight sulfides) also required two ligands for stabilizing Au NPs of 1.1 nm diameter. The second generation dendrimers consisting of 20 thioether moieties were able to stabilize an entire Au NP of 1.2 nm diameter. This already gave the desired one-to-one ratio of NP and ligand, although the NPs still had no functionality as unfunctional dendrimers were used. This research was published in *Chemistry – A European Journal* and Figure 15 shows the respective TOC graphic.<sup>[6]</sup>

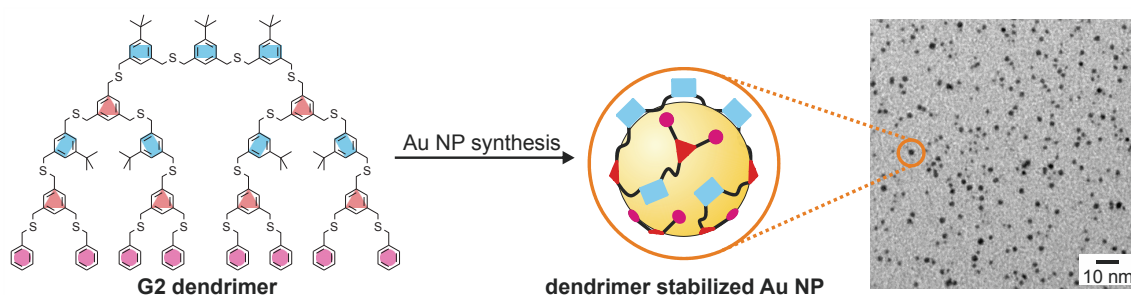


Figure 15. TOC graphic of the research published in *Chemistry – A European Journal*.

We also performed theoretical calculations in order to support the assumption that the dendrimer ligands enwrap the NP (see cartoon of dendrimer-NP assembly in Figure 15). In collaboration with Damien Thompson (Tyndall Institute, Cork, Ireland) the energies of NPs stabilized with one or two dendrimers were calculated, showing clear preferences for just one dendrimer. Besides this the geometry of the functional anchor point on the NP surface was also modeled. We found that the coordination of the nitrogen's lonepair leads to the perpendicular arrangement of the OPE rod on the NPs. The expected steric repulsion of the benzene's additional hydrogen leading to a tilted angle was not supported. We further proposed that monofunctionalized Au NPs will be obtained upon functionalization of the dendrimer. The work was published in *ACS Nano* and Figure 16 depicts the respective TOC graphic.<sup>[7]</sup>

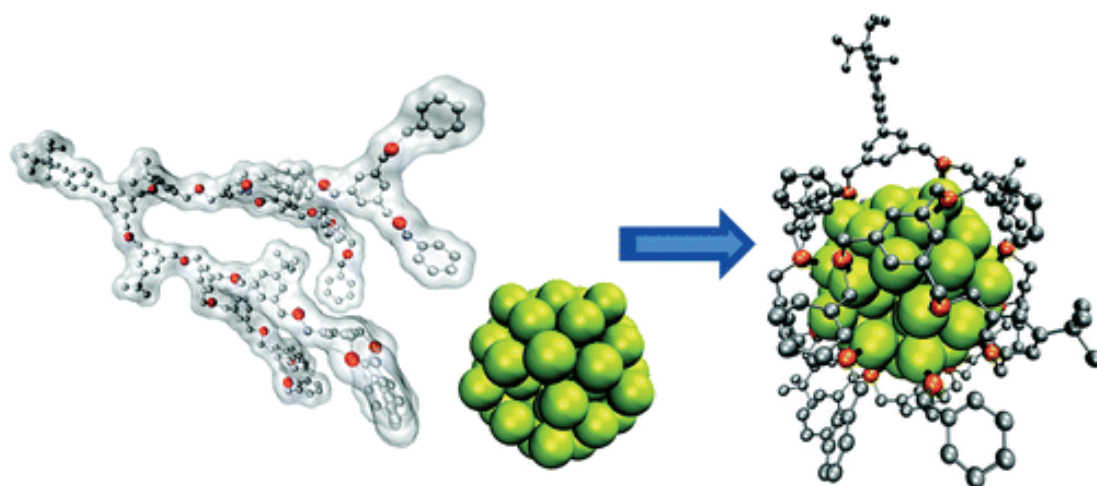


Figure 16. The TOC graphic of the theoretical research published in *ACS Nano*.

A central functionality based on pyridine was introduced in order to obtain functional dendrimers suited to form monofunctional Au NPs. These dendritic ligands were present during the Brust-Schiffrin method and stable NPs were formed. Investigation

showed that the first generation produced bifunctional NP while the second generation indeed carried just one functionality. These functional monomers were assembled to form dumbbell structures with yields close to 50% and interparticle distances expected for a perpendicular arrangement of the OPE rod on the NP surface. The research will be published in the *Journal of the American Chemical Society (J. Am. Chem. Soc)* and the respective TOC graphic is depicted in Figure 17.<sup>[8]</sup>

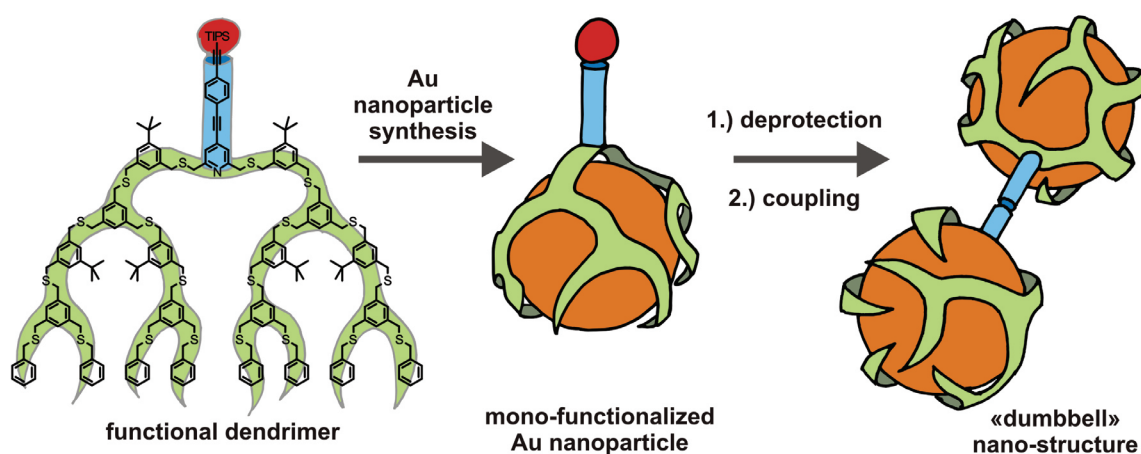


Figure 17. TOC graphic of the research published in *J. Am. Chem. Soc.*

## 2.3 References

- [1] T. Peterle, A. Leifert, J. Timper, A. Sologubenko, U. Simon, M. Mayor, *Chem. Commun.* **2008**, 3438–3440.
- [2] T. Peterle, P. Ringler, M. Mayor, *Adv. Funct. Mater.* **2009**, *19*, 3497–3506.
- [3] M. Brust, M. Walker, D. Bethell, D. J. Schiffrin, R. Whyman, *J. Chem. Soc., Chem. Commun.* **1994**, 801–802.
- [4] J. P. Hermes, F. Sander, T. Peterle, M. Mayor, *CHIMIA* **2011**, *65*, 219–222.
- [5] J. P. Hermes, F. Sander, T. Peterle, C. Cioffi, P. Ringler, T. Pfohl, M. Mayor, *Small* **2011**, *7*, 920–929.
- [6] J. P. Hermes, F. Sander, T. Peterle, R. Urbani, T. Pfohl, D. Thompson, M. Mayor, *Chem. Eur. J.* **2011**, *17*, 13473–13481.
- [7] D. Thompson, J. P. Hermes, A. J. Quinn, M. Mayor, *ACS Nano* **2012**, *6*, 3007–3017.
- [8] J. P. Hermes, F. Sander, U. Fluch, T. Peterle, D. Thompson, R. Urbani, T. Pfohl, M. Mayor, *J. Am. Chem. Soc.* **2012**, *134*, 14674–14677.

### **3 Publications**

# From Ligand-Stabilized Gold Nanoparticles to Hybrid Organic-Inorganic Superstructures

Jens Peter Hermes<sup>§a</sup>, Fabian Sander<sup>a</sup>, Torsten Peterle<sup>ab</sup>, and Marcel Mayor<sup>\*ac</sup>

<sup>§</sup>SCS Metrohm Prize for best oral presentation

**Abstract:** Gold nanoparticles (Au NPs) have many potential applications including nanoelectronics, catalysts and sensors. These future devices depend on stable and monodisperse NPs and their directed assembly. Herein we review our efforts to develop oligomeric thioether ligands able to direct the synthesis of Au NPs and their surface functionalization. A screening of different oligomeric thioethers indicates that the NPs become more stable and monodisperse with increasing length of the thioether oligomer. The heptameric benzylic thioether **4** stabilizes monodisperse NPs with a diameter of 1 nm and excellent long-term stability in solution. It is further monofunctionalized with a central protected acetylene. After NP formation in the presence of the ligands we utilize the peripheral functionality to interlink the NPs. A mild oxidative diacetylene coupling protocol is used to covalently bind these ‘artificial molecules’. This wet-chemical procedure leads to the formation of hybrid organic–inorganic superstructures.

**Keywords:** Gold nanoparticles · Hybrid materials · Organic–inorganic superstructures

## Introduction

Gold is the most frequently used material for metal nanoparticles (NPs). This is due to the efficient synthesis of Au NPs, the advanced state of surface chemistry and their potential as model system for colloids and surfaces.<sup>[1–3]</sup> Au NPs show size-dependent features, providing interesting physical properties, such as room temperature *Coulomb* blockade for small NPs.<sup>[4–6]</sup> Stable and monodisperse NPs are essential for their use in many future technologies, including electronic devices,<sup>[7–11]</sup> sensor applications<sup>[12–17]</sup> and catalysis.<sup>[18,19]</sup> The stabilizing agents in organic solvents are mainly based on thiols<sup>[20]</sup> that show covalent interactions with the gold surface. In

general, thioethers form weak interactions to gold compared to thiols.<sup>[21]</sup> There are however some examples where thioethers have been proven to be suitable ligands for the stabilization of Au NPs.<sup>[22–26]</sup> Increased stability and monodispersity have been reported for multidentate ligands comprising more than one thioether unit.

Below we describe the screening of several multidentate thioether oligomers to find a suitable ligand that enables the formation of stable and monodisperse NPs. A large multidentate structure favors monodisperse NP sizes by enwrapping the whole NP by a well-defined small number of ligands. This concept enables control of the number and nature of functional groups on the NPs’ surface simply by attaching the desired functional group to the ligand. To our knowledge only a few examples describe the realization of mono- and bifunctionalized NPs in organic solvents. The former was realized *via* ligand polymerization on the NPs’ surface<sup>[27]</sup> and reaction on solid supports<sup>[28,29]</sup> and the latter by profiting from the exposed pole positions of monodisperse NPs.<sup>[30,31]</sup> Another major challenge for the integration of NPs in hybrid materials and future devices is their tailored spatial arrangement. Numerous studies geared towards the directed assembly of Au NPs have been reported and several review articles highlight the importance of the field.<sup>[32–37]</sup>

Herein we summarize three recent publications on our research towards in-

terlinked Au NPs. In a first screening of thioether oligomers, a benzylic thioether heptamer was found to be a very promising ligand to stabilize Au NPs.<sup>[38]</sup> It was further functionalized with a protected acetylene. This peripheral functionality was connected *via* an oligophenylene ethynylene (OPE) spacer of different lengths. The acetylene enabled the covalent interlinking of NPs by a mild oxidative diacetylene coupling. The NP size and the spatial arrangement of these hybrid organic–inorganic superstructures were investigated by transmission electron microscopy (TEM).<sup>[39]</sup> In addition we investigated self-assembled monolayers of model compounds to study the sulfur–gold interactions. High-resolution X-ray photoelectron spectroscopy (HRXPS), near-edge X-ray absorption fine structure (NEXAFS) spectroscopy and scanning tunneling microscopy (STM) were used for this purpose.<sup>[21]</sup>

## Ligand-stabilized Gold Nanoparticles

The linear oligothioether ligands **1–4** (Fig. 1) were synthesized and their ability to stabilize and ensnare Au NPs was investigated.<sup>[38]</sup> The goal of this series was to find a ligand that directs the size of small NPs leading to stable and monodisperse NPs. The thioether structure was intended to enable an evenly dispersed surface coverage with a low integer number of ligands.

\*Correspondence: Prof. Dr. M. Mayor<sup>ac</sup>

Tel.: + 41 61 267 71006

Fax: + 41 61 267 71016

E-mail: marcel.mayor@unibas.ch

<sup>a</sup>Department of Chemistry

University of Basel

St. Johannisring 19

CH-4056 Basel

<sup>b</sup>Creavis Technologies & Innovation

Evonik Degussa GmbH

Paul-Baumann-Str. 1

D-45772 Marl, Germany

<sup>c</sup>Karlsruhe Institute of Technology (KIT)

Institute of Nanotechnology

P.O. Box 3640, D-76021 Karlsruhe, Germany



The number of ligands should be transferable to the number of functionalities that could be introduced with the ligand. Au NPs were formed following a protocol developed by Brust *et al.*<sup>[20]</sup> In a two-phase system of water and dichloromethane with tetra-*n*-octylammoniumbromid (TOAB) as phase transfer agent, chloroauric acid was reduced by sodium borohydride in the presence of oligomers **1–4**. Monomer **1** could not prevent the bulk precipitation of gold but also stabilized some NPs. UV/vis spectroscopy showed the presence of a plasmon resonance band in the UV spectrum of Au-**1** indicating NPs larger than 3 nm.<sup>[40]</sup> After several hours these NPs further coagulate and precipitate. Oligomers **2**, **3** and **4** led to the formation of soluble NPs without precipitation. As the ligand-stabilized NPs Au-**2** precipitated within days upon storage in dispersion, we only determined the diameter of NPs Au-**3** and Au-**4** using transmission electron microscopy (TEM). While NPs Au-**3** range from 1 nm to 5 nm, NPs Au-**4** showed a narrow size distribution with a mean diameter of 1 nm (see below). UV/vis spectroscopy proved the excellent long-term stability, as the spectrum of NPs Au-**4** did not change upon storage in dichloromethane over several months. TEM, elemental analysis and thermogravimetry revealed a particle-to ligand ratio of 1:2. Upon ligand functionalization NPs with two peripheral groups should become available. Interestingly, these NPs might be exposed subsequently to wet chemical procedures acting as ‘artificial molecules’.

### Self-assembled Monolayers of Thiol/Thioether Ligands

Self-assembled monolayers (SAMs) of model compounds **5–8** (Fig. 1) were formed on Au(111) to study the gold–li-

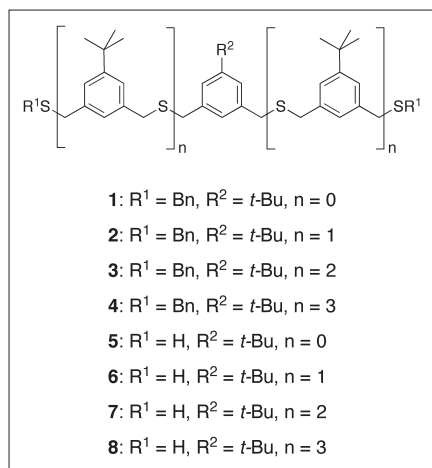


Fig. 1. Model compounds **1–8** used to investigate nanoparticle stabilizing features as well as binding behaviors on gold surfaces.

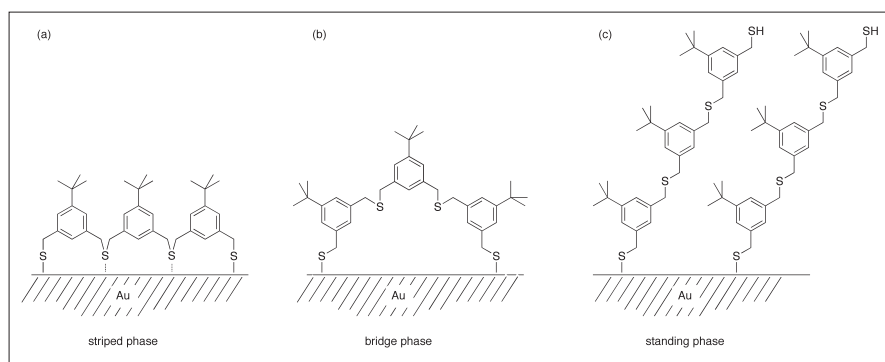


Fig. 2. Schematic representation of possible binding modes of the thiol-thioether oligomer **6** to the gold substrate.

gand interactions.<sup>[21]</sup> These assemblies were investigated by high-resolution X-ray photoelectron spectroscopy (HRXPS), near-edge X-ray absorption fine structure (NEXAFS) spectroscopy and, in the case of molecules **5** and **6**, also by scanning tunneling microscopy (STM).

The question addressed within these investigations is the contribution and quality of the different binding sites. Thus, we were wondering if such oligomers are binding with all binding sites (striped phase, Fig. 2a) or only with the two terminal thiols forming bridge phase arrangements (Fig. 2b). A standing phase (Fig. 2c) would result if only one terminal thiol group were bound to the surface.

The relation of SAM thickness to oligomer size, found by HRXPS, favors the bridge phase assembly displayed in Fig. 2 for these ligands. The monolayer thickness increased with oligomer size showing heights which matched the calculated values for bridge phase arrangements. This hypothesis is further supported by the analysis of the sulfur signals of the HRXPS spectra. In particular the expected ratios of strongly bound and uncoordinated sulfurs were found for the model compounds.

While additional NEXAFS spectra also confirmed the bridge phase model, STM investigations of shorter oligomers **5** and **6** revealed a further insight. The monomer **5** formed a dense packed SAM that was in excellent agreement with the bridge phase model. However the trimer **6** showed a few features with heights indicating unfolded upright standing molecules. This led to the estimation that about 10–20% of the molecules bind only with one thiol group to the substrate (Fig. 2b).

We propose that the observed bridged geometry is driven by the strong thiol–gold interaction. The strongly binding terminal thiols push the weakly coordinating thioether binding sites away from the surface, reducing the ligands’ multidenticity. As the multidentate coordination is desired, a homogeneously balanced sulfur–gold interaction over all binding sites is fundamental.

Therefore we omitted the use of free thiols in our future ligand design.

### Hybrid Organic–Inorganic Superstructures

Based on the ligand investigations described above we choose heptamer **4** for addition of a peripheral functional group. A rigid OPE of different lengths was introduced with a terminal silyl-protected acetylene to obtain ligands **9–11** (Fig. 3).<sup>[39]</sup>

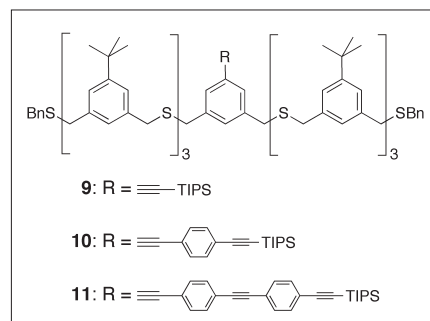


Fig. 3. Ligands **9–11** comprising a protected acetylene as an additional peripheral functional group for interlinking nanoparticles to organic–inorganic superstructures.

NPs were formed in the presence of these monofunctionalized ligands following the same protocol as for Au-(**1–4**). After removal of excess ligand the samples only contained ligand-stabilized NPs Au-**9**, Au-**10** and Au-**11**. The obtained UV/vis spectra were very similar to the spectrum of heptamer-stabilized NPs Au-**4** with differences between 300 nm and 400 nm, due to the elongation of the functional OPE unit in the ligands center. As this feature was clearly visible we confirmed that we obtained functional NPs with the OPE structure at their periphery. The ligand-stabilized NPs were further investigated by TEM. The analysis of micrographs indicated the same narrow NP size distributions of 1 nm as the unfunctionalized heptamer **4** (see below). This indicates that the

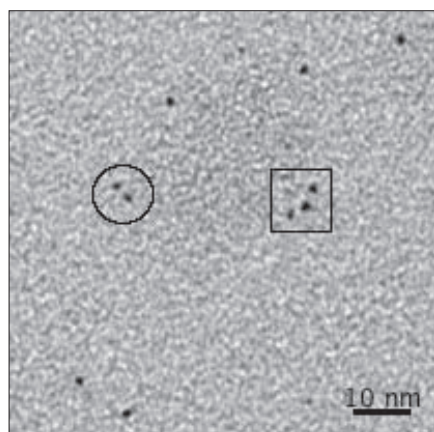


Fig. 4. Representative TEM micrograph of gold nanoparticle oligomers ( $\text{Au-10}_n$ ), a dimer (circle) and a trimer (rectangle) are present as well as monomeric nanoparticles.

thioether oligomer stabilizes the NPs and is not affected by the new functionality. Thus, we assume that again two ligands are needed to stabilize one NP, which was corroborated by combining TEM results with thermogravimetric analysis data.

The protected acetylene of these 'artificial molecules' enabled the covalent coupling of NPs with a mild oxidative diacetylene coupling protocol developed by Hay.<sup>[41]</sup> This copper-catalyzed wet-chemical process was performed after deprotection of the acetylene and led to hybrid organic-inorganic superstructures ( $\text{Au-9}_n$ ), ( $\text{Au-10}_n$ ) and ( $\text{Au-11}_n$ ). Fig. 4 depicts a representative TEM micrograph showing a dimer ( $n = 2$ ), trimer ( $n = 3$ ) and monomeric NPs. Besides dimers and trimers tetramers ( $n = 4$ ) were also obtained. These three different oligomers were used for further analysis. Higher oligomers precipitated from solution due to their low solubility. The reaction time was thus reduced to

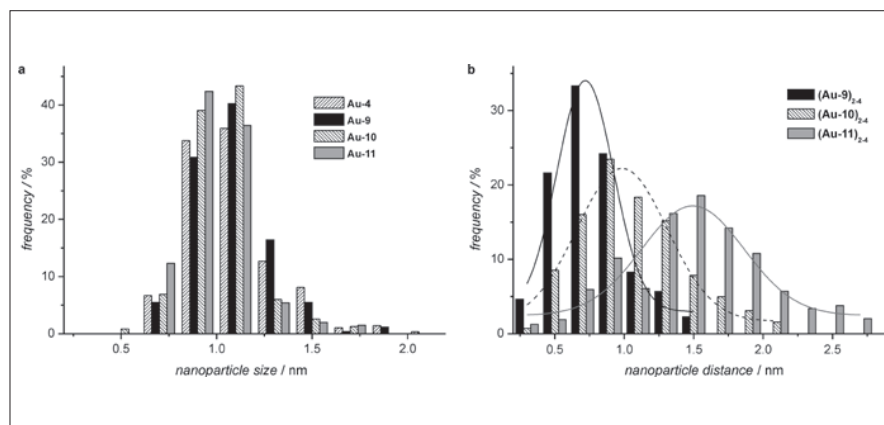


Fig. 5. a) Size distribution of ligand-stabilized particles, b) distance distribution of superstructures reflecting the various spacer lengths.

15 minutes to favor short oligomers instead of long insoluble polymers. The success of the coupling was preliminary detected by UV/vis. The elongation of OPE due to diacetylene formation was clearly shown by a bathochromic shift. Investigations of the interparticle spacings of these superstructures *via* TEM revealed that the different lengths of rigid-rod linkers were reflected in the interparticle distances (Fig. 5).

We obtained Gaussian-like distance distributions with increasing maxima for larger spacer lengths. The shape of the Gaussian-like fit broadens with each extension of the OPE linker and the maxima are at shorter values than the calculated distances for the outstretched rods. These two aspects lead to the assumption that the ligands arrange with various possible angles on the NP's surface. A tangential alignment is favored over a perpendicular arrangement probably due to the steric repulsion of the aromatic hydrogen, which

anchors the central functionality. This hypothesis was further corroborated by recent studies with model ligands comprising a central pyridine unit.<sup>[42]</sup> The coordination of the pyridine's nitrogen to the Au NP resulted in a perpendicular arrangement of the rod at the NP's surface. Thus the calculated length of the rod and the observed interparticle spacings perfectly matched.

## Summary and Conclusion

Our efforts towards the realization of covalently bound NPs are presented. After two 'casting' series we choose a ligand design that is able to stabilize Au NPs with a narrow size distribution and controlled thioether gold interactions. It was found that two ligands stabilize one NP. The ligand structure was further functionalized with a peripheral protected acetylene providing bifunctional NPs (see Fig. 6).

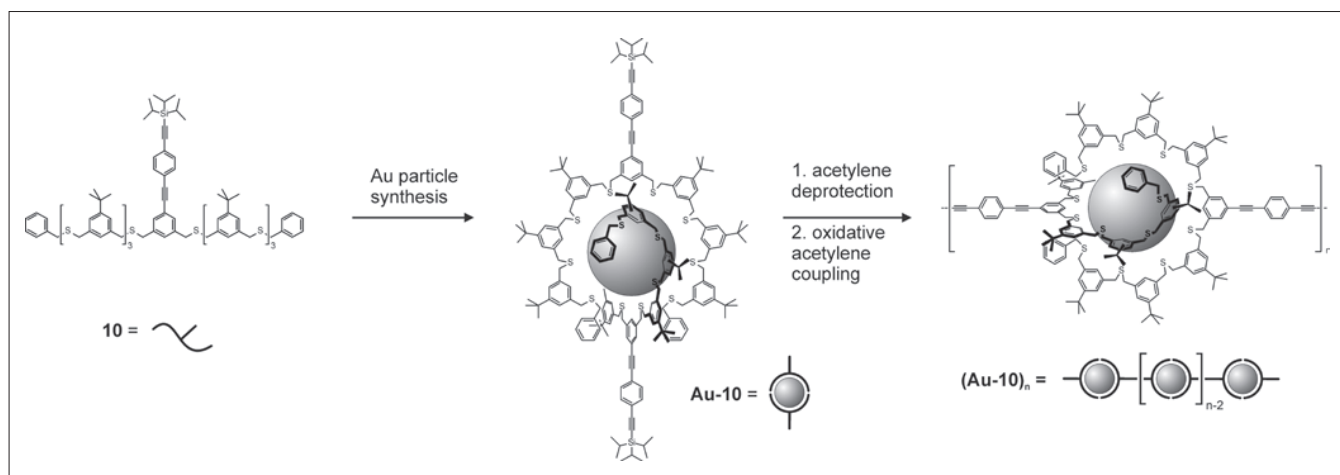


Fig. 6. The concept of using ligand-functionalized nanoparticles as 'artificial molecules'. The oligomeric ligand **10** stabilizes particles with diameters of about 1 nm by covering its surface. As two ligands are required to cover the particles surface, exactly two triisopropylsilyl (TIPS) protected acetylenes are available as functional group on the periphery of the particle allowing their interlinking to form hybrid organic-inorganic oligomers or polymers by wet chemistry.

These ‘artificial molecules’ enabled the formation of organic–inorganic architectures *via* diacetylene coupling. In a series of interlinked NPs the spacer length was reflected in the spatial arrangement of the NPs in these hybrid superstructures.

Currently we are working on a greater control over the arrangement of the spacer group at the NP’s surface, the realization of increased NP sizes, other metal NPs and hybrid materials consisting of periodically arranged subunits.

#### Acknowledgements

We are grateful for financial support from the EU through the project FUNMOL (number 213382) of the call FP7-NMP-2007-SMALL-1, the Gebert Rūf Foundation, the Swiss National Science Foundation and the National Research Project No. 62 Smart Materials.

Received: January 14, 2011

- [1] M. Daniel, D. Astruc, *Chem. Rev.* **2004**, *104*, 293.
- [2] R. Sardar, A. M. Funston, P. Mulvaney, R. W. Murray, *Langmuir* **2009**, *25*, 13840.
- [3] M. Homberger, U. Simon, *Phil. Trans. R. Soc. A* **2010**, *368*, 1405.
- [4] G. Schmid, *Adv. Eng. Mater.* **2001**, *3*, 737.
- [5] L. M. Liz-Marzán, *Langmuir* **2006**, *22*, 32.
- [6] A. J. Quinn, G. Redmond, *Surf. Sci.* **2007**, *601*, 2740.
- [7] R. P. Andres, J. D. Bielefeld, J. I. Henderson, D. B. Janes, V. R. Kolagunta, C. P. Kubiak, W. J. Mahoney, R. G. Osifchin, *Science* **1996**, *273*, 1690.
- [8] G. Schmid, U. Simon, *Chem. Commun.* **2005**, 697.
- [9] J. Liao, L. Bernard, M. Langer, C. Schönenberger, M. Calame, *Adv. Mater.* **2006**, *18*, 2444.
- [10] S. W. Boettcher, N. C. Strandwitz, M. Schierhorn, N. Lock, M. C. Lonergan, G. D. Stucky, *Nat. Mater.* **2007**, *6*, 592.
- [11] S. Kim, J. Lee, *Nano Lett.* **2010**, *10*, 2884.
- [12] C. Zhong, R. C. Brush, J. Anderegg, M. D. Porter, *Langmuir* **1999**, *15*, 518.
- [13] S. D. Evans, S. R. Johnson, Y. L. Cheng, T. Shen, *J. Mater. Chem.* **2000**, *10*, 183.
- [14] Y. Kim, R. C. Johnson, J. T. Hupp, *Nano Lett.* **2001**, *1*, 165.
- [15] M. Riskin, R. Tel-Vered, T. Bourenko, E. Granot, I. Willner, *J. Am. Chem. Soc.* **2008**, *130*, 9726.
- [16] Y. Zhou, S. Wang, K. Zhang, X. Jiang, *Angew. Chem. Int. Ed.* **2008**, *47*, 7454.
- [17] X. Zhang, Q. Guo, D. Cui, *Sensors* **2009**, *9*, 1033.
- [18] C. Della Pina, E. Falletta, L. Prati, M. Rossi, *Chem. Soc. Rev.* **2008**, *37*, 2077.
- [19] A. Corma, H. Garcia, *Chem. Soc. Rev.* **2008**, *37*, 2096.
- [20] M. Brust, M. Walker, D. Bethell, D. J. Schiffrin, R. Whyman, *J. Chem. Soc., Chem. Commun.* **1994**, 801.
- [21] F. Sander, T. Peterle, N. Ballav, F. V. Wrochem, M. Zharnikov, M. Mayor, *J. Phys. Chem. C* **2010**, *114*, 4118.
- [22] X. Li, M. R. D. Jong, K. Inoue, S. Shinkai, J. Huskens, D. N. Reinhoudt, *J. Mater. Chem.* **2001**, *11*, 1919.
- [23] E. J. Shelley, D. Ryan, S. R. Johnson, M. Couillard, D. Fitzmaurice, P. D. Nellist, Y. Chen, R. E. Palmer, J. A. Preece, *Langmuir* **2002**, *18*, 1791.
- [24] A. Taubert, U. Wiesler, K. Müllen, *J. Mater. Chem.* **2003**, *13*, 1090.
- [25] A. D’Aléo, R. M. Williams, F. Osswald, P. Edamana, U. Hahn, J. van Heyst, F. D. Tichelaar, F. Vögtle, L. De Cola, *Adv. Funct. Mater.* **2004**, *14*, 1167.
- [26] W. M. Pankau, S. Mönninghoff, G. von Kiedrowski, *Angew. Chem. Int. Ed.* **2006**, *45*, 1889.
- [27] C. Krüger, S. Agarwal, A. Greiner, *J. Am. Chem. Soc.* **2008**, *130*, 2710.
- [28] K. Sung, D. W. Mosley, B. R. Peelle, S. Zhang, J. M. Jacobson, *J. Am. Chem. Soc.* **2004**, *126*, 5064.
- [29] J. G. Worden, A. W. Shaffer, Q. Huo, *Chem. Commun.* **2004**, 518.
- [30] G. A. DeVries, M. Brunnbauer, Y. Hu, A. M. Jackson, B. Long, B. T. Neltner, O. Uzun, B. H. Wunsch, F. Stellacci, *Science* **2007**, *315*, 358.
- [31] D. F. Perepichka, F. Rosei, *Angew. Chem. Int. Ed.* **2007**, *46*, 6006.
- [32] Y. Min, M. Akbulut, K. Kristiansen, Y. Golan, J. Israelachvili, *Nat. Mater.* **2008**, *7*, 527.
- [33] F. Westerlund, T. Bjørnholm, *Curr. Opin. Colloid In.* **2009**, *14*, 126.
- [34] S. Srivastava, N. A. Kotov, *Soft Matter* **2009**, *5*, 1146.
- [35] K. J. M. Bishop, C. E. Wilmer, S. Soh, B. A. Grzybowski, *Small* **2009**, *5*, 1600.
- [36] C. L. Choi, A. P. Alivisatos, *Annu. Rev. Phys. Chem.* **2010**, *61*, 369.
- [37] P. K. Jain, M. A. El-Sayed, *Chem. Phys. Lett.* **2010**, *487*, 153.
- [38] T. Peterle, A. Leifert, J. Timper, A. Sologubenko, U. Simon, M. Mayor, *Chem. Commun.* **2008**, 3438.
- [39] T. Peterle, P. Ringle, M. Mayor, *Adv. Funct. Mater.* **2009**, *19*, 3497.
- [40] M. M. Alvarez, J. T. Khoury, T. G. Schaaff, M. N. Shafiqullin, I. Vezmar, R. L. Whetten, *J. Phys. Chem. B* **1997**, *101*, 3706.
- [41] A. S. Hay, *J. Org. Chem.* **1962**, *27*, 3320.
- [42] J. P. Hermes, F. Sander, T. Peterle, C. Cioffi, P. Ringle, M. Mayor, *Small* **2011**, *7*, 920.

# Direct Control of the Spatial Arrangement of Gold Nanoparticles in Organic–Inorganic Hybrid Superstructures

Jens P. Hermes, Fabian Sander, Torsten Peterle, Carla Cioffi, Philippe Ringler, Thomas Pfohl, and Marcel Mayor\*

*The directed assembly of gold nanoparticles is essential for their use in many kinds of applications, such as electronic devices, biological labels, and sensors. Herein an atomic alteration in the molecular structure of ligand-stabilized gold nanoparticles that can shift the interparticle distance up to 1 nm upon covalent coupling to organic–inorganic superstructures is presented. Gold nanoparticles are stabilized by two octadentate thioether ligands and have a mean diameter of 1.1 nm. The ligands contain a central rigid rod varying in length and terminally functionalized with a protected acetylene. The two peripheral functional groups on each particle enable the directed assembly of nanoparticles to dimers, trimers, and tetramers by oxidative acetylene coupling. This is a wet chemical protocol resulting in covalently bound nanoparticles. These organic–inorganic hybrid superstructures are analyzed by transmission electron microscopy, small angle X-ray scattering, and UV/vis spectroscopy. The focus of the comparison here is the subunit, which is anchoring the bridgehead, either a pyridine or benzene moiety. The pyridine-based ligands reflect the calculated length of the rigid-rod spacer in their interparticle distances in the obtained hybrid structures. This suggests a perpendicular arrangement that results from the coordination of the pyridine's lone pair to the gold surface. An atomic variation in the ligand's center leads to smaller interparticle distances in the case of hybrid structures obtained from benzene ligands. This large difference in the spatial arrangement suggests a tangential arrangement of the interparticle bridging structure in the latter case. Consequently a rather flat arrangement parallel to the particle surface must be assumed for the central benzene unit of the benzene-based ligand.*

J. P. Hermes, F. Sander, Dr. T. Peterle, Dr. C. Cioffi, Prof. M. Mayor  
Department of Chemistry  
University of Basel

St. Johanns-Ring 19, 4056 Basel, Switzerland  
E-mail: marcel.mayor@unibas.ch

Dr. T. Peterle  
Creavis Technologies & Innovation  
Evonik Degussa GmbH  
Paul-Baumann-Str. 1, 45772 Marl, Germany

Dr. P. Ringler  
C–CINA Biozentrum  
University of Basel  
Mattenstrasse 26, 4002 Basel, Switzerland

DOI: 10.1002/smll.201002101

Prof. T. Pfohl  
Department of Chemistry  
University of Basel  
Klingelbergstrasse 80, 4056 Basel, Switzerland

Prof. M. Mayor  
Karlsruhe Institute of Technology (KIT)  
Institute of Nanotechnology  
P.O. Box 3640, 76021 Karlsruhe, Germany

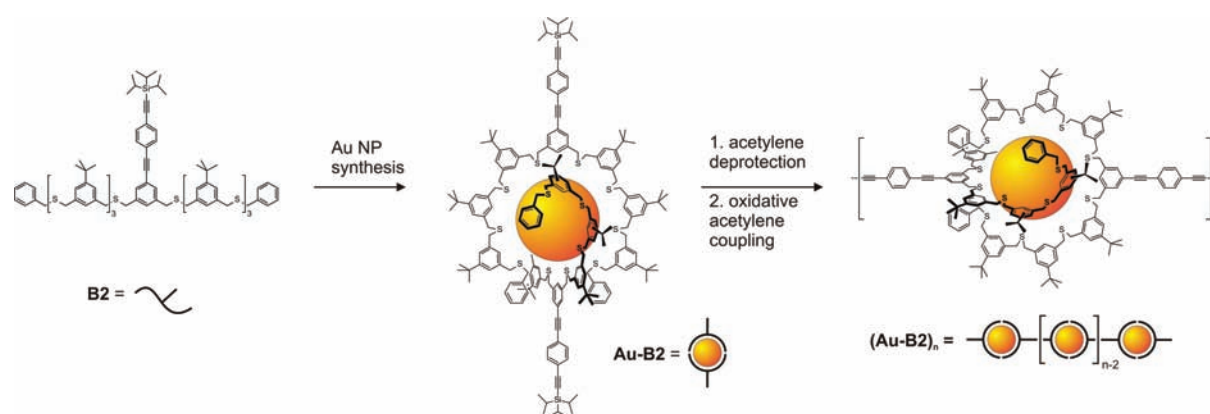


**Figure 1.** The concept of using ligand-functionalized nanoparticles as “artificial molecules.” The oligomeric ligand stabilizes particles with diameters of about 1 nm by covering its surface. Because two ligands are required to cover the particles surface, exactly two triisopropylsilyl (TIPS)-protected acetylenes are available as functional groups on the periphery of the particle allowing their interlinking to form organic–inorganic hybrid oligomers or polymers by wet chemistry.

## 1. Introduction

Nanoparticles (NPs) have size-dependent physical properties. This provides optical labels with tunable colors in the case of semiconducting particles<sup>[1,2]</sup> and interesting physical properties, such as a room-temperature Coulomb blockade for small metallic NPs.<sup>[3–5]</sup> Gold is the most used material for metal NPs due to their efficient synthesis, highly advanced surface chemistry, and potential as model system for colloids and surfaces.<sup>[6,7]</sup> The diversity of potential applications of Au NPs is huge, ranging from electronic<sup>[8–11]</sup> and photonic<sup>[12,13]</sup> devices to chemical sensors<sup>[14–18]</sup> and biological labeling.<sup>[19–24]</sup> A major challenge for the integration of NPs in hybrid materials and future devices is the control of their size (diameter) and spatial arrangement. Numerous studies geared towards the directed assembly of Au NPs have been reported, and several review articles highlight the importance of the field.<sup>[4,6,8,25–30]</sup> Recently, the role of interparticle forces and the resulting assemblies have been reviewed.<sup>[31–33]</sup>

NP assemblies, using DNA<sup>[34–43]</sup> or host–guest interactions<sup>[44–47]</sup> for example, lead to beautiful arrangements, but we wish to focus on assemblies that are formed in non-polar organic solvents. Arrangements of Au NPs can be realized via  $\pi$ – $\pi$ <sup>[48]</sup> and charge-transfer<sup>[49]</sup> interactions, hydrogen bonding,<sup>[50–52]</sup> or coordination bonds.<sup>[53]</sup> These approaches, like the use of dithiol<sup>[9,10,54–59]</sup> or thioether<sup>[60–64]</sup> linkers, usually lead to larger networks. Our goal is to obtain dumbbell structures<sup>[65,66]</sup> and short 1D chains of NPs that are covalently coupled<sup>[67]</sup> and controlled by a distinct and known number of functionalities on the NPs’ surfaces.

First attempts to obtain monofunctionalized NPs were based on DNA or peptides<sup>[24,34,68,69]</sup> and therefore were limited to aqueous media. NPs in organic solvents were monofunctionalized via ligand polymerization on the NPs’ surface<sup>[70]</sup> and reactions on solid supports<sup>[71,72]</sup> or bifunctionalized by profiting from the exposed pole positions of monodispersed NPs.<sup>[73,74]</sup>

We recently developed oligomeric multidendate ligands based on a benzyl thioether motif, which enabled the formation of Au NPs in good yields with a narrow size distribution

of around 1 nm, as detected by transmission electron microscopy (TEM), and excellent long-term stability in solution.<sup>[75]</sup> As only two macromolecular ligands were required to stabilize the NP by covering its surface, the system provided easy access to Au NPs as “artificial molecules” in a wet chemistry process. Exposure of NPs with peripheral ethynyl groups (**Figure 1**) to oxidative acetylene coupling conditions provided organic–inorganic hybrid superstructures<sup>[76]</sup> consisting of NPs interlinked by a single diacetylene spacer. The interparticle distances of these superstructures reflected the length trend of the organic linkers. However, a closer inspection of these interparticle distances revealed a Gaussian-like distribution with a maximum population at shorter distances than the full length of the linker.

We explain the systematically smaller interparticle distance by a tangential arrangement of the interlinking rigid-rod structure at the NPs’ surface. Along these lines we present an alternative ligand design and its capability to form stable NPs with a narrow size distribution. The subsequent coupling of ligand-stabilized NPs provides hybrid oligomers with well-defined interparticle distances matching the length of the formed spacer unit. The studies demonstrate how structural design provides control of the spatial arrangement of the inorganic NPs in organic–inorganic hybrid structures.

## 2. Results and Discussion

### 2.1. Concept and Strategy

The thioether ligands **B1–B2** (**Figure 2**) efficiently stabilize Au NPs with diameters of about 1 nm and their triisopropylsilyl (TIPS)-masked acetylene enables their directed assembly to dimeric dumbbell structures and chainlike oligomers.<sup>[76]</sup> The variation of the length of the oligo(phenyleneethynyl) (OPE) rod was reflected in the observed interparticle distances. However, the measured distances were shorter than expected. As displayed in **Figure 3A**, an interparticle distance ( $d$ ) that is shorter than the linker length ( $l$ ) may indicate a

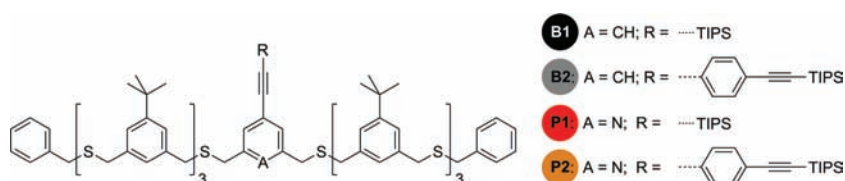


**Figure 2.** Chemical structures of the octadentate thioether ligands **B1**, **B2**, **P1**, and **P2** comprising a TIPS-protected acetylene mounted on rigid rods of various lengths.

tangential arrangement of the rigid-rod structure at the NP<sup>+</sup> surface. Considering the chemical structure at the bridgehead of the linker displayed in Figure 3B, a tangential arrangement is expected to emerge from the steric repulsion between the central aromatic hydrogen and the Au NP surface. By replacing the central benzene unit of the oligomer with a pyridine subunit, the disruptive hydrogen atom and thus the steric repulsion should be removed. Furthermore, pyridines are known to coordinate to Au surfaces with the nitrogen's lone pair.<sup>[77–80]</sup> As this coordination is reported to depend on the electrochemical potential of the Au surface, it might even provide new molecular switching mechanisms.<sup>[81,82]</sup> As displayed in Figure 3D, the lone pair of the central pyridine unit may coordinate to the metal surface of the NP. This further stabilizes a perpendicular arrangement of the rigid-rod structure as sketched in Figure 3C. Interestingly, this atomic alteration should be reflected in the resulting interparticle spacing

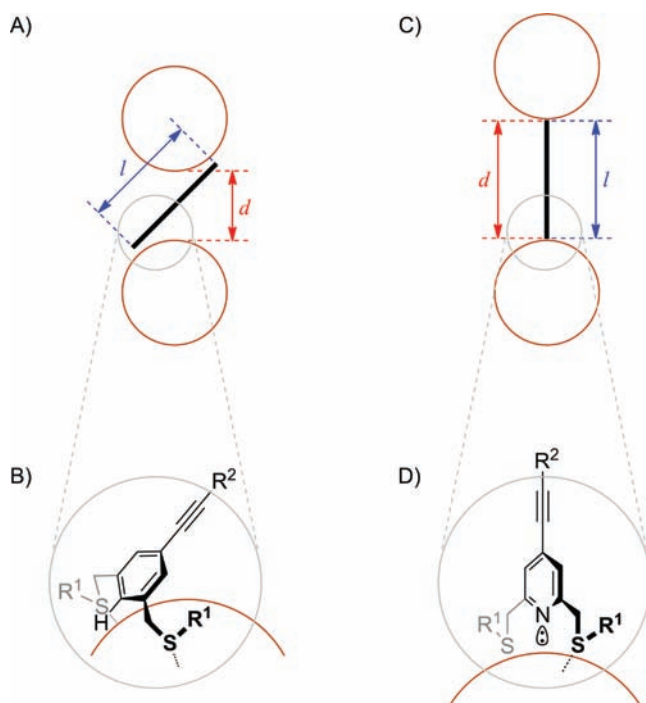


**Figure 3.** Dumbbell structure A) with a reduced interparticle distance due to a tangential arrangement of the rigid-rod linker that is expected to result from B) a steric repulsion between the central hydrogen and the NP surface for ligands with a benzene subunit at the bridgehead. C) Maximized interparticle distance due to a perpendicular arrangement of the rigid-rod linker at the NPs surface presumably caused by D) the coordination of the nitrogen's lone pair.

of the obtained organic–inorganic hybrid superstructures. The electronic coupling between the inorganic NP and organic bridging structure is expected to depend on the interactions of the bridgehead with the Au NP, and the extra coordination of a nitrogen lone pair should aid this.

Inspired by these considerations we decided to synthesize the required ligands with a central pyridine subunit **P1** and **P2** (Figure 2), investigate their Au NP stabilizing properties, and interlink the obtained NPs by applying wet chemical procedures.

## 2.2. Ligand-Stabilized Nanoparticles

NPs were synthesized in the presence of ligands **B1**, **B2**, **P1**, and **P2**, and the obtained NPs **Au-B1**, **Au-B2**, **Au-P1**, and **Au-P2** were analyzed. The absence of gold plasmon bands around 520 nm in the UV/vis spectra of all ligand-stabilized NPs pointed at NPs with diameters below 2 nm.<sup>[83]</sup> The presence of the stabilizing ligand at the NP surface was displayed by <sup>1</sup>H NMR spectroscopy. In addition the <sup>1</sup>H NMR spectra also proved the completeness of the tetraoctylammonium bromide (TOAB) removal procedure. The removal of excess ligand by size-exclusion chromatography (SEC) was monitored by UV/vis spectroscopy.

The diameters of the NPs formed were measured with TEM, by applying an automatized diameter analyzing procedure (see Supporting Information (SI) for detailed descriptions). All samples of ligand-stabilized NPs showed narrow size distributions of around 1.0–1.1 nm with a standard deviation of 0.3 nm. As displayed in **Figure 4**, the NPs stabilized by the pyridine-based ligands have an average diameter ( $\phi_{av}$ ) of 1.1 nm slightly larger than the ones stabilized by the

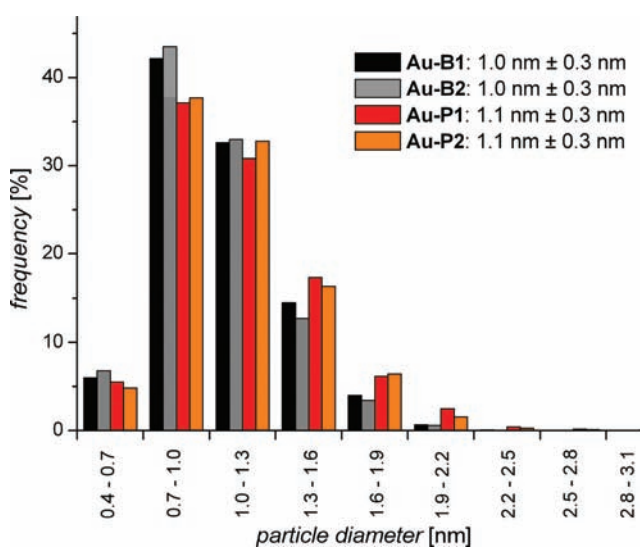


**Figure 4.** Size distributions (mean values ± standard deviation) of gold nanoparticles **Au-B1**, **Au-B2**, **Au-P1**, and **Au-P2**, between 3000 and 10 000 nanoparticles were automatically measured.

benzene-based ligands ( $\phi_{av} = 1.0$  nm). As one pixel has a size of 0.26 nm, this small size difference is within the detection limits; note that identical recording conditions were used in all cases. Minor differences already present in the brightness of the TEM image may increase or decrease the apparent diameter of the NPs.

Comparing the surface area of 1.0–1.1 nm Au NPs and the dimensions of the octasulfide ligands, there is only enough space to arrange two ligands at the NPs' surface with all eight sulfur atoms pointing towards the Au surface. This hypothesis was confirmed by thermogravimetric analysis; however, minor amounts of mono-, tri-, or higher-functionalized NPs may also be present in the NP samples, each with a suboptimal coordination.

### 2.3. Covalently Coupled Gold Nanoparticles

The purified NPs **Au-B1**, **Au-B2**, **Au-P1**, and **Au-P2** having peripheral TIPS-protected acetylenes were exposed to the deprotection and coupling conditions described in the Experimental Section. We obtained interlinked chains of  $n$  NPs (**Au-B1**) $_n$ , (**Au-B2**) $_n$ , (**Au-P1**) $_n$ , and (**Au-P2**) $_n$ . As chains of interlinked NPs with too many NPs ( $n > 5$ ) tend to precipitate, the duration of the coupling reaction was restricted to 15 min in order to favor the formation of shorter hybrid oligomers. Due to the short reaction time, only about 15% of the peripheral acetylene groups were involved in a coupling reaction. Monitoring the reaction by UV/vis spectroscopy revealed an increase and red-shift of the absorption between 300 and 400 nm, characteristic for the formation of longer delocalized  $\pi$ -systems due to the interlinking of the OPE rods by oxidative acetylene coupling (see Figure S1 in the SI). The average NP diameter does not change upon this process; they simply exhibit a small increase in the polydispersity (see Figure S3 in the SI) due to the formation of some larger NPs (see Figure S11 in the SI).

The organic–inorganic hybrid oligomers were analyzed by TEM, after the deposition of highly diluted solutions on carbon-coated copper grids that spanned a holey carbon support film. Highly diluted solutions are essential to avoid the coincidental proximity of two lonesome particles, which cannot be distinguished from dumbbells in the TEM image.<sup>[84]</sup> However, too low concentrations would not allow the observation of sufficient amounts of NP oligomers per image, and thus, a reasonable concentration window was determined empirically. Typical TEM images of samples (**Au-B1**) $_n$ , (**Au-B2**) $_n$ , (**Au-P1**) $_n$ , and (**Au-P2**) $_n$  are displayed in Figure 5 (larger areas of TEM images are displayed in the SI, Figure S7–S11). Mainly individual NPs and clusters consisting of a very low number of NPs can be observed. Obviously the reduction of the exposure time to coupling conditions results in short, soluble hybrid oligomers (**Au-X**) $_n$  with  $n \leq 5$ . Interestingly, the NPs forming trimers ( $n = 3$ ) and tetramers ( $n = 4$ ) have the tendency to arrange in elongated, almost linear structures, supporting the hypothesized picture of having two acetylenes at opposed sides of the NPs as sketched in Figure 1.

In order to investigate the NP interlinking reaction and to analyze the yields of the different hybrid oligomers formed,

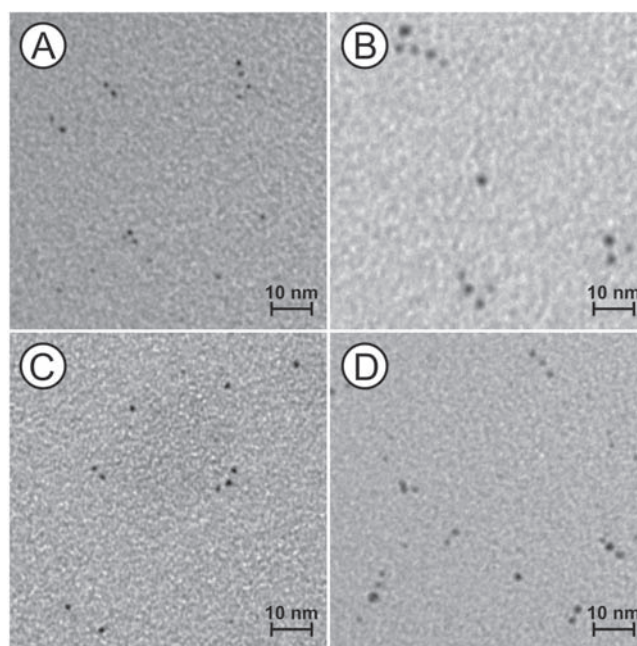


Figure 5. Representative TEM images of highly diluted samples of a) (**Au-B1**) $_n$ , b) (**Au-B2**) $_n$ , c) (**Au-P1**) $_n$ , and d) (**Au-P2**) $_n$ .

large-area TEM micrographs were analyzed. The relative yields of monomeric NPs and short hybrid oligomers are displayed in Figure 6. For all samples very comparable fractions of the different oligomers formed were observed. The obvious similarity of their behavior during the interlinking reaction points at very comparable structures at the NPs' periphery. Their reactivity is neither controlled by the Au-NP-stabilizing octasulfide ligand nor by the length of the rigid-rod structure, but exclusively by the similar number of exposed acetylene groups. Again, these experimental findings are in agreement with the model sketched in Figure 1, namely exactly two acetylenes exposed at the NP surface for all ligand-stabilized NPs, **Au-B1**, **Au-B2**, **Au-P1**, and **Au-P2**. While precipitates are successfully avoided by the short exposure to coupling conditions, this comes at the price of a lower coupling efficiency;

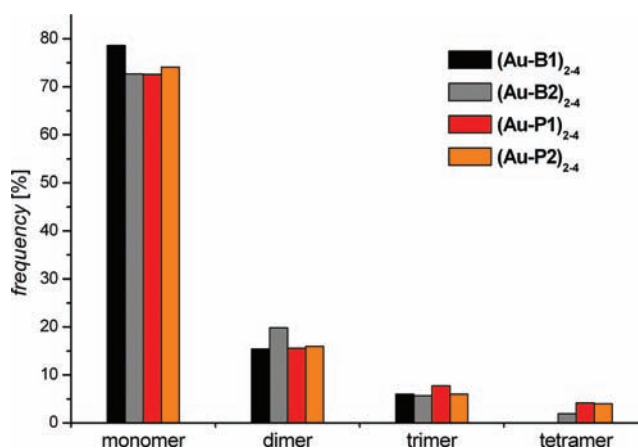
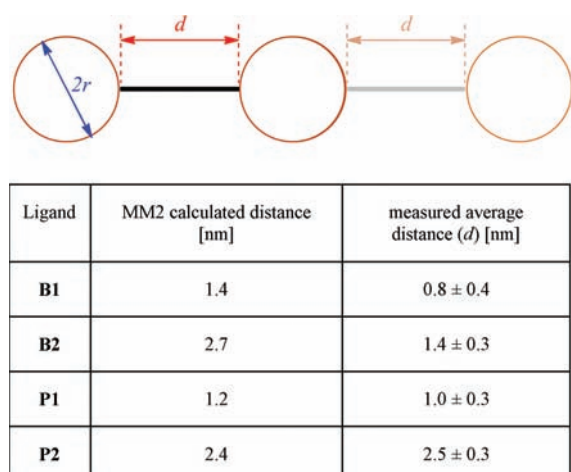


Figure 6. Distribution of monomers and oligomers (**Au-B1**) $_n$ , (**Au-B2**) $_n$ , (**Au-P1**) $_n$ , and (**Au-P2**) $_n$  formed after the diacetylene coupling reaction; between 200 and 400 particles were counted.



**Figure 7.** Nanoparticle size: diameter ( $2r$ , where  $r$  is the radius of the particle) and interparticle distance ( $d$ );  $d$  is measured between the nanoparticle edges of dimers, trimers, and tetramers. The table shows a comparison of calculated and measured distances for each sample of interlinked NPs.

thus, the majority (73–78%) of NPs remained as monomers for each ligand while about 16–20% formed dumbbell hybrids consisting of two interlinked NPs. Between 6–8% of the NPs are subunits of trimeric hybrid structures, and even minor traces (below 5%) of tetramers were observed. These short, almost linear oligomers are expected to lie flat on the TEM grid and are thus ideally suited to investigate the interparticle spacing of these hybrid structures.

The TEM micrographs were prepared from diluted solutions of superstructures and were used to manually measure the interparticle spacings. The images were transformed into black and white using the same threshold settings as before. This ensures the comparability of length and distance measurements. The interparticle distances ( $d$ ) were measured between the edges of adjacent NPs (see **Figure 7**). For this purpose dimers, trimers, and tetramers were considered. **Figure 8** displays the distance distributions of all samples of interlinked NPs. Oligomers of NPs coated with ligands comprising a benzene-based central unit (**Au-B1**)<sub>2,4</sub> show considerably shorter interparticle distances than the calculated length of the rigid-rod linker. Simple MM2 calculations of the short rigid-rod 1,4-diphenylbuta-1,3-diyne gave a length of 1.4 nm between the terminal hydrogens (black dashed line in **Figure 8**). The histogram of distances observed for NP oligomers (**Au-B1**)<sub>2,4</sub> shows a Gaussian-like distribution with a maximum at 0.8 nm (black bars and black solid line). A similar distribution with a maximum at 1.4 nm is observed for hybrid oligomers (**Au-B2**)<sub>2,4</sub> comprising a benzene-based central unit with the long linker (gray bars and gray solid line). A length of about 2.7 nm was calculated for the longer rigid-rod substructure (gray dashed line); thus, both samples of NP oligomers coated with ligands comprising a benzene-based central unit display a considerably smaller interparticle distance than expected for the fully stretched rigid-rod linking unit (arrows c and d in **Figure 8**). However, the length trend of the spacer is nicely reflected in the observed NP distances,

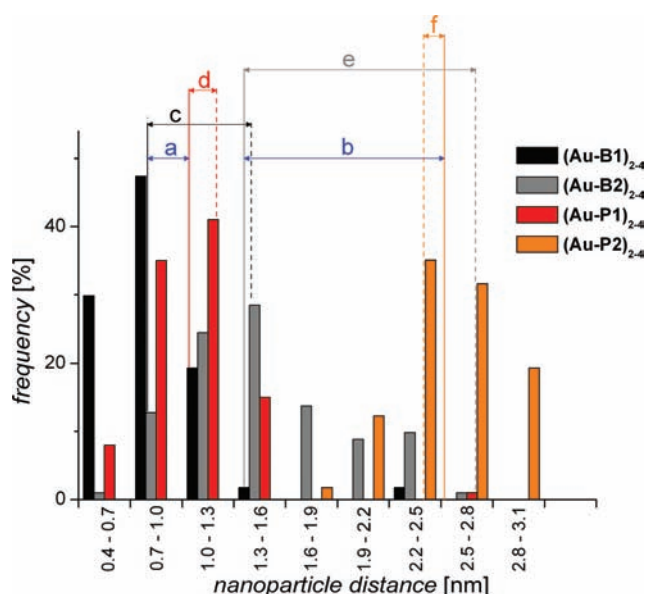


**Figure 8.** Interparticle distance distributions measured from TEM micrographs of organic–inorganic hybrid dimers (**Au-X**)<sub>2</sub>, trimers (**Au-X**)<sub>3</sub>, and tetramers (**Au-X**)<sub>4</sub>; (**Au-B1**)<sub>2,4</sub> (black), (**Au-B2**)<sub>2,4</sub> (gray), (**Au-P1**)<sub>2,4</sub> (red) and (**Au-P2**)<sub>2,4</sub> (orange). Solid lines represent the mean distance found for each sample, and the dashed line the calculated length of the diacetylene linker. The blue arrows compare the interparticle distance obtained by the short (arrow a, **B1** and **P1**) and long spacer (arrow b, **B2** and **P2**) with each other, indicating the large effect on the nanoparticles' arrangement arising from a small atomic alteration at the ligands' center. Arrows c–f (with respective colors) compare the deviation of the calculated and measured interparticle spacings. Between 50 and 100 oligomers were counted.

corroborating the wet chemical interparticle coupling reaction as the origin of the formed hybrid oligomers.

The comparison of interparticle distances of hybrid oligomers (**Au-P1**)<sub>2,4</sub> and (**Au-P2**)<sub>2,4</sub> formed from NPs coated with ligands based on pyridine-type central units also reflect the length of the rigid-rod linker. NP oligomers (**Au-P1**)<sub>2,4</sub> show a sharper distance distribution (red bars in **Figure 8**) with a maximum of 1.0 nm (red solid line). The nitrogen-to-nitrogen distance of the interlinking 1,4-di(pyridin-4-yl)buta-1,3-diyne structure is 1.2 nm according to MM2 calculations (red dashed line), matching the observed interparticle spacing. Hybrid oligomers (**Au-P2**)<sub>2,4</sub> consisting of NPs coated with a pyridine-based ligand with the long spacer led to an interparticle spacing distribution with a maximum at 2.5 nm (orange bars and orange solid line in **Figure 8**). This matches the calculated nitrogen–nitrogen distance of the rigid-rod-like structure of 2.4 nm (dashed orange line). The broadness of the distributions displayed in **Figure 8** does not exclusively reflect variations in the NP distances, but also the imperfection of the distance determination by manually measuring distances on the TEM micrographs.

While benzene-based ligands (**Au-B1**)<sub>2,4</sub> and (**Au-B2**)<sub>2,4</sub> showed shorter distances than calculated, the ligands (**Au-P1**)<sub>2,4</sub> and (**Au-P2**)<sub>2,4</sub> comprising the pyridine anchor matched the expected linker length. This supports the hypothesis discussed in the “Concept & Strategy” section (Section 2.1) and sketched in **Figure 3** of a tangential arrangement in the case



of the benzene-type central unit and a perpendicular arrangement in the case of the pyridine-type central unit. The comparison of the mean interparticle distances of NP oligomers  $(\text{Au-B2})_{2,4}$  and  $(\text{Au-P2})_{2,4}$  (blue arrow b in Figure 8) nicely depicts this difference. The atomic alteration in the molecular structure of the respective ligands led to a large difference in the interparticle spacing of 1.1 nm.

In order to verify the reproducibility and validity of these findings, several control experiments were performed. First the deposition behavior of uncoupled protected NPs was analyzed in terms of NP spacing and compared with the small hybrid structures obtained after applying the coupling conditions. These experiments were performed with simple carbon film on copper TEM grids in order to exclude potential NP steering features of the additional holey carbon solid support of the grids used at the first place. Furthermore the maximum spacing between two NPs to be considered was enlarged to 4 nm. Indeed the protected and uncoupled NPs also displayed a tendency to aggregate upon deposition on the TEM grid. For all four NPs broad distributions between 0.7 and 3.5 nm were observed (see Figure S2B in the SI). Subsequently the entire series of NPs was exposed to the coupling conditions. In order to also detect uncoupled NPs, the coupling reaction was quenched at an earlier stage. After deposition on a TEM grid, the interparticle distances were analyzed again, and indeed, the distances expected for the interlinked NPs can clearly be observed as increasing populations arising from the broad background (Figure S2A in the SI). The visibility was further increased by subtracting the broad background (Figure S2B) from the observed distribution after the coupling reaction (Figure S2C). This method provides the same distances as in the first series for hybrid structures  $(\text{Au-B2})_{2,4}$  and  $(\text{Au-P2})_{2,4}$  interlinked by the longer rod. The distances observed for the hybrid structures  $(\text{Au-B1})_{2,4}$  and  $(\text{Au-P1})_{2,4}$  interlinked by a short rod are systematically larger than before. This variation might originate from counting aggregated but not interlinked NPs. Thus, the second series displays small differences in the exact values of the maxima, probably emerging from the differences in the data analysis, but it has the same tendency as the first series of coupled NPs (see Figure S2A,C and Table S1 in the SI).

Additional NP diameter analyses were performed by small angle X-ray scattering (SAXS) experiments. Diluted samples were measured in toluene to investigate the diameter of the NPs. In Figure 9 the SAXS data in a log-log representation of the protected uncoupled NPs (left) and of the solutions comprising oligomeric structures (right) are displayed. The X-ray data of the monomeric NPs stabilized with different ligands (Figure 9, left) show almost the same scattering pattern. All samples show very similar plots with pronounced minima. This indicates that the NPs have a low degree of polydispersity as expected from the TEM investigations. The shape of the

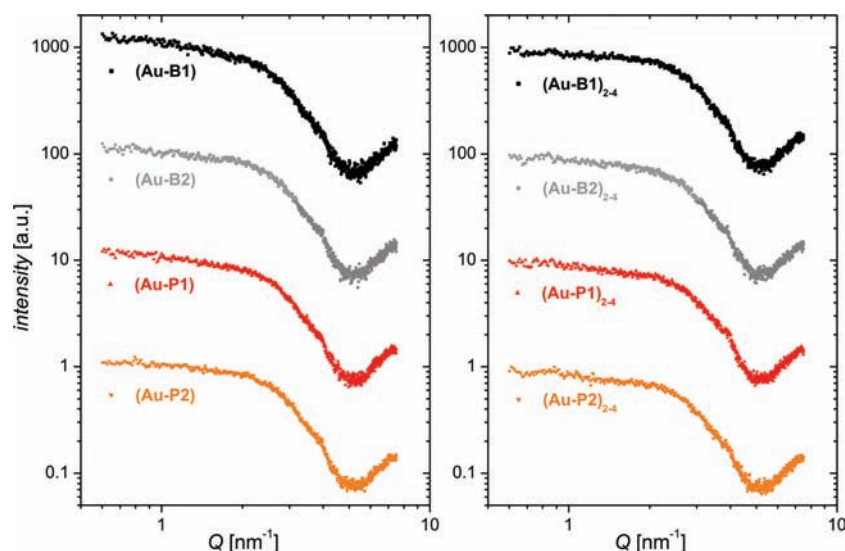
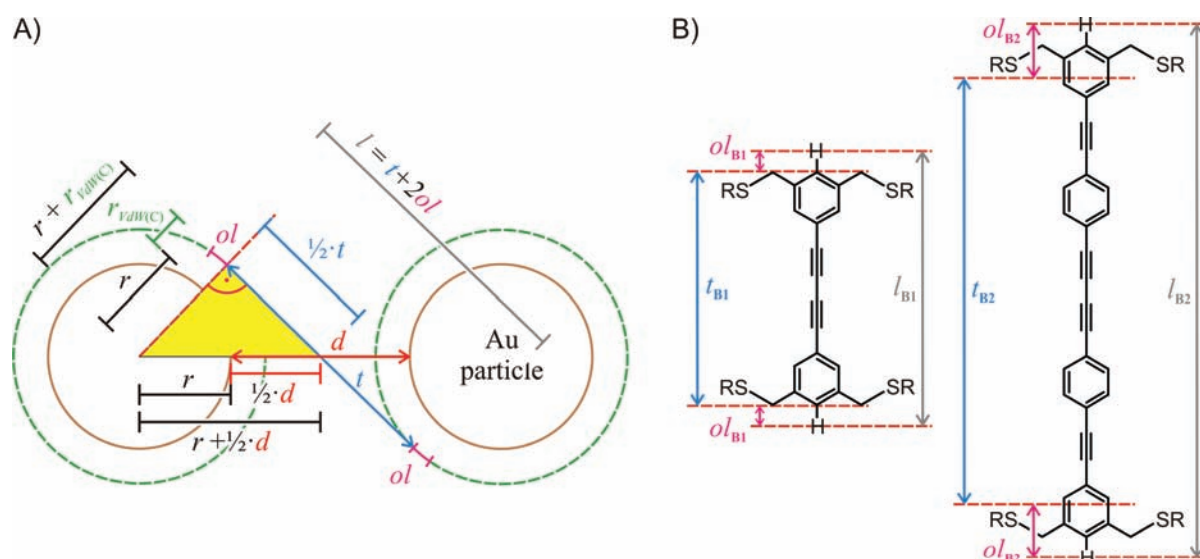


Figure 9. SAXS intensity data of monomeric (left) and coupled particles (right), the plots are shifted by a constant factor for clarity.

plots suggest form factors for homogeneous spheres with an average radius of about  $0.78 \pm 0.05$  nm. In comparison, the data of the coupled NPs (Figure 9, right) show the same position of the minima, corroborating the identity of the NPs after the coupling reaction. The only difference in the SAXS data of the monomers and the solutions comprising oligomeric structures is a minor broadening of the minima, which might indicate the presence of dimers. Apart from that, major differences in the SAXS data upon coupling were not observed. In analogy to DNA-interlinked Au NPs with a diameter of 1.4 nm, a variation of the form factor could have been expected upon interlinking.<sup>[85]</sup> However, the absence of a detectable change can be explained by the low percentage of actually coupled NPs in the solution. The NP diameter, which was determined by SAXS, differs from the size that was measured by TEM investigations (radii around 0.5 nm). This difference probably occurs due to an agglomeration of the NPs upon heating. The increased temperatures can be induced by the X-ray beam, and a heat-induced growth of the NPs in solution was reported before.<sup>[75]</sup> The ligand shell might also add to the scattering signal and thus indicate larger NPs than actually present. Another study also found a difference in the NP sizes, depending on which method was used;<sup>[86]</sup> only in this case, TEM led to larger radii for the NPs than SAXS. Because the interparticle distances are also based on TEM investigations and taken with the same threshold settings, we refer to the NP size using the diameter that was determined by TEM.

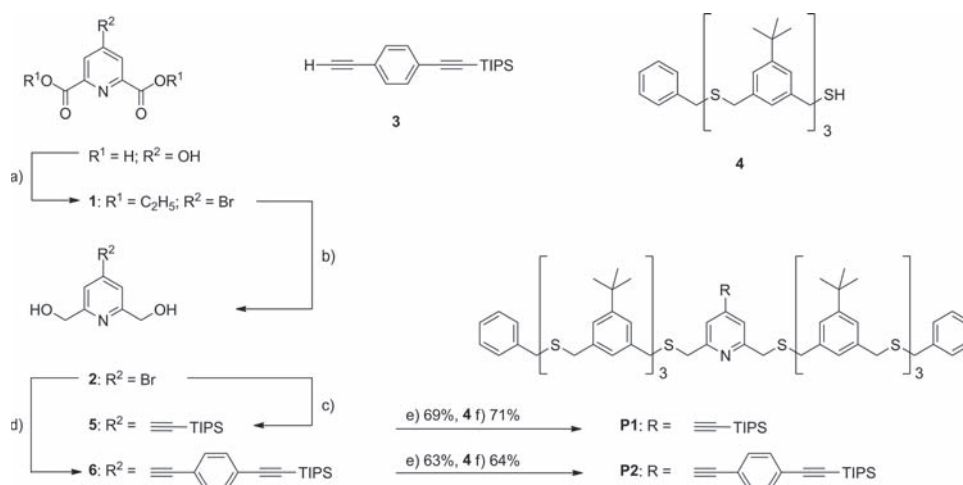
The TEM micrographs indicate spherical Au NPs. If we assume a symmetric tangential arrangement of the rigid-rod type linker at the surface of two interlinked NPs, the available data even allow for an estimate of the geometric arrangement of the rigid rod comprising terminal benzene units at the NPs' surface. Because thioethers are expected to equally coordinate to gold,<sup>[87]</sup> we assume that the geometry of the linker at the surface is not affected. Thus, we only consider the arrangement of the benzene-anchored linker at the



**Figure 10.** A) Calculation of distances between two interlinked particles assuming a tangential arrangement of the interlinking rigid rod in organic–inorganic hybrid oligomers. Assuming that the rigid rod must be separated by the Van der Waals radius of carbon ( $r_{\text{vdW(C)}}$ ) from the particle surface, the length of the tangential contact  $t$  can be calculated from the measured distance  $d$ . Its comparison with the calculated length of the rigid-rod structure  $l$  is displayed in B and allows determination of the “overlap length” ( $ol$ ) of the rod’s subunit interacting with the surface.

surface. The average radius  $r$  of the NPs stabilized by the benzene-type ligands **(Au-B1)<sub>2-4</sub>** and **(Au-B2)<sub>2-4</sub>** was determined to be 0.5 nm in both cases. The distance between the termini of the interlinking rod and the NP surface is estimated to be 0.2 nm, the Van der Waals radius of carbon. The calculated length ( $l$ ) between the terminal hydrogens of the rigid-rod linker are 1.4 nm in the case of **(Au-B1)<sub>2-4</sub>** and 2.7 nm for **(Au-B2)<sub>2-4</sub>**. The average interparticle distance ( $d$ ) was determined to be 0.8 nm for **(Au-B1)<sub>2-4</sub>** and 1.4 nm for **(Au-B2)<sub>2-4</sub>**. Thus, as displayed in **Figure 10A**, the lengths of two sides of the yellow right-angled triangle are known, and hence also the third, which corresponds to a length of  $\frac{1}{2}t$  (blue in **Figure 10**) according to the Pythagoras rule. The tangential distance ( $t$ ) can be compared with the calculated length ( $l$ ). This comparison shows that  $t$  is slightly shorter than  $l$  in both cases and

that a short part at the end of the linker lays flat on the NP surfaces, labeled  $ol$  for “overlap length” in **Figure 10A**. To visualize the size of the “overlap length,” the obtained tangential length  $t_{\text{B1}}$  and  $t_{\text{B2}}$  of both linkers are compared with the length of the corresponding rigid-rod structure in **Figure 10B**. In the case of the short linker, the difference between  $t_{\text{B1}}$  and its length  $l_{\text{B1}}$  is only 0.2 nm, and thus, the value for  $ol$  amounts to 0.1 nm (10%), which is in the range of the length of the terminal C–H bond. Only the terminal C–H bond is aligned to the NP surface, and the length of the linker almost matches the calculated tangential length  $t_{\text{B1}}$ . For the longer linker a slightly different scenario was observed. The value calculated for the “overlap length” is 0.4 nm (14%) and thus considerably longer than in the case of the short linker. The tangential length  $t_{\text{B2}}$  ends on the terminal benzene ring of



**Scheme 1.** a)  $\text{PBr}_5$ , 90 °C, 90 min;  $\text{CHCl}_3$ , rt (room temperature), EtOH, 0 °C; 79% yield; b)  $\text{NaBH}_4$ , EtOH, 20 h reflux, 93% yield; c) TIPS-C $\equiv$ CH, TEA,  $\text{Pd}(\text{PPh}_3)_2\text{Cl}_2$ , CuI, 80 °C, 15 h, 81% yield; d) **3**, TEA,  $\text{Pd}(\text{PPh}_3)_2\text{Cl}_2$ , CuI, 80 °C, 1.5 h, 81% yield; e) THF,  $\text{CBr}_4$ , PPh $_3$ , rt, 2 h; f) THF, NaH, rt, 2 h.

the rigid-rod substructure indicating a planar arrangement of this aromatic subunit on the NP surface. Besides the coordinative bonds of the benzylic thioethers, there seems to be an additional weak interaction involved in the arrangement of the terminal benzene subunit. We currently hypothesize that these interactions are either Van der Waals or  $\pi$ -metal (cation) interactions.

### 3. Conclusion

An atomic variation in the molecular structure of ligand-stabilized Au NPs enabled the control of their interparticle spacing in organic-inorganic hybrid superstructures. This was achieved by covalently interlinking bifunctionalized NPs. The interparticle distance in the obtained hybrid oligomers matched the length of the rigid-rod linker that is anchored via a central pyridine unit. This points at a perpendicular arrangement of the rod at the NP surface and suggests the coordination of the pyridine's lone pair to the NP. We thus expect an enhanced electronic coupling between the NP and the rigid-rod linker, which is of particular interest since hybrid oligomers are currently used as bottom-up assembled objects for the assembly of molecular junctions. For this purpose a separation of the different oligomers is envisaged. Based on these new findings, we hypothesize that the use of other coupling protocols such as "click-chemistry" or Sonogashira cross-couplings would extend the use of our functional NPs.

### 4. Experimental Section

**Ligand Synthesis:** The synthesis of ligands **B1** and **B2** has already been reported.<sup>[76]</sup> The assembly of ligands **P1** and **P2** is displayed in **Scheme 1**, and synthetic protocols together with analytical data are provided in the SI. The central pyridine subunit was assembled starting from chelidamic acid. Bromination with phosphorus pentabromide followed by an in situ esterification with ethanol provided diethyl 4-bromopyridine-2,6-dicarboxylate **1** as white solid in 79% yield.<sup>[88]</sup> Subsequent reduction with sodium borohydride gave the diol **2**<sup>[89]</sup> as white solid in good yields. In the next step the rigid-rod structure comprising a terminal TIPS-protected acetylene was assembled. In a Sonogashira reaction sequence,<sup>[90]</sup> the bromine was substituted either by a TIPS-protected acetylene or by the mono-TIPS-protected diacetylene **3**.<sup>[91]</sup> Thus the bromo-pyridine diol **2** was treated at 80 °C with the corresponding acetylene in the presence of catalytic amounts of Pd(PPh<sub>3</sub>)<sub>2</sub>Cl<sub>2</sub> and CuI in triethylamine (TEA), which acts as solvent and base to provide the OPE-like diol intermediates **5** and **6**, both in isolated yields of 81% as white and slightly yellow solids, respectively. Finally the oligomeric benzyl thioether subunit was assembled as a multidentate ligand for the Au NPs. To enhance the quality of the benzylic leaving group, the diols **5** and **6** were converted to the corresponding benzylic dibromides by treatment with carbon tetrabromide (CBr<sub>4</sub>) and triphenylphosphine (PPh<sub>3</sub>). In a final step, the multidentate ligand was assembled by substituting both benzylic bromides by the trimeric benzylthiol **4** as nucleophile in an S<sub>N</sub>2 reaction.<sup>[76]</sup> Thus the benzylic dibromide intermediates were treated with two equivalents of thiol **4** in tetrahydrofuran (THF) in

the presence of sodium hydride as base to provide the target ligands **P1** and **P2** as colorless and slightly yellow oils, respectively, in yields of 71% and 64%, respectively.

The new compounds were characterized by <sup>1</sup>H and <sup>13</sup>C NMR spectroscopy, mass spectrometry, elemental analysis.

**Nanoparticle Preparation and Purification:** The NPs were formed in the presence of the ligands **B1**, **B2**, **P1**, and **P2** using a two-phase method in CH<sub>2</sub>Cl<sub>2</sub>/H<sub>2</sub>O, developed by Brust et al. (see SI for the synthetic protocol).<sup>[92]</sup> TOAB was used as the phase transfer agent and sodium borohydride as the reducing agent. The NP formation was followed by an aqueous work-up and the removal of TOAB by a precipitation/centrifugation sequence. To remove the excess ligand, the ligand-stabilized particles were further purified by SEC.<sup>[76]</sup> While so far the applied synthesis and purification procedures were (within the detection limits) quantitative as far as gold atoms were concerned, about 10–20% of particles were sacrificed during SEC in order to obtain exclusively ligand-stabilized particles as starting material for subsequent coupling reactions.

The obtained NPs were analyzed by UV/vis, <sup>1</sup>H NMR, SAXS, and TEM on carbon-coated copper grids. NP diameters from TEM micrographs were determined by using the software *ImageJ*.<sup>[93]</sup> The grayscale TEM images (see original TEM micrographs Figure S4–S7 in the SI) were converted to black and white, and the areas of the particles were measured automatically (see SI for detailed description). Thermogravimetric analysis (TGA) of the purified and extensively dried NPs displayed a weight loss of 21%, which is assumed to be a direct investigation of the weight contribution of the stabilizing ligands. This knowledge allows the calculation of the amount of gold in the NPs after all purification steps and therefore the final yield. We also used the TGA results to calculate that two ligands stabilize one NP.

**Coupling of Acetylene-Functionalized Particles:** The oxidative coupling of acetylene-functionalized Au NPs was reported previously.<sup>[76]</sup> After deprotection of the acetylene by fluoride ions, an oxidative acetylene coupling protocol developed by Hay was applied (see SI for the synthetic protocol).<sup>[94]</sup> After the short coupling reaction (15 min), an aqueous work-up of the mixture was performed. The yield of this homocoupling was determined with the relative yields of the NP oligomers formed. While none of the acetylene groups in a monomer reacted, a dimer has two reacted acetylenes out of four. Trimers have four out of six and tetramers six out of eight coupled moieties. With the mean fractions of oligomers, the yield of the coupling reaction was determined to be 15% of the initially present acetylenes. The hybrid structures were analyzed by UV/vis spectroscopy and spread on carbon-coated copper grids for subsequent TEM analysis. Highly diluted solutions were used for deposition on the grids to avoid accidental proximity of noncovalently linked particles. Interparticle distances were measured manually on the TEM micrographs mainly from dimers and some tri- and tetramers (see SI for detailed description and Figure S8–S11 for original TEM micrographs).

### Supporting Information

Supporting Information is available from the Wiley Online Library or from the author.

## Acknowledgements

We are grateful for financial support from the EU through the project FUNMOL (number 213382) of the call FP7-NMP-2007-SMALL-1, the Gebert Rűf Foundation, the Swiss National Science Foundation (SNF 200020-116033, SNF 200020-122096 and SNF R'EQUIP 206021\_128747) and the National Research Project No. 62 Smart Materials.

- [1] H. Weller, *Angew. Chem. Int. Ed.* **1993**, *32*, 41–53.
- [2] G. Schmid, M. Baumle, M. Geerkens, I. Heim, C. Osemann, T. Sawitowski, *Chem. Soc. Rev.* **1999**, *28*, 179–185.
- [3] G. Schmid, *Adv. Eng. Mater.* **2001**, *3*, 737–743.
- [4] L. M. Liz-Marzán, *Langmuir* **2006**, *22*, 32–41.
- [5] A. J. Quinn, G. Redmond, *Surf. Sci.* **2007**, *601*, 2740–2745.
- [6] M. Daniel, D. Astruc, *Chem. Rev.* **2004**, *104*, 293–346.
- [7] R. Sardar, A. M. Funston, P. Mulvaney, R. W. Murray, *Langmuir* **2009**, *25*, 13840–13851.
- [8] G. Schmid, U. Simon, *Chem. Commun.* **2005**, 697–710.
- [9] R. P. Andres, J. D. Bielefeld, J. I. Henderson, D. B. Janes, V. R. Kolagunta, C. P. Kubiak, W. J. Mahoney, R. G. Osifchin, *Science* **1996**, *273*, 1690–1693.
- [10] J. Liao, L. Bernard, M. Langer, C. Schönenberger, M. Calame, *Adv. Mater.* **2006**, *18*, 2444–2447.
- [11] S. W. Boettcher, N. C. Strandwitz, M. Schierhorn, N. Lock, M. C. Lonergan, G. D. Stucky, *Nat. Mater.* **2007**, *6*, 592–596.
- [12] S. A. Maier, M. L. Brongersma, H. A. Atwater, *Appl. Phys. Lett.* **2001**, *78*, 16.
- [13] Y. Leroux, J. C. Lacroix, C. Fave, V. Stockhausen, N. Félidj, J. Grand, A. Hohenau, J. R. Krenn, *Nano Lett.* **2009**, *9*, 2144–2148.
- [14] S. D. Evans, S. R. Johnson, Y. L. Cheng, T. Shen, *J. Mater. Chem.* **2000**, *10*, 183–188.
- [15] Y. Kim, R. C. Johnson, J. T. Hupp, *Nano Lett.* **2001**, *1*, 165–167.
- [16] H. Zhang, S. D. Evans, J. R. Henderson, R. E. Miles, T. Shen, *Nanotechnology* **2002**, *13*, 439–444.
- [17] Y. Zhou, S. Wang, K. Zhang, X. Jiang, *Angew. Chem.* **2008**, *47*, 7454–7456.
- [18] M. Riskin, R. Tel-Vered, T. Bourenko, E. Granot, I. Willner, *J. Am. Chem. Soc.* **2008**, *130*, 9726–9733.
- [19] D. A. Schultz, *Curr. Opin. Biotech.* **2003**, *14*, 13–22.
- [20] C. M. Niemeyer, *Angew. Chem. Int. Ed.* **2003**, *42*, 5796–5800.
- [21] E. Katz, I. Willner, *Angew. Chem. Int. Ed.* **2004**, *43*, 6042–6108.
- [22] N. L. Rosi, C. A. Mirkin, *Chem. Rev.* **2005**, *105*, 1547–1562.
- [23] P. Kessler, F. Kotzyba-Hibert, M. Leonetti, F. Bouet, P. Ringler, A. Brisson, A. Ménez, M. P. Goeldner, C. Hirth, *Bioconjug. Chem.* **1994**, *5*, 199–204.
- [24] J. F. Hainfeld, R. D. Powell, *J. Histochem. Cytochem.* **2000**, *48*, 471–480.
- [25] S. Srivastava, N. A. Kotov, *Soft Matter* **2009**, *5*, 1146–1156.
- [26] F. Westerlund, T. Bjørnholm, *Curr. Opin. Colloid In.* **2009**, *14*, 126–134.
- [27] C. L. Choi, A. P. Alivisatos, *Annu. Rev. Phys. Chem.* **2010**, *61*, 369–389.
- [28] C. Sanchez, G. J. D. A. A. Soler-Illia, F. Ribot, T. Lalot, C. R. Mayer, V. Cabuil, *Chem. Mater.* **2001**, *13*, 3061–3083.
- [29] A. B. Descalzo, R. Martínez-Máñez, F. Sancenón, K. Hoffmann, K. Rurack, *Angew. Chem. Int. Ed.* **2006**, *45*, 5924–5948.
- [30] J. Yuan, A. H. Müller, *Polymer* **2010**, *51*, 4015–4036.
- [31] Y. Min, M. Akbulut, K. Kristiansen, Y. Golan, J. Israelachvili, *Nat. Mater.* **2008**, *7*, 527–538.
- [32] K. J. M. Bishop, C. E. Wilmer, S. Soh, B. A. Grzybowski, *Small* **2009**, *5*, 1600–1630.
- [33] P. K. Jain, M. A. El-Sayed, *Chem. Phys. Lett.* **2010**, *487*, 153–164.
- [34] F. Huo, A. Lytton-Jean, C. Mirkin, *Adv. Mater.* **2006**, *18*, 2304–2306.
- [35] C. A. Mirkin, R. L. Letsinger, R. C. Mucic, J. J. Storhoff, *Nature* **1996**, *382*, 607–609.
- [36] A. P. Alivisatos, K. P. Johnsson, X. Peng, T. E. Wilson, C. J. Loweth, M. P. Bruchez, P. G. Schultz, *Nature* **1996**, *382*, 609–611.
- [37] Z. Deng, Y. Tian, S. Lee, A. E. Ribbe, C. Mao, *Angew. Chem. Int. Ed.* **2005**, *44*, 3582–3585.
- [38] F. A. Aldaye, H. F. Sleiman, *Angew. Chem. Int. Ed.* **2006**, *45*, 2204–2209.
- [39] M. Fischler, A. Sologubenko, J. Mayer, G. Clever, G. Burley, J. Gierlich, T. Carell, U. Simon, *Chem. Commun.* **2008**, 169–171.
- [40] J. H. Lee, D. Wernet, M. Yigit, J. Liu, Z. Wang, Y. Lu, *Angew. Chem. Int. Ed.* **2007**, *46*, 9006–9010.
- [41] S. Y. Park, A. K. R. Lytton-Jean, B. Lee, S. Weigand, G. C. Schatz, C. A. Mirkin, *Nature* **2008**, *451*, 553–556.
- [42] M. H. S. Shyr, D. P. Wernet, P. Wiltzius, Y. Lu, P. V. Braun, *J. Am. Chem. Soc.* **2008**, *130*, 8234–8240.
- [43] S. E. Stanca, R. Eritja, D. Fitzmaurice, *Faraday Discuss.* **2006**, *131*, 155–165.
- [44] Q. Zeng, R. Marthi, A. McNally, C. Dickinson, T. E. Keyes, R. J. Forster, *Langmuir* **2010**, *26*, 1325–1333.
- [45] J. Liu, S. Mendoza, E. Román, M. J. Lynn, R. Xu, A. E. Kaifer, *J. Am. Chem. Soc.* **1999**, *121*, 4304–4305.
- [46] M. A. Olson, A. Coskun, R. Klajn, L. Fang, S. K. Dey, K. P. Browne, B. A. Grzybowski, J. F. Stoddart, *Nano Lett.* **2009**, *9*, 3185–3190.
- [47] R. Klajn, M. A. Olson, P. J. Wesson, L. Fang, A. Coskun, A. Trabolsi, S. Soh, J. F. Stoddart, B. A. Grzybowski, *Nat. Chem.* **2009**, *1*, 733–738.
- [48] M. Kanehara, E. Kodzuka, T. Teranishi, *J. Am. Chem. Soc.* **2006**, *128*, 13084–13094.
- [49] K. Naka, H. Itoh, Y. Chujo, *Langmuir* **2003**, *19*, 5496–5501.
- [50] A. K. Boal, F. Ilhan, J. E. DeRouchey, T. Thurn-Albrecht, T. P. Russell, V. M. Rotello, *Nature* **2000**, *404*, 746–748.
- [51] C. R. V. D. Brom, P. Rudolf, T. T. M. Palstra, B. Hessen, *Chem. Commun.* **2007**, 4922–4924.
- [52] S. Fullam, H. Rensmo, S. N. Rao, D. Fitzmaurice, *Chem. Mater.* **2002**, *14*, 3643–3650.
- [53] H. Ozawa, M. Kawao, H. Tanaka, T. Ogawa, *Langmuir* **2007**, *23*, 6365–6371.
- [54] M. Brust, D. J. Schiffrin, D. Bethell, C. J. Kiely, *Adv. Mater.* **1995**, *7*, 795–797.
- [55] R. Klajn, T. P. Gray, P. J. Wesson, B. D. Myers, V. P. Dravid, S. K. Smoukov, B. A. Grzybowski, *Adv. Funct. Mater.* **2008**, *18*, 2763–2769.
- [56] L. Bernard, Y. Kamdzhilov, M. Calame, S. J. Van Der Molen, J. Liao, C. Schönenberger, *J. Phys. Chem. C* **2007**, *111*, 18445–18450.
- [57] G. Zotti, B. Vercelli, A. Berlin, *Chem. Mater.* **2008**, *20*, 397–412.
- [58] J. Liao, M. A. Mangold, S. Grunder, M. Mayor, C. Schönenberger, M. Calame, *New J. Phys.* **2008**, *10*, 065019.
- [59] V. Torma, O. Vidoni, U. Simon, G. Schmid, *Eur. J. Inorg. Chem.* **2003**, 1121–1127.
- [60] M. P. Stemmler, Y. Fogel, K. Mullen, M. Kreiter, *Langmuir* **2009**, *25*, 11917–11922.
- [61] X. M. Lin, C. M. Sorensen, K. J. Klabunde, *Chem. Mater.* **1999**, *11*, 198–202.
- [62] M. M. Maye, S. C. Chun, L. Han, D. Rabinovich, C. Zhong, *J. Am. Chem. Soc.* **2002**, *124*, 4958–4959.
- [63] A. Taubert, U. Wiesler, K. Müllen, *J. Mater. Chem.* **2003**, *13*, 1090–1093.
- [64] H. Yan, S. I. Lim, Y. Zhang, Q. Chen, D. Mott, W. Wu, D. An, S. Zhou, C. Zhong, *Chem. Commun.* **2010**, *46*, 2218–2220.
- [65] L. C. Brousseau III, J. P. Novak, S. M. Marinakos, D. L. Feldheim, *Adv. Mater.* **1999**, *11*, 447–449.
- [66] T. Dadoosh, Y. Gordin, R. Krahn, I. Khivrich, D. Mahalu, V. Frydman, J. Sperling, A. Yacoby, I. Bar-Joseph, *Nature* **2005**, *436*, 677–680.
- [67] X. Liu, H. Liu, W. Zhou, H. Zheng, X. Yin, Y. Li, Y. Guo, M. Zhu, C. Ouyang, D. Zhu, A. Xia, *Langmuir* **2010**, *26*, 3179–3185.
- [68] D. Zanchet, C. M. Micheel, W. J. Parak, D. Gerion, A. P. Alivisatos, *Nano Lett.* **2001**, *1*, 32–35.

- [69] R. Lévy, Z. Wang, L. Duchesne, R. C. Doty, A. I. Cooper, M. Brust, D. G. Fernig, *ChemBioChem* **2006**, *7*, 592–594.
- [70] C. Krüger, S. Agarwal, A. Greiner, *J. Am. Chem. Soc.* **2008**, *130*, 2710–2711.
- [71] K. Sung, D. W. Mosley, B. R. Peelle, S. Zhang, J. M. Jacobson, *J. Am. Chem. Soc.* **2004**, *126*, 5064–5065.
- [72] J. G. Worden, A. W. Shaffer, Q. Huo, *Chem. Commun.* **2004**, 518–519.
- [73] G. A. DeVries, M. Brunnbauer, Y. Hu, A. M. Jackson, B. Long, B. T. Neltner, O. Uzun, B. H. Wunsch, F. Stellacci, *Science* **2007**, *315*, 358–361.
- [74] D. F. Perepichka, F. Rosei, *Angew. Chem. Int. Ed.* **2007**, *46*, 6006–6008.
- [75] T. Peterle, A. Leifert, J. Timper, A. Sologubenko, U. Simon, M. Mayor, *Chem. Commun.* **2008**, 3438–3440.
- [76] T. Peterle, P. Ringer, M. Mayor, *Adv. Funct. Mater.* **2009**, *19*, 3497–3506.
- [77] B. Xu, N. J. Tao, *Science* **2003**, *301*, 1221–1223.
- [78] M. Kamenetska, S. Y. Quek, A. C. Whalley, M. L. Steigerwald, H. J. Choi, S. G. Louie, C. Nuckolls, M. S. Hybertsen, J. B. Neaton, L. Venkataraman, *J. Am. Chem. Soc.* **2010**, *132*, 6817–6821.
- [79] T. Wandlowski, K. Ataka, D. Mayer, *Langmuir* **2002**, *18*, 4331–4341.
- [80] D. Mayer, T. Dretschkow, K. Ataka, T. Wandlowski, *J. Electroanal. Chem.* **2002**, *524–525*, 20–35.
- [81] S. Grunder, R. Huber, S. Wu, C. Schönenberger, M. Calame, M. Mayor, *Eur. J. Org. Chem.* **2010**, *2010*, 833–845.
- [82] S. Grunder, R. Huber, V. Horhoiu, M. T. González, C. Schönenberger, M. Calame, M. Mayor, *J. Org. Chem.* **2007**, *72*, 8337–8344.
- [83] M. M. Alvarez, J. T. Khoury, T. G. Schaaff, M. N. Shafiqullin, I. Vezmar, R. L. Whetten, *J. Phys. Chem. B* **1997**, *101*, 3706–3712.
- [84] C. M. Micheel, D. Zanchet, A. P. Alivisatos, *Langmuir* **2008**, *24*, 10084–10088.
- [85] R. S. Mathew-Fenn, R. Das, P. A. B. Harbury, *Science* **2008**, *322*, 446–449.
- [86] J. M. Jørgensen, K. Erlacher, J. S. Pedersen, K. V. Gothelf, *Langmuir* **2005**, *21*, 10320–10323.
- [87] F. Sander, T. Peterle, N. Ballav, F. V. Wrochem, M. Zharnikov, M. Mayor, *J. Phys. Chem. C* **2010**, *114*, 4118–4125.
- [88] H. Takalo, J. Kankare, *Acta Chem. Scand., Ser. B* **1987**, 291.
- [89] H. Takalo, P. Pasanen, J. Kankare, *Acta Chem. Scand., Ser. B* **1988**, 373.
- [90] K. Sonogashira, Y. Tohda, N. Hagihara, *Tetrahedron Lett.* **1975**, *16*, 4467–4470.
- [91] Y. Nakano, K. Ishizuka, K. Muraoka, H. Ohtani, Y. Takayama, F. Sato, *Org. Lett.* **2004**, *6*, 2373–2376.
- [92] M. Brust, M. Walker, D. Bethell, D. J. Schiffrin, R. Whyman, *J. Chem. Soc., Chem. Commun.* **1994**, 801–802.
- [93] P. J. Magelhaes, S. J. Ram, M. D. Abramoff, *Biophotonics Int.* **2004**, *11*, 36–42.
- [94] A. S. Hay, *J. Org. Chem.* **1962**, *27*, 3320–3321.

Received: November 22, 2010  
Published online: March 11, 2011

Copyright WILEY-VCH Verlag GmbH & Co. KGaA, 69469 Weinheim, Germany,  
2010.

NANO MICRO  
**small**

## Supporting Information

for *Small*, DOI: 10.1002/smll.201002101

Direct Control of the Spatial Arrangement of Gold Nanoparticles in Organic–  
Inorganic Hybrid Superstructures

Jens P. Hermes, Fabian Sander, Torsten Peterle, Carla Cioffi,  
Philippe Ringler, Thomas Pfohl, and Marcel Mayor\*

Supporting Information for the manuscript:

**Direct control of the Spatial Arrangement of Gold Nanoparticles in Organic-Inorganic Hybrid Superstructures**

By *Jens P. Hermes, Fabian Sander, Torsten Peterle, Carla Cioffi, Philippe Ringler, Thomas Pfohl and Marcel Mayor\**

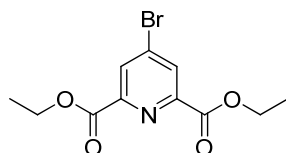
**Table of Contents:**

General Methods . . . . .	S2
Experimental Procedures for the Synthesis of <b>1, 2, 5, 6, P1</b> and <b>P2</b> . . . . .	S2
Au NPs formation, hybrid oligomer formation . . . . .	S9
Small Angle X-Ray Scattering . . . . .	S10
Transmission Electron Microscopy . . . . .	S10
References . . . . .	S22

## General Methods

All commercially available starting materials were of reagent grade and used as received. Absolute tetrahydrofuran (THF) was purchased from *Fluka*, stored over 4 Å molecular sieves, and handled under Argon. *tert*-Butylmethylether (MTBE), hexane and dichloromethane were of technical grade and distilled prior to use. Column chromatography purifications were carried out on *silica gel 60* (particle size 40-63 µm) from *Fluka*. Deuterated solvents were purchased from *Cambridge Isotope Laboratories*.  $^1\text{H}$  and  $^{13}\text{C}$  NMR spectra were recorded with a *Bruker DMX 400* instrument ( $^1\text{H}$  resonance 400 MHz) or a *Bruker DRX 500* instrument ( $^1\text{H}$  resonance 500 MHz) at 298 K. Matrix Assisted Laser Desorption Ionisation Time of Flight (MALDI-ToF) mass spectra were performed on an *Applied Bio Systems Voyager-De™ Pro* mass spectrometer. Electron Impact (EI) mass spectra were recorded on a *Finnigan MAT 95Q* by H. Nadig. Elemental analyses were performed by W. Kirsch on a *Perkin-Elmer Analyticator 240*. Thermogravimetric analysis was performed on a *Mettler Toledo TGA/SDTA851<sup>e</sup>*. UV/vis spectra were recorded on an *Agilent 8453E* spectrophotometer. Size exclusion chromatography (SEC) was performed using *Bio-Rad Bio-Beads S-XI Beads* (operating range 600 – 14000 g mol<sup>-1</sup>) with toluene as eluent. Gel Permeations Chromatography (GPC) was performed on a *Shimadzu Prominence System* with *PLGel* preparative columns from *Polymer Laboratories* (2 columns in series, operating ranges: up to 4000 g mol<sup>-1</sup> and 500 – 30000 g mol<sup>-1</sup>) using toluene as eluent.

## Diethyl 4-bromopyridine-2,6-dicarboxylate<sup>[1]</sup> (1)



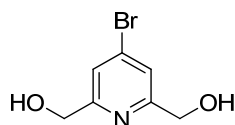
To a solution of bromine (2.7 ml, 8.34 g, 52 mmol, 3.2 eq) in hexane under argon was added slowly phosphorus tribromide (5.9 ml, 17.96 g, 63 mmol, 3.9 eq) with a syringe. Phosphorus pentabromide precipitated as yellow solid, which was washed four times with hexane (10 ml) and then dried under high vacuum. To the powder was added chelidamic acid (3.4 g, 16.9 mmol, 1 eq) and the mixture was heated to 90°C for 1.5 hours. After cooling to room temperature, dry chloroform (17 ml) was added to the black solid and the slurry was filtered



under argon. To the slight red filtrate was added absolute ethanol (50 ml) at 0°C, resulting in a blue solution. The solvent was evaporated and the residue was taken up in dichloromethane and extracted with a saturated aqueous solution of sodium hydrogen carbonate. The organic fraction was dried over magnesium sulfate, filtered and evaporated to dryness, leaving some colorless solid material in some highly boiling liquid (together 5.5 g). The crude was purified by recrystallization from ethanol, giving the title compound **1** (4.03 g, 13.3 mmol, 79 %) as white solid.

$^1\text{H}$  NMR (400 MHz,  $\text{CDCl}_3$ ):  $\delta$  = 8.41 (*s*, 2H, Ar-*H*), 4.48 (*q*,  $J$  = 7.05 Hz, 4H,  $\text{CH}_2$ ) 1.44 (*t*,  $J$  = 7.08 Hz, 6H,  $\text{CH}_3$ );  $^{13}\text{C}$ -NMR (100 MHz,  $\text{CDCl}_3$ ):  $\delta$  = 163.5, 149.4, 134.9, 131.0, 62.7, 14.1; FABMS ( $m/z$ ): 301.9 [ $M+\text{H}$ ] $^+$ .

#### 4-Bromopyridine-2,6-dimethanol<sup>[2]</sup> (**2**)

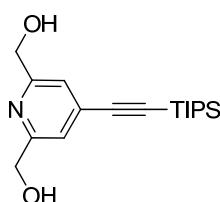


To a solution of diethyl 4-bromopyridine-2,6-dicarboxylate (**1**) (3.75 g, 12.4 mmol, 1 eq) in absolute ethanol (150 ml) was added sodium borohydride (3.29 g, 86.9 mmol, 7 eq). The mixture was heated to reflux for 20 hours, before the solvent was removed by evaporation. A saturated aqueous solution of sodium hydrogen carbonate (23 ml) was added to the residue and the mixture was heated to reflux until all solid material was dissolved. Water (28 ml) was then added and the mixture was left for 14 hours at 4°C. The formed oily solid was collected by decantation and the dried under vacuum. The white powder was extracted 5 times with acetone (100 ml) and the combined acetone fractions were evaporated to dryness, giving 4-bromopyridine-2,6-dimethanol (**2**) (1.49 g, 6.8 mmol, 55 %) as colorless solid.

TLC revealed the presence of the desired product **2** in the extracted solid. Therefore this residue was dissolved in water (800 ml) and this solution was extracted 4 times with ethyl acetate (200 ml). The combined organic fractions were dried over magnesium sulfate, filtered and evaporated to dryness, giving more of the desired product **2** (1.01 g, 4.6 mmol, 38%, total: 2.50 g, 11.5 mmol, 93%).

$^1\text{H}$  NMR (400 MHz, DMSO- $d_6$ ):  $\delta$  = 7.51 (s, 2H, Ar-H), 5.54 (t,  $J$  = 5.91 Hz, 2H, OH) 4.52 (d,  $J$  = 5.87 Hz, 4H, CH<sub>2</sub>);  $^{13}\text{C}$  NMR (100 MHz, DMSO- $d_6$ ):  $\delta$  = 163.2, 133.3, 121.1, 63.7; EIMS ( $m/z$  (%)): 216.0 (100) [ $M^+$ ].

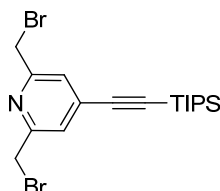
#### (4-((Triisopropylsilyl)ethynyl)pyridine-2,6-diyl)dimethanol (**5**)



(4-Bromopyridine-2,6-diyl)dimethanol (**80**) (86.5 mg, 0.40 mmol, 1 eq) was dissolved in degassed triethylamine (10 ml) under an atmosphere of argon. (Triisopropylsilyl)acetylene (240  $\mu\text{l}$ , 217 mg, 1.19 mmol, 3 eq), bis(triphenylphosphine)palladium(II) chloride (28 mg, 0.04 mmol, 10 mol%) and copper(I) iodide (7.6 mg, 0.04 mmol, 10 mol%) were added and the mixture was heated to 80°C for 15 hours. After cooling to room temperature, the solvent was evaporated under vacuum. Dichloromethane was added and the resulting mixture was extracted with water. The aqueous phase was then extracted two more times with dichloromethane. The combined organic fractions were dried over magnesium sulfate and evaporated to dryness after filtration. Purification of the crude product by column chromatography (ethyl acetate, then ethyl acetate/acetone 1:1) yielded the desired product **5** (113.5 mg, 0.32 mmol, 81%) as colorless solid.

$^1\text{H}$  NMR (400 MHz, CDCl<sub>3</sub>):  $\delta$  = 7.24 (s, 2H, Ar-H), 4.76 (s, 4H, CH<sub>2</sub>), 3.16 (br, 2H, OH), 1.13 (m, 21H, *i*Pr-H);  $^{13}\text{C}$  NMR (100 MHz, CDCl<sub>3</sub>):  $\delta$  = 158.6, 132.9, 121.4, 104.0, 97.1, 64.2, 18.6, 11.1; EIMS ( $m/z$  (%)): 319.2 (2) [ $M^+$ ], 276.2 (100) [ $M^+$ -C<sub>3</sub>H<sub>7</sub>]; Anal calcd. for C<sub>18</sub>H<sub>29</sub>NO<sub>2</sub>Si: C 67.66, H 9.15, N 4.38; found: C 67.97, H 8.66, N 3.95.

### 2,6-Bis(bromomethyl)-4-((triisopropylsilyl)ethynyl)pyridine

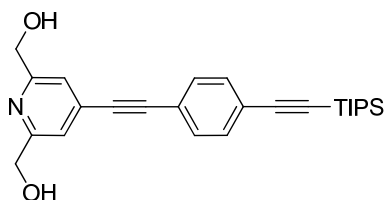


(4-((Triisopropylsilyl)ethynyl)pyridine-2,6-diyl)dimethanol (**5**) (86.4 mg, 0.27 mmol, 1 eq) was dissolved in dry tetrahydrofuran (12 ml) under an atmosphere of argon. To this solution was added triphenylphosphine (213 mg, 0.81 mmol, 3 eq), followed by carbon tetrabromide (269 mg, 0.81 mmol, 3 eq). The solution was stirred at room temperature for 2 hours, during which a white precipitate formed. A saturated aqueous solution of sodium hydrogen carbonate was added and the mixture was extracted three times with MTBE. The combined organic fractions were washed with brine, dried over magnesium sulfate, filtered and then evaporated to dryness. Purification of the crude by column chromatography (hexane/dichloromethane 2:1, then 1:2) gave the title compound (83.0 mg, 0.19 mmol, 69%) as colorless solid.

$^1\text{H}$  NMR (400 MHz,  $\text{CDCl}_3$ ):  $\delta$  = 7.38 (s, 2H, Ar-H), 4.50 (s, 4H,  $\text{CH}_2$ ), 1.13 (m, 21H, *i*Pr-H);  
 $^{13}\text{C}$  NMR (100 MHz,  $\text{CDCl}_3$ ):  $\delta$  = 156.9, 133.7, 125.0, 103.2, 98.0, 33.0, 18.6, 11.1.

EIMS ( $m/z$  (%)): 545.1 (9) [ $M^+$ ], 502.0 (100) [ $M^+ - \text{C}_3\text{H}_7$ ]; Anal. calcd. for  $\text{C}_{18}\text{H}_{27}\text{Br}_2\text{NSi}$ : C 48.55, H 6.11; N 3.15; found: C 48.76, H 6.15, N 3.06

### (4-(((4-((Triisopropylsilyl)ethynyl)phenyl)ethynyl)pyridine-2,6-diyl)dimethanol (**6**)

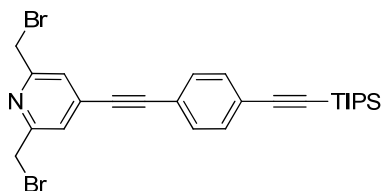


(4-Bromopyridine-2,6-diyl)dimethanol (**2**) (201.8 mg, 0.93 mmol, 1 eq) and ((4-ethynylphenyl)ethynyl)triisopropylsilane<sup>[3]</sup> (**3**) (313.8 mg, 1.11 mmol, 1.2 eq) were dissolved in degassed triethylamine (7 ml) under an atmosphere of argon. Argon was then bubbled through the solution for 10 minutes, before bis(triphenylphosphine)palladium(II) chloride (65 mg,

0.09 mmol, 10 mol%) and copper(I) iodide (17.8 mg, 0.09 mmol, 10 mol%) were added. The dark brown mixture was heated under stirring to 80°C for 1.5 hours. Dichloromethane and a saturated aqueous solution of ammonium chloride were added and the two phases were separated. The aqueous phase was washed twice with dichloromethane and the combined organic fractions were dried over magnesium sulfate. After filtration, the solvent was removed by rotary evaporation. The crude mixture was purified by column chromatography (ethyl acetate, then ethyl acetate/acetone 2:1) to give the desired product **6** (315.3 mg, 0.75 mmol, 81%) as colorless solid.

<sup>1</sup>H NMR (400 MHz, CDCl<sub>3</sub>): δ = 7.47 (br, 4H, Ar-H), 7.31 (br, 2H, Ar-H), 4.78 (s, 4H, CH<sub>2</sub>), 3.20 (br, 2H, OH), 1.13 (m, 21H, *i*Pr-H); <sup>13</sup>C NMR (100 MHz, CDCl<sub>3</sub>): δ = 158.8, 132.6, 132.1, 131.7, 124.5, 121.6, 121.0, 106.3, 93.7, 91.1, 88.3, 64.3, 18.6, 11.3; EIMS (*m/z* (%)): 419.2 (11) [*M*<sup>+</sup>], 376.3 (100) [*M*<sup>+</sup>-C<sub>3</sub>H<sub>7</sub>]; Anal. calcd. for C<sub>26</sub>H<sub>33</sub>NO<sub>2</sub>Si: C 74.42; H 7.93; N 3.34; found: C 72.20, H 8.01, N 3.56.

### 2,6-Bis(bromomethyl)-4-((4-((triisopropylsilyl)ethynyl)phenyl)ethynyl)pyridine

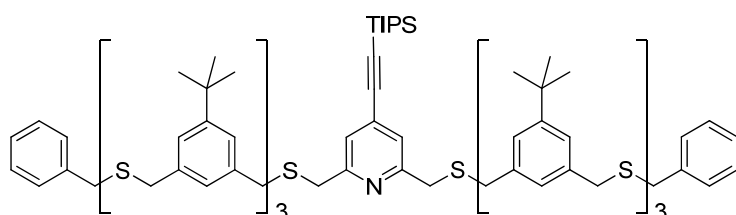


The OPE dihydroxide **6** (278.1 mg, 0.66 mmol, 1 eq) was dissolved in dry tetrahydrofuran (20 ml) under an atmosphere of argon. To this solution was added triphenylphosphine (521.9 mg, 1.99 mmol, 3 eq), followed by carbon tetrabromide (660.0 mg, 1.99 mmol, 3 eq). The solution was stirred at room temperature for 1 hour, during which a white precipitate formed. A saturated aqueous solution of sodium hydrogen carbonate was added and the mixture was extracted three times with MTBE. The combined organic fractions were washed with brine, dried over magnesium sulfate, filtered and then evaporated to dryness. Purification of the crude by column chromatography (hexane/dichloromethane 2:1, then 1:1) gave the title compound (228.9 mg, 0.42 mmol, 63%) as slightly yellow oil, which slowly solidified.

<sup>1</sup>H NMR (400 MHz, CDCl<sub>3</sub>): δ = 7.48 (br, 4H, Ar-H), 7.47 (br, 2H, Ar-H), 4.53 (s, 4H, CH<sub>2</sub>), 1.13 (m, 21H, *i*Pr-H); <sup>13</sup>C NMR (100 MHz, CDCl<sub>3</sub>): δ = 157.0, 133.4, 132.1, 131.7, 124.6,

124.5, 121.4, 106.2, 94.4, 93.8, 87.7, 33.0, 18.6, 11.3; EIMS ( $m/z$  (%)): 545.1 (9) [ $M^+$ ], 502.0 (100) [ $M^+ - C_3H_7$ ]; Anal. calcd. for  $C_{26}H_{31}Br_2NSi$ : C 57.25; H 5.73; N 2.57; found: C 56.43, H 5.78, N 2.78.

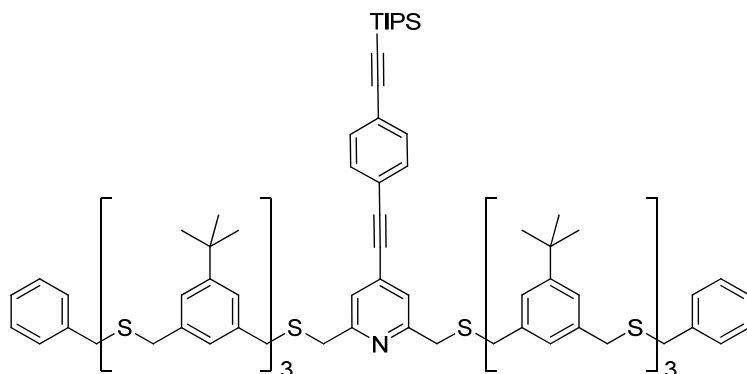
**2,6-bis(((3-(((3-(((3-((benzylthio)methyl)-5-(*tert*-butyl)benzyl)thio)methyl)-5-(*tert*-butyl)benzyl)thio)methyl)-5-(*tert*-butyl)benzyl)thio)methyl)-4-((triisopropylsilyl)ethynyl)pyridine (P1)**



2,6-Bis(bromomethyl)-4-((4-((triisopropylsilyl)ethynyl)phenyl)ethynyl)pyridine (23 mg, 52  $\mu$ mol, 1 eg) and the BnS-SH-Trimer **4** (80 mg, 0.11 mmol, 2.2 eg.) were dissolved in dry THF under an atmosphere of Argon. The mixture was degassed by bubbling Argon through the solution for 10 minutes. Afterwards sodium hydride (60% in mineral oil, 9 mg, 0.23 mmol, 4.5 eg.) was added and the mixture was left stirring at room temperature for 1.5 h. The reaction was quenched with water and extracted with *t*-butyl methyl ether three times. The combined organic fractions were washed with brine, dried over magnesium sulfate, and evaporated to dryness. Purification of the crude product was achieved by CC (hexane/ $CH_2Cl_2$  1:1, then 1:1 with 1% triethylamine) to yield the ligand **P1** (62 mg, 37  $\mu$ mol, 71%) as colorless oil. The ligand was further purified by recycling GPC (4 cycles) to obtain a higher purity. As the elemental analysis of **P2** perfectly matched the calculated values after this procedure a new EA for **P1** was not performed.

$^1H$  NMR (500 MHz,  $CDCl_3$ ):  $\delta$  = 7.30-7.07 (m, 30H, Ar-H), 3.71 (s, 8H,  $CH_2$ ), 3.60 (s, 24H,  $CH_2$ ), 1.31 (m, 54H, *t*Bu-H), 1.13 (m, 21H, *i*Pr-H);  $^{13}C$  NMR (125 MHz,  $CDCl_3$ ):  $\delta$  = 158.5, 151.5 (2 $\times$ ), 138.2, 138.1, 138.0, 137.8, 129.0, 128.4, 126.9, 126.8, 125.0, 124.9, 124.7, 123.4, 104.6, 37.3, 36.1, 35.9, 35.8, 35.7, 34.6, 31.4 (2 $\times$ ), 18.6, 11.2; MALDI-ToFMS ( $m/z$ ): broad peak at 1707 [ $M+Na$ ] $^+$ ; Anal. calcd. for  $C_{104}H_{137}NS_8Si$ : C 74.10; H 8.19; N 0.83; found C 73.34; H 8.35; N 1.00.

**2,6-bis(((3-(((3-(((3-((benzylthio)methyl)-5-(*tert*-butyl)benzyl)thio)methyl)-5-(*tert*-butyl)benzyl)thio)methyl)-5-(*tert*-butyl)benzyl)thio)methyl)-4-((4-((triisopropylsilyl)ethynyl)phenyl)ethynyl)pyridine (P2)**



2,6-Bis(bromomethyl)-4-((4-((triisopropylsilyl)ethynyl)phenyl)ethynyl)pyridine (94 mg, 0.17 mmol, 1 eg) and the BnS-SH-Trimer **4** (265 mg, 0.38 mmol, 2.2 eg.) were dissolved in dry THF under an atmosphere of Argon. The mixture was degassed by bubbling Argon through the solution for 10 minutes. Afterwards sodium hydride (60% in mineral oil, 31 mg, 0.77 mmol, 4.5 eg.) was added and the mixture was left stirring at room temperature for 1.5 h. The reaction was quenched with water and extracted with *t*-butyl methyl ether three times. The combined organic fractions were washed with brine, dried over magnesium sulfate, and evaporated to dryness. Purification of the crude product was achieved by CC (hexane/CH<sub>2</sub>Cl<sub>2</sub> 1:1, then 1:1 with 1% triethylamine) to yield the ligand **P2** (196 mg, 0.11 mmol, 64%) as slight yellow oil. The ligand was further purified by recycling GPC (11 cycles) to obtain a purity of 99.9%.

<sup>1</sup>H NMR (500 MHz, CDCl<sub>3</sub>): δ = 7.50-7.46 (m, 4H, Ar-H), 7.31-7.07 (m, 30H, Ar-H), 3.74 (s, 4H, CH<sub>2</sub>), 3.71 (s, 4H, CH<sub>2</sub>), 3.61-3.58 (m, 24H, CH<sub>2</sub>), 1.32 (m, 54H, *t*Bu-H), 1.15 (m, 21H, *i*Pr-H); <sup>13</sup>C NMR (125 MHz, CDCl<sub>3</sub>): δ = 158.6, 151.5 (3×), 138.2, 138.1, 138.0, 137.8, 137.6, 132.1, 131.6, 129.0, 128.4, 126.9, 126.8, 125.0, 124.8 (2x), 124.7, 123.0, 106.3, 93.5, 93.3, 88.6, 37.3, 36.2, 35.9, 35.8, 35.7, 34.6, 31.4, 31.3, 18.6, 11.3; MALDI-ToFMS (*m/z*): broad peak at 1807 [M+Na]<sup>+</sup>; Anal. calcd. for C<sub>112</sub>H<sub>141</sub>NS<sub>8</sub>Si: C 75.32; H 7.96; N 0.78; found C 75.34; H 8.02; N 0.85.

**Gold nanoparticle formation and purification, general procedure:**

Gold nanoparticle (Au NP) syntheses were carried out on a 2.5–3.5 mmol scale with respect to the thioether ligands **B1**, **B2**, **P1** or **P2**. Tetrachloroauric acid (8 eq) was dissolved in deionized water (2.5 mL). A solution of TOAB (16 eq) in CH<sub>2</sub>Cl<sub>2</sub> (2.5 mL) was added, and the two-phase mixture stirred until the aqueous phase became colorless. The respective ligand **B1**, **B2**, **P1** or **P2** (1 equivalent) was dissolved in dichloromethane (2.5 mL) and then added to the reaction mixture, followed by a freshly prepared solution of sodium borohydride (64 eq) in water (2.5 mL). After 10 min stirring, the resulting strongly colored CH<sub>2</sub>Cl<sub>2</sub> phase was separated, and the aqueous phase was washed twice with CH<sub>2</sub>Cl<sub>2</sub>. The combined organic fractions were dried over magnesium sulfate, filtered, and concentrated to a volume of ca. 2 mL. Ethanol (20 mL) was added to precipitate the NPs, which were then centrifuged. The supernatant was discarded, and the procedure was repeated one more time. After this procedure, the NPs were subjected to size exclusion chromatography (SEC). The colored, NP-containing fractions were collected, the removal of excess ligand checked by UV/vis and the solvent was removed using a rotary evaporator without heating.

**Formation of gold nanoparticle hybrid oligomers, general procedure:**

The formation of Au NP aggregates and superstructures (**Au-Ax**)<sub>n</sub> was done on a 0.9 – 1.1 mg scale regarding **Au-Ax**. The acetylene functionalized Au NPs were dispersed in dichloromethane (200 µl) and tetra-*n*-butylammonium fluoride (1M in tetrahydrofuran, 5 µl) was added. The mixture was left stirring for 1 hour, after which *N,N,N',N'*-tetramethylethylenediamine (5 µl) and copper(I) chloride (0.5 mg) were added. After 15 minutes, a small amount of the reaction mixture was removed, diluted with dichloromethane and investigated by UV/vis spectroscopy to analyze the progress of the reaction. An increase and redshift of the absorption below 400 nm, due to the elongation of the π-system, points at the successful dimerization of the interparticle OPE rods (Figure S1). The mixture was diluted with dichloromethane, extracted with a saturated aqueous solution of ammonium chloride, dried, evaporated and analyzed by UV/vis spectroscopy and TEM on carbon coated copper grids. Highly diluted solutions were used for deposition on the grids to avoid accidental proximity of not covalently linked NPs. Interparticle distances were measured manually on the TEM micrographs mainly from dimers and some tri- and tetramers.

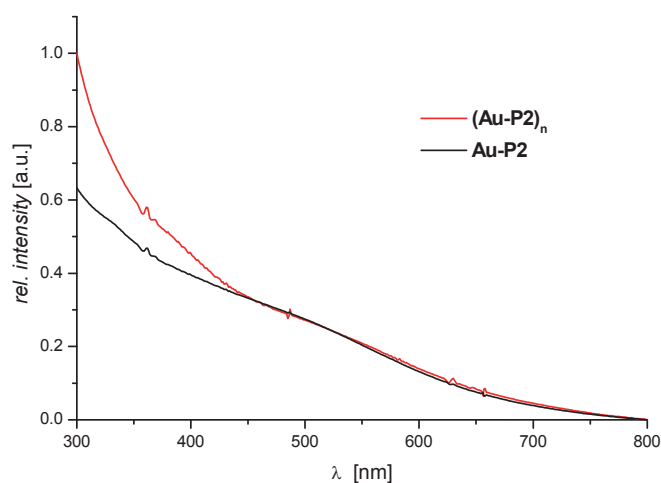


**Figure S1.** Representative UV/vis spectra of gold nanoparticles **Au-P2** and **(Au-P2)<sub>n</sub>** to monitor the oxidative diacetylene coupling.

### (Small) Angle X-Ray Scattering, SAXS

A Bruker AXS Nanostar setup, including an Incoatec Cu- $\mu$ S microfocused X-ray source ( $\lambda = 0.154$  nm) with Montel multilayer optics at a generator power of 40W (45kV, 630 $\mu$ A) and a virtually noise-free, real-time Vântec 2D-detector with photon counting ability, was used to perform X-ray measurements in the range of scattering vectors from 0.5 - 7.5 nm<sup>-1</sup>. All 2D detector images of the samples in quartz capillaries (diameter 1.5 mm) were taken at ambient temperatures with exposure times of 4 h per sample and azimuthally-averaged using Fit2D software to produce 1D intensity profiles.

### Transmission Electron Microscopy (TEM)

TEM was performed on a *Philips CM100* transmission electron microscope at 80 kV. Electron micrographs were recorded on a 2000 by 2000 pixel charge-coupled device camera *Veleta* from *Olympus*. The micrographs were recorded with a magnification of 180kx leading to micrographs with 520 nm by 520 nm and a size of 0.26 nm per pixel. Therefore the column width of the histograms was chosen to be 0.3 nm. One NP has a diameter of four pixels and an area of ten to twelve pixels.

The NPs were deposited by carefully putting a drop of the NP dispersion on top of a thin carbon film that spanned a perforated holey carbon support film covering a gold-plated copper microscopy grid. The remaining solvent was directly blotted with filter paper and the grid air dried.



### Nanoparticle Analysis

The NP diameters were measured automatically using the program *imageJ*. The rather dense images (see micrographs: Figure S4-S7) were first transferred into a 8-bit greyscale and then into black and white using the function “Threshold” and the setting “intermodes”. The area of the NPs was measured with “Analyze particles”. The particles on edges were excluded and holes included. Au NPs were measured with areas from  $0.3 \text{ nm}^2$  till infinity and with circularities from 0.95-1. As the final diameters were calculated from the measured areas we needed to focus on perfectly spherical NPs to avoid mistakes upon calculation. More than 80 % percent of NPs were within this range. NP sizes were measured from two to four dense micrographs (3k to 10k counts of NPs).

The oligomer fractions were measured from one representative diluted image (see Figure S8-S11) by first counting all NPs automatically (similar to above described procedure) and further subtraction of the amount of dimers, trimers and tetramers that were counted manually. For this study one or two micrographs were investigated (200 to 400 counts of NP oligomers)

The interparticle distances were measured manually from similar diluted samples, after transferring the images to black and white using the same threshold settings as before. This ensures the comparability of length and distance measurements. All NP aggregates with a distance up to 10 % above the calculated length were measured. Four to twelve micrographs were analyzed to finally have between 50 and 100 counts of NP oligomers. However for **(Au-P2)<sub>2-4</sub>** all counts were taken from one image. By fitting the data of each histogram with a Gaussian fit we could determine the maximum of the distance distribution to obtain the final values of NP distances.

### Control Experiments

To support the presented results we performed distance measurements of uncoupled monomers (more than 200 counts of NP oligomers) to prove that the presented tendencies result from the coupling, not from deposition artifacts. Uncoupled protected NPs were deposited on carbon coated copper grids (without holey carbon support film) from much diluted solutions. The distances of NPs were measured up to 4 nm. This range is at least 50% longer than the calculated distances. The control series shows that monomeric NPs tend to lie next to each other but their distance distribution shows a very broad distribution between 0.7 nm to 3.5 nm for each sample (Figure S1B). This shows that NPs have the tendency to lie

close to each other with a certain distance range but this range is the same for all samples and is much broader than the distance distribution for coupled NPs.

To ensure the comparability of the control series with the distance distribution of coupled NPs we prepared a second series of covalently coupled NPs. Those were also analyzed from much diluted solutions deposited on carbon coated copper grids without holey carbon support film and with distances up to 4 nm. 12 to 14 micrographs were analyzed to finally have more than 200 counts of NP oligomers. The distance distribution obtained (**Figure S1A**) and the measured interparticle spacings (Table S1) show the same trend as the first series of interlinked hybrid structures.

By subtracting the control measurements from the distances of coupled NPs we obtain a histogram that presents the results more clearly without changing the outcome (Figure S1C).

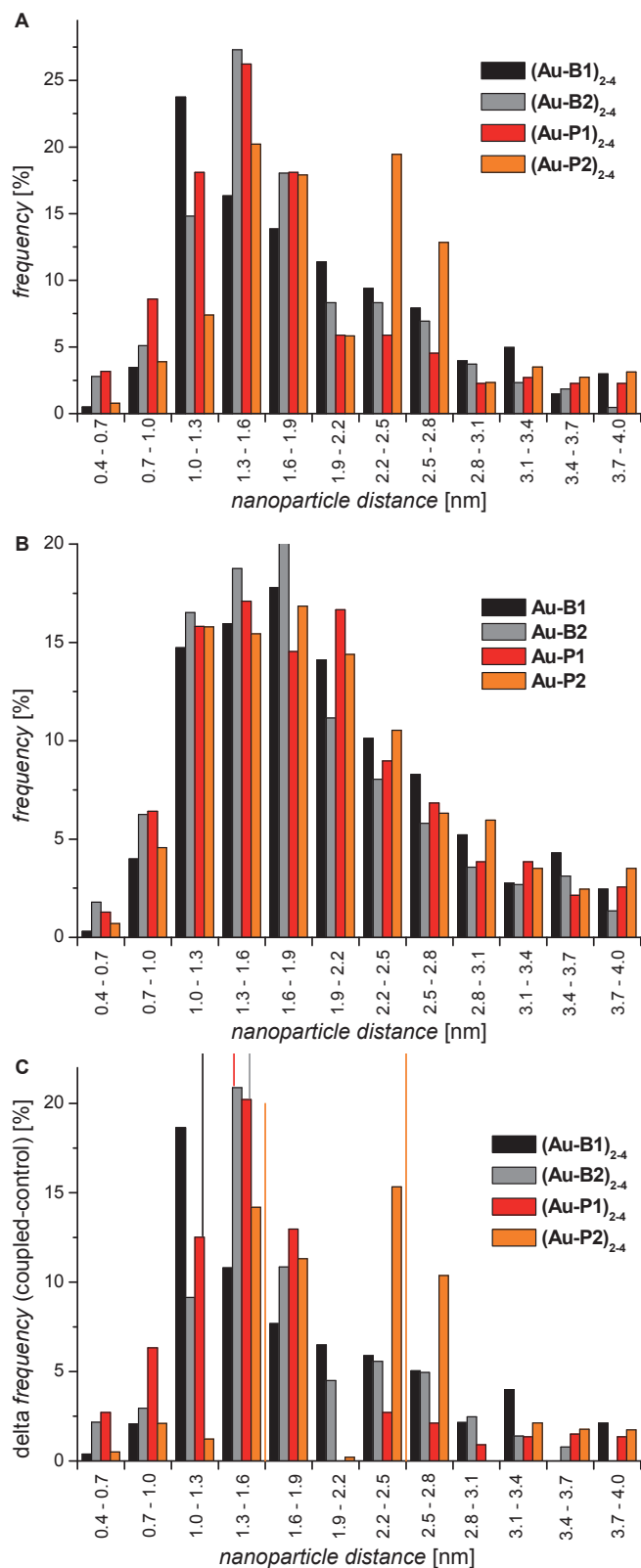


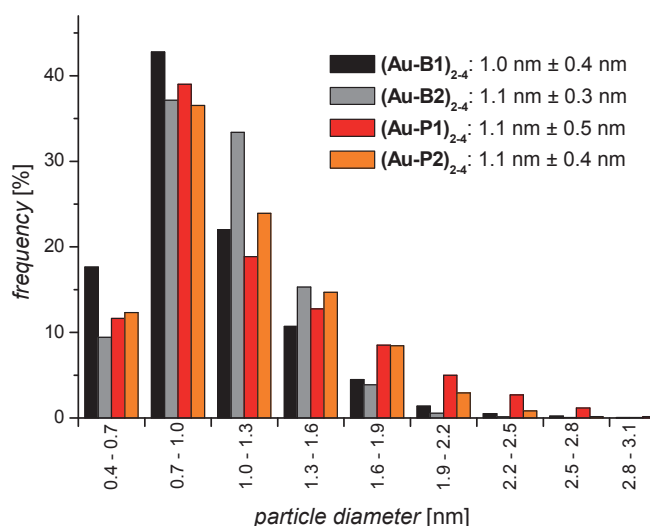
**Figure S2.** A) Nanoparticle distance distribution of coupled particles; B) nanoparticle distance distribution of monomeric particles; C) difference of other histograms (C = A-B), solid lines represent the mean distance found for each sample

Sample - distance / nm	Second series	MM2 length	Calculated	First series
<b>B1</b>	1.2	1.4		0.8
<b>B2</b>	1.5	2.7		1.4
<b>P1</b>	1.4	1.2		1.0
<b>P2</b>	2.5 (1.6)	2.4		2.5

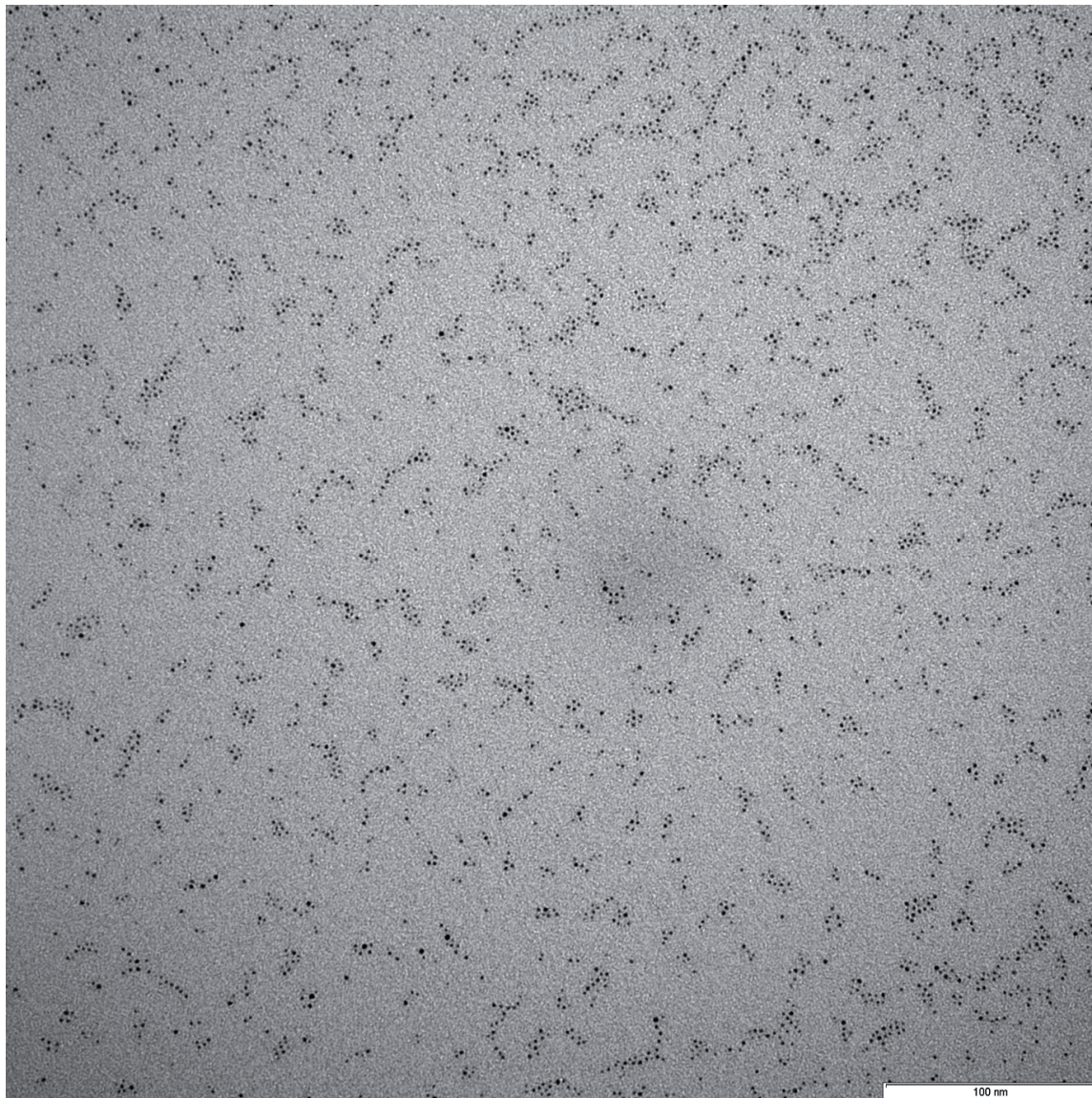
**Table S1.** Maxima of nanoparticle distance distributions of first and second series in comparison with the calculated values, ligand **P2** shows two maxima in the second series.

The distances of samples  $(\text{Au-B1})_{2-4}$  and  $(\text{Au-P1})_{2-4}$  increase 0.4 nm in the second series while the maxima of  $(\text{Au-B2})_{2-4}$  and  $(\text{Au-P2})_{2-4}$  stay the same. The main difference is that  $(\text{Au-P2})_{2-4}$  shows a bimodal distribution with a second maximum at 1.6 nm. This second maximum could have several reasons. It could derive from NPs that are interlinked in a tangential manner (similar to  $(\text{Au-B2})_{2-4}$ ) or interlinked by half of a rod. This could happen, if the acetylene coordinates to the surface of the NP. The second peak could also arise from monomeric structures. Therefore this second series supports the first one to prove the concept (Figure 2).

We also performed diameter measurements of the coupled NPs (Figure S3) using the same protocol as for the size determination of monomeric NPs. The mean diameter did not change but the standard deviation increased slightly. This is due to a few larger NPs that are obtained after the coupling.



**Figure S3.** Size distribution of coupled gold nanoparticles  $(\text{Au-B1})_n$ ,  $(\text{Au-B2})_n$ ,  $(\text{Au-P1})_n$  and  $(\text{Au-P2})_n$ .

**TEM Micrographs**

**Figure S4.** Original TEM micrograph of **Au-B1**.

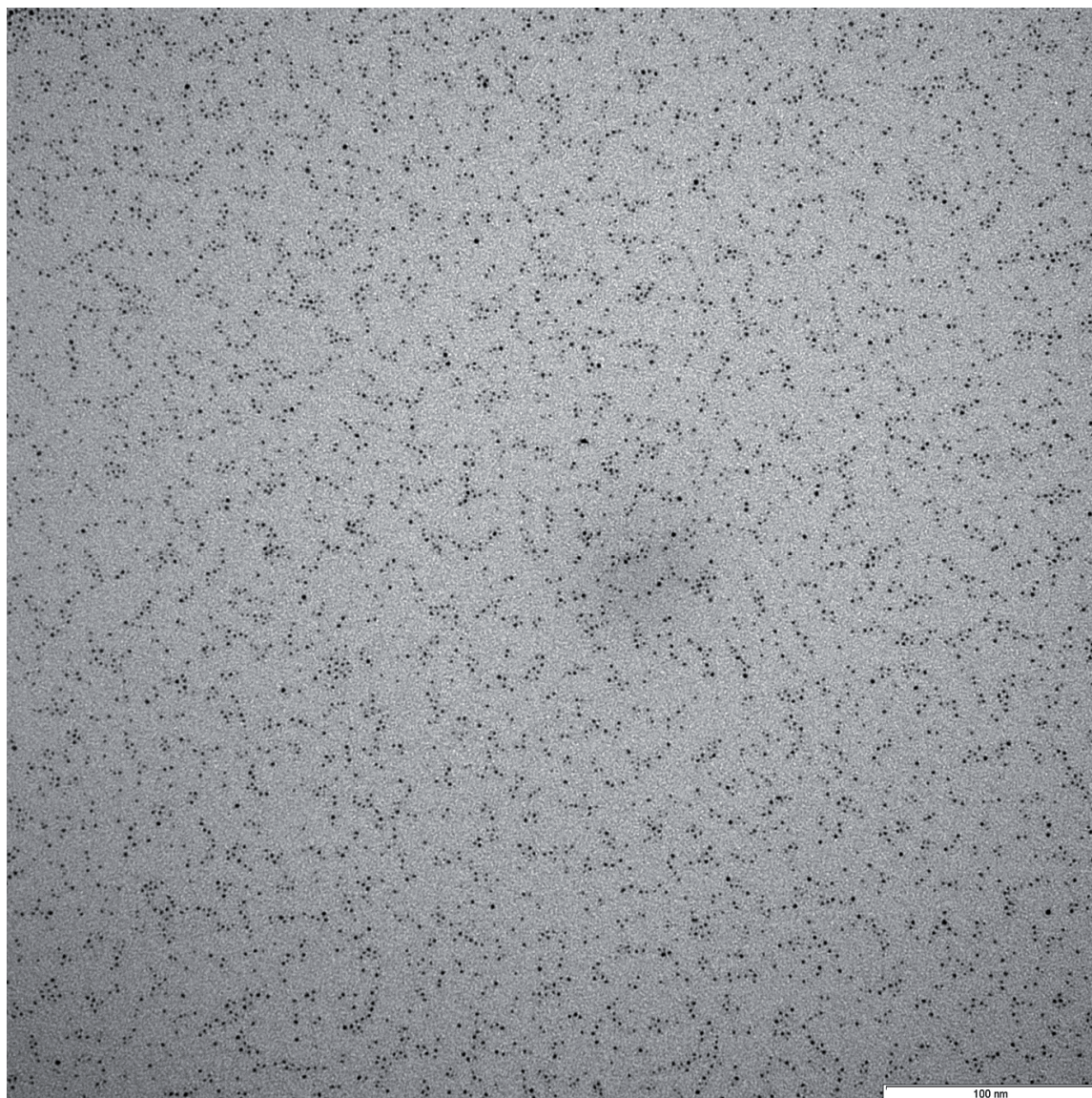


**Figure S5.** Original TEM micrograph of **Au-B2**.

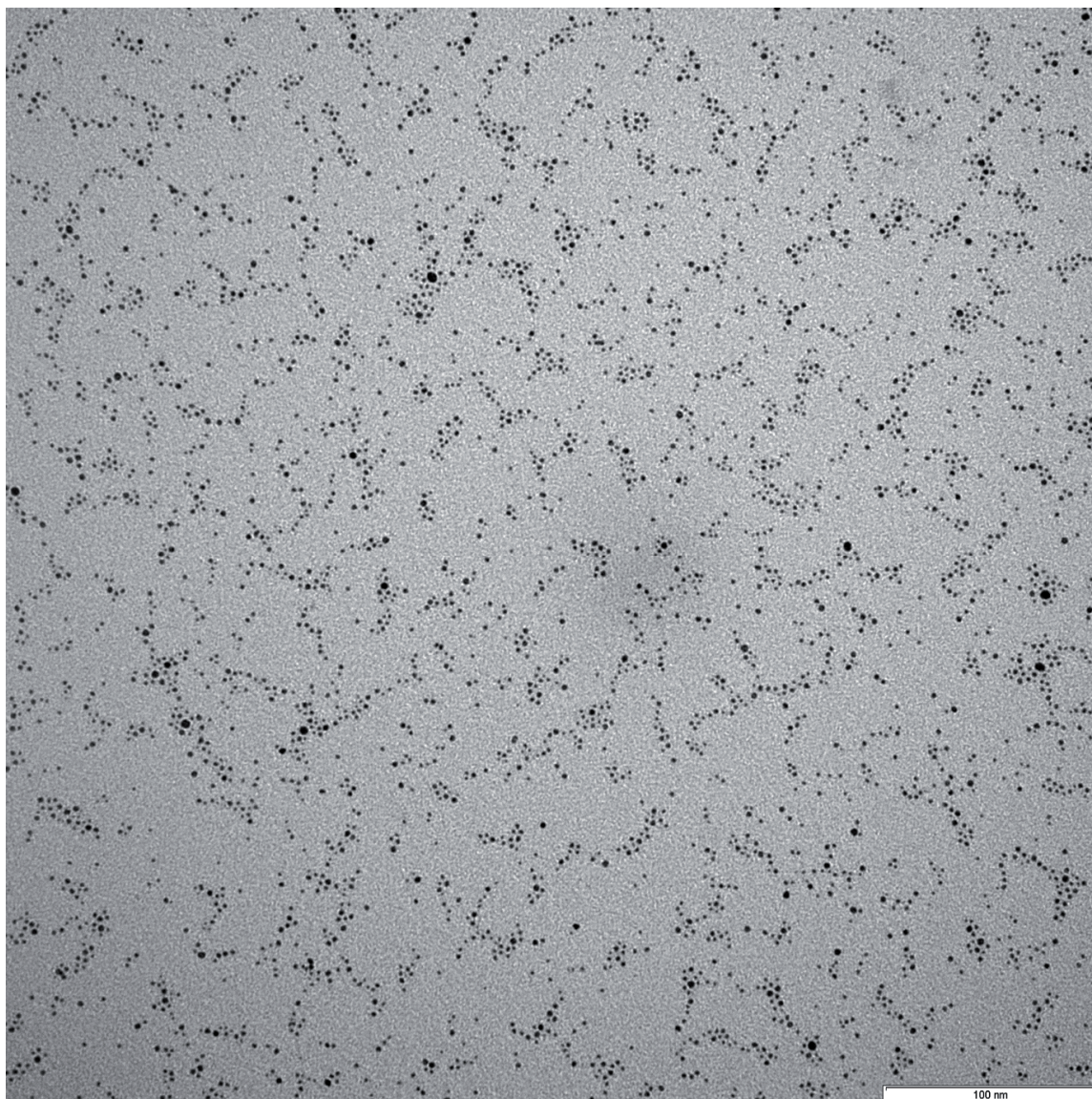


**Figure S6.** Original TEM micrograph of **Au-P1**.

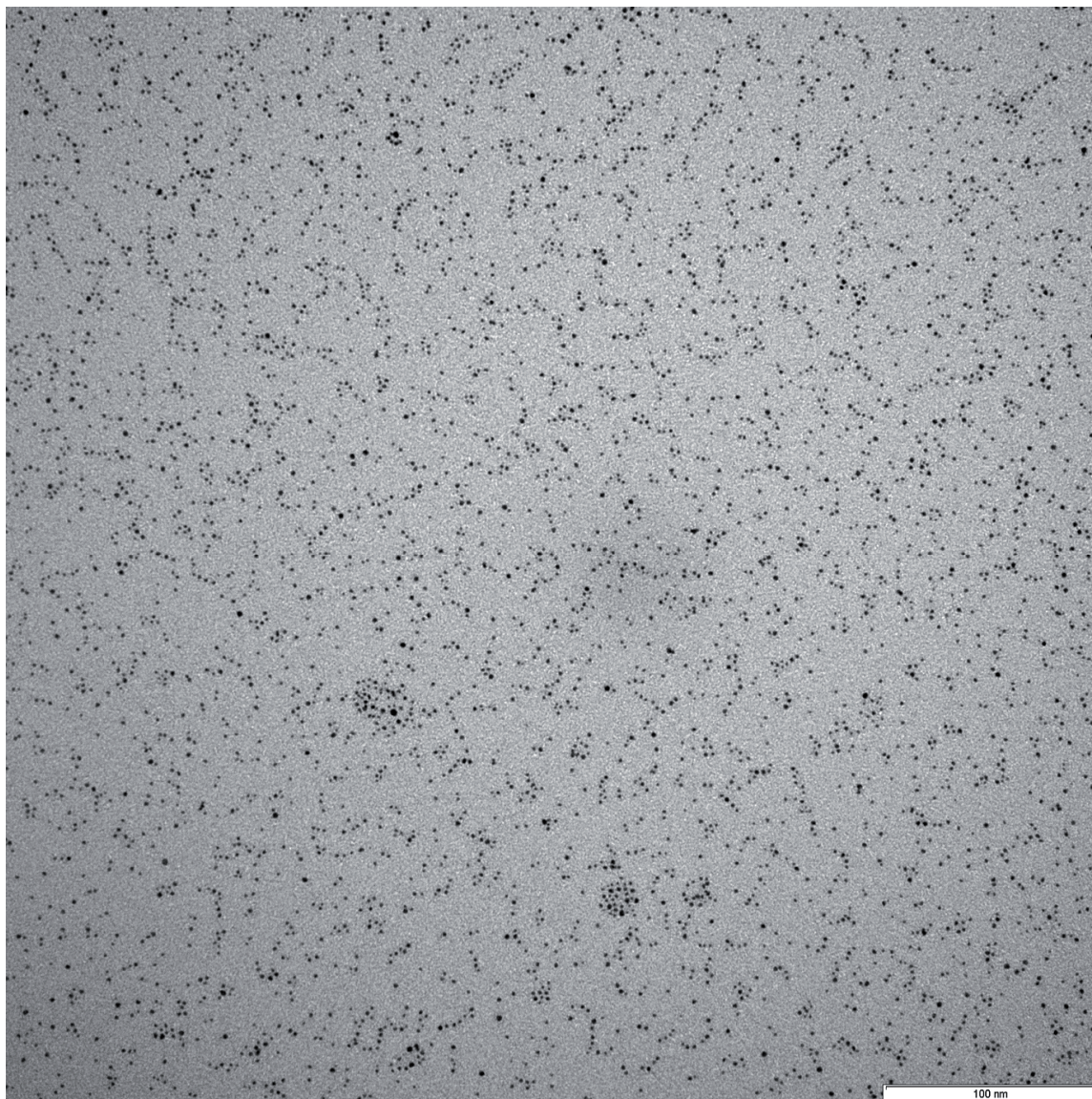


**Figure S7.** Original TEM micrograph of **Au-P2**.



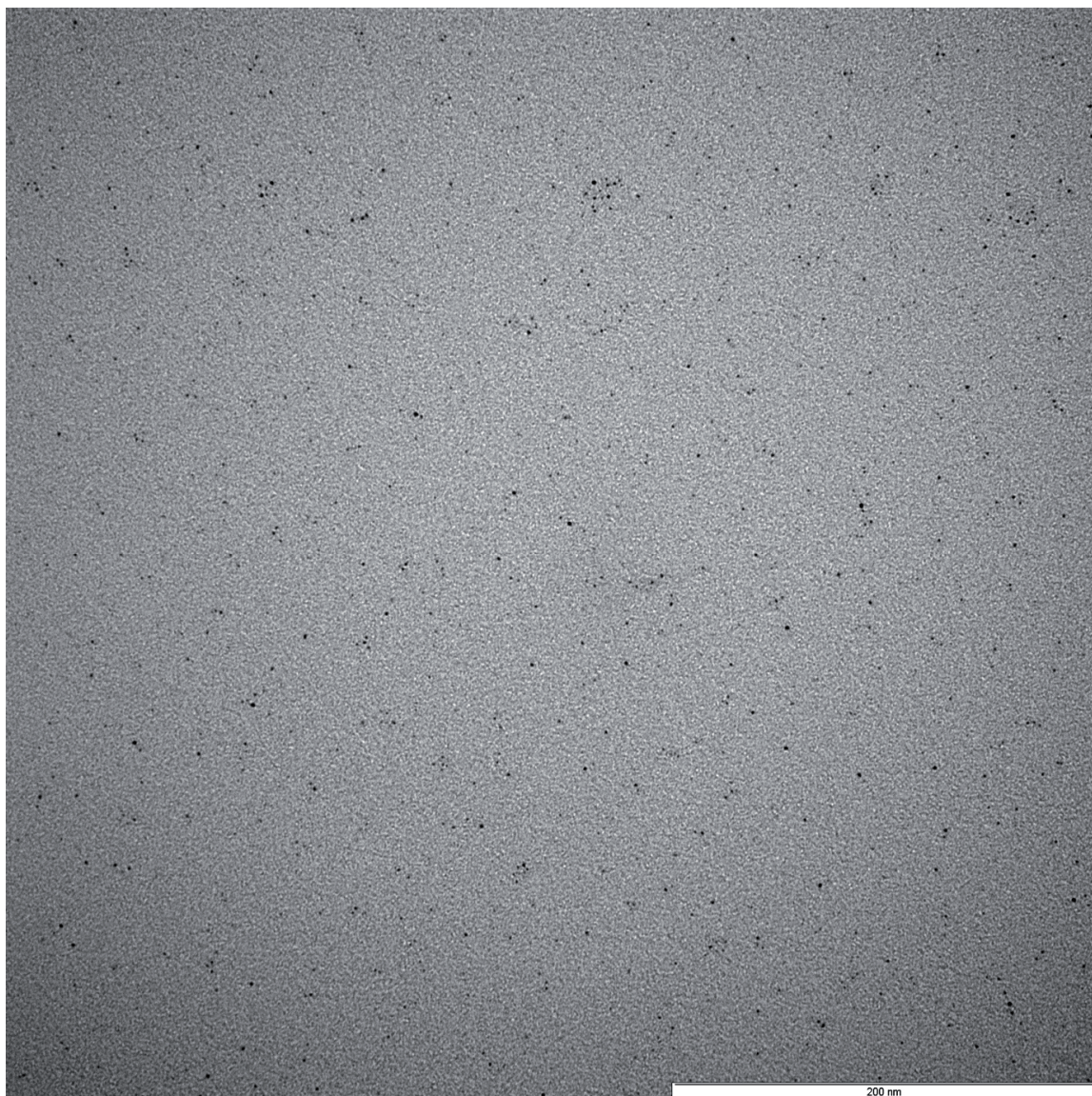


**Figure S8.** Original TEM micrograph of  $(\text{Au-B1})_{2.4}$ .

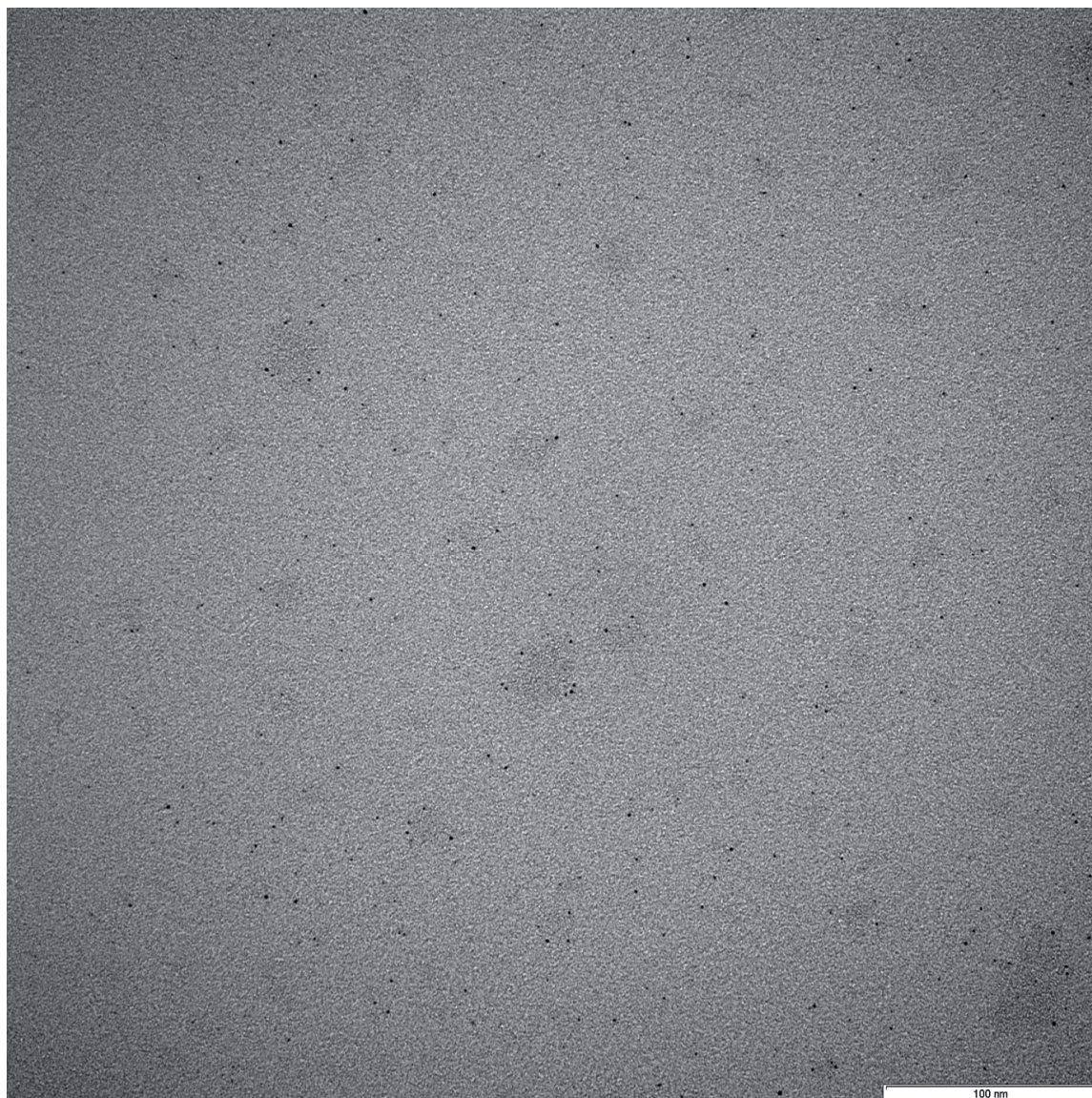


**Figure S9.** Original TEM micrograph of  $(\text{Au-B2})_{2-4}$ .

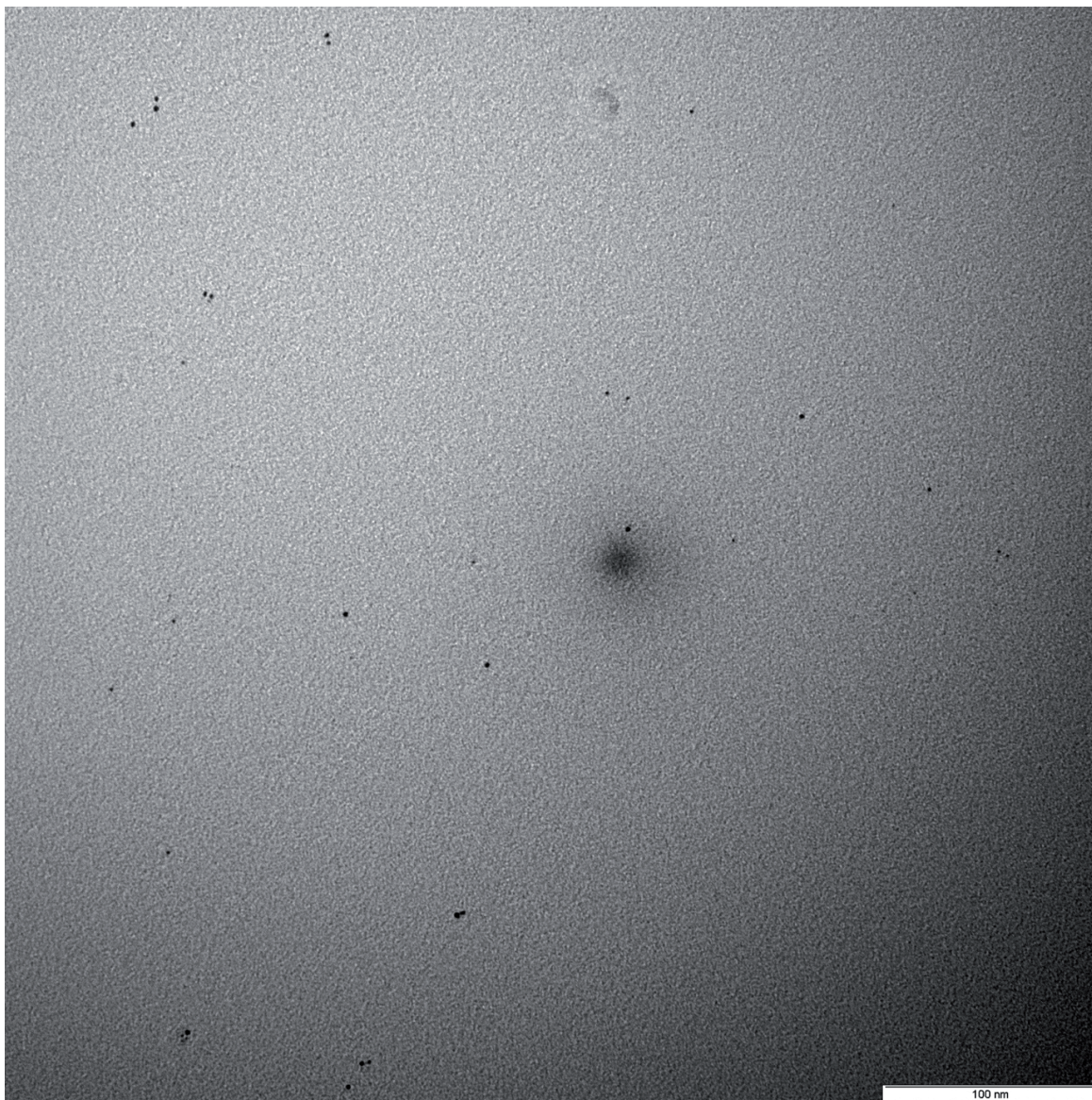


**Figure S10.** Original TEM micrograph of  $(\text{Au-P1})_{2-4}$ .

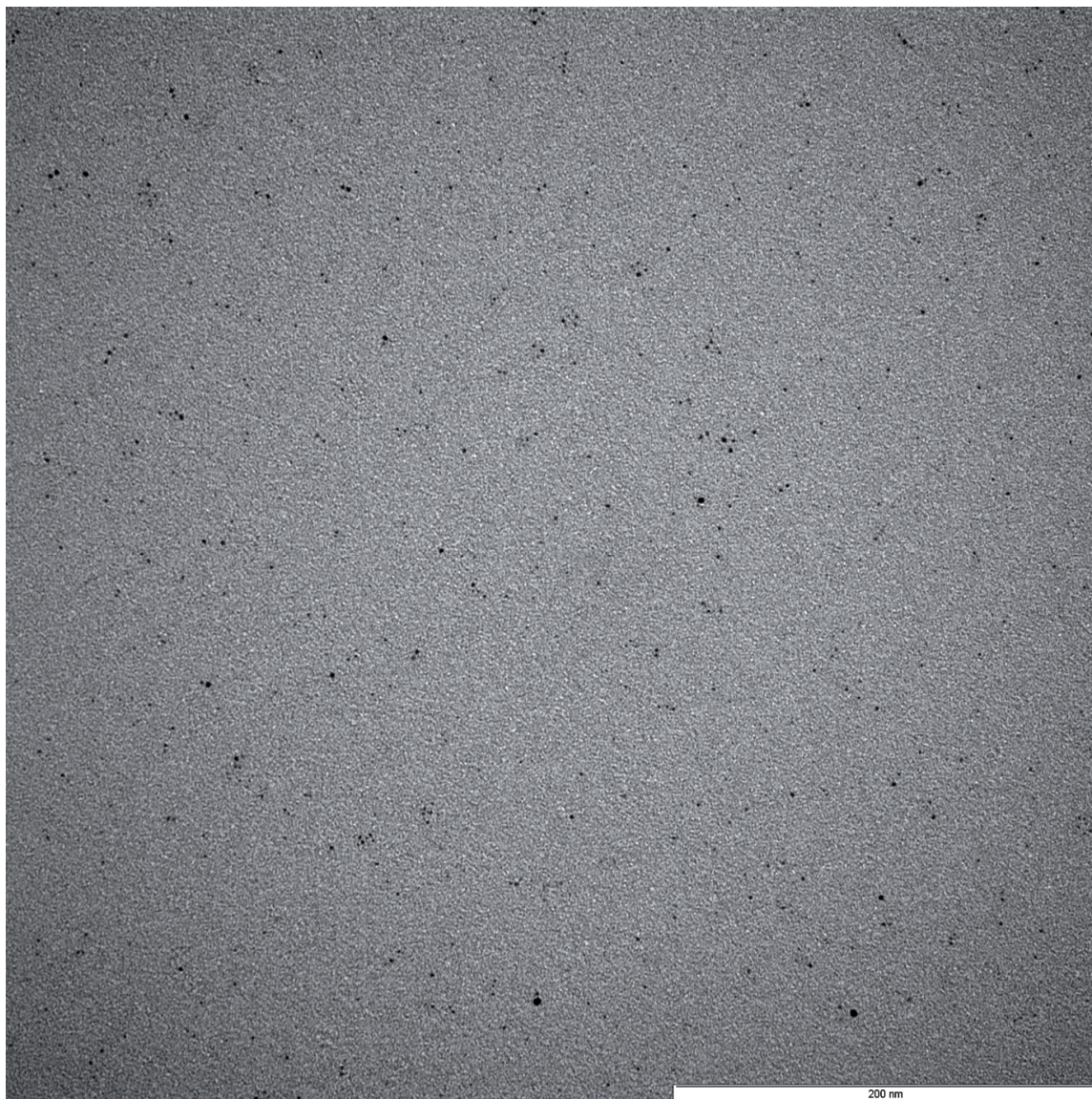


**Figure S11.** Original TEM micrograph of  $(\text{Au-P2})_{2-4}$ .

### References

- [1] H. Takalo, J. Kankare, *Acta Chem. Scand., Ser. B* **1987**, 291.
- [2] H. Takalo, P. Pasanen, J. Kankare, *Acta Chem. Scand., Ser. B* **1988**, 373.
- [3] Y. Nakano, K. Ishizuka, K. Muraoka, H. Ohtani, Y. Takayama, F. Sato, *Org. Lett.* **2004**, *6*, 2373-2376.



## Gold Nanoparticles Stabilized by Thioether Dendrimers

Jens Peter Hermes,<sup>[a]</sup> Fabian Sander,<sup>[a]</sup> Torsten Peterle,<sup>[a, b]</sup> Raphael Urbani,<sup>[c]</sup>  
Thomas Pfohl,<sup>[c]</sup> Damien Thompson,<sup>[d]</sup> and Marcel Mayor\*<sup>[a, e]</sup>

**Abstract:** Ligand-stabilized gold nanoparticles (Au NPs) are promising materials for nanotechnology with applications in electronics, catalysis, and sensors. These applications depend on the ability to synthesize stable and monodisperse NPs. Herein, the design and synthesis of two series of dendritic thioether ligands and their ability to stabilize Au NPs is presented. The dendrimers have 1,3,5-trisubstituted benzene branching units bridged by either *meta*-xylene or ethylene moi-

ties. A comparison between the two ligands shows how both size control and the stability of the NPs are influenced by the nature of the ligand–NP wrapping interaction. The *meta*-xylene-bridged ligands provided NPs with a narrow size distribution centered around a diameter of 1.2 nm, whereas

**Keywords:** dendrimers • gold • ligand design • nanoparticles • thioethers

the NPs formed with ethylene-bridged dendrimers lack long-term stability with NP aggregation detected by UV/Vis spectroscopy and transmission electron microscopy. The bulkier *tert*-butyl-functionalized *meta*-xylene bridges form larger ligand shells that inhibit further growth of the NPs and thus provide a simple route to stable and monodisperse Au NPs that may find use as functional components in nano-electronic devices.

### Introduction

The research field of gold nanoparticles (Au NPs) has been steadily advancing in the past decade. The chemical stability and size-dependent properties of Au NPs make them attractive materials for use in nanotechnology.<sup>[1–4]</sup> The scope of future applications is broad,<sup>[1]</sup> ranging from advanced electronic<sup>[5–9]</sup> and photonic<sup>[10,11]</sup> devices to ultrasensitive chemical<sup>[12–16]</sup> and biological sensors.<sup>[17]</sup> In addition, Au NPs have current and potential applications in biological labeling,<sup>[18–22]</sup> medical diagnostics,<sup>[23]</sup> and catalysis.<sup>[24,25]</sup> Aqueous Au NPs are often formed as citrate-stabilized NPs and then functionalized by using peptides<sup>[26,27]</sup> or DNA.<sup>[20,21]</sup> However, within this study we focused on nonpolar organic solvents in which mainly alkanethiols have been used to stabilize Au NPs, an

approach widely used since the pioneering work of Brust et al.<sup>[28]</sup> In addition to free thiols, the less reactive thioethers have also been used to ligate NP surfaces.<sup>[29–34]</sup> The thioether–gold coordination is much weaker than the covalent thiolate–gold interaction.<sup>[35]</sup> Therefore multidentate thioether ligands may be used to form self-assembled, multivalent—bound, stable and monodisperse ligand-wrapped NPs with a distinct low-integer number of ligands wrapping and effectively ensnaring each NP.<sup>[31–33]</sup> The first application of multidentate macromolecular ligands for the stabilization of Au NPs was the use of thioether polymers.<sup>[36–39]</sup> The use of thioether dendrimers as stabilizing ligands has also been reported.<sup>[40–43]</sup> The advantage of dendrimers over polymers is the control over their monodispersity. The molecular structures of reported dendritic ligands vary from stiff arylc sulfides<sup>[40,41]</sup> to partially flexible benzylic/arylic sulfides<sup>[42]</sup> and highly flexible benzylic thioether dendrimers.<sup>[43]</sup> Superior stability and monodispersity has been reported for the latter. Unfortunately, one cannot unambiguously relate these findings to thioether properties as the presence of additional ether moieties may have played a role, with recent work showing that ether moieties present in poly(ethylene glycol) (PEG) dendrimers are also able to stabilize Au NPs.<sup>[44]</sup> Other known stabilizing units for the formation of dendrimer-encapsulated metal NPs are poly(amidoamine) (PAMAM)<sup>[45–47]</sup> and poly(propyleneimine) (PPI) structures.<sup>[48,49]</sup> Thioether dendrimers used for applications other than the stabilization of NPs have also been reported.<sup>[50–53]</sup>

The goal of this work was to develop dendritic thioether structures that are able to stabilize Au NPs with monodisperse size through the formation of NP–ligand complexes that allow a low-integer number of ligands to cover each NP

[a] J. P. Hermes, F. Sander, Dr. T. Peterle, Prof. Dr. M. Mayor  
Department of Chemistry, University of Basel  
St. Johannis-Ring 19, 4056 Basel (Switzerland)  
E-mail: marcel.mayor@unibas.ch

[b] Dr. T. Peterle  
Evonik Degussa GmbH  
Untere Kanalstraße 3, 79618 Rheinfelden (Germany)

[c] R. Urbani, Prof. Dr. T. Pfohl  
Department of Chemistry, University of Basel  
Klingelbergstrasse 80, 4056 Basel (Switzerland)

[d] Dr. D. Thompson  
Theory Modelling and Design Centre, Tyndall National Institute  
Lee Maltings, University College Cork, Cork (Ireland)

[e] Prof. Dr. M. Mayor  
Institute of Nanotechnology, Karlsruhe Institute of Technology (KIT)  
P.O. Box 3640, 76021 Karlsruhe (Germany)

Supporting information for this article is available on the WWW under <http://dx.doi.org/10.1002/chem.201101837>.

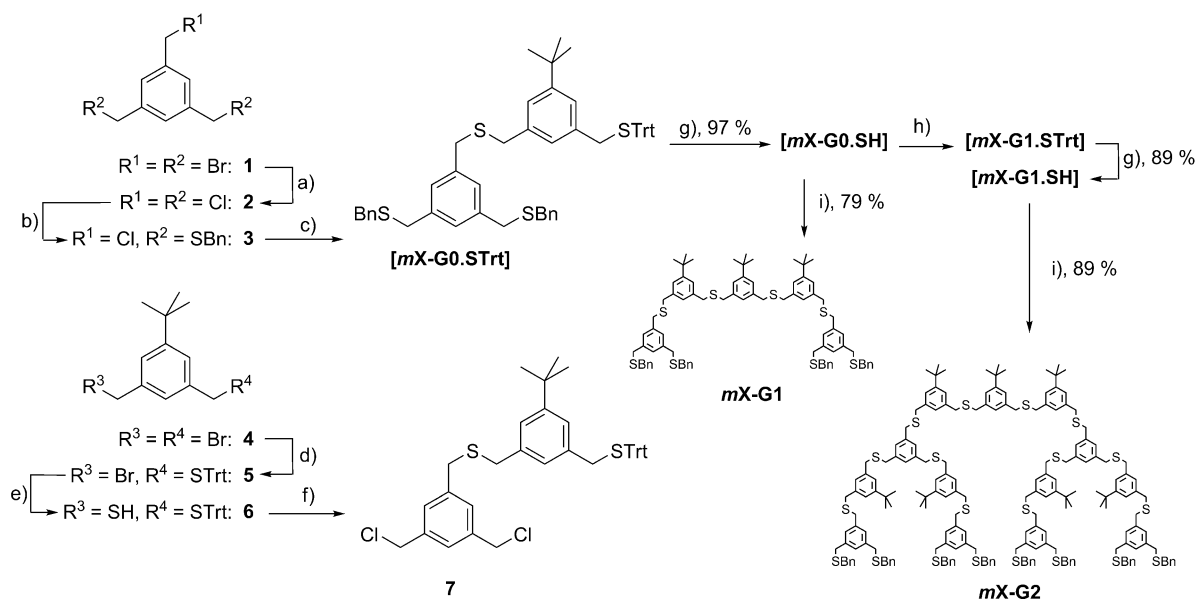
while also providing the long-term stability that is a prerequisite for technological applications. Dendrimers are ideal candidate ligands with their branched, flexible architecture potentially allowing for extensive NP surface coverage and therefore providing monodisperse NPs that do not aggregate over time. The two dendritic ligands synthesized in this work are both based on benzylic thioethers, the combination of flexibility and weak individual thioether anchoring groups providing a multivalent ligand for the assembly of NPs complexed by a low number of ligands. Different generations and structural motifs of the dendritic ligands were synthesized to determine their NP-stabilizing abilities and their influence on the size distributions of the NPs obtained. The NPs were investigated by UV/Vis and  $^1\text{H}$  NMR spectroscopy, thermogravimetric analysis (TGA), small-angle X-ray scattering (SAXS), and both standard transmission electron microscopy (TEM) and high-resolution scanning transmission electron microscopy (HRSTEM).

## Results and Discussion

**Concept and strategy:** We have recently shown that linear, unbranched thioether ligands with a certain threshold length are able to stabilize Au NPs and provide a narrow size distribution of NPs with a diameter of around 1.1 nm that do not aggregate over time.<sup>[31–33]</sup> These linear thioethers are oligomeric structures constructed from a *meta*-xylene-bridged thioether motif. In this work we designed and synthesized two series of dendritic thioether ligands (Scheme 1 and Scheme 2) and investigated their potential for stabilizing Au NPs. The dendrimers were synthesized by a convergent ap-

proach. The dendrons were synthesized by starting from the terminal groups and working back towards the central unit. The dendritic ligands are branched with a 1,3,5-trisubstituted benzene. The use of benzylic thioethers should give flexible molecular structures that allow all three sulfide groups to be orientated towards the NP surface. Note that a similar building block has already been reported to stabilize  $\text{Au}_{55}$ .<sup>[54]</sup> The dendrimers differ by the bridging unit that separates the branching units from each other. The nomenclature of the ligands emphasizes the different bridging units, which are a focus of this work. The bridges were introduced into the ligand design to 1) provide more separated thioether anchoring points and 2) to increase the amount of free space in the center of the dendrimers. This reduced branching density should improve the ability of the dendrimers to adapt to the convex NP surface by forming a concave pocket. We thus hypothesized considerably improved wrapping features for such dendrimers with “diluted” branching units. The first series (**mX** ligands, Scheme 1) use a *tert*-butyl-functionalized *meta*-xylene to interconnect two sulfur atoms, the same moieties used for the previously studied linear ligands.<sup>[31–33]</sup> The second series (**Et** ligands, Scheme 2) uses ethylene bridges for the interconnection of two neighboring sulfur atoms. Two generations of dendrimers were synthesized for each dendrimer series to investigate the correlation between dendrimer generation and stabilizing or size-steering features.

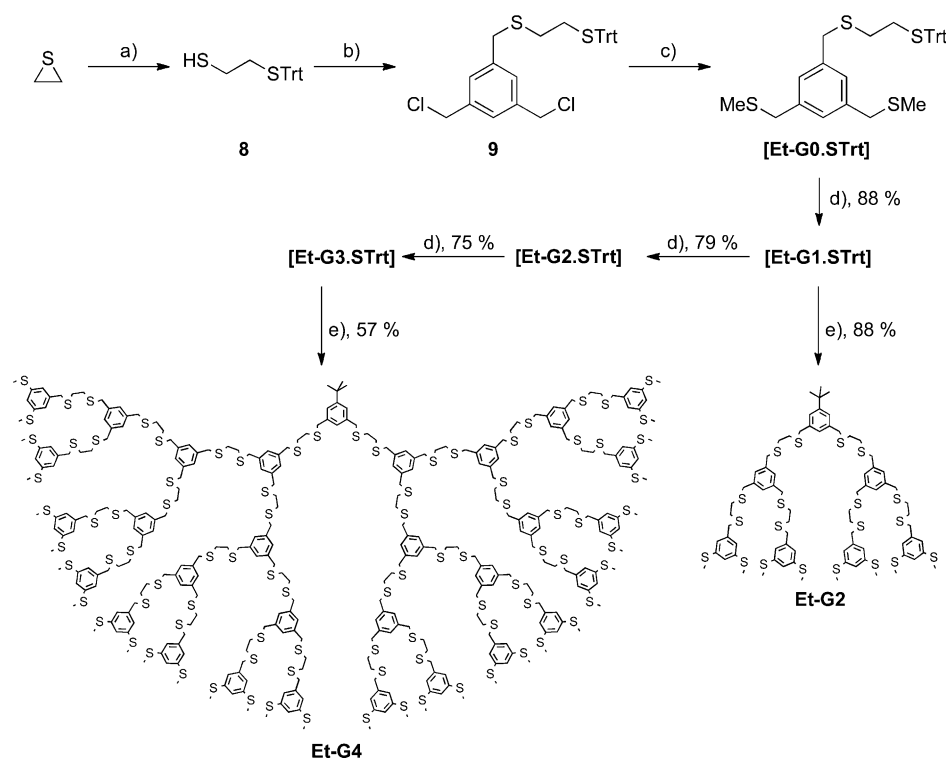
**Ligand synthesis:** The synthesis of the **mX** dendrimers is shown in Scheme 1. The basic building blocks **1** and **4** were synthesized by using literature protocols.<sup>[55,56]</sup> The branching unit **2** was obtained after substitution of the bromides of starting material **1** with lithium chloride in dimethylforma-



Scheme 1. Synthesis of  $\alpha, \alpha'$ -*meta*-xylene-bridged dendrons and dendrimers of various generations. Reagents and conditions: a) LiCl, DMF, 0°C, 30 min, RT, 2 h, 90%; b) BnSH, NaH, THF, RT, 1 h, 44%; c) **6**, NaH, THF, RT, 1 h, 99%; d) TrtSH, NaH, THF, RT, 2 h, 49%; e) 1. KSAc, THF, RT, 1 h; 2. MeOH,  $\text{K}_2\text{CO}_3$ , RT, 1 h, 80%; f) **2**, NaH, THF, RT, 2 h, 49%; g) TFA,  $\text{Et}_3\text{SiH}$ ,  $\text{CH}_2\text{Cl}_2$ , RT, 15 min; h) **7**, NaH, THF, RT, 1 h, 90%; i) **4**, NaH, THF, RT, 1 h.

amide (DMF). The bromides were substituted because chlorides are more stable in the presence of protected thiols. The dendron terminal unit **3** was synthesized by statistical nucleophilic substitution with benzyl mercaptan (BnSH) and sodium hydride (NaH) as base in tetrahydrofuran (THF). The G0 dendron [**mX-G0.STrt**] was formed from the terminal unit **3** with the monothiol **6**. Compound **6** was prepared from the monofunctionalized bromide **5** by a mild one-pot procedure for the conversion of benzylic bromides into thiols.<sup>[57]</sup> After deprotection of the trityl group with trifluoroacetic acid (TFA), the [**mX-G0.SH**] dendron can be extended by branching unit **7** to the next generation dendron. Precursor **7** was assembled from the bridging unit **6** with an excess of the dendritic branching unit **2**. The respective [**mX-Gn.SH**] dendrons were used to form the final dendrimers **mX-G1** and **mX-G2** with central unit **4**. In view of the statistical nature of some monofunctionalizations, all the reactions gave good-to-excellent yields.

Scheme 2 depicts the synthesis of the **Et** dendrons. The first dendron [**Et-G0.STrt**] was synthesized starting from thiirane (ethylene sulfide). The bridging unit **8** was synthesized by ring-opening of thiirane with an excess of trityl thiol (TrtSH) in the presence of triethylamine (TEA) as base. As for the **mX** ligands, subsequent nucleophilic substitution and deprotection reactions of the trityl groups led to the terminal thiols as powerful nucleophiles. All the reactions gave good-to-excellent yields considering the statistical nature of the monofunctionalization reactions.



Scheme 2. Synthesis of ethylene-bridged dendrons and dendrimers of various generations. Reagents and conditions: a) TrtSH, TEA, DMF, RT, 92%; b) **2**, K<sub>2</sub>CO<sub>3</sub>, THF, reflux, 46%; c) NaSMe, DMF, RT, 88%; d) 1. Et<sub>3</sub>SiH, TFA, CH<sub>2</sub>Cl<sub>2</sub>, RT; 2. **9**, NaH, THF, RT; e) 1. Et<sub>3</sub>SiH, TFA, CH<sub>2</sub>Cl<sub>2</sub>, RT; 2. **4**, NaH, THF, RT, 1 h.

**Ligand-stabilized nanoparticles:** Au NPs were prepared in the presence of the dendritic thioether ligands **mX-Gn** and **Et-Gn** to investigate the ability of these ligands to stabilize NPs by preventing aggregation. The NPs were prepared in a two-phase water/dichloromethane system closely following the procedure developed by Brust et al.<sup>[28]</sup> (see the Experimental Section for the synthetic protocol). The gold(III) precursor, tetrachloroauric acid, dissolved in water was transferred to the organic phase by tetra-*n*-octylammonium bromide (TOAB). To keep the ratio between the gold(III) precursor and thioether moieties comparable to earlier studies,<sup>[31–33]</sup> the amount of added ligand was normalized to the number of thioether groups. The starting point for investigating the ability of a ligand to stabilize Au NPs was in all cases equal numbers of ligand sulfur atoms and gold atoms in the precursor. Thus, an eight-fold excess of the gold(III) precursor was used for **mX-G1** and a twenty-fold excess was used for **mX-G2**. Although for these **mX** ligands the ratios were maintained, the concentration of the ligand was raised in the case of the **Et** ligands. The reduction of gold(III) in the presence of the thioether ligands was carried out by quickly adding an aqueous solution of sodium borohydride to the two-phase system. After aqueous workup, the organic phases were dried over MgSO<sub>4</sub> and filtered.

In the case of the **mX** ligands, the change in color to dark brown indicated the formation of the NPs **Au-mX-G1** and **Au-mX-G2**. Precipitation of gold was not observed, which indicates an efficient stabilization of the Au NPs formed. In analogy to linear oligomers,<sup>[31–33]</sup> coating by **mX** ligands provided the NPs with enough stability to allow removal of TOAB by applying a precipitation and centrifugation protocol<sup>[32]</sup> and of the excess ligand by size exclusion chromatography (SEC). Analysis by <sup>1</sup>H NMR spectroscopy (see Figure S1 in the Supporting Information, SI) corroborated the total removal of TOAB. The spectra also showed the presence of surface-bound dendrimer ligands, corroborating their stabilizing nature as a coating of NPs. As far as the gold atoms were concerned, the synthetic procedure and removal of TOAB led to the formation of NPs in a yield of around 95%. However, approximately 10–20% of the NPs were lost during SEC because some late SEC vials still showed the presence of excess ligand and were therefore discarded to obtain only ligand-stabilized NPs. This loss is due



to the overlap in the retention times of ligand-stabilized NPs and the free ligand.

The formation of NPs in the presence of **Et-G2** led to immediate and complete precipitation of aggregated NPs after addition of the reducing agent. The 1:1 ratio of gold equivalents to sulfur atoms in the ligand design used initially was then adjusted to a ratio of 1:2. A quick and complete precipitation of aggregated NPs was still observed. The same 1:2 ratio was used during the formation of NPs in the presence of the fourth generation ligand **Et-G4**. In this case, upon addition of the reducing agent, the organic phase turned a reddish brown color pointing to the formation of stable NPs; the precipitation of NPs was not observed for **Et-G4**.

To analyze the ligand-stabilized NPs UV/Vis spectra were recorded (Figure 1). In the case of the stable and redissolvable **mX**-ligand-stabilized NPs new solutions were prepared from dried NPs in  $\text{CH}_2\text{Cl}_2$ , whereas in the case of **Et-G4**-stabilized NPs, the organic layer was investigated directly by UV/Vis spectroscopy. The organic layer of **Au-Et-G4** showed a weak plasmon resonance band, which indicates a NP distribution comprising a few NPs with diameters of

around 2 nm from the very beginning (Figure 1A, black line). A color change from reddish brown to dark red was observed upon storing the isolated and dried organic phase under ambient conditions in  $\text{CH}_2\text{Cl}_2$  in the presence of excess ligand for several weeks. As shown in Figure 1A (gray line), a prominent plasmon resonance band was observed after 4 weeks, which indicates an increase in NP size upon storage. Interestingly, in spite of this aggregation of initially formed NPs to give larger NPs, the precipitation of aggregated NPs was not observed.

The weak plasmon resonance band in the UV/Vis spectra of both the **mX-G1**- and **mX-G2**-stabilized NPs (Figure 1B) point to NP sizes of around and below 1.6 nm.<sup>[58,59]</sup> The two samples show similar absorption spectra. The minor differences between 300 and 400 nm may be ascribed to the presence of different amounts of excess ligand. Interestingly, these UV/Vis spectra remained unchanged when the solutions were retested after 6 months, which indicates the excellent long-term stability of **mX**-ligand-stabilized NPs even on exposure to air and light. However, higher temperatures than room temperature were avoided as a slight growth of NPs has previously been reported at temperatures of around 40 °C.<sup>[31]</sup>

HRSTEM analysis of the **Et**-ligand-stabilized NPs and TEM analysis of the **mX**-ligand-stabilized NPs were performed to determine the diameters (sizes) of the NPs formed. Micrographs were taken of  $\text{CH}_2\text{Cl}_2$  solutions of NPs deposited on carbon-coated copper grids (Figure 2). Large differences between the **Et-G4**- (Figure 2A) and **mX**-ligand-stabilized NPs (Figure 2B and C) are readily visible to the naked eye. A solution of  $\text{CH}_2\text{Cl}_2$ , aged for 4 weeks, was deposited on the carbon grid (Figure 2A) and the diameters of about 500 **Au-Et-G4** NPs were measured. As expected on the basis of the UV/Vis investigation, rather large NPs with diameters of up to 15 nm were observed. Analysis of the observed size distribution (Figure 3A) revealed a large dispersity of 1–15 nm. The broad distribution of **Au-Et-G4** NPs has a mean value of 6.2 nm with a standard deviation of  $\pm 2.4$  nm. Although the NP growth of **Au-Et-G4** is interesting, we did not investigate it further because nanoelectronic device components require NPs with a distinct number of ligands for further coupling to organic–inorganic superstructures.<sup>[32,33]</sup> In contrast to these large NPs stabilized by the **Et-G4** dendrimer, very different NP diameters were observed for the **mX-Gn**-stabilized NPs. In this case the recorded TEM micrographs were analyzed by an automated procedure using imageJ<sup>[60]</sup> (see the SI for a detailed description). The size distributions for both NPs are displayed in Figure 3B and C. Interestingly, within the precision of the measurement, similar NP sizes of  $1.1 \pm 0.3$  nm and  $1.2 \pm 0.4$  nm were determined for **Au-mX-G1** and **Au-mX-G2**, respectively.

The diameters of the NPs were also analyzed by SAXS, performed by dissolving the Au NPs in benzene. The 2D scattering signal was integrated to obtain intensity profiles, which are shown as log–log representations in Figure 4. The plots of **Au-mX-G1** and **Au-mX-G2** are similar, indicating

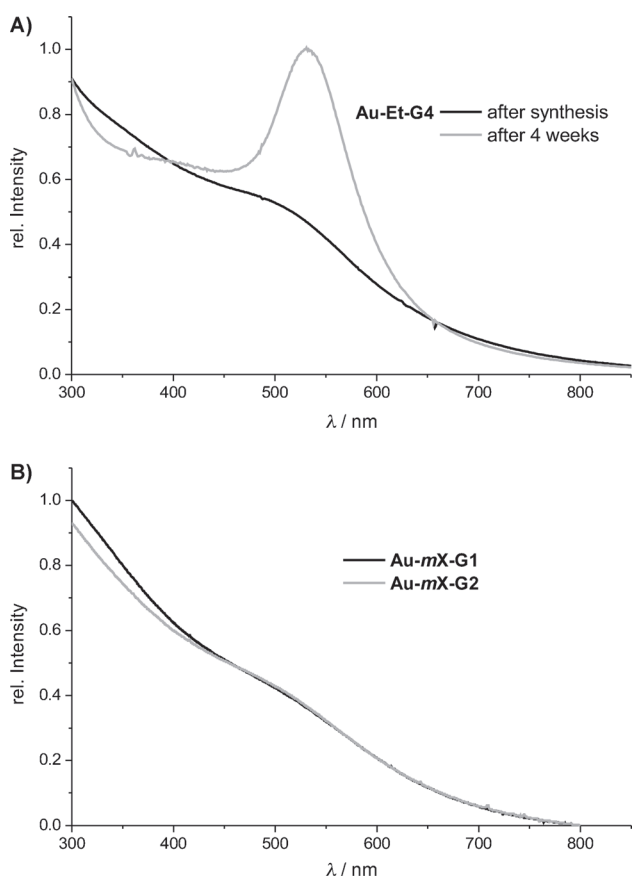


Figure 1. UV/Vis absorption spectra in  $\text{CH}_2\text{Cl}_2$  of ligand-stabilized Au NPs. A) Spectra of **Au-Et-G4** NPs directly after NP formation (black) and after 4 weeks (gray) in  $\text{CH}_2\text{Cl}_2$ . The arising plasmon resonance band indicates the aggregation of NPs. B) Spectra of **Au-mX-G1** (black) and **Au-mX-G2** (gray). The spectra are normalized to match at 520 nm. The weak plasmon resonance peaks indicate NPs with diameters of around and below 1.6 nm.<sup>[59]</sup>

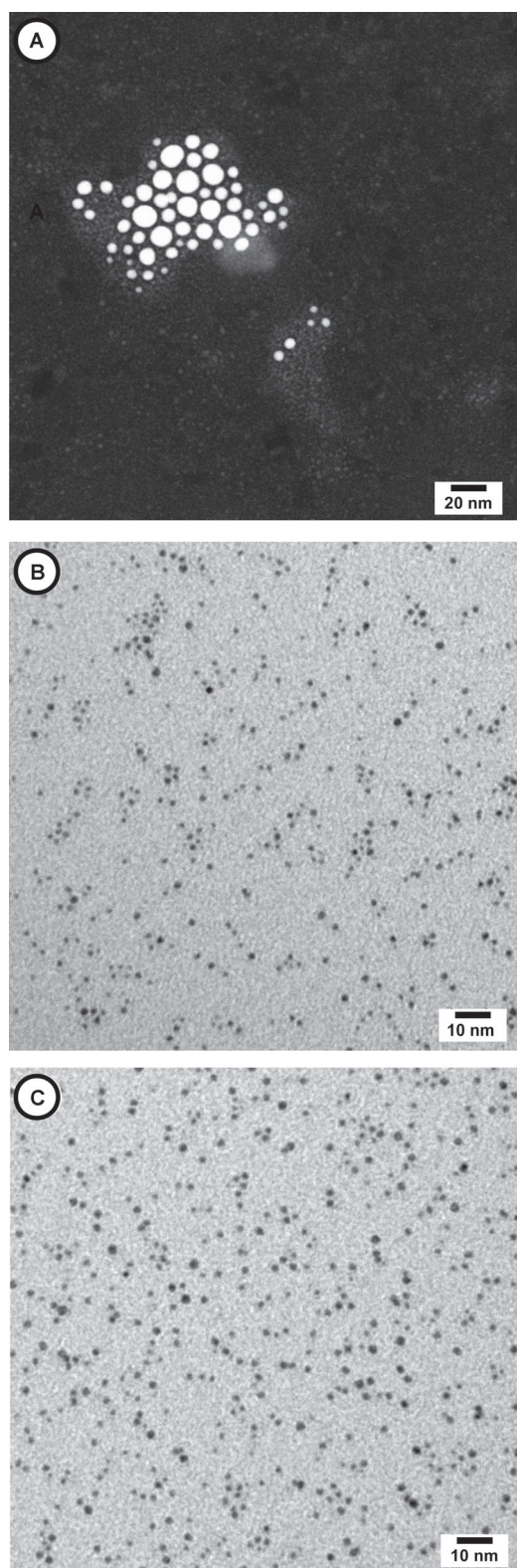


Figure 2. A) Representative HRSTEM image of **Au-Et-G4** after being dissolved in  $\text{CH}_2\text{Cl}_2$  for 4 weeks. Representative TEM images of B) **Au-mX-G1** and C) **Au-mX-G2** NPs, respectively.

similar NP sizes, as expected on the basis of TEM investigations. The shapes of the plots suggest form factors for

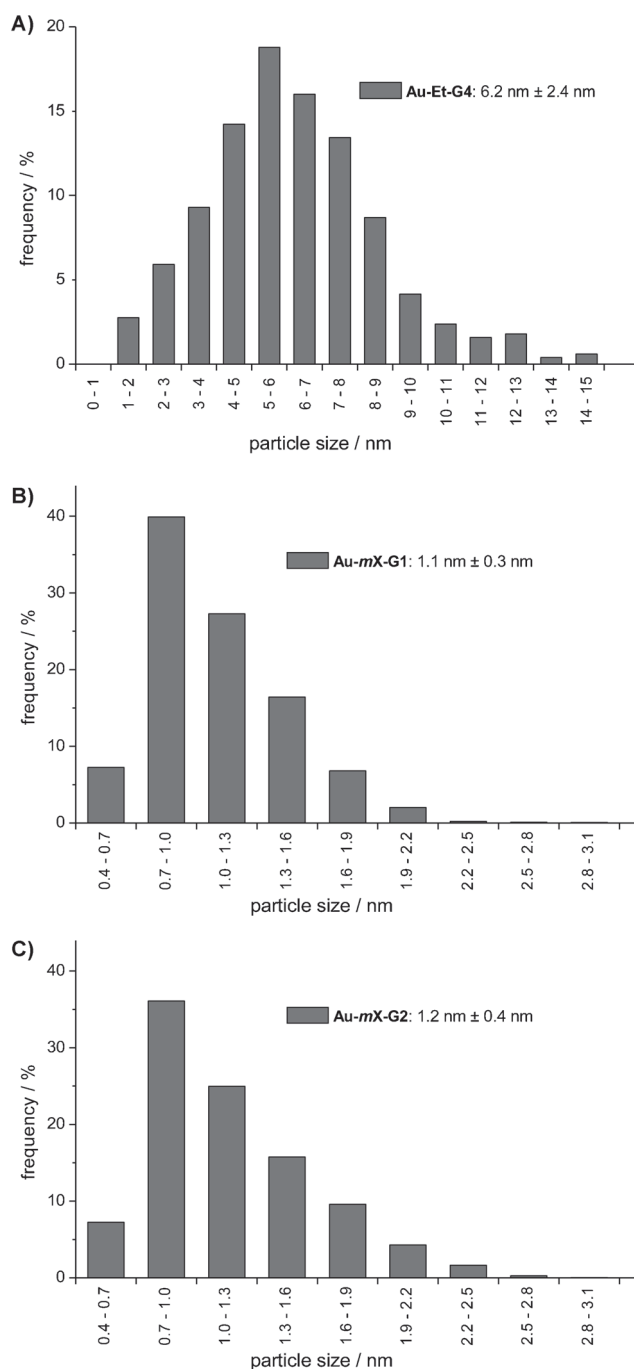


Figure 3. Size distributions of ligand-stabilized Au NPs: A) **Au-Et-G4** after storage in solution (500 NPs were measured manually), B) **Au-mX-G1**, and C) **Au-mX-G2** (5000 NPs were measured automatically for B and C).

spheres. The intensity plots were fitted with Nanofit software version 1.2 from Bruker, using a least-squares method for polydisperse, spherical particles. The analysis revealed both samples to have diameters of around 1.6 nm by assuming a Gaussian distribution of the NP diameters of  $\sigma = 0.4$  nm.

The diameters of the NPs measured by small-angle X-ray scattering (SAXS) differ from the values found in TEM in-

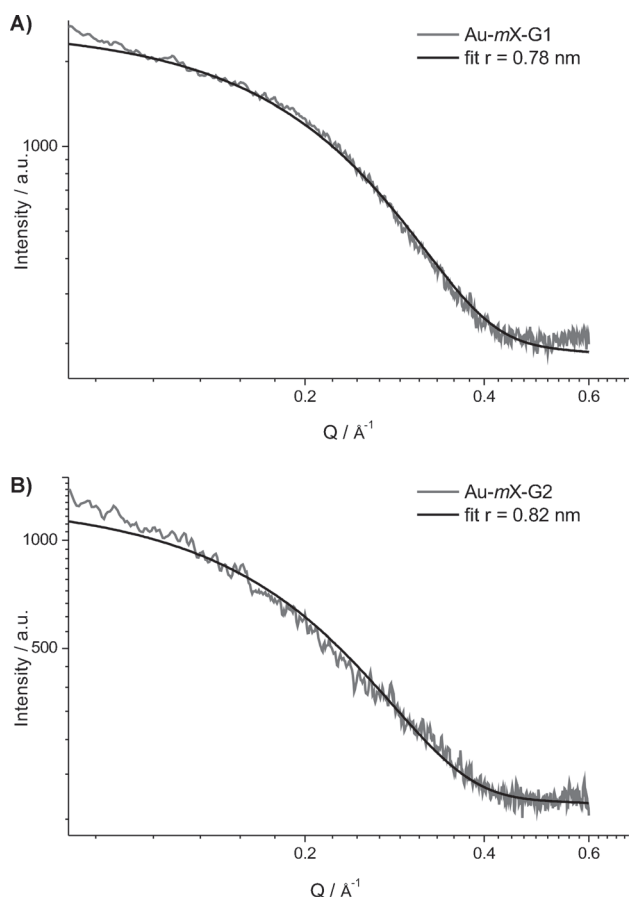


Figure 4. SAXS intensity plots as log-log representations and best fits for A) **Au-mX-G1** and B) **Au-mX-G2**.

vestigations (diameters 1.1 and 1.2 nm). This deviation has only recently been reported<sup>[33]</sup> and may be due to a slight growth of the Au NPs triggered by the X-ray irradiation; similar thermal expansion has previously been reported.<sup>[31]</sup> In addition, the organic ligand shell might add to the scattering signal leading to larger radii. Although the SAXS measurements corroborate the similarity of the sizes of both NPs, the deviation from the diameters measured by TEM is not yet understood and is the topic of further investigations. Our previous studies relied on diameters measured by TEM assuming ligand coating, which were corroborated by the chemical behavior of these NPs.<sup>[32,33]</sup> We thus currently prefer to refer to the diameters obtained by TEM over those measured by SAXS to allow comparison between the results obtained.

Despite the considerable increase in the number of sulfide groups from eight for the dendritic ligand **mX-G1** to twenty for **mX-G2**, similar NP sizes were stabilized, as found by TEM and SAXS analyses. This indicates that increasing the dendrimer generation from G1 to G2 has no significant influence on the size of the NP obtained. It rather seems that NPs grow until they reach a size that allows their enwrapping by the dendritic ligand. However, with more than twice the number of sulfide groups, the dendritic ligand **mX-G2**

should be able to coat a considerably larger surface area than **mX-G1**. The ratio of organic ligand to gold should give a closer insight into the assembly of the NP and ligand shell. The excess ligand was first removed by SEC. Small amounts of dried NPs were then studied by thermogravimetric analysis (TGA). The sample was heated up to 900 °C to remove all organic components. The results for **Au-mX-G1** and **Au-mX-G2** are shown in Figure 5. The weight loss for both sam-

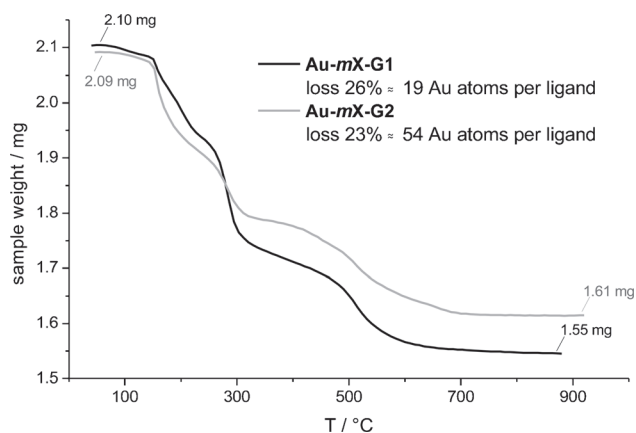


Figure 5. Thermogravimetric analyses of **Au-mX-G1** (black) and **Au-mX-G2** (gray).

ples follows the same trend. Decomposition starts at around 200 °C and reaches a plateau between 600 and 700 °C. The weight loss is attributed to the decomposition and removal of the organic shell from the NP surface and the plateau is interpreted as the end of this process, when all the organic coating has been removed. Comparable weight losses of 26 and 23% were measured for **Au-mX-G1** and **Au-mX-G2**, respectively.

Knowing the size of the NPs from the TEM investigations allows calculation of their mass and thus the average mass of ligand coating per NP can be estimated from the weight percentage obtained by TGA. First, the mass of gold per ligand is derived from the rule of proportion from the mass of the ligand and the mass percentage of both the gold and ligand [Eq. (1) in the SI]. This value is divided by the molecular mass of gold to obtain the number of gold atoms per ligand [Eq. (2) in the SI]. For the **Au-mX-G1** NPs a ratio of 19 gold atoms per **mX-G1** ligand was obtained. By using the density of bulk gold ( $\rho_{\text{Au}}$ ) the number of gold atoms per NP was estimated to be 41 for NPs with an average diameter of 1.1 nm (from TEM). The calculated 19 gold atoms per octadentate **mX-G1** ligand indicate a ratio of two **mX-G1** ligands per gold NP. A similar pairwise coating of the NP surface has been observed for linear octadentate ligands.<sup>[32,33]</sup>

For the **Au-mX-G2** NPs, the ratio of gold atoms per **mX-G2** ligand was determined to be 54. The number of gold atoms per 1.2 nm NP was calculated to be 53 atoms on average, which indicates that a single **mX-G2** ligand can stabilize the entire 1.2 nm NP. Note that  $\text{Au}_{55}$  clusters are known to have a diameter of 1.4 nm.<sup>[8]</sup> The calculation with  $\rho_{\text{Au}}$  seems

to overestimate the number of gold atoms in the NP. As the sizes of the NPs determined by TEM are smaller than those determined by SAXS studies, this overestimation to some extent compensates the deviation in size. In view of the extended structure of the **mX-G2** ligand with more than twice the number of phenyl subunits and sulfide groups compared with the first generation analogue **mX-G1**, this ability to enwrap the entire surface of a NP of comparable size is not surprising. This specific ratio of one ligand stabilizing one NP is very rare. To our knowledge this has only been achieved by the use of a single polymer chain<sup>[61]</sup> or by radical-chain polymerization on the NP surface.<sup>[62]</sup>

A molecular dynamics model of a Au<sub>55</sub> cluster coated with **mX-G2** is depicted in Figure 6. The greed of the sulfide groups for noble metal surfaces guarantees the adhesion of

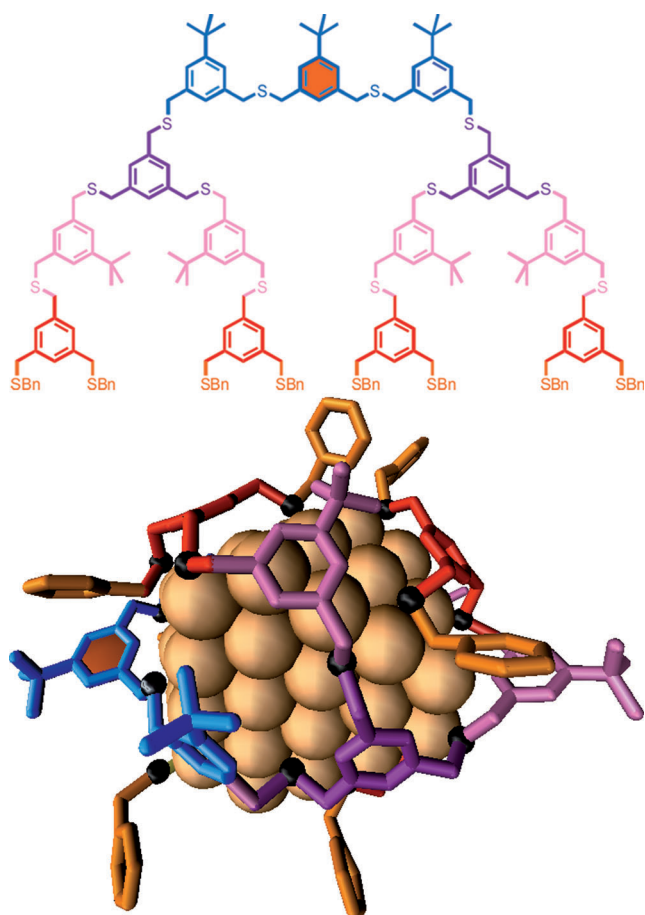


Figure 6. Quantum mechanical calculations of thioether-gold bond strengths were combined with a classical molecular dynamics model to calculate one-dendrimer (shown) and alternative two-dendrimer complexes with the Au NP, modeled to a first approximation by a 55-atom cluster (diameter 1.4 nm)<sup>[8]</sup> in dichloromethane. The details of the calculations will be presented elsewhere.<sup>[65]</sup> The calculations indicate that the alternative two-dendrimer state is less stable for these sized NPs. The low likelihood of replacement of the fully bound single dendrimer by two partially bound dendrimers was determined by using an energy function summed over beneficial wrapping interactions (individual thioether-gold bond strengths plus van der Waals dendrimer-gold contacts) and wrapping penalties (loss in dendrimer conformational freedom plus dendrimer and gold desolvation).

the branched ligand structure to the NP surface and the considerable dimension of the ligand only allows for a single ligand per NP in the case of **Au-mX-G2**. As the thioether-gold bond is weak we can expect that the NP-ligand assembly does not contain any “staples”, which have been found in the crystal structures of several thiol-stabilized Au NPs.<sup>[63,64]</sup> The discrete and integer number of ligands per NP may even allow use of the supramolecular notations Au<sub>41</sub>C-(**mX-G1**)<sub>2</sub> and Au<sub>53</sub>C**mX-G2** for the NPs **Au-mX-G1** and **Au-mX-G2**, respectively. However, this notation is misleading as it suggests that the number of gold atoms forming the NPs is not controlled. In view of the NP size distributions displayed in Figure 3B and C, a more appropriate description would be Au<sub>41±8</sub>C(**mX-G1**)<sub>2</sub> and Au<sub>53±10</sub>C**mX-G2**, respectively. To avoid confusion we prefer the old notations **Au-mX-G1** and **Au-mX-G2**, respectively.

The two dendrimer structures **Et-G4** and **mX-G2** display large differences in the long-term stability of the coated Au NPs. Although NPs stabilized by **Et-G4** quickly aggregate to form larger NPs, **mX-G2**-stabilized NPs display excellent long-term stability, which makes them very interesting ligand structures for obtaining monofunctionalized NPs, for example, for use as TEM labels. As a working hypothesis we attribute this unequal long-term stability of ligand-stabilized NPs to the different bridging units. The bulky *tert*-butyl-functionalized *meta*-xylene bridges create a large ligand shell around the Au NP surface preventing further aggregation. This steric protection of the NP surface provides not only a certain size control during the growth of the NPs, but also long-term stability for the NPs **Au-mX-G1** and **Au-mX-G2**. The loss of long-term stability in the case of **Au-Et-G4** is attributed to the reduced bulkiness of the ethylene bridges in this dendritic structure. It seems that this motif is not able to provide a strong protective shell and thus NPs get close enough to aggregate. In addition, both series of dendritic ligands differ in their terminal groups: The **mX-Gn** series has terminal benzyl sulfides whereas the terminal groups of the **Et-Gn** series are methyl sulfides. However, the considerable differences in long-term stability probably arise from the dendritic skeleton and not from the terminal groups. This assumption is supported by a model in which the terminal benzene rings (orange) do not coordinate to the gold surface.

## Conclusion

Two dendrimer motifs have been synthesized, both based on thioethers mounted on a 1,3,5-trimethylbenzene scaffold as branching units but with different spacers to “expand” the dendrimer structure. The spacer units reduce the density of the branching units and should therefore allow the dendritic ligand to adapt to the convex curvature of NPs. As spacer units,  $\alpha,\beta$ -ethynyl bridges and  $\alpha,\alpha'$ -*meta*-xylene structures comprising a bulky *tert*-butyl group have been considered. Although from the ethynyl-bridged dendrimer the second and fourth generation ligands **Et-G2** and **Et-G4** were syn-

thesized, the first and second generation ligands **mX-G1** and **mX-G2** were prepared in the case of the *meta*-xylene spacers. The ability of these dendrimers to control the growth and to stabilize particular sizes of Au NPs was investigated by using them as reagents during the biphasic reduction of chloroauric acid. With the two ethynyl-bridged dendrimers only the larger **Et-G4** displayed some limited NP stabilizing features. **Et-G4** was neither able to control the size of NPs during their formation nor to stabilize the formed NPs in solution over time. In contrast, both *meta*-xylene-bridged dendrimers were able to stabilize small Au NPs with average diameters of between 1.1 and 1.2 nm (from TEM) in very good yields and with excellent long-term stability. The limited surface area of these small NPs allows all the thioethers of only two dendritic ligands **mX-G1** to coordinate to a NP. In the case of the further expanded dendrimer **mX-G2**, the spatial limitation only allows a single ligand to coordinate its 20 thioethers to the NP surface. Thermogravimetric analysis corroborated the expected 1:2 and 1:1 ratios between the NP and dendritic ligands **mX-G1** and **mX-G2**, respectively. The considerable increase in both the control over NP size and NP stability has been attributed to the bulkiness of the dendritic coating with a *tert*-butyl-functionalized *meta*-xylene linker, which prevents aggregation by sterically separating the metal cores of the NPs.

These NPs coated with a controlled low number of dendritic ligands may pave the way towards mono- and bifunctionalized Au NPs. We are currently investigating the potential of these organic/inorganic hybrid structures as “artificial molecules” by exploring their tolerance to wet chemical conditions.

## Experimental Section

General methods and experimental procedures for all compounds are described in the Supporting Information.

**Gold nanoparticle formation and purification:** The Au NPs were formed on a 4–7  $\mu\text{mol}$  (9–15 mg) scale with respect to dendritic ligands **mX-Gn** (the same synthetic protocol was applied to **Au-Et-Gn** NPs). Chloroauric acid (**mX-G1**: 8 equiv; **mX-G2**: 20 equiv) was dissolved in DI water (2 mL) and transferred to the organic phase by adding tetra-*n*-octylammonium bromide (TOAB; **mX-G1**: 16 equiv; **mX-G2**: 40 equiv) in  $\text{CH}_2\text{Cl}_2$  (2 mL). After the addition of dendritic ligand **mX-Gn** (1 equiv) in  $\text{CH}_2\text{Cl}_2$  (2 mL) this mixture was stirred for 5 min before sodium borohydride (**mX-G1**: 64 equiv, **mX-G2**: 160 equiv) was added quickly in DI water (2 mL). The color of the solution turned dark brown, which indicated the formation of Au NPs. This mixture was stirred for 15 min before the organic phase was separated; the aqueous phase was washed twice with  $\text{CH}_2\text{Cl}_2$ . The combined organic phases were dried with  $\text{MgSO}_4$  and filtered. The solvent was evaporated with a stream of nitrogen or by using a rotary evaporator without heating. The dried NPs **Au-mX-Gn** were redissolved in  $\text{CH}_2\text{Cl}_2$  (<1.5 mL) and ethanol was added (20 mL). The NPs were then precipitated by centrifugation (5 rpm, 45 min, 5 °C) to remove the TOAB. Subsequently the NPs were subjected to size exclusion chromatography (SEC) to remove excess of the ligand. Before this step, the yield of the NPs was around 95% (based on the number of gold atoms). However, about 10–20% of the NPs were lost during SEC because some late SEC vials still showed excess ligand and were therefore

discarded. Some loss also occurred during the filtration in advance of SEC, performed to protect the column.

## Acknowledgements

We gratefully acknowledge financial support by the EU through the project FUNMOL (number 213382 of the call FP7-NMP-2007-SMALL-1), the Gebert R uf Foundation, the Swiss National Science Foundation, and the National Research Project (No. 62 Smart Materials).

- [1] M. Homberger, U. Simon, *Phil. Trans. R. Soc. A* **2010**, *368*, 1405–1453.
- [2] R. Sardar, A. M. Funston, P. Mulvaney, R. W. Murray, *Langmuir* **2009**, *25*, 13840–13851.
- [3] M.-C. Daniel, D. Astruc, *Chem. Rev.* **2004**, *104*, 293–346.
- [4] R. W. Murray, *Chem. Rev.* **2008**, *108*, 2688–2720.
- [5] G. Schmid, U. Simon, *Chem. Commun.* **2005**, 697–710.
- [6] R. P. Andres, J. D. Bielefeld, J. I. Henderson, D. B. Janes, V. R. Kola-gunta, C. P. Kubiak, W. J. Mahoney, R. G. Osifchin, *Science* **1996**, *273*, 1690–1693.
- [7] J. Liao, L. Bernard, M. Langer, C. Sch onenberger, M. Calame, *Adv. Mater.* **2006**, *18*, 2444–2447.
- [8] G. Schmid, *Chem. Soc. Rev.* **2008**, *37*, 1909–1930.
- [9] S.-J. Kim, J.-S. Lee, *Nano Lett.* **2010**, *10*, 2884–2890.
- [10] S. A. Maier, M. L. Brongersma, H. A. Atwater, *Appl. Phys. Lett.* **2001**, *78*, 16.
- [11] Y. Leroux, J. C. Lacroix, C. Fave, V. Stockhausen, N. Fe’lidj, J. Grand, A. Hohenau, J. R. Krenn, *Nano Lett.* **2009**, *9*, 2144–2148.
- [12] S. D. Evans, S. R. Johnson, Y. L. Cheng, T. Shen, *J. Mater. Chem.* **2000**, *10*, 183–188.
- [13] Y. Kim, R. C. Johnson, J. T. Hupp, *Nano Lett.* **2001**, *1*, 165–167.
- [14] H.-L. Zhang, S. D. Evans, J. R. Henderson, R. E. Miles, T.-H. Shen, *Nanotechnology* **2002**, *13*, 439–444.
- [15] Y. Zhou, S. Wang, K. Zhang, X. Jiang, *Angew. Chem.* **2008**, *120*, 7564–7566; *Angew. Chem. Int. Ed.* **2008**, *47*, 7454–7456.
- [16] M. Riskin, R. Tel-Vered, T. Bourenko, E. Granot, I. Willner, *J. Am. Chem. Soc.* **2008**, *130*, 9726–9733.
- [17] X. Zhang, Q. Guo, D. Cui, *Sensors* **2009**, *9*, 1033–1053.
- [18] D. A. Schultz, *Curr. Opin. Biotechnol. Curr. Opin. Biotech.* **2003**, *14*, 13–22.
- [19] C. M. Niemeyer, *Angew. Chem.* **2003**, *115*, 5974–5978; *Angew. Chem. Int. Ed.* **2003**, *42*, 5796–5800.
- [20] E. Katz, I. Willner, *Angew. Chem.* **2004**, *116*, 6166–6235; *Angew. Chem. Int. Ed.* **2004**, *43*, 6042–6108.
- [21] N. L. Rosi, C. A. Mirkin, *Chem. Rev.* **2005**, *105*, 1547–1562.
- [22] J. F. Hainfeld, R. D. Powell, *J. Histochem. Cytochem.* **2000**, *48*, 471–480.
- [23] R. Wilson, *Chem. Soc. Rev.* **2008**, *37*, 2028–2045.
- [24] A. Corma, H. Garcia, *Chem. Soc. Rev.* **2008**, *37*, 2096–2126.
- [25] C. Della Pina, E. Falletta, L. Prati, M. Rossi, *Chem. Soc. Rev.* **2008**, *37*, 2077–2095.
- [26] R. L vy, N. T. K. Thanh, R. C. Doty, I. Hussain, R. J. Nichols, D. J. Schiffrin, M. Brust, D. G. Fernig, *J. Am. Chem. Soc.* **2004**, *126*, 10076–10084.
- [27] D. Aili, M. M. Stevens, *Chem. Soc. Rev.* **2010**, *39*, 3358.
- [28] M. Brust, M. Walker, D. Bethell, D. J. Schiffrin, R. Whyman, *J. Chem. Soc. Chem. Commun.* **1994**, 801–802.
- [29] X.-M. Li, M. R. de Jong, K. Inoue, S. Shinkai, J. Huskens, D. N. Reinhoudt, *J. Mater. Chem.* **2001**, *11*, 1919–1923.
- [30] E. J. Shelley, D. Ryan, S. R. Johnson, M. Couillard, D. Fitzmaurice, P. D. Nellist, Y. Chen, R. E. Palmer, J. A. Preece, *Langmuir* **2002**, *18*, 1791–1795.
- [31] T. Peterle, A. Leifert, J. Timper, A. Sologubenko, U. Simon, M. Mayor, *Chem. Commun.* **2008**, 3438–3440.
- [32] T. Peterle, P. Ringler, M. Mayor, *Adv. Funct. Mater.* **2009**, *19*, 3497–3506.

- [33] J. P. Hermes, F. Sander, T. Peterle, C. Cioffi, P. Ringler, T. Pfohl, M. Mayor, *Small* **2011**, *7*, 920–929.
- [34] J. P. Hermes, F. Sander, T. Peterle, M. Mayor, *CHIMIA* **2011**, *65*, 219–222.
- [35] F. Sander, T. Peterle, N. Ballav, F. von Wrochem, M. Zharnikov, M. Mayor, *J. Phys. Chem. C* **2010**, *114*, 4118–4125.
- [36] H.-M. Huang, C.-Y. Chang, I.-C. Liu, H.-C. Tsai, M.-K. Lai, R. C.-C. Tsiang, *J. Polym. Sci., Part A: Polym. Chem.* **2005**, *43*, 4710–4720.
- [37] I. Hussain, S. Graham, Z. Wang, B. Tan, D. C. Sherrington, S. P. Rannard, A. I. Cooper, M. Brust, *J. Am. Chem. Soc.* **2005**, *127*, 16398–16399.
- [38] D. Wan, Q. Fu, J. Huang, *J. Appl. Polym. Sci.* **2006**, *101*, 509–514.
- [39] Z. Wang, B. Tan, I. Hussain, N. Schaeffer, M. F. Wyatt, M. Brust, A. I. Cooper, *Langmuir* **2007**, *23*, 885–895.
- [40] A. Taubert, U.-M. Wiesler, K. Müllen, *J. Mater. Chem.* **2003**, *13*, 1090–1093.
- [41] G. Bergamini, P. Ceroni, V. Balzani, M. Gingras, J.-M. Raimundo, V. Morandi, P. G. Merli, *Chem. Commun.* **2007**, 4167.
- [42] A. D'Aléo, R. M. Williams, F. Osswald, P. Edamana, U. Hahn, J. van Heyst, F. D. Tichelaar, F. Vögtle, L. De Cola, *Adv. Funct. Mater.* **2004**, *14*, 1167–1177.
- [43] Y. Hosokawa, S. Maki, T. Nagata, *Bull. Chem. Soc. Jpn.* **2005**, *78*, 1773–1782.
- [44] E. Boisselier, A. K. Diallo, L. Salmon, C. Ornelas, J. Ruiz, D. Astruc, *J. Am. Chem. Soc.* **2010**, *132*, 2729–2742.
- [45] K. Esumi, A. Kameo, A. Suzuki, K. Torigoe, *Colloids Surf. A* **2001**, *189*, 155–161.
- [46] J. D. Gilbertson, G. Vijayaraghavan, K. J. Stevenson, B. D. Chandler, *Langmuir* **2007**, *23*, 11239–11245.
- [47] M. Pittelkow, T. Brock-Nannestad, K. Moth-Poulsen, J. B. Christensen, *Chem. Commun.* **2008**, 2358–2360.
- [48] R. M. Crooks, M. Zhao, L. Sun, V. Chechik, L. K. Yeung, *Acc. Chem. Res.* **2001**, *34*, 181–190.
- [49] J. J. Michels, J. Huskens, D. N. Reinhoudt, *J. Chem. Soc., Perkin Trans. 2* **2002**, 102–105.
- [50] H.-F. Chow, M.-K. Ng, C.-W. Leung, G.-X. Wang, *J. Am. Chem. Soc.* **2004**, *126*, 12907–12915.
- [51] A. Dahan, A. Weissberg, M. Portnoy, *Chem. Commun.* **2003**, 1206–1207.
- [52] A. Dahan, M. Portnoy, *J. Am. Chem. Soc.* **2007**, *129*, 5860–5869.
- [53] A. Van Bierbeek, M. Gingras, *Tetrahedron Lett.* **1998**, *39*, 6283–6286.
- [54] W. M. Pankau, S. Mönninghoff, G. von Kiedrowski, *Angew. Chem.* **2006**, *118*, 1923–1926; *Angew. Chem. Int. Ed.* **2006**, *45*, 1889–1891.
- [55] W. Offermann, F. Vögtle, *Synthesis* **1977**, 1977, 272–273.
- [56] R. C. Fuson, B. Freedmann, *J. Org. Chem.* **1958**, *23*, 1161–1166.
- [57] C.-C. Han, R. Balakumar, *Tetrahedron Lett.* **2006**, *47*, 8255–8258.
- [58] M. M. Alvarez, J. T. Khoury, T. G. Schaaff, M. N. Shafiqullin, I. Vezmar, R. L. Whetten, *J. Phys. Chem. B* **1997**, *101*, 3706–3712.
- [59] M. J. Hostettler, J. E. Wingate, C.-J. Zhong, J. E. Harris, R. W. Vachet, M. R. Clark, J. D. Londono, S. J. Green, J. J. Stokes, G. D. Wignall, G. L. Glish, M. D. Porter, N. D. Evans, R. W. Murray, *Langmuir* **1998**, *14*, 17–30.
- [60] P. J. Magelhaes, S. J. Ram, M. D. Abramoff, *Biophotonics Int.* **2004**, *11*, 36–42.
- [61] R. Wilson, Y. Chen, J. Aveyard, *Chem. Commun.* **2004**, 1156.
- [62] C. Krüger, S. Agarwal, A. Greiner, *J. Am. Chem. Soc.* **2008**, *130*, 2710–2711.
- [63] P. D. Jadzinsky, G. Calero, C. J. Ackerson, D. A. Bushnell, R. D. Kornberg, *Science* **2007**, *318*, 430–433.
- [64] M. W. Heaven, A. Dass, P. S. White, K. M. Holt, R. W. Murray, *J. Am. Chem. Soc.* **2008**, *130*, 3754–3755.
- [65] D. Thompson, J. P. Hermes, A. Quinn, M. Mayor, in preparation.

Received: June 16, 2011  
Published online: October 26, 2011



# CHEMISTRY

---

## A EUROPEAN JOURNAL

---

### Supporting Information

© Copyright Wiley-VCH Verlag GmbH & Co. KGaA, 69451 Weinheim, 2011

#### Gold Nanoparticles Stabilized by Thioether Dendrimers

**Jens Peter Hermes,<sup>[a]</sup> Fabian Sander,<sup>[a]</sup> Torsten Peterle,<sup>[a, b]</sup> Raphael Urbani,<sup>[c]</sup>  
Thomas Pfohl,<sup>[c]</sup> Damien Thompson,<sup>[d]</sup> and Marcel Mayor\*<sup>[a, e]</sup>**

chem\_201101837\_sm\_miscellaneous\_information.pdf

General methods . . . . .	S2
Nanoparticle analysis . . . . .	S2
Representative TEM images . . . . .	S5
Experimental procedures for the synthesis of dendrons and dendrimers . . . . .	S7
References . . . . .	S20



## General methods

All commercially available starting materials were of reagent grade and used as received. Absolute tetrahydrofuran (THF) was purchased from *Fluka*, stored over 4 Å molecular sieves, and handled under Argon. Methyl *tert*-butyl ether (MTBE), hexane and dichloromethane were of technical grade and distilled prior to use. Column chromatography purifications were carried out on *silica gel 60* (particle size 40-63 µm) from *Fluka*. Deuterated solvents were purchased from *Cambridge Isotope Laboratories*. <sup>1</sup>H and <sup>13</sup>C NMR spectra were recorded with a *Bruker DMX 400* instrument (<sup>1</sup>H resonance 400 MHz) or a *Bruker DRX 500* instrument (<sup>1</sup>H resonance 500 MHz) at 298 K. Matrix Assisted Laser Desorption Ionisation Time of Flight (MALDI-ToF) mass spectra were performed on an *Applied Bio Systems Voyager-De™ Pro* mass spectrometer. Electron Impact (EI) mass spectra were recorded on a *Finnigan MAT 95Q* by H. Nadig. Elemental analyses were performed by W. Kirsch on a *Perkin-Elmer Analyticator 240*. UV/vis spectra were recorded on an *Agilent 8453E* spectrophotometer. Size exclusion chromatography (SEC) was performed using *Bio-Rad Bio-Beads S-XI Beads* (operating range 600 – 14000 g mol<sup>-1</sup>) with toluene as eluent.

## Nanoparticle analysis

### Thermogravimetric analysis (TGA)

Thermogravimetric analysis was performed on a *Mettler Toledo TGA/SDTA851<sup>e</sup>*. The loss of weight was interpreted as the amount of ligand. The mass of gold per organic ligand was calculated from the ratio

$$\text{mass}(\text{Au per ligand}) = \frac{\text{mass}\%(\text{Au})}{\text{mass}\%(\text{ligand})} \cdot \text{mass}(\text{ligand}) \quad (1)$$

The number of gold atoms per ligand is calculated from

$$\text{Au atoms per ligand} = \frac{\text{mass}(\text{Au per ligand})}{\text{molecular weight}(\text{Au})} \quad (2)$$

### <sup>1</sup>H-NMR

Figure S1 shows the <sup>1</sup>H-NMR spectra of dendritic ligands **mX-Gn** and ligand-stabilized-Au NPs **Au-mX-Gn**, respectively. The spectra are very similar. Therefore, the dendritic ligands are able to stabilize the Au NPs on their own. The phasetransfer agent TOAB can be completely removed, as no further significant signal appeared. The ligand-gold coordination

is visible due to a slight peak broadening in the Au-NP spectra without changes in the chemical shifts.

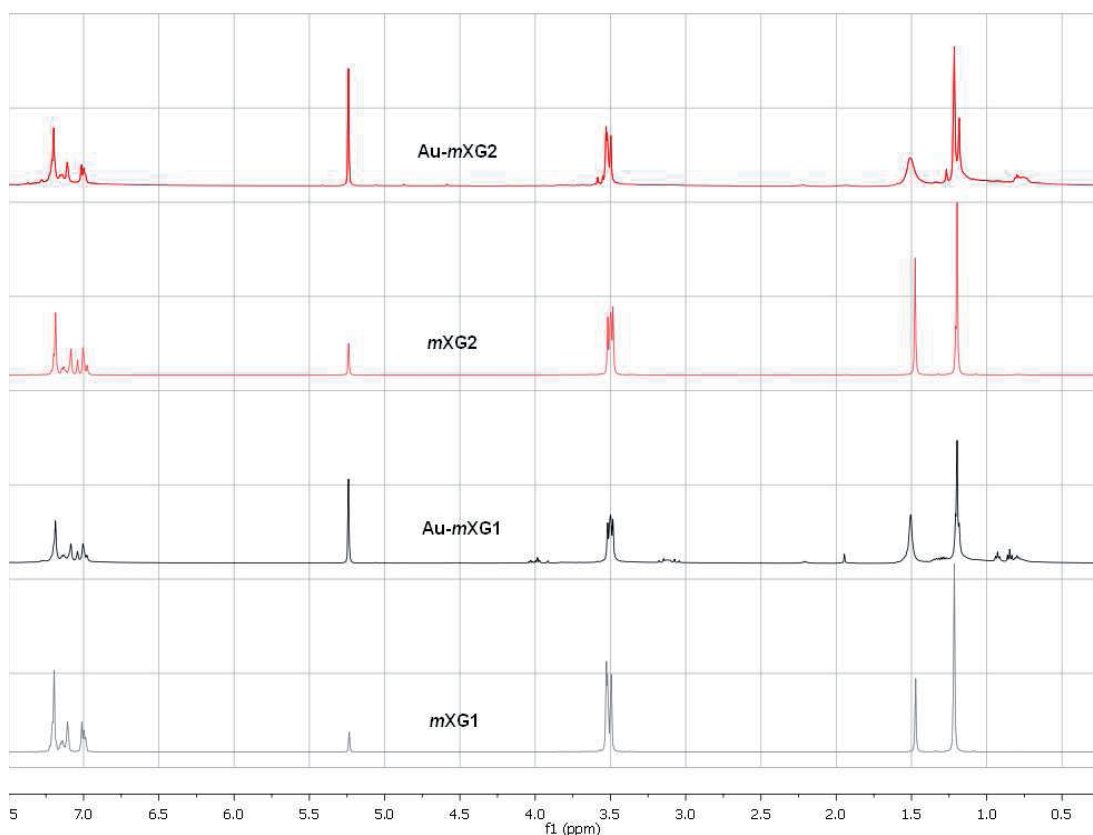


**Figure S1.** <sup>1</sup>H-NMR-spectra in CD<sub>2</sub>Cl<sub>2</sub> of dendrimer ligands *mX-G1* and *mX-G2* and the spectra of dendrimer-stabilized Au NPs **Au-*mX-G1*** and **Au-*mX-G2***.

#### *Transmission Electron Microscopy (TEM)*

TEM was performed on a *Philips CM100* transmission electron microscope at 80 kV. Electron micrographs were recorded on a 2000 by 2000 pixel charge-coupled device camera *Veleta* from *Olympus*. The micrographs were recorded with a magnification of 180kx leading to micrographs with 520 nm by 520 nm and a size of 0.26 nm per pixel. Therefore the column width of the histograms was chosen to be 0.3 nm. One NP has a diameter of four pixels and an area of ten to twelve pixels.

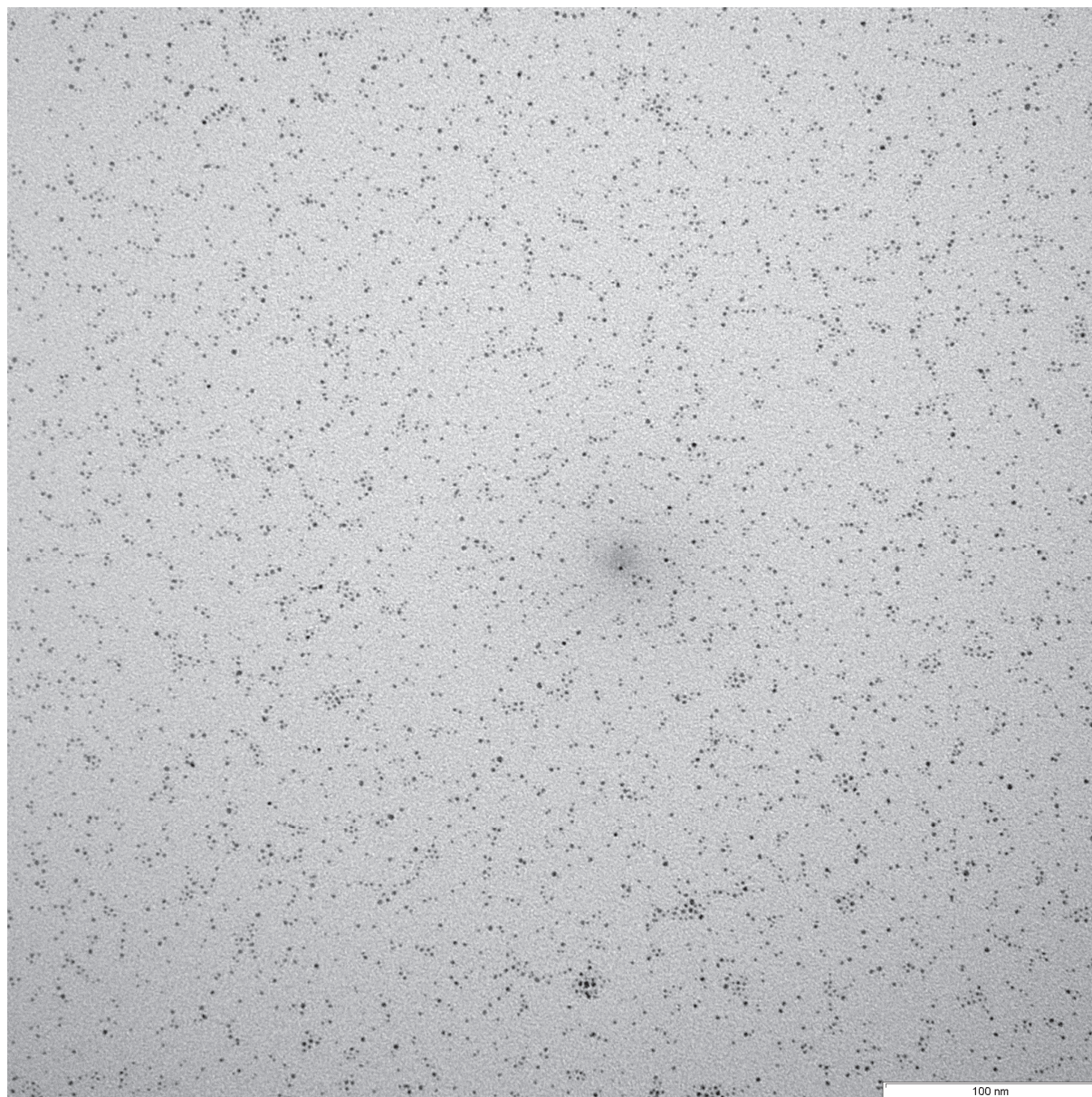
The NPs were deposited by carefully putting a drop of the NP dispersion on top of a thin carbon film that spanned a perforated holey carbon support film covering a gold-plated copper microscopy grid. The remaining solvent was directly blotted with filter paper and the grid air dried.

### *Nanoparticle diameter*

The NP diameters were measured automatically using the program *imageJ*. The rather dense images (see micrographs: Figure S2-S3) were first transferred into 8-bit greyscale and then into black and white using the function “Threshold” and the setting “intermodes”. The area of the NPs was measured with “Analyze particles”. The particles on edges were excluded and holes included. Au NPs were measured with areas from 0.3 nm<sup>2</sup> till infinity. We did not consider particles with an area less than 0.3 nm<sup>2</sup> because otherwise the general noise would be counted as particles. As the transformation in black and white already removed some noise, we assume that the automatic measurement does not consider noise or artifacts as NPs. The final diameters were calculated from the measured areas, thus we needed to focus on perfectly spherical NPs to avoid mistakes upon calculation. Therefore NPs were only measured with circularities from 0.9-1. More than 80 % percent of NPs showed this circularity. NP sizes were measured from two to four dense micrographs (around 5,000 counts of NPs).

### *Small angle X-ray scattering (SAXS)*

SAXS experiments were performed at  $\lambda = 0.15418$  nm using a Bruker-AXS Nanostar with a virtually noise-free 2D-Hi-Star detector. All measurements were taken at ambient temperature in benzene with exposure times of 3600–7200 s. 2D-Images were azimuthally averaged to produce 1D intensity profiles for scattering vectors  $q \in [0.8 \text{ nm}^{-1}, 6 \text{ nm}^{-1}]$ . Background measurements (solvent only) were subtracted from the obtained intensity profiles. Nanofit software from Bruker was used to fit the data. A Gaussian distribution of diameters with  $\sigma = 0.4$  nm was applied to determine the radius of spherical NPs.

**Representative TEM images of ligand-stabilized gold nanoparticles****Figure S2.** Representative TEM image of Au NPs **Au-*mX*-G1**.

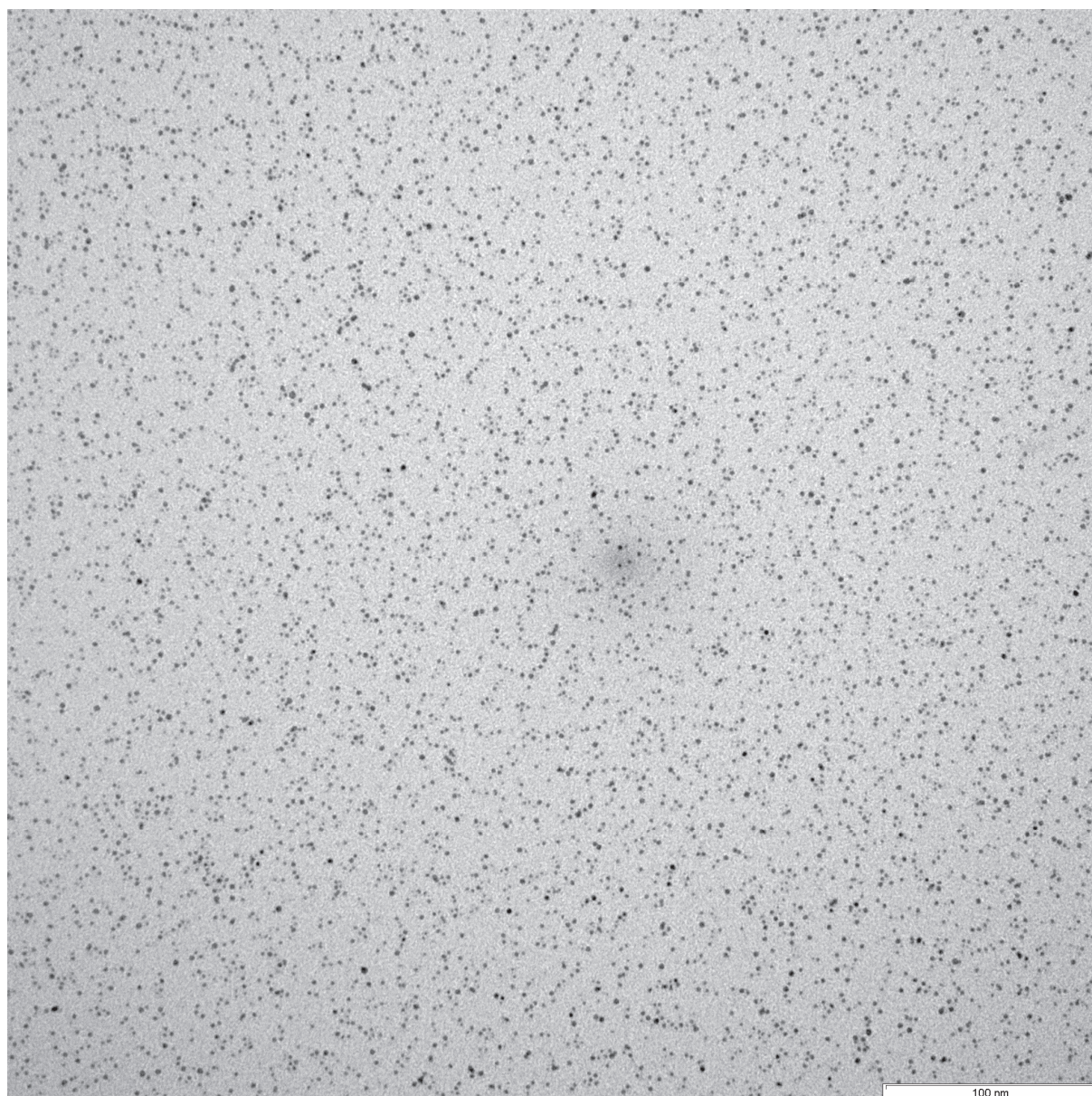
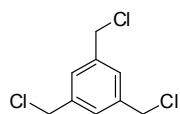


**Figure S3.** Representative TEM image of Au NPs **Au-*mX*-G2**.

## Experimental procedures for the synthesis of dendrons and dendrimers

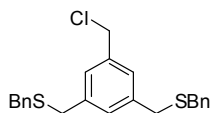
### 1,3,5-tris(chloromethyl)benzene<sup>[1]</sup> (**2**)



1,3,5-Tris(bromomethyl)benzene (**1**) (9.92 g, 28 mmol, 1 eq) was dissolved in dry *N,N*-dimethylformamide (50 ml) under an atmosphere of argon. Lithium chloride (17 g, 410 mmol, 14.7 eq) was slowly added at 0°C. The reaction mixture was left stirring for 30 minutes at that temperature and was then allowed to warm to room temperature. After two hours stirring at room temperature, MTBE was added and the mixture was extracted four times with water followed once by brine. The organic fraction was dried over magnesium sulfate and evaporated to dryness. Recrystallization from dichloromethane/hexane gave 1,3,5-tris(chloromethyl)benzene (**2**) (5.57 g, 25 mmol, 90%) as colorless crystals.

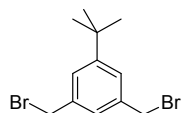
<sup>1</sup>H NMR (400 MHz, CDCl<sub>3</sub>): δ = 7.38 (*s*, 3H, Aryl-*H*), 4.59 (*s*, 6H, CH<sub>2</sub>); <sup>13</sup>C NMR (100 MHz, CDCl<sub>3</sub>): δ = 138.6, 128.6, 45.3.

### (5-(Chloromethyl)-1,3-phenylene)bis(methylene)bis(benzylsulfane) (**3**)



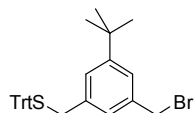
To a solution of 1,3,5-tris(chloromethyl)benzene (**2**) (1.980 g, 8.9 mmol, 1 eq) and benzyl mercaptan (1.87 ml, 1.98 g, 15.9 mmol, 1.8 eq) in dry tetrahydrofuran (40 ml) under an atmosphere of argon was added sodium hydride (60% in mineral oil, 1.28 g, 32.0 mmol, 3.6 eq) at 0°C. After the gas formation had ceased, the mixture was allowed to come to room temperature and stirred at that temperature for 1 hour. Water was then added to quench the reaction and the mixture was extracted 3 times with MTBE. The combined organic fractions were washed with brine, dried over magnesium sulfate, filtered and evaporated to dryness. After purification by column chromatography (hexane/dichloromethane 3:2, then 1:1), the title compound **3** (1.562 g, 3.9 mmol, 44%) was obtained as colorless liquid. The dichloride side product was also isolated (0.776 g, 2.5 mmol, 28%) and was reused in further attempts to synthesize **3**.

<sup>1</sup>H NMR (400 MHz, CDCl<sub>3</sub>): δ = 7.36 – 7.20 (*m*, 10H, Aryl-*H*), 7.16 (*s*, 2H, Aryl-*H*), 7.14 (*s*, 1H, Aryl-*H*), 4.55 (*s*, 2H, CH<sub>2</sub>), 3.61 (*s*, 4H, CH<sub>2</sub>), 3.57 (*s*, 4H, CH<sub>2</sub>); <sup>13</sup>C NMR (100 MHz, CDCl<sub>3</sub>): δ = 139.0, 137.9, 137.8, 129.7, 129.0, 128.5, 127.9, 127.1, 46.0, 35.7, 35.2; Anal calcd. for C<sub>23</sub>H<sub>23</sub>ClS<sub>2</sub>: C 69.24, H 5.81; found: C 68.89, H 5.85

**1,3-Bis(bromomethyl)-5-*tert*-butylbenzene**<sup>[2]</sup> (**4**)

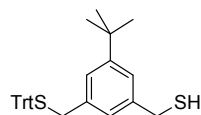
*N*-Bromosuccinimide (30.17 g, 170 mmol, 2.1 eq) and 5-*tert*-butyl-*m*-xylene (15.0 ml, 12.98 g, 80 mmol, 1 eq) were dissolved in methyl formate (150 ml). 2,2'-Azobis(2-methylpropionitrile) (75 mg) was then added and the reaction mixture was illuminated by a 500 W halogen lamp for 3 hours. The solvent was evaporated by using a rotary evaporator and the residue was redissolved in dichloromethane. The organic solution was washed twice with a saturated aqueous solution of sodium hydrogen carbonate and then once with water. After drying with magnesium sulfate, the dichloromethane was removed by evaporation. The residue was recrystallized from dichloromethane/hexane twice to give product **3** (18.02 g, 56.3 mmol, 70%) as colorless crystals.

<sup>1</sup>H NMR (400 MHz, CDCl<sub>3</sub>): δ = 7.34 (*br*, 2H, Aryl-*H*), 7.27 (*br*, 1H, Aryl-*H*), 4.49 (*s*, 4H, CH<sub>2</sub>), 1.34 (*s*, 9H, C(CH<sub>3</sub>)<sub>3</sub>); <sup>13</sup>C NMR (100 MHz, CDCl<sub>3</sub>): δ = 153.0, 138.4, 127.3, 126.7, 35.2, 33.9, 31.6.

**(3-(Bromomethyl)-5-*tert*-butylbenzyl)(trityl)sulfane** (**5**)

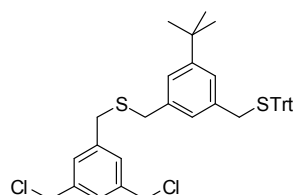
1,3-bis(bromomethyl)-5-*tert*-butylbenzene (**3**) (1.00 g, 3.1 mmol, 1 eq) and triphenylmethane-thiol (863 mg, 3.1 mmol, 1 eq) were dissolved in 20 ml dry tetrahydrofuran under an atmosphere of argon. Potassium carbonate (650 mg, 4.7 mmol, 1.5 eq) was added and the mixture was heated to reflux for 20 hours. After cooling to room temperature, 100 ml water was added and the mixture was extracted three times with 50 ml MTBE. The combined organic fractions were washed with brine, dried over magnesium sulfate and evaporated to dryness. After purification by column chromatography (hexane/dichloromethane 4:1), the product **4** (818 mg, 1.6 mmol, 51%) was obtained as colorless solid.

<sup>1</sup>H NMR (400 MHz, CDCl<sub>3</sub>): δ = 7.49 – 7.44 (*m*, 6H, Aryl-*H*, Trt-*H*), 7.35 – 7.20 (*m*, 10H, Trt-*H*), 7.03 (*s*, 1H, Aryl-*H*), 6.95 (*s*, 1H, Aryl-*H*), 4.43 (*s*, 2H, CH<sub>2</sub>), 3.33 (*s*, 2H, CH<sub>2</sub>), 1.27 (*s*, 9H, C(CH<sub>3</sub>)<sub>3</sub>); <sup>13</sup>C NMR (100 MHz, CDCl<sub>3</sub>): δ = 151.97, 144.65, 137.50, 137.46, 129.65, 127.94, 126.82, 126.72, 126.30, 124.81, 67.60, 36.95, 34.65, 33.95, 31.23; MS (MALDI-TOF, *m/z*): 537.0 [*M*+Na]<sup>+</sup>; Anal. calcd. for C<sub>31</sub>H<sub>31</sub>BrS: C 72.22, H 6.06; found 71.92, H 6.20; MP: 140.1°C.

**(3-*tert*-Butyl-5-(tritylthiomethyl)phenyl)methanethiol (6)**

To a solution of (3-(bromomethyl)-5-*tert*-butylbenzyl)(trityl)sulfane (**4**) (1.184 g, 2.3 mmol, 1 eq) in dry tetrahydrofuran (15 ml) under an atmosphere of argon was added potassium thioacetate (525 mg, 4.6 mmol, 2 eq). After 1 hour stirring at room temperature, dry methanol (15 ml) and potassium carbonate (950 mg, 6.9 mmol, 3 eq) were added and the mixture was left stirring for 1 hour. Water was added and the solution was extracted three times with MTBE. The combined organic fractions were washed with brine, dried over magnesium sulfate, filtered and evaporated to dryness. After purification by column chromatography (hexane/dichloromethane 4:1, then 3:1), the title compound **6** (855 mg, 1.8 mmol, 80%) was obtained as colorless oily solid.

<sup>1</sup>H NMR (400 MHz, CDCl<sub>3</sub>): δ = 7.50 – 7.44 (*m*, 6H, Aryl-*H*), 7.34 – 7.29 (*m*, 6H, Aryl-*H*), 7.26 – 7.20 (*m*, 3H, Aryl-*H*), 7.16 (*br*, 1H, Aryl-*H*), 6.99 (*br*, 1H, Aryl-*H*), 6.90 (*br*, 1H, Aryl-*H*), 3.68 (*d*, *J* = 7.5 Hz, 2H, CH<sub>2</sub>), 3.32 (*s*, 2H, CH<sub>2</sub>), 1.71 (*t*, *J* = 7.5 Hz, 1H, SH), 1.27 (*s*, 9H, C(CH<sub>3</sub>)<sub>3</sub>); <sup>13</sup>C NMR (100 MHz, CDCl<sub>3</sub>): δ = 152.1, 144.9, 141.1, 137.5, 129.7, 128.2, 126.9, 126.0, 125.1, 124.1, 67.8, 37.3, 34.7, 31.5, 29.3; MS (MALDI-TOF, *m/z*): 491.5 [*M*+Na]<sup>+</sup>, 507.4 [*M*+K]<sup>+</sup>; Anal calcd. for C<sub>31</sub>H<sub>32</sub>S<sub>2</sub>: C 79.44, H 6.88; found: C 78.89, H 6.96

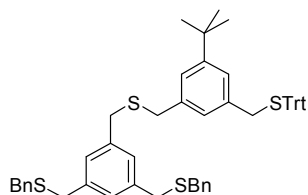
**(3,5-Bis(chloromethyl)benzyl)(3-*tert*-butyl-5-(tritylthiomethyl)benzyl)sulfane (7)**

To a solution of 1,3,5-tris(chloromethyl)benzene (**2**) (1.376 g, 6.2 mmol, 1.25 eq) and (3-*tert*-butyl-5-(tritylthiomethyl)phenyl)methanethiol (**6**) (2.322 g, 4.9 mmol, 1 eq) in dry tetrahydrofuran (50 ml) under an atmosphere of argon was added sodium hydride (60% in mineral oil, 400 mg, 10.0 mmol, 2 eq) at 0°C. After the gas formation had ceased, the mixture was allowed to come to room temperature and stirred at that temperature for 2 hours. Water was then added to quench the reaction and the mixture was extracted 3 times with MTBE. The combined organic fractions were washed with brine, dried over magnesium sulfate, filtered and evaporated to dryness. After purification by column chromatography (hexane/dichloromethane 3:1, then 2:1), the compound **7** (1.578 g, 2.4 mmol, 49%) was obtained as colorless solid.



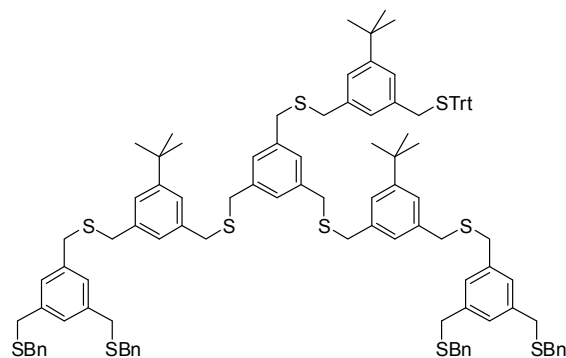
$^1\text{H NMR}$  (400 MHz,  $\text{CDCl}_3$ ):  $\delta = 7.50 - 7.44$  (*m*, 6H, Aryl-*H*),  $7.35 - 7.27$  (*m*, 7H, Aryl-*H*),  $7.26 - 7.20$  (*m*, 5H, Aryl-*H*),  $7.13$  (*br*, 1H, Aryl-*H*),  $7.00$  (*br*, 1H, Aryl-*H*),  $6.88$  (*br*, 1H, Aryl-*H*),  $4.53$  (*s*, 4H,  $\text{CH}_2$ ),  $3.55$  (*s*, 2H,  $\text{CH}_2$ ),  $3.54$  (*s*, 2H,  $\text{CH}_2$ ),  $3.32$  (*s*, 2H,  $\text{CH}_2$ ),  $1.28$  (*s*, 9H,  $\text{C}(\text{CH}_3)_3$ );  $^{13}\text{C NMR}$  (100 MHz,  $\text{CDCl}_3$ ):  $\delta = 151.7, 144.7, 139.6, 138.2, 137.5, 137.1, 129.7, 129.1, 127.9, 127.3, 126.8, 126.7, 124.9, 124.8, 67.6, 45.6, 37.2, 35.8, 34.9, 34.6, 31.3$ .  
Anal calcd. for  $\text{C}_{40}\text{H}_{40}\text{Cl}_2\text{S}_2$ : C 73.26, H 6.15; found: C 73.24, H 6.24.

### [*mX-G0.STrt*] dendron



To a solution of the monochloride **3** (1.263 g, 3.2 mmol, 1 eq) and (3-*tert*-butyl-5-(tritylthiomethyl)phenyl)methanethiol (**6**) (1.514 g, 3.2 mmol, 1.05 eq) in dry tetrahydrofuran (30 ml) under an atmosphere of argon was added sodium hydride (60% in mineral oil, 260 mg, 6.5 mmol, 2.1 eq) at  $0^\circ\text{C}$ . After the gas formation had ceased, the mixture was allowed to come to room temperature and stirred at that temperature for 2 hours. Water was then added to quench the reaction and the mixture was extracted 3 times with MTBE. The combined organic fractions were washed with brine, dried over magnesium sulfate, filtered and evaporated to dryness. After purification by column chromatography (hexane/dichloromethane 3:2, then 1:1), [*mX-G0.STrt*] (2.649 g, 3.2 mmol, quant.) was obtained as colorless oil.

$^1\text{H NMR}$  (400 MHz,  $\text{CDCl}_3$ ):  $\delta = 7.50 - 7.44$  (*m*, 6H, Aryl-*H*),  $7.35 - 7.20$  (*m*, 19H, Aryl-*H*),  $7.15$  (*br*, 1H, Aryl-*H*),  $7.08$  (*br*, 3H, Aryl-*H*),  $7.00$  (*br*, 1H, Aryl-*H*),  $6.91$  (*br*, 1H, Aryl-*H*),  $3.60$  (*s*, 4H,  $\text{CH}_2$ ),  $3.58 - 3.52$  (*m*, 8H,  $\text{CH}_2$ ),  $3.33$  (*s*, 2H,  $\text{CH}_2$ ),  $1.28$  (*s*, 9H,  $\text{C}(\text{CH}_3)_3$ );  $^{13}\text{C NMR}$  (100 MHz,  $\text{CDCl}_3$ ):  $\delta = 151.6, 144.7, 138.6, 138.0, 137.7, 137.1, 129.7, 127.9, 127.0, 126.8, 126.7, 124.8, 67.5, 37.1, 35.9, 35.7, 35.4, 34.6, 31.3$ ; **MS** (MALDI-TOF, *m/z*): 854.1 [ $M+\text{Na}$ ] $^+$ , 871.1 [ $M+\text{K}$ ] $^+$ ; Anal calcd. for  $\text{C}_{54}\text{H}_{54}\text{S}_4$ : C 78.03, H 6.55; found: C 77.65, H 6.51.

**[mX-G1.STrt] dendron**

The G0 dendron **[mX-G0.STrt]** (1.616 g, 1.94 mmol, 1 eq) was dissolved in a mixture of dichloromethane (20 ml) and triethylsilane (470  $\mu$ l, 339.2 mg, 2.92 mmol, 1.5 eq). Trifluoroacetic acid (800  $\mu$ l, 4% v/v of dichloromethane) was added dropwise to this solution. The mixture was stirred for 15 minutes, quenched with a saturated aqueous solution of sodium hydrogen carbonate and the organic phase was separated. The aqueous phase was washed twice with dichloromethane and the combined organic fractions were dried over magnesium sulfate. After filtration and evaporation of the solvent, the crude product was purified by column chromatography (hexane/dichloromethane 3:2) to yield the free thiol **[mX-G0.SH]** (1.104 g, 1.88 mmol, 97%), which was directly used in the next step.

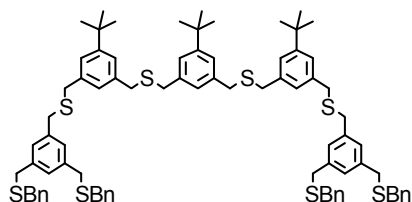
$^1\text{H NMR}$  (400 MHz,  $\text{CDCl}_3$ ):  $\delta$  = 7.32 – 7.15 (*m*, 12H, Aryl-*H*), 7.08 (*br*, 2H, Aryl-*H*), 7.06 (*br*, 2H, Aryl-*H*), 3.70 (*d*,  $J$  = 7.5 Hz, 2H,  $\text{CH}_2$ ), 3.60 (*s*, 4H,  $\text{CH}_2$ ), 3.57 (*s*, 2H,  $\text{CH}_2$ ), 3.56 (*s*, 4H,  $\text{CH}_2$ ), 3.55 (*s*, 2H,  $\text{CH}_2$ ), 1.75 (*t*,  $J$  = 7.5 Hz, 1H, *SH*), 1.29 (*s*, 9H,  $\text{C}(\text{CH}_3)_3$ ).

The free thiol **[mX-G0.SH]** (1.104 g, 1.88 mmol, 2.2 eq) and (3,5-bis(chloromethyl)benzyl)-(3-*tert*-butyl-5-(tritylthiomethyl)benzyl)sulfane (**7**) (560 mg, 0.85 mmol, 1 eq) were dissolved in dry tetrahydrofuran (20 ml) under an atmosphere of argon. The mixture was degassed by bubbling argon through the solution to avoid disulfide formation during the reaction. After this procedure, sodium hydride (60 % in mineral oil, 150 mg, 3.76 mmol, 4.4 eq) was added and the mixture was left stirring at room temperature for 45 minutes. The reaction was quenched with water and extracted with MTBE three times. The combined organic fractions were washed with brine, dried over magnesium sulfate and evaporated to dryness. Purification of the crude product was achieved by column chromatography (hexane/dichloromethane 2:3, then 1:2, then 1:3) to yield the first generation dendron **[mX-G1.STrt]** (1.353 g, 0.77 mmol, 90%) as colorless oil.

$^1\text{H NMR}$  (400 MHz,  $\text{CDCl}_3$ ):  $\delta$  = 7.47 – 7.43 (*m*, 6H, Aryl-*H*), 7.32 – 7.04 (*m*, 45H, Aryl-*H*), 6.97 (*br*, 1H, Aryl-*H*), 6.90 (*br*, 1H, Aryl-*H*), 3.61 – 3.51 (*m*, 36H,  $\text{CH}_2$ ), 3.30 (*s*, 2H,  $\text{CH}_2$ ), 1.29 (*s*, 18H,  $\text{C}(\text{CH}_3)_3$ ), 1.25 (*s*, 9H,  $\text{C}(\text{CH}_3)_3$ );  $^{13}\text{C NMR}$  (100 MHz,  $\text{CDCl}_3$ ):  $\delta$  = 151.7,

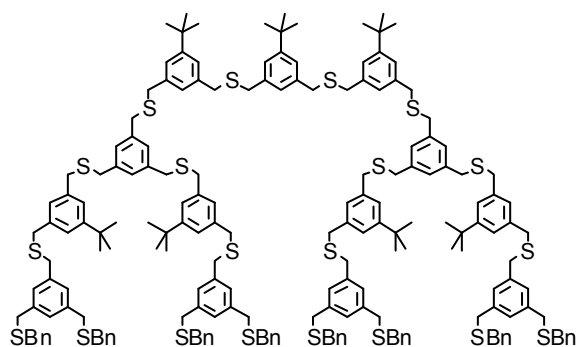
144.7, 138.7, 138.6, 138.0, 137.9, 137.7, 137.1, 129.7, 129.0, 128.5, 128.4, 127.9, 127.3, 127.0, 126.9, 126.8, 126.7, 124.8, 67.5, 37.2, 35.9, 35.8, 35.6, 35.5, 34.6 (2 $\times$ ), 31.4, 31.3; Anal. calcd. for C<sub>110</sub>H<sub>118</sub>S<sub>10</sub>: C 75.04, H 6.75; found: C 75.12, H 6.69.

### ***mX-G1* dendrimer**



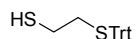
The free thiol [***mX-G0.SH***] (176.0 mg, 0.30 mmol, 2.1 eq) and 1,3-bis(bromomethyl)-5-tert-butylbenzene (45.6 mg, 0.14 mmol, 1 eq) were dissolved in dry tetrahydrofuran (10 ml) under an atmosphere of argon. The mixture was degassed by bubbling argon through the solution to avoid disulfide formation during the reaction. After this procedure, sodium hydride (60 % in mineral oil, 24 mg, 0.60 mmol, 4.2 eq) was added and the mixture was left stirring at room temperature for 1 h. The reaction was quenched with water and extracted with MTBE three times. The combined organic fractions were washed with brine, dried over magnesium sulfate and evaporated to dryness. Purification of the crude product was achieved by column chromatography (hexane/dichloromethane 2:3, then 1:2, then 1:3) to yield ***mX-G1*** (149.9 mg, 0.11 mmol, 79%) as colorless oil.

<sup>1</sup>H-NMR (500 MHz, CDCl<sub>3</sub>):  $\delta$  = 7.33 – 7.21 (*m*, 20H, Ar-*H*), 7.19 (*br*, 6H, Ar-*H*), 7.10 (*br*, 7H, Ar-*H*), 7.06 (*br*, 2H, *H* an Benzol), 3.64 – 3.55 (*m*, 32H, Benzyl*H*), 1.31 (*m*, 27H, Butyl*H*); <sup>13</sup>C-NMR (100 MHz, CDCl<sub>3</sub>):  $\delta$  = 151.6 (2 $\times$ ), 138.7, 138.6, 138.0, 138.0, 137.8, 129.0, 128.5, 128.4, 127.0, 126.8 (2 $\times$ ), 124.8, 124.7, 36.0, 35.9, 35.8, 35.5, 34.6, 31.4; MS (MALDI-TOF, *m/z*): broad peak starting at 1334 [*M*<sup>+</sup>]; Anal. calcd. for C<sub>82</sub>H<sub>94</sub>S<sub>8</sub>: C 73.71, H 7.09; found: C 73.27, H 7.04.

***mX-G2* dendrimer**

**[*mX-G1.SH*]** (67.8 mg, 0.045 mmol, 2.1 eq) and 1,3-bis(bromomethyl)-5-tert-butylbenzene (6.8 mg, 0.021 mmol, 1 eq) were dissolved in dry tetrahydrofuran (5 ml) under an atmosphere of argon. The mixture was degassed by bubbling argon through the solution to avoid disulfide formation during the reaction. After this procedure, sodium hydride (60 % in mineral oil, 4 mg, 0.1 mmol, 4.5 eq) was added and the mixture was left stirring at room temperature for 2 h. The reaction was quenched with water and extracted with MTBE three times. The combined organic fractions were washed with brine, dried over magnesium sulfate and evaporated to dryness. Purification of the crude product was achieved by column chromatography (hexane/dichloromethane 1:3, then 1:4, then dichloromethane) to yield ***mX-G2*** (58.1 mg, 0.018 mmol, 87%) as colorless oil.

**<sup>1</sup>H-NMR** (250 MHz, CDCl<sub>3</sub>): δ = 7.33 – 7.05 (m, 79H, ArH), 3.59 – 3.55 (m, 80H, benzylic-H), 1.29 (s, 63H, tert-ButylH); **<sup>13</sup>C-NMR** (100 MHz, CDCl<sub>3</sub>): δ = 151.7, 144.7, 138.7, 138.6, 138.0, 137.9, 137.7, 137.1, 129.7, 129.0, 128.5, 128.4, 127.9, 127.3, 127.0, 126.9, 126.8, 126.7, 124.8, 67.5, 37.2, 35.9, 35.8, 35.6, 35.5, 34.6 (2x), 31.4, 31.3; **MS** (MALDI-TOF, m/z): broad peak starting at 3191 [M<sup>+</sup>]; Anal. calcd. for C<sub>194</sub>H<sub>222</sub>S<sub>20</sub>: 72.93, H 7.00, found: C 73.15, H 6.91.

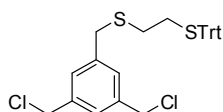
**2-(Tritylthio)ethanethiol<sup>[3]</sup> (**8**)**

Triphenylmethanethiol (4.56 g, 16 mmol, 2 eq) and triethylamine (280 μl, 2 mmol, 25 mol%) were dissolved in dry *N,N*-dimethylformamide (50 ml) under an atmosphere of argon. Ethylenesulfide (475 μl, 480 mg, 8 mmol, 1 eq) was added and the mixture was left stirring overnight. MTBE was added and the solution was extracted three times with water in order to remove the *N,N*-dimethylformamide, followed once by brine. The organic fraction was dried over magnesium sulfate, filtered and evaporated to dryness. The pure title compound **8** (2.47 g, 7.3 mmol, 92 %) was obtained after column chromatography

(hexane/dichloromethane 4:1, then 3:1, then 2:1) as colorless crystals. The excess of the starting material triphenylmethanethiol was also separated by this procedure and could be reused.

$^1\text{H NMR}$  (400 MHz,  $\text{CDCl}_3$ ):  $\delta = 7.46 - 7.41$  (*m*, 6H, Aryl-*H*),  $7.33 - 7.20$  (*m*, 9H, Aryl-*H*),  $2.52 - 2.46$  (*m*, 2H,  $\text{CH}_2$ ),  $2.32 - 2.24$  (*m*, 2H,  $\text{CH}_2$ ),  $1.44$  (*t*,  $J = 8.3$  Hz, 1H, *SH*);  $^{13}\text{C NMR}$  (100 MHz,  $\text{CDCl}_3$ ):  $\delta = 144.7, 129.6, 127.9, 126.7, 67.0, 36.0, 23.8$ ; Anal calcd. for  $\text{C}_{21}\text{H}_{20}\text{S}_2$ : C 74.96, H 5.99; found: C 74.49, H 6.02.

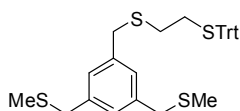
### (3,5-Bis(chloromethyl)benzyl)(2-(tritylthio)ethyl)sulfane (**9**)



1,3,5-tris(chloromethyl)benzene (**2**) (3.81 g, 17.0 mmol, 1 eq), 2-(tritylthio)ethanethiol (**8**) (5.73 g, 17.0 mmol, 1 eq) and potassium carbonate (4.70 g, 34.0 mmol, 2 eq) were added to dry tetrahydrofuran (250 ml) under an atmosphere of argon. The mixture was heated to reflux and left at that temperature for 36 hours. After cooling to room temperature, water was added and the mixture was extracted three times with MTBE. The combined organic fractions were washed with brine, dried over magnesium sulfate and evaporated to dryness. After purification by column chromatography (hexane/dichloromethane 2:1, then 3:2), the title compound **9** (4.09 g, 7.8 mmol, 46%) was obtained as colorless solid.

$^1\text{H NMR}$  (400 MHz,  $\text{CDCl}_3$ ):  $\delta = 7.42 - 7.15$  (*m*, 18H, Aryl-*H*),  $4.53$  (*s*, 4H,  $\text{CH}_2$ ),  $3.51$  (*s*, 2H,  $\text{CH}_2$ ),  $2.42 - 2.25$  (*m*, 4H,  $\text{CH}_2$ );  $^{13}\text{C NMR}$  (100 MHz,  $\text{CDCl}_3$ ):  $\delta = 144.7, 139.4, 138.3, 129.6, 128.9, 127.9, 129.4, 126.7, 67.0, 45.6, 35.7, 31.7, 30.6$ ; Anal calcd. for  $\text{C}_{30}\text{H}_{28}\text{Cl}_2\text{S}_2$ : C 68.82, H 5.39; found: C 67.93, H 5.47.

### [Et-G0.STrt] dendron

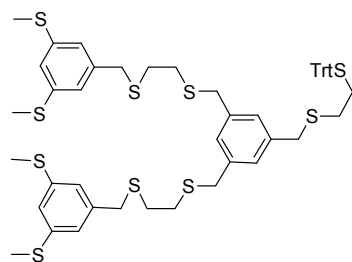


(3,5-Bis(chloromethyl)benzyl)(2-(tritylthio)ethyl)sulfane (**9**) (2.26 g, 4.3 mmol, 1 eq) was dissolved in dry *N,N*-dimethylformamide (30 ml) under an atmosphere of argon. Sodium methanethiolate (666 mg, 9.5 mmol, 2.2 eq) was added and the mixture was left stirring for 2 hours at room temperature. MTBE was added and the solution was extracted 4 times with water. After washing with brine and drying with magnesium sulfate, the solvent was removed. Purification by column chromatography (hexane/dichloromethane 2:3, then 1:2) gave the

**[Et-G0.STrt]** dendron (2.06 g, 3.8 mmol, 88%) as colorless oil, which slowly solidifies at 4°C.

<sup>1</sup>H NMR (400 MHz, CDCl<sub>3</sub>): δ = 7.44 – 7.18 (*m*, 15H, Aryl-*H*), 7.11 (*br*, 1H, Aryl-*H*), 7.02 (*br*, 2H, Aryl-*H*), 3.61 (*s*, 4H, CH<sub>2</sub>H), 3.50 (*s*, 2H, CH<sub>2</sub>), 2.42 – 2.25 (*m*, 4H, CH<sub>2</sub>), 1.97(*s*, 6H, CH<sub>3</sub>); <sup>13</sup>C NMR (100 MHz, CDCl<sub>3</sub>): δ = 145.1, 139.2, 138.9, 130.0, 128.6, 128.4, 128.3, 127.1, 67.4, 38.5, 36.4, 32.2, 30.9, 15.4; Anal calcd. for C<sub>32</sub>H<sub>34</sub>S<sub>4</sub>: C 70.28%, H 6.27; found: C 70.22%, H 6.23.

### **[Et-G1.STrt]** dendron



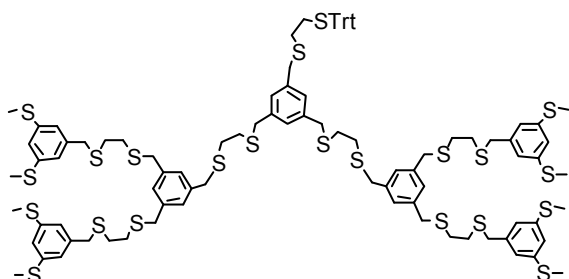
The G0 dendron **[Et-G0.STrt]** (1.416 g, 2.6 mmol, 2.05 eq) and triethylsilane (619 μl, 451.6 mg, 3.9 mmol, 3.08 eq) were dissolved in dichloromethane (15 ml). Trifluoroacetic acid (600 μl, 4% v/v) was slowly added under stirring, which was maintained for further 15 minutes after the addition. A saturated aqueous solution of sodium hydrogen carbonate was then added to quench the reaction. After the gas formation had ceased, the two phases were separated and the aqueous phase was washed twice with dichloromethane. The combined organic fractions were dried over magnesium sulfate, filtered and evaporated to dryness.

The crude thiol was then dissolved in dry tetrahydrofuran (10 ml) under an atmosphere of argon together with (3,5-bis(chloromethyl)benzyl)(2-(tritylthio)ethyl)sulfane (**9**) (657 mg, 1.25 mmol, 1 eq) and sodium hydride (60% in mineral oil, 210 mg, 5.2 mmol, 4.1 eq) was added. The mixture was left stirring for 2 hours at room temperature. Water was then added to quench the reaction and the mixture was extracted 3 times with MTBE. The combined organic fractions were washed with brine, dried over magnesium sulfate, filtered and evaporated to dryness. After purification by column chromatography (dichloromethane, then hexane/dichloromethane 2:3 with 2 % ethyl acetate), the first generation dendron **[Et-G1.STrt]** (1.162 g, 1.10 mmol, 88%) was obtained as colorless oil.

<sup>1</sup>H NMR (400 MHz, CDCl<sub>3</sub>): δ = 7.42 – 7.20 (*m*, 15H, Aryl-*H*), 7.13 – 7.08 (*m*, 7H, Aryl-*H*), 7.00 (*br*, 2H, Aryl-*H*), 3.67 (*s*, 4H, CH<sub>2</sub>), 3.63 (*br*, 12H, CH<sub>2</sub>), 3.47 (*s*, 2H, CH<sub>2</sub>), 2.56 (*br*, 8H, CH<sub>2</sub>), 2.42 – 2.23 (*m*, 4H, CH<sub>2</sub>), 1.98 (*s*, 12H, CH<sub>3</sub>); <sup>13</sup>C NMR (100 MHz, CDCl<sub>3</sub>): δ =

145.1, 139.3, 139.2 (2×), 139.0, 130.0, 128.6, 128.5, 128.4 (2×), 128.3, 127.1, 68.9, 38.5, 36.6, 36.5, 36.3, 32.2, 31.7, 31.6, 31.0, 15.5; Anal calcd. for C<sub>56</sub>H<sub>66</sub>S<sub>10</sub>: C 63.47, H 6.28; found: C 62.68, H 6.29.

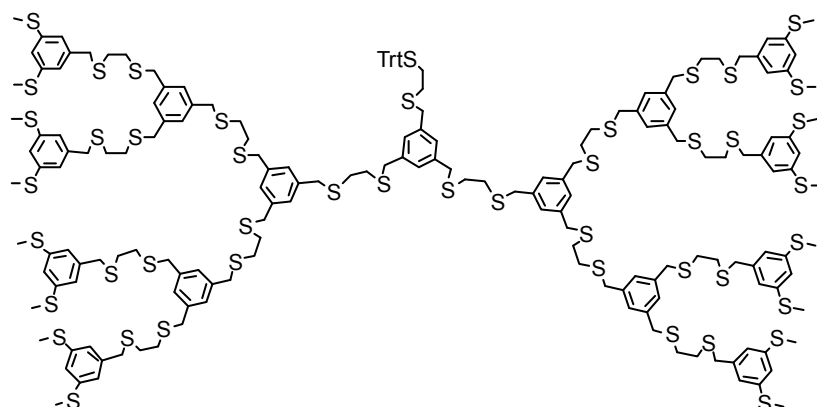
### [Et-G2.STrt] dendron



The trityl protected first generation dendron [Et-G1.STrt] (452.5 mg, 0.43 mmol, 2.2 eq) and triethylsilane (103  $\mu$ l, 75 mg, 0.65 mmol, 3.3 eq) were dissolved in dichloromethane (8 ml). Trifluoroacetic acid (320  $\mu$ l, 4% v/v) was slowly added under stirring, which was maintained for further 15 minutes after the addition. A saturated aqueous solution of sodium hydrogen carbonate was then added to quench the reaction. After the gas formation had ceased, the two phases were separated and the aqueous phase was washed twice with dichloromethane. The combined organic fractions were dried over magnesium sulfate, filtered and evaporated to dryness.

The crude thiol was then dissolved in dry tetrahydrofuran (20 ml) under an atmosphere of argon together with (3,5-bis(chloromethyl)benzyl)(2-(tritylthio)ethyl)sulfane (**9**) (101.6 mg, 0.19 mmol, 1 eq) and sodium hydride (60% in mineral oil, 35 mg, 0.86 mmol, 4.4 eq) was added. The mixture was left stirring for 2 hours at room temperature. Water was then added to quench the reaction and the mixture was extracted 3 times with MTBE. The combined organic fractions were washed with brine, dried over magnesium sulfate, filtered and evaporated to dryness. After purification by column chromatography (hexane/dichloromethane 2:3 with 4 % ethyl acetate), the second generation dendron [Et-G2.STrt] (305.0 mg, 0.15 mmol, 79%) was obtained as colorless oil.

<sup>1</sup>H NMR (400 MHz, CDCl<sub>3</sub>):  $\delta$  = 7.44 – 7.15 (*m*, 15H, Aryl-*H*), 7.13 – 7.08 (*m*, 19H, Aryl-*H*), 7.00 (*br*, 2H, Aryl-*H*), 3.69 – 3.61 (*m*, 40H, CH<sub>2</sub>), 3.46 (*s*, 2H, CH<sub>2</sub>), 2.59 – 2.54 (*m*, 24H, CH<sub>2</sub>), 2.42 – 2.23 (*m*, 4H, CH<sub>2</sub>), 1.97 (*s*, 24H, CH<sub>3</sub>); <sup>13</sup>C NMR (100 MHz, CDCl<sub>3</sub>):  $\delta$  = 144.6, 138.7 (2×), 138.6, 138.5, 129.4, 128.1, 128.0 (2×), 127.9, 127.8, 126.6, 66.9, 38.0, 35.8, 31.7, 31.2, 31.1, 30.5, 15.0; Anal calcd. for C<sub>104</sub>H<sub>130</sub>S<sub>22</sub>: C 59.89, H 6.28; found: C 59.19, H 6.20.

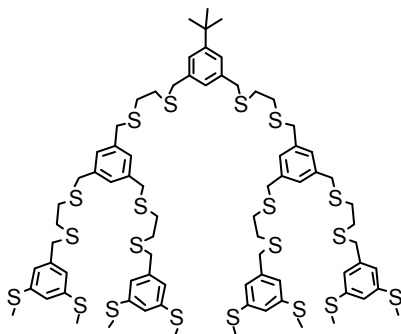
**[Et-G3.STrt] dendron**

The trityl protected second generation **[Et-G2.STrt]** (182.0 mg, 0.09 mmol, 2.2 eq) and triethylsilane (21  $\mu$ l, 15.2 mg, 0.13 mmol, 3.3 eq) were dissolved in dichloromethane (5 ml). Trifluoroacetic acid (200  $\mu$ l, 4% v/v) was slowly added under stirring, which was maintained for further 15 minutes after the addition. A saturated aqueous solution of sodium hydrogen carbonate was then added to quench the reaction. After the gas formation had ceased, the two phases were separated and the aqueous phase was washed twice with dichloromethane. The combined organic fractions were dried over magnesium sulfate, filtered and evaporated to dryness.

The crude thiol was then dissolved in dry tetrahydrofuran (20 ml) under an atmosphere of argon together with (3,5-bis(chloromethyl)benzyl)(2-(tritylthio)ethyl)sulfane (**9**) (20.7 mg, 0.04 mmol, 1 eq) and sodium hydride (60% in mineral oil, 7.2 mg, 0.18 mmol, 4.4 eq) was added. The mixture was left stirring for 1 hour at room temperature. Water was then added to quench the reaction and the mixture was extracted 3 times with ethyl acetate. The combined organic fractions were washed with brine, dried over magnesium sulfate, filtered and evaporated to dryness. After purification by column chromatography (hexane/dichloromethane 1:4 with 4 % ethyl acetate), the third generation Dendron **[Et-G3.STrt]** (121.6 mg, 0.03 mmol, 75%) was obtained as colorless oil.

$^1\text{H NMR}$  (400 MHz,  $\text{CDCl}_3$ ):  $\delta$  = 7.43 – 7.15 (*m*, 15H, Aryl-*H*), 7.13 – 7.08 (*m*, 43H, Aryl-*H*), 7.00 (*br*, 2H, Aryl-*H*), 3.69 – 3.61 (*m*, 88H,  $\text{CH}_2$ ), 3.46 (*s*, 2H,  $\text{CH}_2$ ), 2.59 – 2.54 (*m*, 56H,  $\text{CH}_2$ ), 2.42 – 2.23 (*m*, 4H,  $\text{CH}_2$ ), 1.97 (*s*, 48H,  $\text{CH}_3$ ).

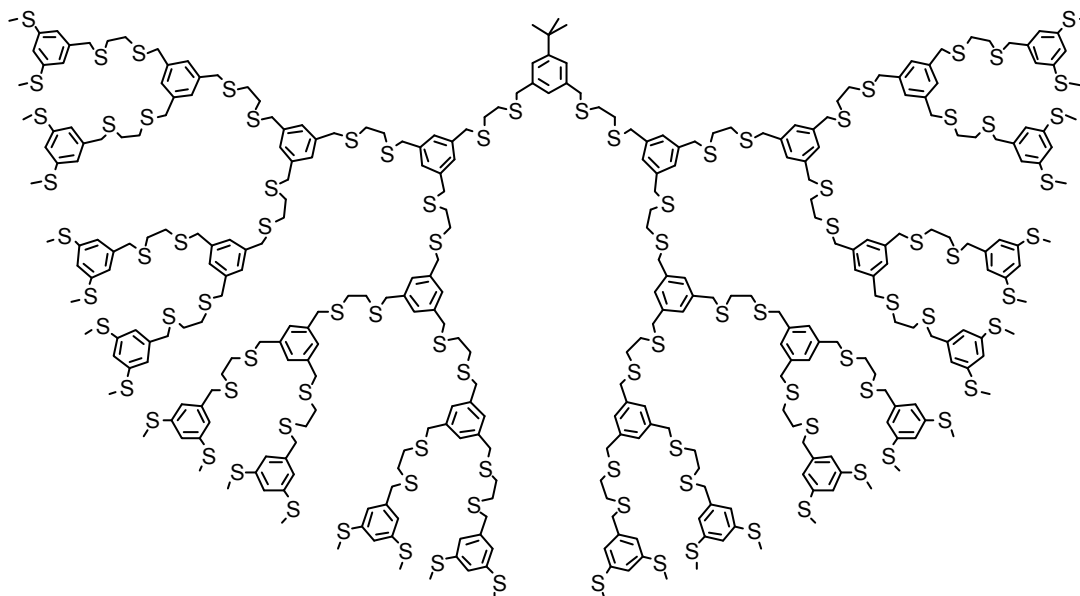


**Et-G2 dendrimer**

The trityl protected first generation dendron [**Et-G1.STrt**] (174.0 mg, 0.16 mmol, 2.1 eq) and triethylsilane (65.5  $\mu$ l, 47.8 mg, 0.41 mmol, 5.4 eq) were dissolved in dichloromethane (4 ml). Trifluoroacetic acid (160  $\mu$ l, 4% v/v) was slowly added under stirring, which was maintained for further 15 minutes after the addition. A saturated aqueous solution of sodium hydrogen carbonate was then added to quench the reaction. After the gas formation had ceased, the two phases were separated and the aqueous phase was washed twice with dichloromethane. The combined organic fractions were dried over magnesium sulfate, filtered and evaporated to dryness.

The crude thiol was then dissolved in dry tetrahydrofuran (10 ml) under an atmosphere of argon together with 1,3-bis(bromomethyl)-5-*tert*-butylbenzene (**4**) (24.7 mg, 0.08 mmol, 1 eq) and sodium hydride (60% in mineral oil, 13 mg, 0.32 mmol, 4.2 eq) was added. The mixture was left stirring for 1.5 hours at room temperature. Water was then added to quench the reaction and the mixture was extracted 3 times with MTBE. The combined organic fractions were washed with brine, dried over magnesium sulfate, filtered and evaporated to dryness. After purification by column chromatography (hexane/dichloromethane 2:3 with 4 % ethyl acetate), the second generation dendrimer **Et-G2** (117.1 mg, 0.07 mmol, 88%) was obtained as colorless oil.

$^1\text{H NMR}$  (400 MHz,  $\text{CDCl}_3$ ):  $\delta$  = 7.17 (*m*, 2H, Aryl-*H*), 7.12 – 7.08 (*m*, 18H, Aryl-*H*), 7.05 (*br*, 1H, Aryl-*H*), 3.69 – 3.61 (*m*, 40H,  $\text{CH}_2$ ), 2.59 – 2.54 (*m*, 24H,  $\text{CH}_2$ ), 1.97 (*s*, 24H,  $\text{CH}_3$ ), 1.29 (*s*, 9H,  $\text{C}(\text{CH}_3)_3$ );  $^{13}\text{C NMR}$  (100 MHz,  $\text{CDCl}_3$ ):  $\delta$  = 151.7, 138.7, 138.5, 137.9, 128.1, 128.0, 127.9, 126.4, 124.7, 38.0, 36.5, 36.1, 36.0, 34.6, 31.3, 31.2, 31.1, 15.0; Anal calcd. for  $\text{C}_{104}\text{H}_{130}\text{S}_{22}$ : C 57.60, H 6.63; found: C 57.42, H 6.53.

**Et-G4 dendrimer**

The trityl protected third generation dendron [**Et-G3.STrt**] (34.1 mg, 8.2  $\mu\text{mol}$ , 2.1 eq) and triethylsilane (3.3  $\mu\text{l}$ , 2.4 mg, 20.6  $\mu\text{mol}$ , 5.3 eq) were dissolved in dichloromethane (1.5 ml). Trifluoroacetic acid (60  $\mu\text{l}$ , 4% v/v) was slowly added under stirring, which was maintained for further 25 minutes after the addition. A saturated aqueous solution of sodium hydrogen carbonate was then added to quench the reaction. After the gas formation had ceased, the two phases were separated and the aqueous phase was washed twice with dichloromethane. The combined organic fractions were dried over magnesium sulfate, filtered and evaporated to dryness.

The crude thiol was then dissolved in dry tetrahydrofuran (20 ml) under an atmosphere of argon together with 1,3-bis(bromomethyl)-5-*tert*-butylbenzene (**4**) (1.2 mg, 3.7  $\mu\text{mol}$ , 1 eq) and sodium hydride (60% in mineral oil, 1.3 mg, 33  $\mu\text{mol}$ , 8.4 eq) was added. The mixture was left stirring for 2 hours at room temperature. Water was then added to quench the reaction and the mixture was extracted 3 times with ethyl acetate. The combined organic fractions were washed with brine, dried over magnesium sulfate, filtered and evaporated to dryness. After purification by column chromatography (hexane/dichloromethane 1:4 with 5 % ethyl acetate), the fourth generation dendrimer **Et-G4** (16.2 mg, 2.1  $\mu\text{mol}$ , 57%) was obtained as colorless oil.

$^1\text{H NMR}$  (400 MHz,  $\text{CDCl}_3$ ):  $\delta$  = 7.19 – 7.05 (*m*, 93H, Aryl-*H*), 3.69 – 3.61 (*m*, 184H,  $\text{CH}_2$ ), 2.59 – 2.54 (*m*, 120H,  $\text{CH}_2$ ), 1.97 (*s*, 96H,  $\text{CH}_3$ ), 1.29 (*s*, 9H,  $\text{C}(\text{CH}_3)_3$ ).

**References**

- [1] W. P. Cochrane, P. L. Pauson, T. S. Stevens, *J. Chem. Soc., C* **1968**, 630.
- [2] R. C. Fuson, B. Freedmann, *J. Org. Chem.* **1958**, *23*, 1161-1166.
- [3] W. R. Chan, D. R. Taylor, C. R. Willis, R. L. Bodden, H.-W. Fehlhaber, *Tetrahedron* **1971**, *27*, 5081-5091.

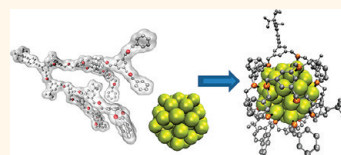
# Scanning the Potential Energy Surface for Synthesis of Dendrimer-Wrapped Gold Clusters: Design Rules for True Single-Molecule Nanostructures

Damien Thompson,<sup>†,\*</sup> Jens P. Hermes,<sup>‡</sup> Aidan J. Quinn,<sup>§</sup> and Marcel Mayor<sup>‡,⊥</sup>

<sup>†</sup>Theory Modelling and Design Centre, Tyndall National Institute, University College Cork, Cork, Ireland, <sup>‡</sup>Department of Chemistry, University of Basel, St. Johanns-Ring 19, CH-4056 Basel, Switzerland, <sup>§</sup>Micro/Nanoelectronics Centre, Tyndall National Institute, University College Cork, Cork, Ireland, and <sup>⊥</sup>Institute of Nanotechnology, Karlsruhe Institute of Technology (KIT), P.O. Box 3640, D-76021 Karlsruhe, Germany

Nanostructured organic–inorganic hybrid materials may be formed *via* self-assembly of organic and inorganic components.<sup>1,2</sup> Surfactant-coated gold nanoparticles (colloidal gold) in particular<sup>3–5</sup> have attracted significant attention in the past decades, and their unique optical and electronic properties have led to technology applications. For example, gold nanoparticles can be used to transfer optical signals in plasmonic devices<sup>6</sup> and to congregate receptor molecules in the liquid-phase sensing<sup>7</sup> used in home pregnancy tests.<sup>8</sup> Current research focuses on emerging applications in nanoelectronics<sup>9,10</sup> and medicine.<sup>11–15</sup> Gold nanoparticles may find use as functional components in printed electronics<sup>16</sup> *via* the integration of synthesized gold nanostructures into lithographically produced structures.<sup>17</sup> In medical diagnostics, the molecular recognition properties of low-diameter gold nanoparticle surfaces make gold particles useful platforms for analyte–receptor interactions,<sup>18,19</sup> while gold particles may also be used for drug delivery applications with (surfactant-controllable) size, surface charge, and shape being the chief parameters for controlling the biological response to medicinal gold complexes.<sup>20</sup> Gold nanoparticles also have numerous current and future applications in, for example, trace analyte detection for security,<sup>21</sup> as well as advanced elements for optoelectronics<sup>22</sup> and information storage devices.<sup>23</sup> A key element in the rational design of gold nanoparticles is the role of ligand conformation and adsorption onto the inorganic surface in order to influence particle growth and assembly. More generally, a molecular-level control of the organic–inorganic interface is required

**ABSTRACT** The formation of true single-molecule complexes between organic ligands and nanoparticles is challenging and requires careful design of molecules with size, shape, and chemical properties tailored for the specific nanoparticle. Here we use computer simulations



to describe the atomic-scale structure, dynamics, and energetics of ligand-mediated synthesis and interlinking of 1 nm gold clusters. The models help explain recent experimental results and provide insight into how multidentate thioether dendrimers can be employed for synthesis of true single-ligand–nanoparticle complexes and also nanoparticle–molecule–nanoparticle “dumbbell” nanostructures. Electronic structure calculations reveal the individually weak thioether–gold bonds ( $325 \pm 36$  meV), which act collectively through the multivalent (multisite) anchoring to stabilize the ligand–nanoparticle complex ( $\sim 7$  eV total binding energy) and offset the conformational and solvation penalties involved in this “wrapping” process. Molecular dynamics simulations show that the dendrimer is sufficiently flexible to tolerate the strained conformations and desolvation penalties involved in fully wrapping the particle, quantifying the subtle balance between covalent anchoring and noncovalent wrapping in the assembly of ligand–nanoparticle complexes. The computed preference for binding of a single dendrimer to the cluster reveals the prohibitively high dendrimer desolvation barrier ( $1.5 \pm 0.5$  eV) to form the alternative double-dendrimer structure. Finally, the models show formation of an additional electron transfer channel between nitrogen and gold for ligands with a central pyridine unit, which gives a stiff binding orientation and explains the recently measured larger interparticle distances for particles synthesized and interlinked using linear ligands with a central pyridine rather than a benzene moiety. The findings stress the importance of organic–inorganic interactions, the control of which is central to the rational engineering and eventual large-scale production of functional building blocks for nano(bio)electronics.

**KEYWORDS:** nanoelectronics · organic–inorganic interfaces · multivalent interactions · molecular dynamics simulations · electronic structure calculations

for any application that couples organic material with metal or semiconductor substrates for integrated bionanoelectronics.<sup>24–26</sup>

Linear thioether ligands have recently been shown to direct the synthesis and interlinking of gold nanoparticles in dichloromethane solvents.<sup>27–30</sup> Gold particles have also been very recently synthesized in the presence of dendritic thioether ligands.<sup>31</sup> The nanoparticles were formed in

\* E-mail: damien.thompson@tyndall.ie.

Received for review November 17, 2011 and accepted March 20, 2012.

Published online March 20, 2012  
10.1021/nn204470g

© 2012 American Chemical Society

the presence of the dendrimer following a protocol developed by Brust as described in ref 31 with  $^1\text{H}$  NMR showing that the particles are solely stabilized by the dendrimer. The phase transfer agent used during the synthesis of the particles was successfully removed by a repeated precipitation and centrifugation protocol, and even the excess of the dendritic ligand was removed by size exclusion chromatography.<sup>31</sup> Understanding and ultimately harnessing the driving forces underlying this ligand-mediated gold nanoparticle synthesis require detailed nanoscale experiments and simulations, and so the focus of the present work is on complementing the experimental synthesis and microscopy characterization,<sup>27–31</sup> using atomic-resolution computer simulations. We focus on the more promising dendritic thioether ligands, which potentially allow very precise control of both covalent and noncovalent ligand stabilization effects in nanoparticle synthesis. The simulations in the present work allow quantification of the forces underlying the assembly of dendrimer–nanoparticle complexes, namely, the multiple (individually weak, reversible) binding interactions that act collectively to give tightly woven self-correcting and self-healing assemblies. By clarifying the atom-scale structure, dynamics, and energetics of complexation, the model may be useful as a computer-aided design tool for the (eventual) generation of libraries of molecular “wrappers” for efficient synthesis of a wide range of building blocks tailored for specific nanoelectronic device applications.

The role of the adsorbed organic molecule in directing the formation of the observed narrow size distribution of  $\sim 1$  nm diameter gold nanoparticles<sup>27–31</sup> is explored *via* a combination of first-principles electronic structure calculations and atomic-resolution molecular dynamics simulations. We use the simulations to address three important questions concerning the synthesis (Figure 1): (1) How stable is a fully bound dendrimer configuration on the nanoparticle surface? Recent experiments show unchanging particle size distributions for the first- and second-generation dendrimers<sup>31</sup> and so suggest that the dendrimers can fully “wrap” the particle. (2) We use the model to measure the binding and dynamics of dendrimers with different central units on the nanoparticle surface. Experiments show a significant difference in interparticle distances for linear ligands with benzene and pyridine central units.<sup>29,30</sup> (3) We measure the relative stabilities of single-dendrimer and double-dendrimer complexes on the nanoparticle. Very recent experiments show predominantly 1:1 dendrimer to particle ratios for the second-generation dendrimer.<sup>31</sup> This suggests the formation of only a very low population of interlinked superstructures containing three or more nanoparticles, once these dendrimers<sup>31</sup> are monofunctionalized and the particles formed in their presence are interlinked using acetylene chemistry.<sup>29,30</sup> Such discrete, regularly sized “dumbbells” may provide a means of

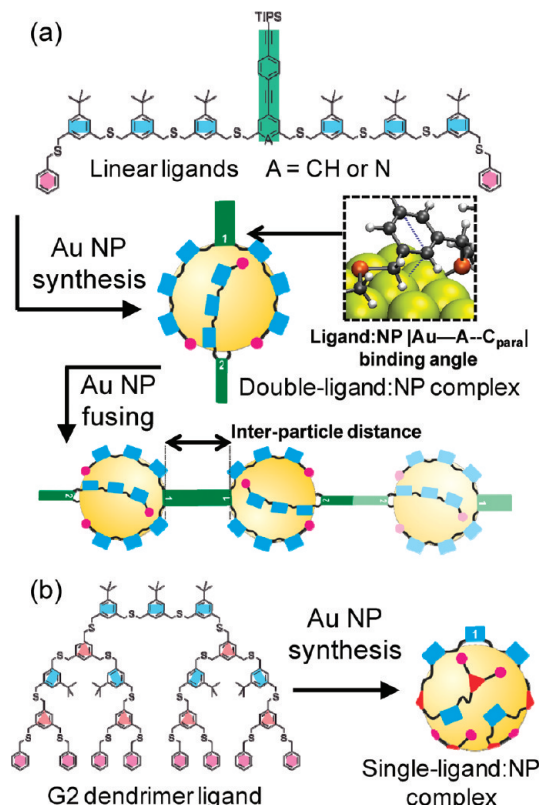


**Figure 1.** Sketch of the ligand-mediated nanoparticle synthesis, showing the key components and structural features. (a) Double-ligand–particle complex formed using linear ligands.<sup>29,30</sup> The ligand–particle binding angle is defined by three atoms as shown: the gold atom between the two gold atoms that bind the central unit sulfurs, and two ligand ring atoms, the carbon of site “A” in benzene (nitrogen in pyridine) and the carbon *para* to A. The multiparticle chain formed *via* acetylene fusing is also shown, with the interparticle distance marked, which depends on both the length of the linker and the binding angle. (b) Single-ligand–particle complex formed using the second-generation dendrimer.<sup>31</sup>

cleanly bridging lithographically defined nanogaps and controlling the electron transport properties of the junction.<sup>32</sup> The computer model confirms and extends the major features observed in the experimental synthesis and characterization of gold nanoparticles stabilized by multidentate thioether ligands, by showing how the organic template structure directs three crucial factors: the individual nanoparticle size distributions, the interparticle distances, and, we predict, the extent of particle interlinking. This new atom-scale detail may inform the synthesis of hybrid organic–inorganic materials with nanostructures and physicochemical properties tailored for specific device applications.<sup>33,34</sup>

## RESULTS AND DISCUSSION

We first describe the electronic structure calculations of thioether–gold bond formation and then present the larger scale molecular dynamics simulations of the room-temperature dichloromethane-solvated dendrimer–nanoparticle complexes. The simulation results are used

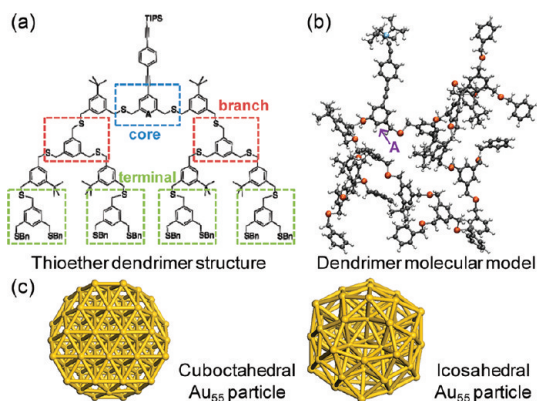


**Figure 2.** (a) Chemical structure of the multidentate thioether dendrimer,<sup>31</sup> with positions of the two core, six branch, and 12 terminal sulfurs marked. Simulations were also performed using dendrimers with the benzene central unit replaced by a pyridine unit,<sup>30</sup> where "A" marks the site of the C–H→N substitution. (b) Dendrimer molecular model, where carbons are colored gray, hydrogen atoms are white, sulfurs are brown, and silicon of the TIPS headgroup is colored blue. This (not yet synthesized) monofunctionalized dendrimer is derived by merging the branch and terminal part of the second-generation dendrimer<sup>31</sup> (panel a) with the core (central unit) of an acetylene-monofunctionalized linear ligand.<sup>29,30</sup> (c) Cuboctahedral and the icosahedral Au<sub>55</sub> clusters (1.2 ± 0.1 nm diameter) used to model the synthesized gold nanoparticles (1.2 ± 0.4 nm diameter<sup>31</sup>).

to rationalize the experimental observations,<sup>28–31</sup> and the combined simulation/experimental data are discussed in relation to the state of the art in hybrid organic–inorganic materials design and synthesis for nanoelectronics, with reference also to more general multivalent ligand–surface interactions<sup>35,36</sup> relevant for nanofabrication,<sup>37</sup> molecular diagnostics,<sup>38</sup> and molecular assembly.<sup>39</sup>

**Computed Thioether–Gold Bond Strengths.** Panels a and b of Figure 2 show the chemical structure and molecular model of the multidentate thioether dendrimer used in the present study. This model was derived from the chemical structure used in recent work<sup>31</sup> including (1) the alternative pyridine central unit as yet only synthesized for the linear ligands<sup>29,30</sup> and (2) the acetylene headgroup required for chemical interlinking<sup>29,30</sup> of the formed dendrimer–particle complexes.<sup>31</sup> Both of these variants are targets of current experiments and allow us to make predictions using the model, while providing insight into some of the recent experimental data.<sup>27–31</sup> Figure 2c shows the nanoparticle shapes used to model the synthesized 1.2 ± 0.4 nm diameter gold nanoparticles,<sup>31</sup> which are represented in the present study by the near-isoenergetic cuboctahedral and icosahedral 55-atom gold (Au<sub>55</sub>) clusters,<sup>40,41</sup> which have calculated diameters of 1.2 ± 0.1 nm. The surface of cuboctahedral Au<sub>55</sub> is composed of eight corner-sharing triangles (111) and six squares (110), while icosahedral Au<sub>55</sub> has 20 equivalent triangular fcc(111)-like faces. Figure 3 summarizes the electronic structure models used to describe bond formation between the thioether

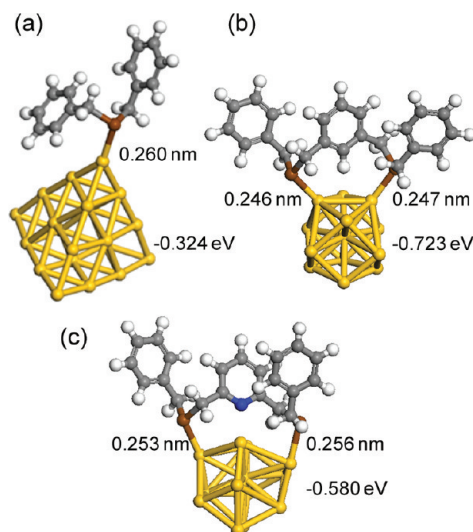


**Figure 3.** Complexes used to calculate the thioether–gold bond strength. (a) *T<sub>d</sub>* tetrahedral Au<sub>20</sub> cluster, with four 10-atom triangular faces exhibiting face-centered cubic (fcc) packing. (b and c) *I<sub>h</sub>* icosahedral Au<sub>13</sub> cluster, which contains 20 three-atom triangles. The same atom representation is used as in Figure 2b. Representative fragments of the dendrimer thioether anchor groups were used as shown: benzyl thioether (panel a) and extended benzene-core (panel b) and pyridine-core (panel c) dithioether moieties. Calculated S–Au bond lengths and molecule binding energies are given.

groups and the gold nanoparticle surface. Given the local nature of the thioether–gold bonding and the computational effort required to compute full ligand–Au<sub>55</sub> complexes,<sup>40–42</sup> we use smaller Au<sub>20</sub> and Au<sub>13</sub> clusters to perform a series of adsorption calculations with different representative dendrimer building blocks and particle (111) and (110) faces to estimate the dendrimer–particle bonding energy per thioether group. As shown by the computed electronic binding energies given in Figure 3, the thioether groups make weak bonds to gold, with an average bond strength of just 325 ± 36 meV averaged over the three representative structures. The similarity in the computed bond strengths indicates only a minor dependence on the fine details of the dendrimer model (size of the representative fragment used for the electronic structure calculation, choice of benzene or pyridine central unit) and the nanoparticle surface geometry ((111) or (110) faces, geometry of the Au–S bonds). The adsorption energy is subchemisorption at approximately 0.3 eV. By comparison, methylthiomethane has a binding energy to gold of approximately 0.5 eV.<sup>43</sup>

The computed thioether bond strength is substantially weaker than a 1.7 eV alkanethiol–gold bond,<sup>44</sup> which has two important consequences for the dendrimer-mediated gold nanoparticle synthesis. First, there is scope for self-correction in the dendrimer–gold complexation with the thioether sulfurs able to distribute themselves on the surface *via* quasi-reversible S–Au bonds so as to obtain favorable

dendrimer conformations. These dendrimer rearrangements on the surface may be accompanied by Au surface diffusion or place-exchange "hopping",<sup>45</sup> which has a very low barrier (<1 eV),<sup>46</sup> that may be further lowered by thioether adsorption. Identification of any consequent dendrimer-directed nanoparticle distortions, defects, or gold adlayer formation<sup>47</sup> would require very high-resolution imaging and/or significantly larger electronic structure calculations, beyond the scope of the present study.

The second important consequence of the computed weak individual thioether–gold bond strengths is that formation of multiple bonds between the nanoparticle and the multivalent dendrimer, in this case a multidentate thioether dendrimer with 20 sulfur anchor groups, will drive the adsorption energy of the complex as a whole toward a more strongly bound, effectively chemisorbed state. Taking the estimate of 325 meV per thioether–gold bond, one fully bound dendrimer or multiple partially bound dendrimers, *e.g.*, two half-bound dendrimers, will provide an effective bond strength of 7 eV, the equivalent of four Au–alkanethiol chemical bonds. The payoff between favorable multivalent attachment and unfavorable dendrimer wrapping penalties (conformational strain plus desolvation costs) may then be used to identify thermodynamically favorable binding modes<sup>48</sup> for the dendrimer–nanoparticle complexes, as described below. The high effective concentration<sup>49,50</sup> of unbound thioether anchor groups close to the nanoparticle surface will drive the complex toward also a *kinetically* stable multivalently bound assembly of the (individually weak) thioether–gold bonds.

Finally, it is important to note that the electronic ligand–particle binding calculations were performed for small benzene/pyridine thioether molecules adsorbed on gold clusters under vacuum at 0 K, which serves as a first approximation to the experimental dichloromethane-solvated dendrimer–nanoparticle structures synthesized in the room-temperature experiments (and modeled explicitly in the present work using classical molecular dynamics). As discussed below, a complex balance of ligand–surface chemical bonding and van der Waals's interactions directs the assembly of the dendrimer-wrapped nanoparticle, and both types of interaction depend on the topography of the nanoparticle surface. Therefore, we extract the estimated bond strength of  $325 \pm 36$  meV over three representative structures; experimentally, we may expect also some complexation geometries with thioether–gold bond strengths outside this range due to, for example, gold surface defects/adatoms and solvent-mediated dendrimer–gold interactions. More details on Au–S bonding calculations, including long-range effects, thermal effects, and a survey of bond strengths as a function of Au coordination in the cluster and sulfur coordination in the molecule, are given in Supporting Information section S1.

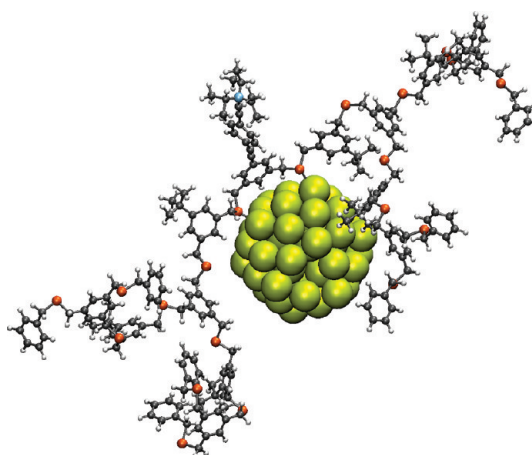


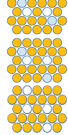
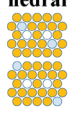
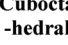
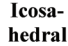
**Figure 4.** Representative dendrimer–gold complex model. In this case the dendrimer is bound using two core thioether–gold bonds with the gold nanoparticle atoms shown as van der Waals's spheres. The complex is immersed in a large box of dichloromethane molecules (11 nm wide), to model the solvated dendrimer–gold complex.

**Computed Dendrimer–Nanoparticle Net Complexation Energies.** Figure 4 shows one representative complex used to describe the structure, dynamics, and energetics of the dendrimer–nanoparticle assembly in dichloromethane. Thirty-six dendrimer-coated gold nanoparticle models (listed in Table 1) were used to determine the stabilities of 1:1 and 2:1 dendrimer–nanoparticle complexes. Their relative stabilities indicate a very low probability for binding of a second dendrimer to exposed areas of some of the 1:1 dendrimer–nanoparticle complexes, providing an explanation for the measured low molecular weight of organic coats on the synthesized nanoparticles.<sup>31</sup> Overall, the atom-scale simulations complement the experiments *via* identification of the principal dendrimer binding modes and thus the ideal dendrimer size required for the dendrimer-mediated gold nanoparticle synthesis.

The net adsorption energy of each solvated dendrimer–gold complex is expressed as the sum of the favorable binding interaction and unfavorable wrapping penalty. The favorable binding interactions for each assembly mode are quantified from the sum of the electronic thioether–gold bonding energies calculated above, which are assumed to be additive,<sup>48</sup> plus the dendrimer–nanoparticle van der Waals interactions. The unfavorable wrapping penalty inherent in dendrimer complexation is estimated as the sum of dendrimer conformational penalties and both dendrimer and gold desolvation penalties, in each case relative to reference solvated but noncomplexed dendrimer and nanoparticle models.

The data in Table 1 show that the net complexation energy fluctuates around zero for all binding modes, indicating a rather flat potential energy surface for dendrimer–particle complexation with many different

**TABLE 1. Computed Dendrimer–Nanoparticle Net Complexation Energies (eV) for a Range of Single-Dendrimer (1:1) and Double-Dendrimer (2:1) Cluster Complexes in Dichloromethane<sup>a</sup>**

Nano-particle shape	Binding mode	Electronic binding	van der Waals binding	Total binding	Dendrimer penalty	Desolvation penalty	Total penalty	Net complexation
<b>Single-dendrimer:nanoparticle complexes</b>								
	<b>Two core</b>	-0.7 (0.1)	-0.2 (0.1)	-0.8 (0.1)	-0.4 (0.5)	+1.0 (0.6)	+0.6 (0.6)	-0.3 (0.6)
		-0.7 (0.1)	-0.1 (0.0)	-0.8 (0.1)	+0.2 (0.6)	+0.3 (0.9)	+0.5 (0.9)	-0.3 (1.0)
	<b>Two core + two branch (configuration A)</b>	-1.3 (0.1)	-0.3 (0.1)	-1.6 (0.1)	-0.1 (0.6)	+1.8 (0.8)	+1.6 (0.8)	0.0 (0.8)
		-1.3 (0.1)	-0.4 (0.1)	-1.7 (0.1)	+0.5 (0.6)	+1.3 (0.9)	+1.8 (0.9)	+0.1 (0.9)
	<b>Two core + two branch (configuration B)</b>	-1.3 (0.1)	-0.3 (0.1)	-1.6 (0.1)	0.0 (0.6)	+1.6 (0.8)	+1.6 (0.8)	0.0 (0.9)
		-1.3 (0.1)	-0.2 (0.1)	-1.5 (0.1)	+0.4 (0.6)	+0.6 (0.9)	+1.0 (0.9)	-0.5 (0.9)
	<b>Two core + two branch (configuration C)</b>	-1.3 (0.1)	-0.3 (0.1)	-1.6 (0.1)	-0.1 (0.6)	+1.6 (0.8)	+1.6 (0.8)	0.0 (0.9)
		-1.3 (0.1)	-0.4 (0.1)	-1.7 (0.1)	+0.1 (0.6)	+1.0 (0.9)	+1.2 (0.9)	-0.5 (0.9)
	<b>Two core + six branch</b>	-2.6 (0.3)	-0.6 (0.1)	-3.2 (0.3)	+0.2 (0.6)	+2.6 (0.8)	+2.7 (0.8)	-0.4 (0.8)
	-2.6 (0.3)	-0.5 (0.1)	-3.1 (0.3)	+0.4 (0.6)	+2.0 (0.9)	+2.4 (0.9)	-0.8 (1.0)	
<b>Two core + six branch + four terminal</b>	-3.9 (0.4)	-0.6 (0.1)	-4.5 (0.4)	-0.4 (0.6)	+4.7 (0.9)	+4.3 (0.9)	-0.3 (1.1)	
	-3.9 (0.4)	-0.7 (0.1)	-4.6 (0.5)	-0.3 (0.6)	+4.5 (0.8)	+4.2 (0.9)	-0.4 (0.9)	
<b>Two core + six branch + twelve terminal</b>	-6.5 (0.7)	-0.8 (0.1)	-7.3 (0.7)	-0.5 (0.6)	+8.0 (0.6)	+7.4 (0.7)	+0.1 (1.0)	
	-6.5 (0.7)	-0.8 (0.1)	-7.3 (0.7)	-0.8 (0.6)	+7.8 (0.9)	+7.1 (0.9)	-0.2 (1.0)	
	<b>Two core</b>	-0.7 (0.1)	-0.1 (0.0)	-0.8 (0.1)	0.0 (0.6)	+0.8 (0.9)	+0.7 (0.9)	0.0 (1.1)
		-0.7 (0.1)	-0.1 (0.0)	-0.8 (0.1)	0.0 (0.6)	+0.8 (1.0)	+0.8 (1.1)	0.0 (1.1)
	<b>Two core + two branch (configuration A)</b>	-1.3 (0.1)	-0.2 (0.1)	-1.5 (0.1)	-0.1 (0.6)	+1.7 (1.0)	+1.6 (1.0)	+0.1 (1.0)
		-1.3 (0.1)	-0.2 (0.0)	-1.5 (0.1)	0.0 (0.6)	+1.3 (0.9)	+1.3 (0.9)	-0.2 (1.1)
	<b>Two core + two branch (configuration D)</b>	-1.3 (0.1)	-0.4 (0.1)	-1.7 (0.1)	0.0 (0.6)	+2.0 (0.8)	+1.9 (0.8)	+0.3 (1.0)
		-1.3 (0.1)	-0.4 (0.1)	-1.7 (0.1)	+0.1 (0.6)	+1.7 (0.9)	+1.8 (0.9)	+0.1 (1.0)
	<b>Two core + six branch</b>	-2.6 (0.3)	-0.4 (0.1)	-3.0 (0.3)	0.0 (0.6)	+2.9 (0.8)	+2.9 (0.8)	-0.1 (1.1)
	-2.6 (0.3)	-0.4 (0.1)	-3.0 (0.4)	-0.2 (0.6)	+3.1 (0.9)	+2.9 (0.9)	-0.2 (1.1)	
<b>Two core + six branch + four terminal</b>	-3.9 (0.4)	-0.6 (0.1)	-4.5 (0.4)	-0.4 (0.6)	+4.8 (0.8)	+4.4 (0.8)	-0.1 (1.0)	
	-3.9 (0.4)	-0.6 (0.1)	-4.5 (0.4)	-0.4 (0.9)	+4.4 (0.8)	+4.1 (0.9)	-0.4 (1.2)	
<b>Double-dendrimer:nanoparticle complexes</b>								
	<b>Two core</b>	-1.3 (0.1)	-0.4 (0.1)	-1.7 (0.1)	-1.2 (0.8)	+3.8 (1.1)	+2.6 (1.1)	+0.9 (1.3)
		-1.3 (0.1)	-0.2 (0.0)	-1.5 (0.1)	-0.3 (1.0)	+2.5 (1.5)	+2.2 (1.5)	+0.6 (1.7)
	<b>Two core + two branch (configuration D)</b>	-2.6 (0.3)	-0.7 (0.1)	-3.3 (0.3)	-1.7 (1.0)	+6.4 (1.5)	+4.6 (1.5)	+1.3 (1.8)
	-2.6 (0.3)	-0.7 (0.1)	-3.3 (0.3)	-1.5 (1.0)	+6.0 (1.5)	+4.5 (1.5)	+1.2 (1.8)	
<b>Two core + six branch</b>	-5.2 (0.6)	-0.9 (0.1)	-6.1 (0.6)	-3.1 (1.0)	+11.0 (1.4)	+7.8 (1.4)	+1.8 (1.7)	
	-5.2 (0.6)	-0.9 (0.1)	-6.1 (0.7)	-3.2 (1.0)	+10.6 (1.4)	+7.5 (1.4)	+1.4 (1.8)	
	<b>Two core</b>	-1.3 (0.1)	-0.3 (0.1)	-1.6 (0.1)	-2.2 (1.0)	+5.5 (1.4)	+3.2 (1.4)	+1.6 (1.8)
		-1.3 (0.1)	-0.4 (0.1)	-1.7 (0.2)	-1.5 (1.0)	+4.4 (1.4)	+2.9 (1.4)	+1.2 (1.8)
	<b>Two core + two branch (configuration D)</b>	-2.6 (0.3)	-0.4 (0.1)	-3.0 (0.4)	-1.9 (1.0)	+6.1 (1.7)	+4.2 (1.7)	+1.2 (1.9)
	-2.6 (0.3)	-0.6 (0.1)	-3.3 (0.3)	-1.7 (1.0)	+6.4 (1.5)	+4.8 (1.6)	+1.6 (1.9)	
<b>Two core + six branch</b>	-5.2 (0.6)	-0.8 (0.1)	-6.0 (0.6)	-2.3 (1.0)	+9.4 (1.2)	+7.1 (1.3)	+1.1 (1.9)	
	-5.2 (0.6)	-0.8 (0.1)	-6.0 (0.6)	-2.5 (1.0)	+10.1 (1.3)	+7.6 (1.3)	+1.6 (1.8)	

<sup>a</sup>For each binding mode, the computed energies for the dendrimer with benzene central unit is given in the top row, with the corresponding pyridine-core dendrimer values given underneath. Structure-averaged uncertainty (standard deviation) for each energy is given in parentheses. Electronic binding energies were calculated as described in Figure 3 and supporting text, with further details in Supporting Information section S1.3. The other terms were computed from the final 5 ns (2000 structures) of 10 ns room-temperature molecular dynamics for each complex. A minus sign indicates net stabilization of the complex relative to reference noncomplexed states. Rounding all energy values to one decimal place gives in some cases apparent discrepancies of 0.1 eV between totals and their components. Sketched in the insets are binding configurations **A–D** on the gold cluster surface, with core binding sites colored white and branch binding sites colored blue. The binding modes refer to the extent of thioether–gold bonding and are described using the dendrimer unit nomenclature given in Figure 2a.

competing binding modes. Each binding configuration will have a population distribution scaled according to its range of net complexation energies. Examination of the mean net complexation energies for single- and double-dendrimer complexes,  $E_1$  and  $E_2$ , respectively, averaged over all structures and plotted in Figure 5, is instructive. The plot indicates a sharp destabilization for double- vs single-dendrimer complexation to the nanoparticle, with an estimated mean barrier to double-dendrimer binding,  $E_2 - E_1 \approx 1.5 \pm 0.5$  eV,

obtained by averaging over all the single- and double-dendrimer data points in Figure 5. Examination of the energy components in Table 1 shows that this barrier arises principally from increased wrapping penalties in the double-dendrimer complexes, which are roughly double the value for single-dendrimer complexes. Conversely, the dendrimer–gold van der Waals binding energies show little dependence on the number of bound dendrimers, comparing single- and double-dendrimer complexes with similar overall numbers of



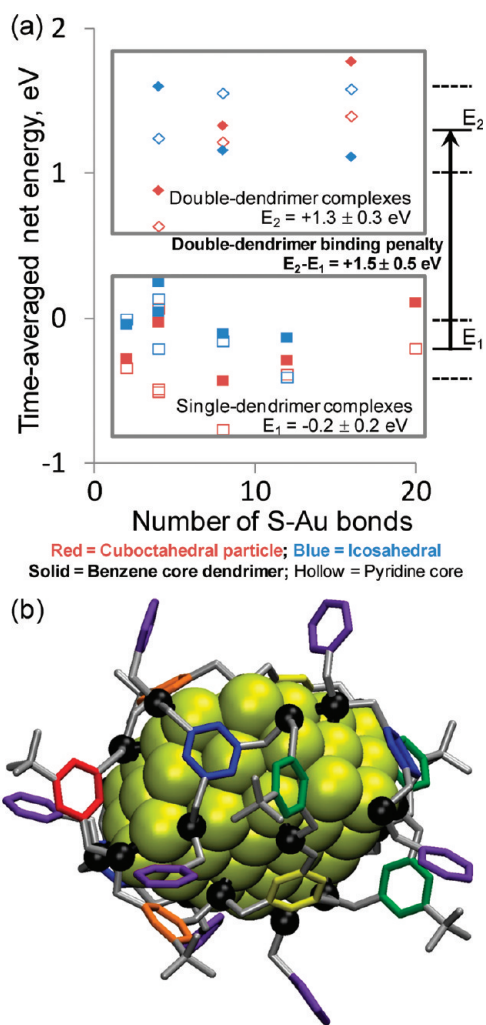


Figure 5. (a) Computed time-averaged net complexation energies for single- and double-dendrimer–nanoparticle complexes with increasing numbers of gold–thioether bonds. Data in red are for the cuboctahedral particle, and data in blue are for the icosahedral particle. Solid and hollow data points are used for the dendrimers with benzene and pyridine central units, respectively. The gray boxes show the clustering of data points for single- and double-dendrimer complexes, with the arrow showing the  $1.5 \pm 0.5$  eV barrier for binding of a second dendrimer. (b) One representative computed single-dendrimer–gold complex. In this picture the dendrimer carbon backbone is shown as gray sticks and thioether sulfurs are black spheres. Hydrogen atoms and the dichloromethane solvent molecules are omitted for clarity. Phenyls are colored according to the visible spectrum, starting from the central unit (red) and radiating outward through to the terminal groups (violet).

S–Au bonds. Similarly, the spread in the data points in terms of particle shape, central unit, and binding configurations (where configurations **A**, **B**, **C**, and **D** denote the alternative surface grafting schemes sketched in the inset figures in Table 1) is generally  $<1$  eV for each binding extent.

The major driver toward single-dendrimer complexes then is the enlarged desolvation contribution that mitigates against binding of the second dendrimer. As shown in Table 1, the net desolvation cost is

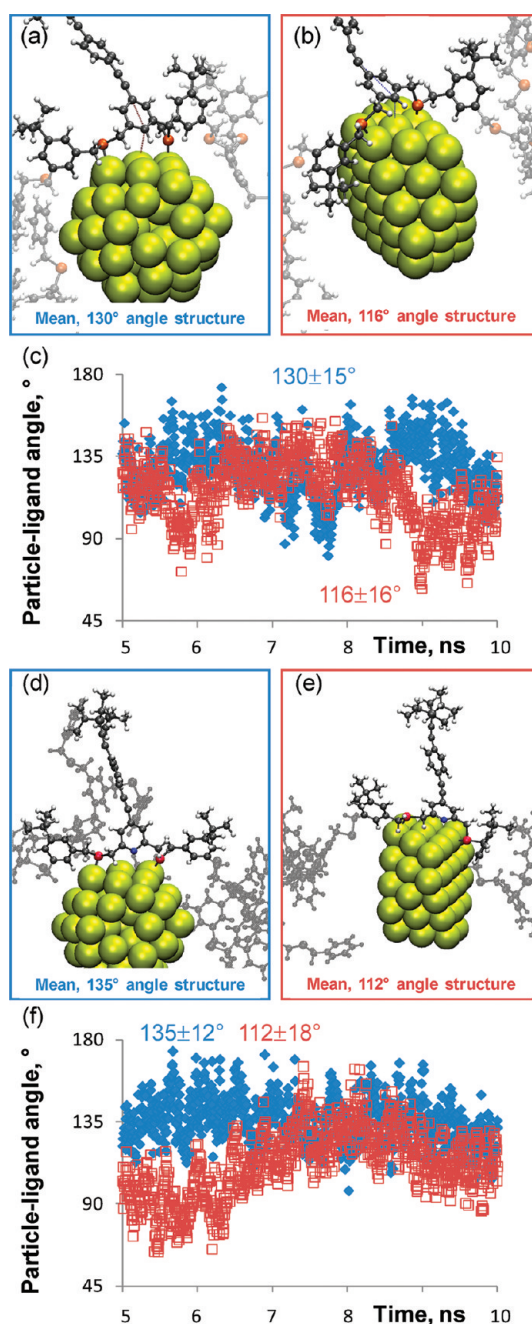


Figure 6. Computed ligand–nanoparticle complexation geometries. (a and b) Representative structures formed using the dendrimer with the benzene central unit, with timelines (c) showing the angle formed between the nanoparticle surface and the dendrimer central unit (as sketched in Figure 1). Data in blue are for the icosahedral particle, and data in red are for the cuboctahedral particle, with timelines showing values sampled over the final 5 ns of 10 ns molecular dynamics trajectories. (d and e) Structures formed with the pyridine central unit and (f) angle timelines. Only the two core sulfurs are bound to the nanoparticle surface in order to allow direct comparison of linear and dendritic ligands; the complexation geometries do not change significantly upon connection of more or all sulfurs.

partially offset by dendrimer “penalties” that become negative for the double-dendrimer–particle complexes and, hence, provide an additional stabilizing

dendrimer energy due to favorable van der Waals interactions between the two dendrimers. The net total penalty however remains large and positive, shifting the double-dendrimer complexes to net positive time-averaged complexation energies, meaning that they will constitute a minor state in the synthesis, in agreement with the experimental microscopy and thermogravimetric data.<sup>31</sup> The synthesis thus “self-terminates” in the majority of cases at the 1:1 dendrimer–gold complexes. Future experiments will fuse the complexes *via* diacetylene bond formation to form 2:2 dimer complexes, or “dumbbells”.<sup>29,30</sup> The computed barrier to binding two dendrimers on one gold cluster (2:1) and hence the small number of states with interlinked  $2n:n$  superstructures predict a very low population of multi-particle networks of trimeric and higher order structures.

In summary, the energetic data in Table 1 show that the dendrimer desolvation energy dictates the number of ligands comprising the moderately polar nanoenvironment of thioether groups in which the gold nanoparticle is stabilized in bulk dichloromethane. Hence it may prove possible to tune the extent of ligand coverage by using solvents of different dielectric constant and/or different ligand anchor groups. It may prove possible to direct the nanoparticle size by tuning also with respect to the desolvation energy of the nanoparticle itself. The information provided by chemical bonding/fusing in this directed assembly is reminiscent of the chemical scission step used between successive rounds of spontaneous assembly/wrapping that provides control of collagen synthesis in complex, multiphase biological environments.<sup>51</sup> Routes to manipulate and ultimately control directed assembly in dendrimer-mediated nanoparticle synthesis could allow for simultaneous production of a wide variety of nanoparticle complexes of different type, size, and shape stabilized by different types and numbers of ligands. In the nearer term the attainment of such control could aid development of ultrasensitive and specific sensing of target molecules for medical diagnostics and therapeutics. Further details on calculated dendrimer–gold wrapping dynamics are given in the Supporting Information. Section S2 describes the more open dendrimer conformations but more solvent-shielded gold complex structures formed in methanol, a more polar solvent than the dichloromethane used in the experiments. Section S3 shows that wrapping *via* binding through core and then peripheral sulfurs is energetically favored over an alternative “feet first” orientation. Section S4 shows that wrapping of a larger 1.4 nm cluster, Au<sub>69</sub>, shows a similar balance between wrapping and desolvation forces, with a slightly better, ~1 eV stabilization of the complex due to reduced desolvation penalties for the more splayed dendrimer conformation on the larger particle.

#### Structural Features of Dendrimer-Coated Gold Nanoparticles.

In contrast to the dendrimers, the linear ligands were already monofunctionalized and used to couple

nanoparticles to superstructures.<sup>29,30</sup> The models of functional dendrimers are now used to explain the differences in interparticle spacing found for linear ligands, as we assume the geometry of the central unit, either a pyridine or benzene moiety, does not depend on the ligand structure. For this simulation only the central two thioethers were bound to the nanoparticle. Even if more thioethers are bound to the surface, the computed angle does not change. This nicely enables the comparison of linear and dendritic ligands. Ligand–particle complexation geometries were computed and are shown in Figure 6 with representative structures and timelines showing the angle formed between the plane of the central unit benzene (or pyridine) and the gold surface. The ligand–particle binding angle (sketched in Figure 1) is the angle formed between the plane of the ligand central ring and the gold surface. The computed angles are used to calculate the interparticle distances by simply multiplying the length of the calculated OPE-type linker, 2.8 nm, and the cosine of the measured time-averaged tilt of the core-to-particle angle away from an ideal, perpendicularly oriented central unit (which would be 180°, as sketched in Figure 1). Interparticle distances of  $1.8 \pm 0.5$  and  $2.0 \pm 0.4$  nm were obtained for icosahedral particles with benzene and pyridine central units, respectively. For the cubo-octahedral particle the distances are  $1.2 \pm 0.7$  and  $1.0 \pm 0.8$  nm. The complete range of experimentally measured interparticle distances for linear acetylene-functionalized octadentate thioether ligands is 0.7–3.1 nm,<sup>30</sup> peaking at  $1.5 \pm 0.5$  nm for the benzene central unit (ligand B2 in ref 30) and  $2.5 \pm 0.3$  nm for the pyridine moiety (P2 in ref 30). The computed angles are thus consistent with the observed interparticle distances<sup>30</sup> and span the full range of observed distances (for a freely rotating core group; the quantum mechanical origin of the pyridine constraint that gives the observed peak shift to 2.5 nm<sup>30</sup> is discussed below), indicating that a mixture of nanoparticle shapes is fabricated. Cubo-octahedral gold particles are ~1 eV less stable than icosahedral particles,<sup>41</sup> and so taken together, the calculations and experiments suggest that the gold clusters produced in dendrimer-mediated synthesis may show deviations from perfect crystallinity. Furthermore, gold atom migration to “fill” the dendrimer wrapper *via* gold adlayer formation may be enabled by the weak individual thioether–gold chemical bonds (Figure 3) and, from the energetic data in Table 1, may be expected to give mutually compensating van der Waals and desolvation interactions. This would provide a significant population of nanoparticles that are slightly larger than the  $1.2 \pm 0.1$  nm Au<sub>55</sub> clusters, in agreement with the broader shoulders at higher diameters in the measured nanoparticle size distributions.<sup>29–31</sup>

The computed ligand–particle angles show a negligible dependence on central unit type, benzene or pyridine (Figure 6), indicating that the experimentally

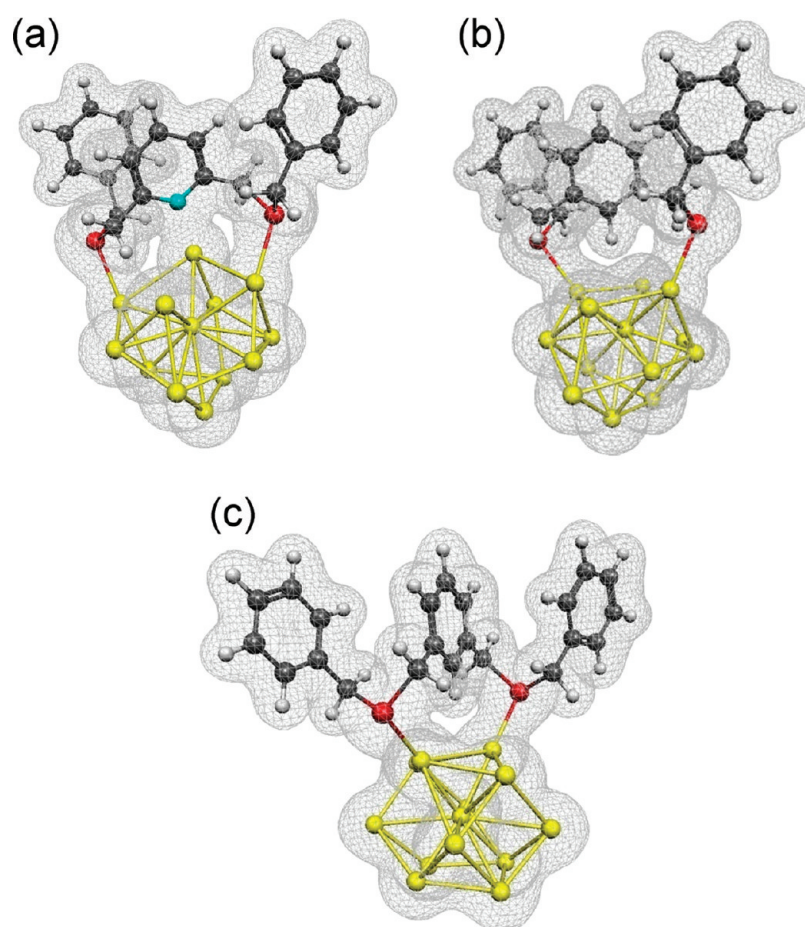


**Figure 7.** (a) The three charge transfer channels for pyridine thioether surface adsorption. (b and c) The two charge transfer channels for benzene thioether adsorption, which features no binding through the benzene central unit. Panel (b) shows the structure formed by replacing the pyridine moiety in the gold-bound pyridine thioether structure with benzene and reoptimizing the complex, while panel (c) shows an alternative benzene dithioether binding mode. Electron density maps (isodensity  $0.001 \text{ e/au}^3$ ) were calculated from the electronic structures described in the text.

observed core-dependent interparticle separations<sup>30</sup> do not originate primarily from differences in noncovalent interactions with the particle surface, as modeled in the molecular dynamics simulations. Rather, as shown in Figure 7, the origin of the different interparticle separations is largely electronic. Figure 7 shows the three charge transfer channels for pyridine thioether surface adsorption, with charge donation of  $2 \times 0.11$  electron charges from the sulfur sites ( $S_{2p} \rightarrow Au_{7d}$ ) and a small back-donation from the surface of 0.04 electron charges to the nitrogen site ( $Au_{7d} \rightarrow N_{2p}$ ). These degrees and sites of charge transfer were estimated from natural population analysis<sup>52</sup> of the computed electronic structures in Figure 7, which are the two dithioether structures from Figure 3 and also an additional control simulation that replaced the central pyridine moiety of pyridine dithioether with benzene and reoptimized the complex. Conversely, only two charge transfer channels exist for benzene thioether adsorption, which features charge donation of  $2 \times 0.16 \text{ e}^-$  from the two sulfur sites but *no* bonding through the benzene central unit.

This striking difference in reactivity and hence binding geometry for ligands with benzene and pyridine central units is further explained by analysis of the local softness,<sup>53</sup> which measures the nucleophilicity and electrophilicity of atoms in the adsorbate molecules. The computed local softness indices  $s(r)$  indicate as expected highly reactive thioether sites with sulfur electron-donor powers  $s^-(r)$  of 0.09 and 0.10 au each in benzene and pyridine dithioether, respectively. All other sites exhibit negligible  $s^-(r)$  values,  $\leq 0.01$  au. On the other hand computed local electrophilicity indices show very delocalized electron-acceptor sites in benzene dithioether with sulfurs exhibiting  $s^+(r) = 0.02$  au and all other atoms  $\leq 0.01$  au, while pyridine dithioether on the other hand shows  $s^+(r) = 0.04$  au on nitrogen, 0.02 au on the *ortho* and *para* ring carbons, and 0.02 au on sulfurs, with all other atoms  $\leq 0.01$  au. Hence the flexible central unit for benzene-based ligands compared with the stiff, more immobilized central unit for pyridine-based ligands manifests itself in the larger interparticle distances measured for linear ligands with pyridine central units.<sup>30</sup> As this difference

was explained just by using the two core sulfurs of the ligand, we are optimistic that we can transfer the experimental finding to future interlinking reactions of functional nanoparticles stabilized by dendrimers.

## CONCLUSIONS

The present study provides the atom-scale mechanism underlying ligand-mediated gold nanoparticle synthesis. The computational analysis based on dendrimer–nanoparticle binding vs wrapping penalties explains some key results from the experimental synthesis and characterization. Namely, the observed particle size distribution ranges,<sup>29–31</sup> the 1:1 dendrimer to particle ratio found for the second-generation dendrimer,<sup>31</sup> the lack of dependence of nanoparticle size on dendrimer generation,<sup>31</sup> and the control of interparticle distance distributions found for nanoparticles stabilized and interlinked by linear thioether ligands.<sup>30</sup> We also use the calculated structures to predict the formation of discrete gold nanoparticle dumbbells upon future diacetylene coupling of monofunctional nanoparticles. More generally, the calculated properties may be useful for rational design of novel dendrimer structures with chemical structures and stereochemistry optimized for the

production of nanoparticle size and shape distributions as required for specific nanoelectronic device components. In the longer term, we hope that the data will contribute toward the atom-scale engineering of organic molecule-based “wrappers” for the development of building blocks with highly controllable electronic properties.

Further simulation and experimental studies will provide more details on the role of nanoparticle surface effects in ligand-directed nanoparticle synthesis, including gold atom defects, gold diffusion, and formation of gold adlayers. Rational control of the organic–inorganic interaction is key, and so deeper understanding of the atom-scale features of the interfaces in hybrid superstructures will aid efforts to design libraries of organic wrappers. Further scientific and technological advances in the application of low-dimensional nanostructures as device components depend on the ability to organize them in complex one- or multidimensional functional architectures, and so atomic-scale descriptions will continue to guide syntheses and speed up development of new materials for next-generation applications in electronics, health, and energy.

## MATERIALS AND METHODS

This section contains further technical details on the simulation protocols used; the main features of the models were summarized at the beginning of the Results section.

**Electronic Structure Calculations.** The cuboctahedral Au<sub>55</sub> nanoparticle was generated from the bulk Au crystal structure, and its electronic structure calculated using the Gaussian03 code<sup>54</sup> with the B3LYP<sup>55</sup> hybrid Hartree–Fock–density functional theory (DFT) wave function and the relativistic LANL2DZ basis set. The geometry of the icosahedral particle, generated using the same protocol as described above, was kindly provided by Françoise Remacle from an earlier study.<sup>41</sup> To quantify the strength of ligand anchoring on the gold nanoparticle surface, smaller representative models were used to describe the local thioether–gold interaction, as shown in Figure 3. The tetrahedral Au<sub>20</sub> cluster has four 10-atom fcc (111) faces, and the icosahedral Au<sub>13</sub> cluster has a rougher local arrangement of gold atoms, containing 20 three-atom triangles with a dihedral angle of 138.19° between planes, while benzyl thioether together with extended benzene-core and pyridine-core dibenzyl thioether moieties represents the local dendrimer molecular structure around the thioether sulfur binding sites. The adsorbate molecules and molecule–surface complexes were described with the B3LYP wave function and a large valence double- $\zeta$  polarized basis set named 6-31G(d,p) for all atoms other than gold, which required the relativistic LANL2DZ basis set. The three models shown in Figure 3 gave stable binding configurations *via* nuclear relaxation to root-mean-square (rms) atomic forces and displacements below 0.0003 and 0.0012 au, respectively. The electronic binding energy was calculated in the usual way, by subtracting the electronic energies of the optimized isolated molecule and cluster from that of the molecule–cluster complex. Further details on the Au–S bond strength estimate are given in Supporting Information section S1.3. Local softness indices  $s(r)$ <sup>53</sup> were calculated from the product of the molecular softness  $S$  (the inverse of half the HOMO–LUMO gap;  $S$  values of 0.37 and 0.39 au respectively

were computed for benzene and pyridine thioether) and atom-sited Fukui functions obtained by subtracting natural population analysis (NPA)<sup>52</sup> charges in neutral and cationic/anionic benzene and pyridine dithioether molecules to identify strong electron donor/acceptor sites. The electron density surfaces shown in Figure 7 were produced using MOLEKEL Unix version 4.3.<sup>56</sup>

**Molecular Dynamics Simulations.** The electronic structure of the dichloromethane (DCM) solvent and thioether-based dendrimers was described using existing force field data.<sup>57,58,48</sup> A total of 12 912 DCM molecules formed a stable cubic box of edge length  $11.16 \pm 0.01$  nm, following 10 ns of constant pressure temperature dynamics with periodic boundary conditions. The corresponding volume per molecule of  $0.11 \text{ nm}^3$  gives a density of  $1.30 \text{ g} \cdot \text{cm}^{-3}$ , in good agreement with the experimental value of  $1.33 \text{ g} \cdot \text{cm}^{-3}$ , and gives computed DCM radial distribution functions (not shown) in excellent agreement with literature diffraction data.<sup>59</sup> Solvated dendrimer–nanoparticle complexes were generated by immersing each complex in a DCM box and deleting overlapping DCM molecules. Each model was relaxed using 2000 steps of steepest descent minimization with respect to the CHARMM22 force field<sup>58</sup> and then brought to room temperature by gradually raising the temperature from 0 to 295 K over 2 ns of dynamics while simultaneously loosening positional constraints on the dendrimer heavy atoms. Gold nanoparticle atoms were constrained to their starting positions throughout the simulations, corresponding to the quantum mechanical optimized nanoparticle geometry described above, with classical gold–sulfur bond potentials for the nanoparticle–thioether linkages fitted to the average bond length obtained in the gold–thioether electronic structure calculations,  $0.251 \pm 0.005$  nm. Each of the 36 models listed in Table 1 was then subjected to 10 ns dynamics runs to allow formation of well-equilibrated solvated, room-temperature dendrimer–gold complexes. This corresponds to over  $0.4 \mu\text{s}$  of dynamics in all, 432 ns, composed of 72 ns for equilibration plus 360 ns of equilibrated dynamics. Additional control simulations featuring solvated but noncomplexed dendrimer and nanoparticle

models provided reference values for the computation of the wrapping penalties in Table 1. Further details on the model geometry and force field parameters are given in Supporting Information section S1.

Molecular Langevin dynamics were performed using the NAMD program<sup>60</sup> with Ewald summation used to calculate the electrostatic interactions and a 2 fs time step used for dynamics by constraining covalent bonds to hydrogen *via* the ShakeH algorithm.<sup>61</sup> Image generation and Tcl script-based trajectory analysis was performed using the VMD program.<sup>62</sup>

**Conflict of Interest:** The authors declare no competing financial interest.

**Acknowledgment.** We acknowledge support for this research from the European Community's Seventh Framework Programme (FP7/2007-2013) under grant agreement number 213382 (FUNMOL). We acknowledge Science Foundation Ireland (SFI) for computing resources at Tyndall National Institute and SFI/Higher Education Authority for computing time at the Irish Centre for High-End Computing (ICHEC).

**Supporting Information Available:** Detailed methods and control simulations describing long-range interactions, thermal effects and gold/sulfur reactivity in Au–S bond formation, dendrimer wrapping around gold in a more polar methanol solvent, wrapping in a less favorable “feet first” orientation, and wrapping of a larger, 1.4 nm Au<sub>69</sub> particle. This material is available free of charge *via* the Internet at <http://pubs.acs.org>.

## REFERENCES AND NOTES

- Sanchez, C.; Julian, B.; Belleville, P.; Popall, M. Applications of Hybrid Organic-Inorganic Nanocomposites. *J. Mater. Chem.* **2005**, *15*, 3559–3592.
- van Schooneveld, M. M.; Gloter, A.; Stephan, O.; Zagonel, L. F.; Koole, R.; Meijerink, A.; Mulder, W. J. M.; de Groot, F. M. F. Imaging and Quantifying the Morphology of an Organic-Inorganic Nanoparticle at the Sub-nanometre Level. *Nat. Nanotechnol.* **2010**, *5*, 538–544.
- Rao, C. N. R.; Kulkarni, G. U.; Thomas, P. J.; Edwards, P. P. Metal Nanoparticles and their Assemblies. *Chem. Soc. Rev.* **2000**, *29*, 27–35.
- Daniel, M. C.; Astruc, D. Gold Nanoparticles: Assembly, Supramolecular Chemistry, Quantum-Size-Related Properties, and Applications toward Biology, Catalysis, and Nanotechnology. *Chem. Rev.* **2004**, *104*, 293–346.
- Parker, J. F.; Fields-Zinna, C. A.; Murray, R. W. The Story of a Monodisperse Gold Nanoparticle: Au<sub>25</sub>L<sub>18</sub>. *Acc. Chem. Res.* **2010**, *43*, 1289–1296.
- Maier, S. A.; Atwater, H. A. Plasmonics: Localization and Guiding of Electromagnetic Energy in Metal/Dielectric Structures. *J. Appl. Phys.* **2005**, *98*, 011101.
- Astruc, D.; Daniel, M. C.; Ruiz, J. Dendrimers and Gold Nanoparticles as Exo-receptors Sensing Biologically Important Anions. *Chem. Commun.* **2004**, 2637–2649.
- Bangs, L. B. New Developments in Particle-Based Immunoassays: Introduction. *Pure Appl. Chem.* **1996**, *68*, 1873–1879.
- Zheng, Y. H.; Lalander, C. H.; Bach, U. Nanoscale Force Induced Size-Selective Separation and Self-Assembly of Metal Nanoparticles: Sharp Colloidal Stability Thresholds and hcp Ordering. *Chem. Commun.* **2010**, *46*, 7963–7965.
- Hombberger, M.; Simon, U. On the Application Potential of Gold Nanoparticles in Nanoelectronics and Biomedicine. *Philos. T. R. Soc. A* **2010**, *368*, 1405–1453.
- Chanda, N.; Kattumuri, V.; Shukla, R.; Zambre, A.; Katti, K.; Upendran, A.; Kulkarni, R. R.; Kan, P.; Fent, G. M.; Casteel, S. W.; *et al.* Bombesin Functionalized Gold Nanoparticles Show *in vitro* and *in vivo* Cancer Receptor Specificity. *Proc. Natl. Acad. Sci. U. S. A.* **2010**, *107*, 8760–8765.
- You, C. C.; Chompoosor, A.; Rotello, V. M. The Biomacromolecule-Nanoparticle Interface. *Nano Today* **2007**, *2*, 34–43.
- Shan, J.; Tenhu, H. Recent Advances in Polymer Protected Gold Nanoparticles: Synthesis, Properties and Applications. *Chem. Commun.* **2007**, 4580–4598.
- Eck, W.; Craig, G.; Sigdel, A.; Ritter, G.; Old, L. J.; Tang, L.; Brennan, M. F.; Allen, P. J.; Mason, M. D. PEGylated Gold Nanoparticles Conjugated to Monoclonal F19 Antibodies as Targeted Labeling Agents for Human Pancreatic Carcinoma Tissue. *ACS Nano* **2008**, *2*, 2263–2272.
- Eck, W.; Nicholson, A. I.; Zentgraf, H.; Semmler, W.; Bartling, S. Anti-CD4-targeted Gold Nanoparticles Induce Specific Contrast Enhancement of Peripheral Lymph Nodes in X-ray Computed Tomography of Live Mice. *Nano Lett.* **2010**, *10*, 2318–2322.
- Perelaer, J.; Smith, P. J.; Mager, D.; Soltman, D.; Volkman, S. K.; Subramanian, V.; Korvink, J. G.; Schubert, U. S. Printed Electronics: The Challenges Involved in Printing Devices, Interconnects, and Contacts Based on Inorganic Materials. *J. Mater. Chem.* **2010**, *20*, 8446–8453.
- Jiang, L.; Wang, W. C.; Fuchs, H.; Chi, L. F. One-Dimensional Arrangement of Gold Nanoparticles with Tunable Interparticle Distance. *Small* **2009**, *5*, 2819–2822.
- So, C. R.; Kulp, J. L.; Oren, E. E.; Zareie, H.; Tamerler, C.; Evans, J. S.; Sarikaya, M. Molecular Recognition and Supramolecular Self-Assembly of a Genetically Engineered Gold Binding Peptide on Au{111}. *ACS Nano* **2009**, *3*, 1525–1531.
- Kang, B.; Mackey, M. A.; El-Sayed, M. A. Nuclear Targeting of Gold Nanoparticles in Cancer Cells Induces DNA Damage, Causing Cytokinesis Arrest and Apoptosis. *J. Am. Chem. Soc.* **2010**, *132*, 1517–1519.
- Aillon, K. L.; Xie, Y. M.; El-Gendy, N.; Berkland, C. J.; Forrest, M. L. Effects of Nanomaterial Physicochemical Properties on *in vivo* Toxicity. *Adv. Drug Delivery Rev.* **2009**, *61*, 457–466.
- Peng, G.; Tisch, U.; Adams, O.; Hakim, M.; Shehata, N.; Broza, Y. Y.; Billan, S.; Abdah-Bortnyak, R.; Kuten, A.; Haick, H. Diagnosing Lung Cancer in Exhaled Breath using Gold Nanoparticles. *Nat. Nanotechnol.* **2009**, *4*, 669–673.
- Maye, M. M.; Gang, O.; Cotlet, M. Photoluminescence Enhancement in CdSe/ZnS-DNA Linked-Au Nanoparticle Heterodimers Probed by Single Molecule Spectroscopy. *Chem. Commun.* **2010**, *46*, 6111–6113.
- Kim, S. J.; Lee, J. S. Flexible Organic Transistor Memory Devices. *Nano Lett.* **2010**, *10*, 2884–2890.
- Ruiz-Hitzky, E.; Darder, M.; Aranda, P.; Ariga, K. Advances in Biomimetic and Nanostructured Biohybrid Materials. *Adv. Mater.* **2010**, *22*, 323–336.
- Laaksonen, P.; Kivioja, J.; Paananen, A.; Kainlauri, M.; Kontturi, K.; Ahopelto, J.; Linder, M. B. Selective Nanopatterning Using Citrate-Stabilized Au Nanoparticles and Cysteine-Modified Amphiphilic Protein. *Langmuir* **2009**, *25*, 5185–5192.
- Noy, A. Bionanoelectronics. *Adv. Mater.* **2011**, *23*, 807–820.
- Hermes, J. P.; Sander, F.; Peterle, T.; Mayor, M. From Ligand-Stabilized Gold Nanoparticles to Hybrid Organic-Inorganic Superstructures. *Chimia* **2011**, *65*, 219–222.
- Peterle, T.; Leifert, A.; Timper, J.; Sologubenko, A.; Simon, U.; Mayor, M. Multidentate Thioether Ligands Coating Gold Nanoparticles. *Chem. Commun.* **2008**, 3438–3440.
- Peterle, T.; Ringler, P.; Mayor, M. Gold Nanoparticles Stabilized by Acetylene-Functionalized Multidentate Thioether Ligands: Building Blocks for Nanoparticle Superstructures. *Adv. Funct. Mater.* **2009**, *19*, 3497–3506.
- Hermes, J. P.; Sander, F.; Peterle, T.; Cioffi, C.; Ringler, P.; Pfohl, T.; Mayor, M. Direct Control of the Spatial Arrangement of Gold Nanoparticles in Organic-Inorganic Hybrid Superstructures. *Small* **2011**, *7*, 920–929.
- Hermes, J. P.; Sander, F.; Peterle, T.; Urbani, R.; Pfohl, T.; Thompson, D.; Mayor, M. Gold Nanoparticles Stabilized by Thioether Dendrimers. *Chem.—Eur. J.* **2011**, *17*, 13473–13481.
- Moth-Poulsen, K.; Bjornholm, T. Molecular Electronics with Single Molecules in Solid-State Devices. *Nat. Nanotechnol.* **2009**, *4*, 551–556.
- Rybtchinski, B. Adaptive Supramolecular Nanomaterials Based on Strong Noncovalent Interactions. *ACS Nano* **2011**, *5*, 6791–6818.
- Qian, M. C.; Reber, A. C.; Ugrinov, A.; Chaki, N. K.; Mandal, S.; Saavedra, H. M.; Khanna, S. N.; Sen, A.; Weiss, P. S. Cluster-Assembled Materials: Toward Nanomaterials with Precise Control over Properties. *ACS Nano* **2010**, *4*, 235–240.

35. Mammen, M.; Choi, S. K.; Whitesides, G. M. Polyvalent Interactions in Biological Systems: Implications for Design and Use of Multivalent Ligands and Inhibitors. *Angew. Chem., Int. Ed.* **1998**, *37*, 2755–2794.
36. Perl, A.; Gomez-Casado, A.; Thompson, D.; Dam, H. H.; Jonkheijm, P.; Reinhoudt, D. N.; Huskens, J. Gradient-Driven Motion of Multivalent Ligand Molecules along a Surface Functionalized with Multiple Receptors. *Nat. Chem.* **2011**, *3*, 317–322.
37. Mulder, A.; Huskens, J.; Reinhoudt, D. N. Multivalency in Supramolecular Chemistry and Nanofabrication. *Org. Biomol. Chem.* **2004**, *2*, 3409–3424.
38. Kim, C.; Agasti, S. S.; Zhu, Z. J.; Isaacs, L.; Rotello, V. M. Recognition-Mediated Activation of Therapeutic Gold Nanoparticles inside Living Cells. *Nat. Chem.* **2010**, *2*, 962–966.
39. Kostianen, M. A.; Kasyutich, O.; Cornelissen, J. J. L. M.; Nolte, R. J. M. Self-Assembly and Optically Triggered Disassembly of Hierarchical Dendron-Virus Complexes. *Nat. Chem.* **2010**, *2*, 394–399.
40. Schmid, G. The Relevance of Shape and Size of Au-55 Clusters. *Chem. Soc. Rev.* **2008**, *37*, 1909–1930.
41. Periyasamy, G.; Remacle, F. Ligand and Solvation Effects on the Electronic Properties of Au-55 Clusters: A Density Functional Theory Study. *Nano Lett.* **2009**, *9*, 3007–3011.
42. Pei, Y.; Shao, N.; Gao, Y.; Zeng, X. C. Investigating Active Site of Gold Nanoparticle Au<sub>55</sub>(PPh<sub>3</sub>)<sub>12</sub>Cl<sub>6</sub> in Selective Oxidation. *ACS Nano* **2010**, *4*, 2009–2020.
43. Lim, J. K.; Kim, I. H.; Kim, K. H.; Shin, K. S.; Kang, W.; Choo, J.; Joo, S. W. Adsorption of Dimethyl Sulfide and Methanethiolate on Ag and Au Surfaces: Surface-Enhanced Raman Scattering and Density Functional Theory Calculation Study. *Chem. Phys.* **2006**, *330*, 245–252.
44. Ulman, A. Formation and Structure of Self-Assembled Monolayers. *Chem. Rev.* **1996**, *96*, 1533–1554.
45. Wu, S. M.; Gonzalez, M. T.; Huber, R.; Grunder, S.; Mayor, M.; Schonenberger, C.; Calame, M. Molecular Junctions Based on Aromatic Coupling. *Nat. Nanotechnol.* **2008**, *3*, 569–574.
46. Strachan, D. R.; Johnston, D. E.; Guiton, B. S.; Datta, S. S.; Davies, P. K.; Bonnell, D. A.; Johnson, A. T. C. Real-Time TEM Imaging of the Formation of Crystalline Nanoscale Gaps. *Phys. Rev. Lett.* **2008**, *100*, 056805.
47. Jadzinsky, P. D.; Calero, G.; Ackerson, C. J.; Bushnell, D. A.; Kornberg, R. D. Structure of a Thiol Monolayer-Protected Gold Nanoparticle at 1.1 Angstrom Resolution. *Science* **2007**, *318*, 430–433.
48. Thompson, D. Free Energy Balance Predicates Dendrimer Binding Multivalency at Molecular Printboards. *Langmuir* **2007**, *23*, 8441–8451.
49. Huskens, J.; Mulder, A.; Auletta, T.; Nijhuis, C. A.; Ludden, M. J. W.; Reinhoudt, D. N. A Model for Describing the Thermodynamics of Multivalent Host-Guest Interactions at Interfaces. *J. Am. Chem. Soc.* **2004**, *126*, 6784–6797.
50. Thompson, D. The Effective Concentration of Unbound Ink Anchors at the Molecular Printboard. *J. Phys. Chem. B* **2008**, *112*, 4994–4999.
51. Jones, R. A. L. *Soft Machines: Nanotechnology and Life*; Oxford University Press: Oxford, 2007 (paperback); Chapter 5, pp 117–120.
52. Reed, A. E.; Weinstock, R. B.; Weinhold, F. Natural Population Analysis. *J. Chem. Phys.* **1985**, *83*, 735–746.
53. Yang, W. T.; Parr, R. G. Hardness, Softness, and the Fukui Function in the Electronic Theory of Metals and Catalysis. *Proc. Natl. Acad. Sci. U. S. A.* **1985**, *82*, 6723–6726.
54. Frisch, M. J.; Trucks, G. W.; Schlegel, H. B.; Scuseria, G. E.; Robb, M. A.; Cheeseman, J. R.; Scalmani, G.; Barone, V.; Mennucci, B.; Petersson, A.; et al. *Gaussian 09*; Gaussian, Inc.: Wallingford, CT, 2009.
55. Becke, A. D. Density-Functional Thermochemistry 0.3. The Role of Exact Exchange. *J. Chem. Phys.* **1993**, *98*, 5648–5652.
56. Varetto, U. *MOLEKEL* Version 4.3; Swiss National Supercomputing Centre: Manno (Switzerland).
57. Richardi, J.; Fries, P. H.; Krienke, H. Liquid Properties of Tetrahydrofuran and Methylene Chloride via the Molecular Hypernetted Chain Approximation. *J. Phys. Chem. B* **1998**, *102*, 5196–5201.
58. MacKerell, A. D.; Bashford, D.; Bellott, M.; Dunbrack, R. L.; Evanseck, J. D.; Field, M. J.; Fischer, S.; Gao, J.; Guo, H.; Ha, S.; et al. All-Atom Empirical Potential for Molecular Modeling and Dynamics Studies of Proteins. *J. Phys. Chem. B* **1998**, *102*, 3586–3616.
59. Balint, S.; Bako, I.; Grosz, T.; Megyes, T. Structure of Liquid Methylene Chloride: Molecular Dynamics Simulation Compared to Diffraction Experiments. *J. Mol. Liq.* **2007**, *136*, 257–266.
60. Phillips, J. C.; Braun, R.; Wang, W.; Gumbart, J.; Tajkhorshid, E.; Villa, E.; Chipot, C.; Skeel, R. D.; Kale, L.; Schulten, K. Scalable Molecular Dynamics with NAMD. *J. Comput. Chem.* **2005**, *26*, 1781–1802.
61. Ryckaert, J. P.; Ciccotti, G.; Berendsen, H. J. C. Numerical-Integration of Cartesian Equations of Motion of a System with Constraints - Molecular-Dynamics of N-Alkanes. *J. Comput. Phys.* **1977**, *23*, 327–341.
62. Humphrey, W.; Dalke, A.; Schulten, K. VMD: Visual Molecular Dynamics. *J. Mol. Graph.* **1996**, *14*, 33–38.



Supporting Information

for

# Scanning the potential energy surface for synthesis of dendrimer-wrapped gold clusters: design rules for true single-molecule nanostructures

*Damien Thompson<sup>1\*</sup>, Jens P. Hermes<sup>2</sup>, Aidan J. Quinn<sup>3</sup> and Marcel Mayor<sup>2,4</sup>*

<sup>1</sup>Theory Modelling and Design Centre, Tyndall National Institute, University College Cork, Cork, Ireland. <sup>2</sup>Department of Chemistry, University of Basel, St. Johannis-Ring 19, CH-4056 Basel, Switzerland. <sup>3</sup>Micro/Nanoelectronics Centre, Tyndall National Institute, University College Cork, Cork, Ireland. <sup>4</sup>Institute of Nanotechnology, Karlsruhe Institute of Technology (KIT), P.O.Box 3640, D-76021 Karlsruhe, Germany.

\*Corresponding author: damien.thompson@tyndall.ie.

This Supporting Information provides further details on the computational model, together with control simulations describing long-range effects in Au-S bonding, solvent effects, dendrimer wrapping dynamics and complexation to a 1.4-nm Au<sub>69</sub> particle.

## **S1. Detailed description of the model**

### **S1.1 More details on the model geometry**

The full dichloromethane-solvated dendrimer:gold model is shown in panel (a) of Figure S1 below. Shown in panel (b) are the alternating wide and narrow faces of cuboctahedral Au<sub>55</sub>; icosahedral Au<sub>55</sub> by contrast has a more isotropic shape (as shown in panel (a) and also main text Figure 2).



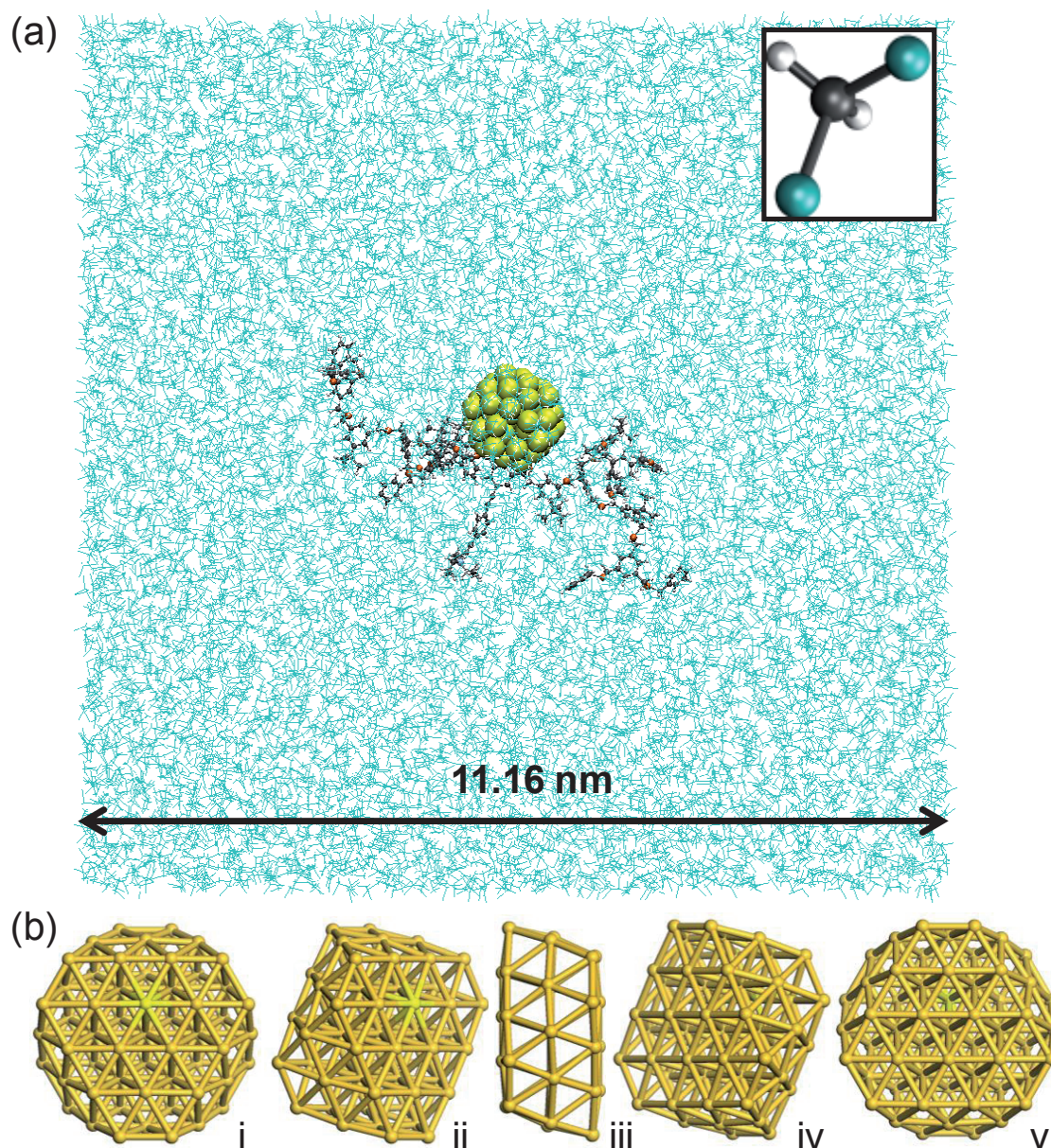


**Figure S1.** (a) The periodic cell used to model the dichloromethane-solvated dendrimer:gold complexes, with one dichloromethane molecule (chlorine atoms are coloured blue) shown in the inset panel and the equilibrated 11.16 nm width of the cubic cell labelled. A representative dendrimer:gold complex is shown immersed in the center of the box; in this case the dendrimer is bound using two core thioether-gold bonds to icosahedral  $\text{Au}_{55}$ , with the dendrimer shown in ball-and-stick representation and the  $\text{Au}_{55}$  gold atoms shown as van der Waals's spheres. (b) The alternating wide and narrow faces of cuboctahedral  $\text{Au}_{55}$ . Subpanels i-v show rotations of the particle by  $45^\circ$  in the plane normal to the page, with one gold atom highlighted in light yellow to guide the eye.

## S1.2 More details on the potential energy function for non-bonded interactions

The force field parameters used for the molecular dynamics simulations are summarised in Figure S2. The dichloromethane parameters were generated using existing CHARMM22 atom types<sup>1</sup> and atomic charges taken from reference<sup>2</sup>. Dendrimer parameters were generated using existing CHARMM data<sup>1</sup>, with core, tail and terminal groups defined and “patched together” using a similar approach to that described in reference<sup>3</sup>. The Gaussian, CHARMM and NAMD input scripts used for the simulations, together with the computed structures, are available on request from the corresponding author.

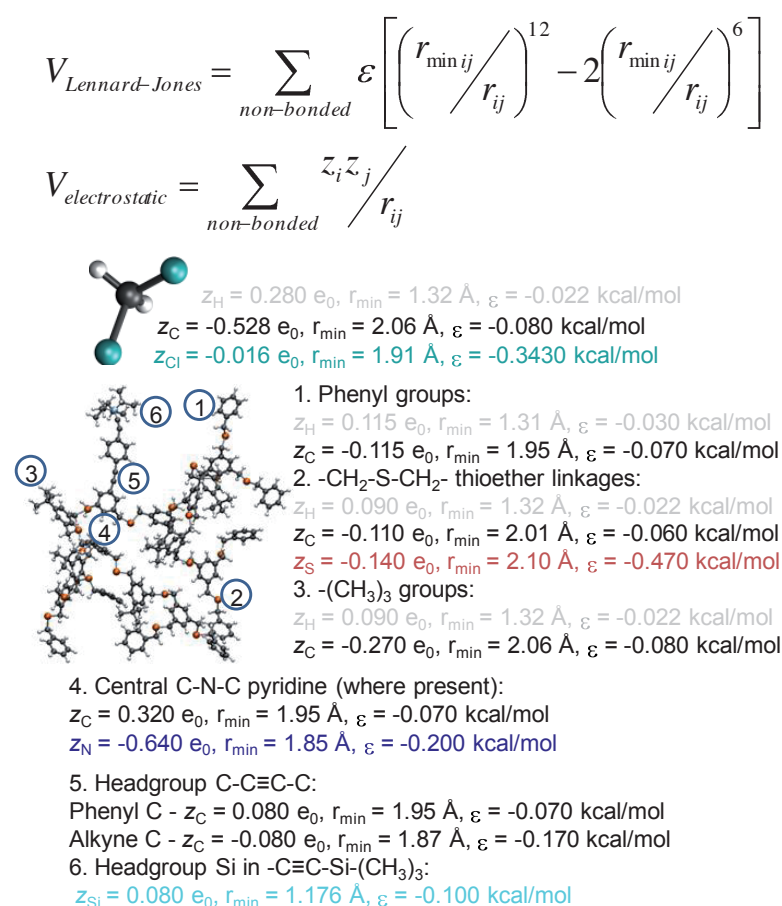


**Figure S2.** CHARMM equations<sup>1</sup> and force field parameters<sup>1,2</sup> used to model non-bonded interactions between atoms (indexed by  $i$  and  $j$ ) in the formation of dendrimer:gold nanoparticle complexes in dichloromethane.

### S1.3. More details on the quantum mechanical calculation of thioether-gold bond strength

Cluster-molecule Au-S bond parameters were generated from new electronic structure calculations and fit to the force field (main text Methods). Where present, Au-S bonds are described using a standard CHARMM harmonic function,  $V_{bond} = k_r(r-r_0)^2$ , with target bond length  $r_0$  of 2.51 Å and force constant  $k_r$  of 198 kcal/mol Å<sup>2</sup>, with  $r_0$  taken from the data in main text Figure 3 and  $k_r$  taken from reference<sup>4</sup>.

We checked for long-range interactions in the Au-S bonding calculations using the CAM-B3LYP functional<sup>5</sup>. Figure S3 shows the calculated geometries, starting from the B3LYP-optimised structures (main text Figure 3). Overall, Au-S bond lengths are shortened by between 0.02 and 0.13 Å upon inclusion of long-range effects and the Au-S bond energies are strengthened by between -0.02 and -0.22 eV. For adsorption of a thioether group at an “apex” site of T<sub>d</sub> Au<sub>20</sub> (Figure S3a and main text Figure 3a), the inclusion of long-range forces gives a very small, ~5% increase in bond strength (-0.34 eV vs. -0.32 eV). For adsorption of the di-thioether fragments on “triangular” gold faces (Au<sub>13</sub>), shown in panels (b) and (c) of Figure S3a and main text Figure 3a, the long-range effects are sizeable, giving ~-0.2 eV (37%) stronger bonds (-0.52, -0.51 eV vs. -0.36, -0.21 eV). Figure S3d replots main text Figure 5a using the CAM-B3LYP average Au-S bond strength of  $-457 \pm 100$  meV. This reduces the time-averaged single vs. double dendrimer preference from -1.5 eV to -1.2 eV, though this may be due to the distribution of bond numbers on the vertical axis; *e.g.*, the complex involving 16 Au-S bonds may well have a more stable *single*-dendrimer binding mode that was not tested in the simulations.

Re-examination of the MD dendrimer:gold non-bonded wrapping terms in dichloromethane gave a time-averaged interaction energy of  $28 \pm 3$  meV/thioether for the interaction between the gold particle and the thioether -CH<sub>2</sub>-S-CH<sub>2</sub>- moieties. Control simulations of dendrimer-wrapped gold in vacuum gave  $90 \pm 2$  meV/thioether. Thus most of the CAM-B3LYP  $132 \pm 103$  meV long-range correction to the Au-S bond strength is accounted for by direct (non solvent mediated) thioether-gold non-bonded interactions in the empirical wrapping calculations.

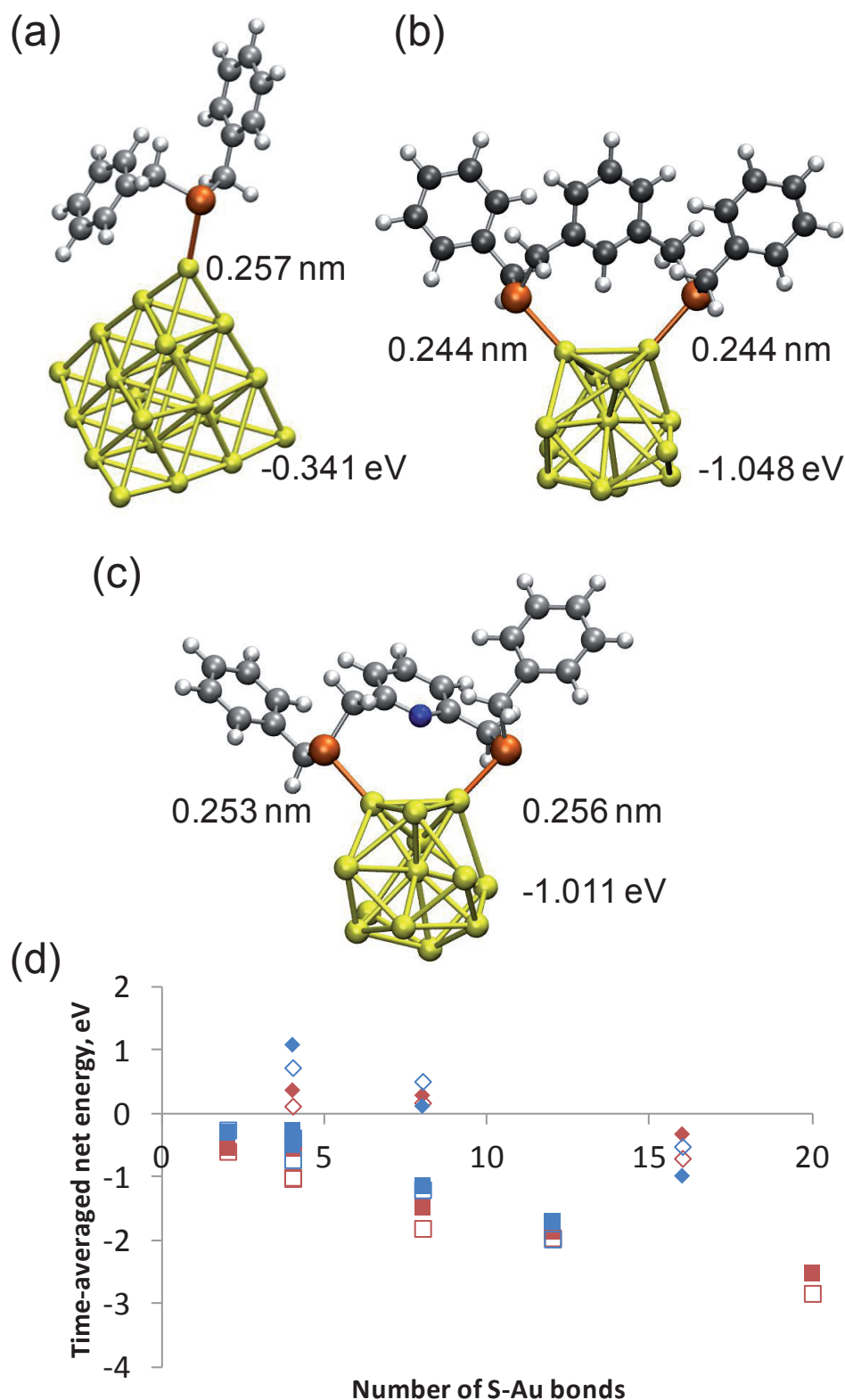


**Figure S3.** Panels (a), (b) and (c) show Au-S bonds formed between dendrimer benzyl thioether groups and gold clusters, recomputed (main text Figure 3) using the long-range corrected CAM-B3LYP functional<sup>5</sup>. Panel (d) shows main text Figure 5a replotted using the CAM-B3LYP Au-S bond strength of -457 meV. Squares and triangles mark values for single and double dendrimer complexes.

We performed also thermochemistry calculations, using the computed frequencies to estimate a thermal correction to Gibbs free energy<sup>6</sup> of  $+283 \pm 32$  meV, averaged over the three structures in Figure S3a-c. The magnitude of this correction does not change significantly on increasing the number of Au-S bonds from one to two in the complexes or on switching from a benzyl to pyridine central unit (Figure S3a-c). For the weakest, singly bound complex this entropic effect cancels the enthalpic bonding, while for the divalent complex it reduces the overall bond strength by  $\sim 1/3$ . For the weak thioether-gold bonding then the electronic energy of the complex is shifted downwards by long-range stabilisation and upwards by entropy (Figure S4), showing the importance of multivalent, collective bonding effects in dendrimer-gold wrapping. In future work we will attempt to calculate the electronic structure of the full dendrimer:cluster complex (including long-range, solvent and thermal corrections); these calculations are made feasible by recent improvements in linear-scaling DFT methods together with access to High-Performance Computing facilities.

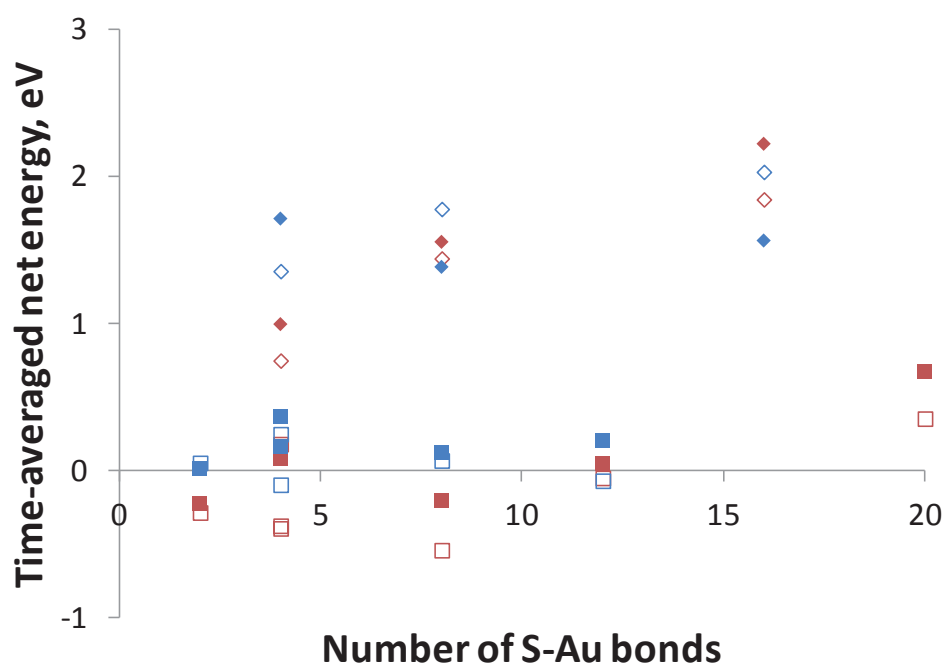


**Figure S4.** Figure S3d replotted using the CAM-B3LYP Au-S bond strength ( $-457$  meV) offset by the entropic destabilisation of  $+324$  meV per dithioether unit. The calculated single (square) vs. double (triangle) dendrimer difference is  $-1.53 \pm 0.57$  eV, very similar to the value of  $-1.46 \pm 0.47$  eV computed using the uncorrected B3LYP bond strength in main text Figure 5a.

As a final test of Au-S thioether binding strengths, we scanned a variety of different gold binding sites for the thioether moiety and also calculated reference values for mono-benzyl and thiol molecules, using the B3LYP functional and the same basis sets / pseudopotentials as described in main text Methods. Figure S5 below summarises the calculated bond strengths, and shows how the sulphur bond to gold gets weaker as one progresses from  $\text{CH}_3\text{CH}_2\text{S}$  to  $(\text{CH}_3\text{CH}_2)_2\text{S}$  to  $\text{C}_6\text{H}_5\text{CH}_2\text{S}$  and finally to the dendrimer  $(\text{C}_6\text{H}_6\text{CH}_2)_2\text{S}$  anchoring site. The strongest bond is as expected for  $\text{CH}_3\text{CH}_2\text{S}$  on gold, with a computed value of  $-0.75$  eV on terrace (111) sites, in line with literature values<sup>7,8</sup>, with the extra 1 eV measured experimentally<sup>9</sup> coming from Au-H bonding (from the H atom formed from S-H scission, present for thiol but not thioether groups). The complexation energies show that the two pendant  $-\text{CH}_2\text{-Ph}$  groups soak up most of the sulphur reactivity in the dendrimer di-benzyl thioether sites; hence, the thioether-gold attachment is weak. As discussed in the main text, this weak bonding is a useful feature of the dendrimer:gold complex formation, because it allows for self-healing in dendrimer wrapping around the particle to form a uniform “cloak”.

In terms of further probing the range of thioether Au-S bond strengths present for the di-benzyl dendrimer binding to the gold clusters, Figure S5 shows how coordinatively-unsaturated “apex” gold atoms are as expected more reactive than sites with higher coordination number in the particle, with the effect most pronounced for the weaker phenyl ligands. The Au-S bond strength for each molecule was measured on three representative gold sites, 9-coordinated terrace sites (equivalent to fcc Au(111)), 6-coordinated ridge sites and 3-coordinated apex sites. Representative computed molecule-gold structures are shown for each molecule in Figure S5:  $\text{CH}_3\text{CH}_2\text{S}$  adsorption on a terrace site;  $(\text{CH}_3\text{CH}_2)_2\text{S}$ , binding to an apex site;  $\text{C}_6\text{H}_6\text{CH}_2\text{S}$  and  $(\text{C}_6\text{H}_6\text{CH}_2)_2\text{S}$  binding to ridge sites. Note that the number of bonds drawn just reflects the proximity of S to one or more gold sites, and should not be taken to indicate an overall stronger interaction, or “stapling”, with increasing S coordination number. Given that the uncertainty of  $\sim 140$  meV in the dendrimer  $(\text{C}_6\text{H}_6\text{CH}_2)_2\text{S}$  anchor site bonding to the gold particle (Figure S5) is similar

in magnitude to the long-range and thermal corrections described above, we use the B3LYP bond strength (for the strongest-binding apex site) for the electronic energy estimate (main text Table 1).

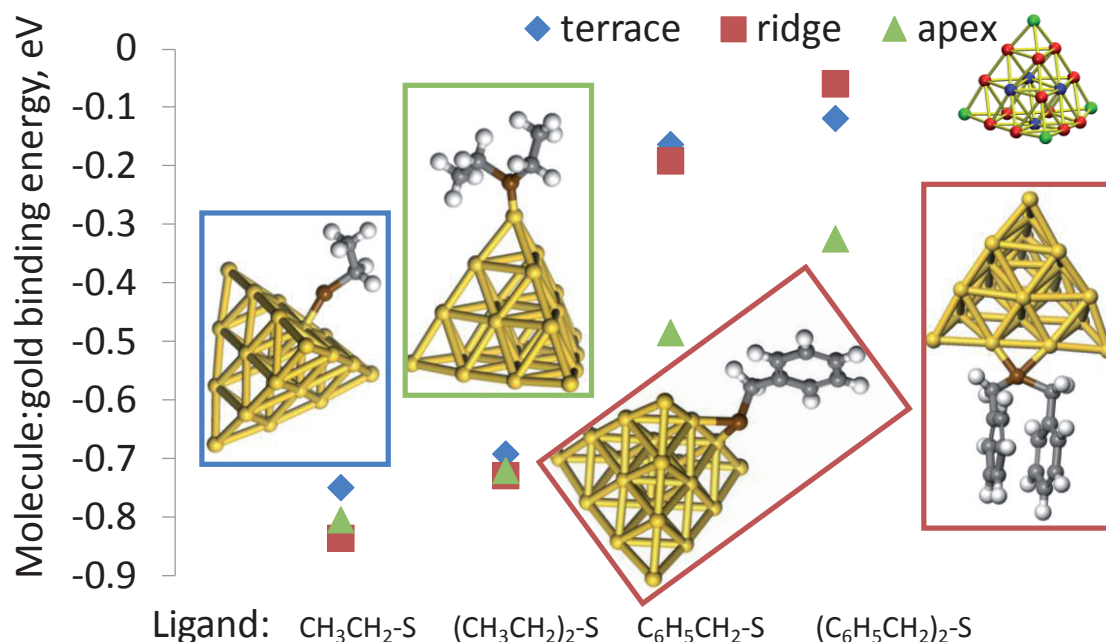


**Figure S5.** Molecule:gold S-Au bond strengths computed for four sulphur-containing molecules binding to three structurally-inequivalent Au<sub>20</sub> particle sites. Ligand (C<sub>6</sub>H<sub>6</sub>CH<sub>2</sub>)<sub>2</sub>S is the thioether anchor group used to immobilise the dendrimer on the Au<sub>55</sub> gold clusters in the main text.

## S2. Influence of environmental effects on structure and shape of dendrimer-gold complexes:

Solvent-mediated changes in functionalised nanoparticle structure and shape can influence their use as drug carriers *in vivo*<sup>10</sup>. As a first step towards assessing the stability and conformational dynamics of the dendrimer-gold complexes when transferred out of the dichloromethane (DCM) solvent, Figure S6 compares solvation shell densities for dendrimer-gold complexes immersed in the DCM solvent used in the experiments, and complexes in an alternative, more polar solvent, methanol. CHARMM force field parameters were used for MeOH<sup>1</sup>. DCM has dielectric constant  $\epsilon=9$ , while MeOH has  $\epsilon=33$ .

The computed radial distribution functions (RDF) show that methanol more tightly surrounds the complex, as illustrated also in the solvent surfaces shown in the inset, computed from the central carbon atom of solvent molecules within 3 Å of the dendrimer-gold complex. The data in Figure S6 was

generated from 100 structures generated over 2 ns of equilibrated molecular dynamics, with the control MeOH simulations performed using the same protocol as for the DCM simulations described in the main text. Given that the driving force for formation of the dendrimer-stabilised gold nanoparticles involves a complex balance of forces at the particle-dendrimer-solvent interface (main text Table 1) it is difficult to speculate on the net effect of MeOH in selecting for single- vs. double-dendrimer complexes. Nevertheless, dendrimer-gold complexes, once formed between any exposed dendrimer and gold faces (involving perhaps kinetic windows in MeOH, as opposed to the net thermodynamic driving forces for complexation present in the less polar DCM (main text Table 1)), will be tightly shielded in solvent. Such shielding is interesting and may be useful for formation of gold particles coated with active compounds for targeted *in vivo* delivery<sup>10</sup>, though practical applications will require clever means (*e.g.*, PEGylation) of controlling phase transfer between low and high polarity solvent “clouds”.

**Radial Distribution Function (RDF) showing contacts between dendrimer:particle complex atoms and solvent carbon atoms for complexes immersed in methanol and dichloromethane solvent boxes**

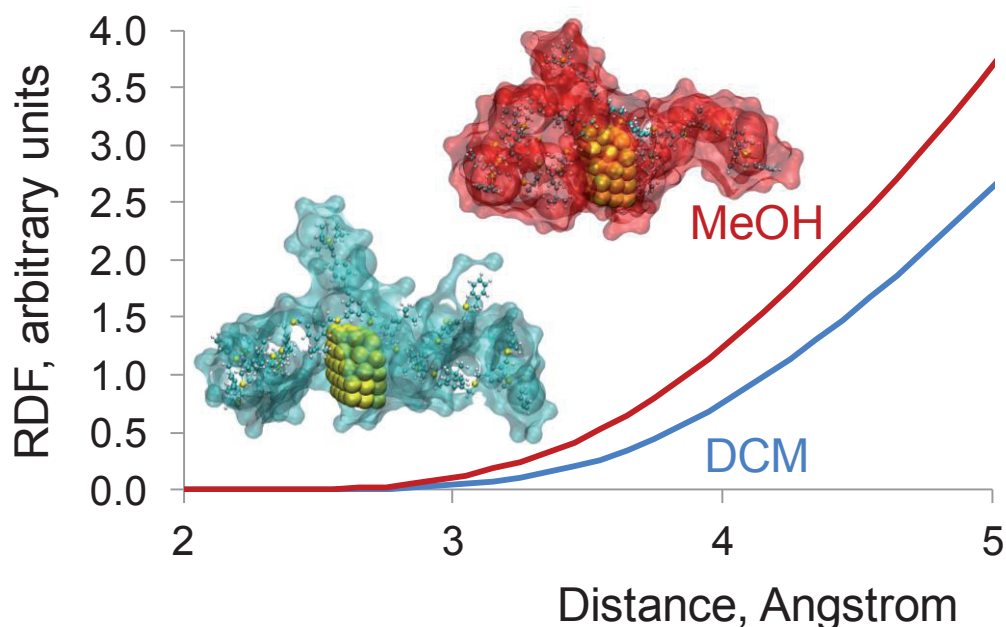


**Figure S6.** Radial distribution function (RDF) plots and computed near-complex solvation shell structures for dendrimer-gold complexes in DCM and MeOH. Shells are computed from solvent carbon atoms within 3 Å of the complex.



A final comment on environmental effects is the “opening” effect of solvents on the dendrimer structure. Figure S7 shows inter-sulphur contacts for the dendrimer molecule in vacuum, and in DCM and MeOH solvents. The dendrimer opens out from a crumpled ball in vacuum to a progressively more open shape in the DCM and MeOH solvents, as evidenced by the increasing population of longer S---S distances in Figure S7. The key to forming tightly-coupled dendrimer-particle complexes is to simultaneously promote dendrimer opening (which requires a more polar solvent) and solvent displacement from the gold surface (which requires a less polar solvent), to drive dendrimer-gold complexation, a balance that the experimentally-used, polar aprotic DCM solvent gets correct.

**Radial Distribution Function (RDF) showing contacts between dendrimer terminal group sulphur atoms for a molecule in vacuum and a molecule immersed in methanol and dichloromethane solvent boxes**

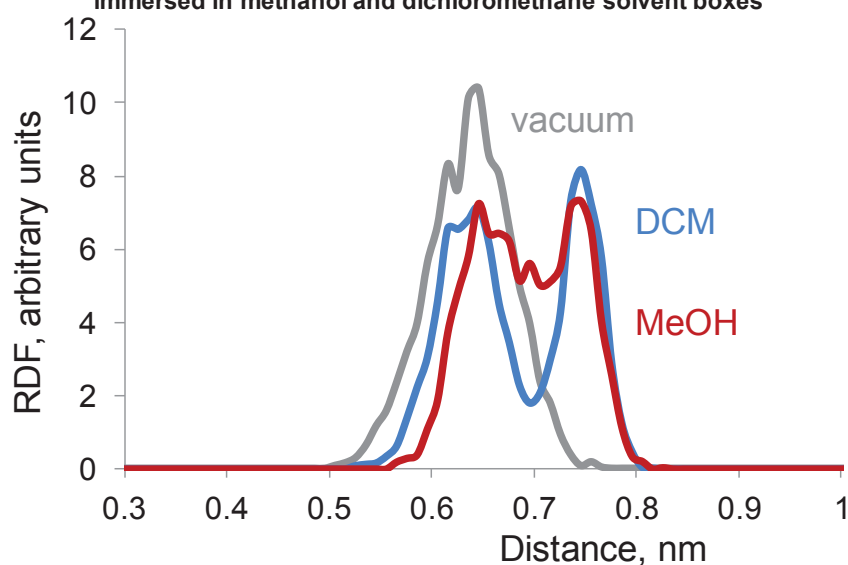


**Figure S7.** RDF plots for sulphur-sulphur contacts in a free, non-complexed dendrimer molecule in vacuum, and a molecule immersed in DCM and MeOH.

### S3. Dynamics of dendrimer-gold complexation in dichloromethane

#### S3.1. Energetics of dendrimer binding in an alternative “feet first” orientation

Table S1 quantifies the energy balance involved in dendrimer complexation to the gold cluster *via* an alternative approach geometry whereby it binds first through its terminal groups, as opposed to the “core first” orientations modelled in the main text (main text Table 1). While van der Waals

wrapping of the particle will drive the complex towards progressively more bound states overall (involving multiple bonds through core and terminal, as well as branch groups), this alternative “feet first” binding sequence could potentially promote the formation of double-dendrimer complexes whereby the two terminal-bound dendrimers become trapped in partially-bound states. As shown in Table S1 however such a situation is not thermodynamically favoured, given the  $\sim 2$  eV average penalty (Table S1  $E_1 = 1.6 \pm 1.3$  eV *vs.* main text Table 1  $E_1 = -0.2 \pm 0.2$  eV) associated with such a “feet first” approach geometry. The energy terms in Table S1 indicate that enlarged dendrimer penalties block this alternative binding mode in which the most flexible terminal regions would be clamped. To further probe the flexibility of the different thioether groups in the dendrimer, we computed root mean square fluctuations (RMSF) for the dendrimer core, branch and terminal sulphurs from reference simulations of the dendrimer immersed alone (not complexed to gold) in dichloromethane. We found values of  $1.9 \pm 0.6$  Å,  $2.4 \pm 0.8$  Å and  $4.3 \pm 1.1$  Å for core, branch and terminal sulphurs. The terminal groups are more than two times more flexible than the core, which may explain the computed preference for binding “core first”, further supporting the experimental evidence for formation of the gold clusters in the dendrimer interior and the computed preference for single-dendrimer complexes (main text Table 1).

This natural tendency of the dendrimer to wrap core-first (see Section S3.1 below) means that stronger binders such as thiols (or, *e.g.*, carboxylates) may retain the preference for single-molecule complexes. The computed dendrimer dynamics (S3.1) indicates that the van der Waals wrapping process avoids loosely-packed “feet first” conformations that would, for the stronger thiol bond (section S1.3), promote formation of loosely-wrapped single-dendrimer complexes and so promote formation of double-dendrimer complexes. For the thioether dendrimer used in the experiments, the combination of core-first wrapping (pre-chemisorption coat dynamics) together with the weak (mobile) thioether bond is a key design feature. This feature promotes efficient, self-healing single molecule wrapping, with the high effective concentration of unbound thioethers on the 20-thioether dendrimer (*vs.* thioethers on a

second, floating dendrimer) during the wrapping process, also aiding formation of single-molecule complexes.

**Table S1.** Computed dendrimer:nanoparticle net complexation energies (eV) for a range of single-dendrimer (1:1) terminal-bound cluster complexes in dichloromethane.

Nano-particle shape	Binding mode	Electronic binding	van der Waals binding	Total binding	Dendrimer penalty	Desolvation penalty	Total penalty	Net complexation
<b>Single-dendrimer:nanoparticle complexes</b>								
<b>Icosahedral</b>	<b>Three terminal</b>	-1.0 (0.1)	0.0 (0.1)	-1.0 (0.1)	+1.2 (0.1)	+1.1 (0.7)	+2.3 (0.6)	<b>+1.3 (0.6)</b>
	<b>Six terminal</b>	-2.0 (0.2)	0.0 (0.1)	-2.0 (0.2)	+1.2 (0.1)	+2.6 (0.9)	+3.7 (1.3)	<b>+1.8 (1.4)</b>
	<b>Nine terminal</b>	-2.9 (0.3)	-0.2 (0.1)	-3.1 (0.3)	+0.7 (0.1)	+3.9 (1.0)	+4.6 (1.1)	<b>+1.5 (1.4)</b>
	<b>Twelve terminal</b>	-3.9 (0.4)	-0.3 (0.1)	-4.2 (0.5)	+0.8 (0.1)	+5.0 (1.5)	+5.8 (1.4)	<b>+1.6 (1.5)</b>

Electronic Au-S binding energies were calculated as described in the main text. The other terms were computed from the final 5 ns (2000 structures) of 10 ns room temperature molecular dynamics for each complex. A minus sign indicates net stabilization of the complex relative to reference non-complexed states. Structure-averaged uncertainties (standard deviations) are given in parentheses. Rounding all energy values to one decimal place gives in some cases apparent discrepancies of 0.1 eV between totals (in parentheses) and their components.

### S3.2 Dynamics of dendrimer unwrapping from gold

Movie unwrapping1.avi shows the dynamics of dendrimer dissociation from icosahedral Au<sub>55</sub>, created by cleaving the gold-sulphur bonds and allowing solvent dynamics to uncloak the gold cluster. In this case the dendrimer was initially bound through core and branch groups. Movie unwrapping2.avi shows dynamics of dissociation for a dendrimer initially bound through terminal groups to cuboctahedral Au<sub>55</sub>. As shown above in section S3.1, this terminal-bound mode is a minor state for the bound dendrimer-gold complex, though we may expect that such partially-bound “feet first” binding modes will be present on the kinetic association/dissociation pathways. Each movie is 13 seconds long, composed of 3 seconds for slow initial dynamics (equilibration and thioether-gold bond cleaving, over 4 ns of simulation time) followed by 10 seconds of free room temperature dynamics (corresponding to 25 ns simulation time). Gold cluster atoms are shown as van der Waals’s spheres and dendrimer heavy atoms are shown in ball-and-stick representation. Hydrogen atoms and DCM molecules are removed for clarity. Time histories (Figure S8) for the dendrimer center of mass position (coloured red to white to

blue) map the dissociation pathways, with a marginally faster unwrapping for the terminal-bound dendrimer, as expected from the lower extent of initial dendrimer “wrapping” of the particle. Both complexes are completely dissociated (minimal van der Waals dendrimer-gold contacts) by 12 ns (so, 8 ns of free room temperature dynamics) and, while the initially core+branch-bound structure persistently “rewraps” the cluster (movie unwrapping1.avi) the initially terminal-bound dendrimer remains dissociated from the cluster (movie unwrapping2.avi), supporting the hypothesis that “core first” is the dominant wrapping mechanism.

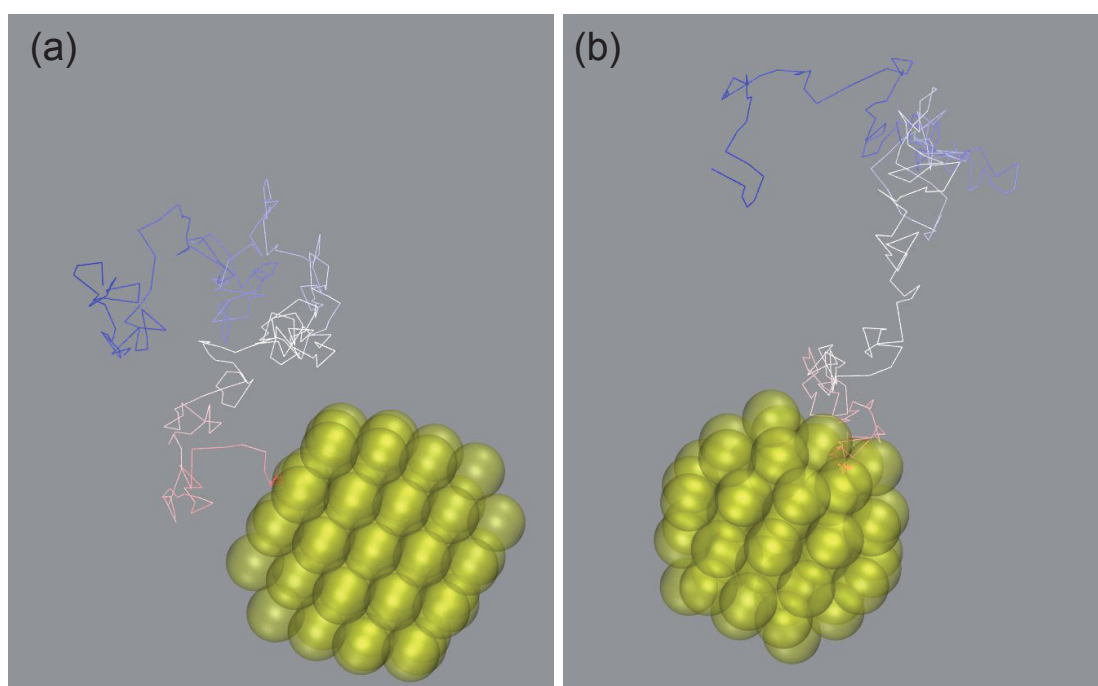


**Figure S8.** Time histories for dendrimer unwrapping from (a) a core+branch-bound complex and (b) a terminal-bound complex, with dendrimer centre of mass positions marked by the line coloured from red (0 ns) to white (4 ns, transition from slow equilibration to room temperature dynamics) to blue (out to 10 ns of free dynamics).

#### **S4. Structure, dynamics and energetics of dendrimer wrapping around a Au<sub>69</sub> particle**

Figure S9 shows the dendrimer:gold complex formed for a larger, less ordered gold nanoparticle, Au<sub>69</sub>. The 1.4 nm particle diameter provides a model for the type of gold particle found towards the upper limit of the experimental size distributions. It also serves as a first approximation to a gold cluster that

has adsorbed extra gold ad-atoms<sup>11</sup> on a Au<sub>55</sub> core. The Au<sub>69</sub> particle geometry was taken from a very recent electronic structure determination<sup>12</sup> and we modelled the formation of a fully-bound one-dendrimer complex. Movie dendrimer\_Au69.avi shows dynamics over the final 1 ns (200 structures) of 10 ns room temperature molecular dynamics.

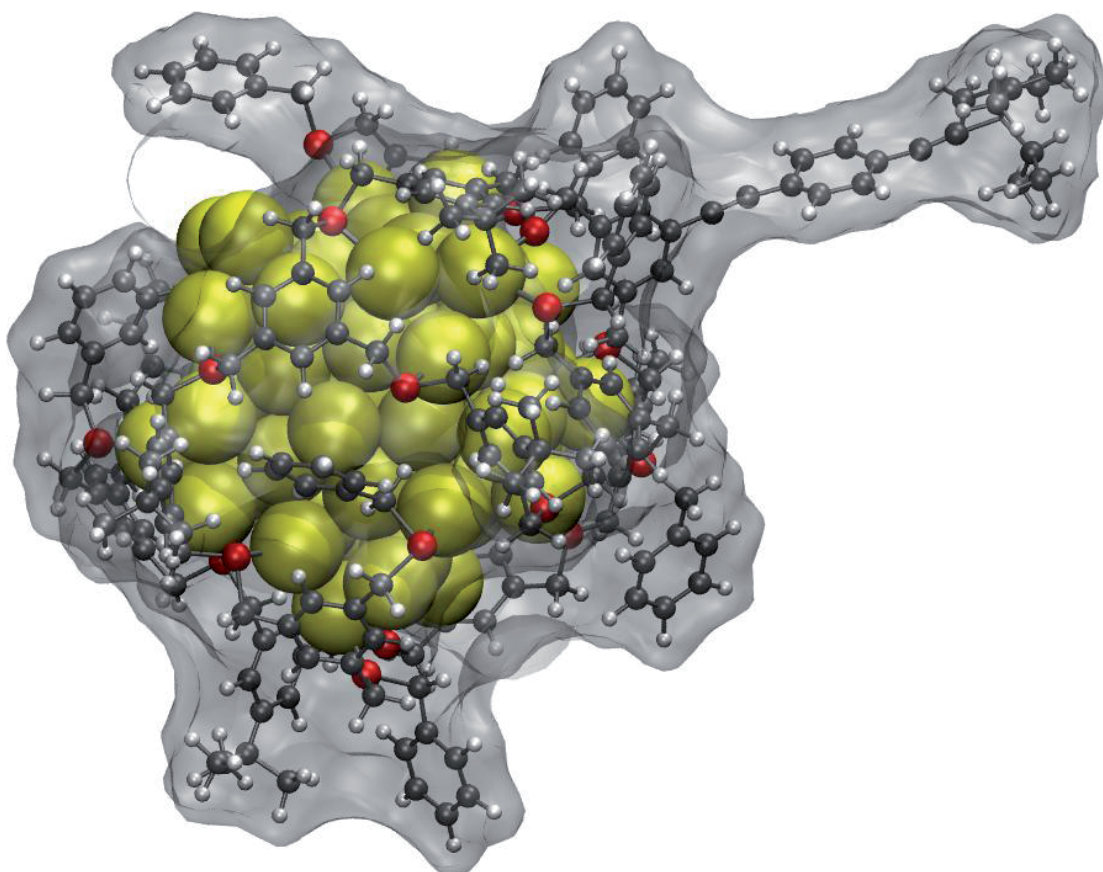


**Figure S9.** A representative computed dendrimer:Au<sub>69</sub> complex; the dendrimer is bound using all twenty thioether-gold bonds, with the gold nanoparticle atoms shown as van der Waals's spheres. The complex is immersed in a large, 11-nm wide box of dichloromethane (DCM) molecules, to model the solvated dendrimer:gold complex. For clarity, explicit DCM molecules are not shown in the picture; rather an implicit DCM solvent surface (probe radius 0.23 nm) is overlaid on the complex. Movie dendrimer\_Au69.avi shows structures formed over the final 1 ns (200 structures) of 10 ns room temperature molecular dynamics.

Table S2 shows the computed energetics of dendrimer wrapping of Au<sub>69</sub>, which gives a net complexation energy of  $-0.9 \pm 0.6$  eV, similar to the energies calculated for Au<sub>55</sub> (main text Table 1).

Comparing the energy terms for full wrapping of Au<sub>69</sub> (Table S2) and Au<sub>55</sub> (row 7 of main text Table 1), we find that the  $\sim 1$  eV time-averaged better wrapping of Au<sub>69</sub> arises from a small decrease in desolvation penalties. As shown in Figure S10 below the larger Au<sub>69</sub> particle gives closer dendrimer-gold contacts, measured between the dendrimer non-headgroup carbons and cluster gold atoms, and hence slightly better solvation for the more splayed dendrimer configuration on Au<sub>69</sub>; the computed time-averaged dendrimer radius of gyration decreases from 17 Å to 11 Å to 10 Å on going from the free dendrimer to the Au<sub>69</sub> and then Au<sub>55</sub> complex.

**Table S2.** Computed dendrimer:nanoparticle net complexation energies (eV) for a fully-bound single-dendrimer (1:1) Au<sub>69</sub> cluster complex in dichloromethane.

Nano-particle shape	Binding mode	Electronic binding	van der Waals binding	Total binding	Dendrimer penalty	Desolvation penalty	Total penalty	Net complexation
<b>Single-dendrimer:nanoparticle complexes</b>								
Au <sub>69</sub>	Two core + six branch + twelve terminal	-6.5 (0.7)	-1.0 (0.1)	-7.5 (0.7)	-0.4 (0.5)	+7.0 (0.6)	+6.4 (0.9)	<b>-0.9 (0.6)</b>

Electronic binding energies were calculated as described in the main text. The other terms were computed from the final 5 ns (2000 structures) of 10 ns room temperature molecular dynamics. A minus sign indicates net stabilization of the complex relative to reference non-complexed states. Structure-averaged uncertainties (standard deviations) are given in parentheses. Rounding all energy values to one decimal place gives in some cases apparent discrepancies of 0.1 eV between totals (in parentheses) and their components.

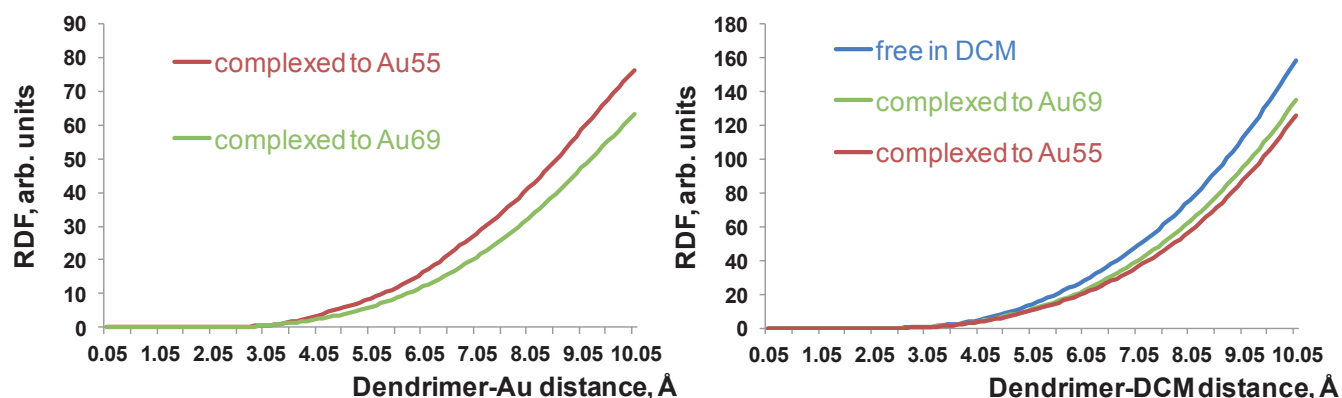


**Figure S10.** Radial distribution function (RDF) plots for dendrimer-gold and dendrimer-solvent contacts, complexed to gold clusters Au<sub>69</sub> and Au<sub>55</sub> in DCM, and free (uncomplexed) in DCM.

**REFERENCES**

1. MacKerell, A. D.; Bashford, D.; Bellott, M.; Dunbrack, R. L.; Evanseck, J. D.; Field, M. J.; Fischer, S.; Gao, J.; Guo, H.; Ha, S.; *et al.*, All-atom empirical potential for molecular modeling and dynamics studies of proteins. *J. Phys. Chem. B* 1998, 102, 3586-3616.
2. Richardi, J.; Fries, P.H.; Krienke, H. Liquid Properties of Tetrahydrofuran and Methylene Chloride via the Molecular Hypernetted Chain Approximation. *J. Phys. Chem. B* 1998, 102, 5196-5201.
3. Thompson, D., Free energy balance predicates dendrimer binding multivalency at molecular printboards. *Langmuir* 2007, 23, 8441-8451.
4. Jung, H.H.; Won, Y.D.; Shin, S.; Kim, K., Molecular dynamics simulation of benzenethiolate and benzyl mercaptide on Au(111), *Langmuir* 1999, 15, 1147-1154.
5. Yanai, T.; Tew, D.; Handy, N., A new hybrid exchange-correlation functional using the Coulomb-attenuating method (CAM-B3LYP). *Chem. Phys. Lett.* 2004, 393, 51-57.
6. Gaussian 09, Revision A.1, Frisch, M. J.; Trucks, G. W.; Schlegel, H. B.; Scuseria, G. E.; Robb, M. A.; Cheeseman, J. R.; Scalmani, G.; Barone, V.; Mennucci, B.; Petersson, G. A.; *et al.*, *Gaussian, Inc., Wallingford CT*, 2009.
7. Sellers, H., On the chemisorption and dissociation of HSCH<sub>3</sub> on the Au(111) surface. *Surf. Sci.* 1993, 294, 99-107.
8. Caruso, A.N.; Wang, L.G.; Jaswal, S.S.; Tsymbal, E.Y.; Dowben, P.A., The interface electronic structure of thiol terminated molecules on cobalt and gold surfaces. *J. Mater. Sci.* 2006, 41, 6198-6206.
9. Ulman, A., Formation and structure of self-assembled monolayers. *Chem. Rev.* 1996, 96, 1533-1554.
10. Galvin, P.; Thompson, D.; Ryan, K.B.; McCarthy, A.; Moore, A.C.; Burke, C.S.; Dyson, M.; MacCraith, B.D.; Gun'ko, Y.K.; Byrne, M.T.; *et al.*, Nanoparticle-based drug delivery: case studies for cancer and cardiovascular applications. *Cell. Mol. Life Sci.* 2011, 69, 389-404.
11. Jadzinsky, P. D.; Calero, G.; Ackerson, C. J.; Bushnell, D. A.; Kornberg, R. D., Structure of a thiol monolayer-protected gold nanoparticle at 1.1 angstrom resolution. *Science* 2007, 318, 430-433.
12. Walter, M.; Moseler, M.; Whetten, R.L.; Hakkinen, H., A 58-electron superatom-complex model for the magic phosphine-protected gold clusters (Schmid-gold, Nanogold®) of 1.4-nm dimension. *Chem. Sci.* 2011, 2, 1583-1587.

# Monofunctionalized Gold Nanoparticles Stabilized by a Single Dendrimer Form Dumbbell Structures upon Homocoupling

Jens Peter Hermes,<sup>†</sup> Fabian Sander,<sup>†</sup> Ulrike Fluch,<sup>†</sup> Torsten Peterle,<sup>†,‡</sup> Damien Thompson,<sup>‡</sup> Raphael Urbani,<sup>§</sup> Thomas Pfohl,<sup>§</sup> and Marcel Mayor<sup>\*,†,||</sup>

<sup>†</sup>Department of Chemistry, University of Basel, St. Johanns-Ring 19, CH-4056 Basel, Switzerland

<sup>‡</sup>Theory Modelling and Design Centre, Tyndall National Institute, University College Cork, Lee Maltings, Cork, Ireland

<sup>§</sup>Department of Chemistry, University of Basel, Klingelbergstrasse 80, CH-4056 Basel, Switzerland

<sup>||</sup>Institute of Nanotechnology, Karlsruhe Institute of Technology (KIT), P.O. Box 3640, D-76021 Karlsruhe, Germany

## Supporting Information

**ABSTRACT:** The assembly of dumbbell structures as organic–inorganic hybrid materials is presented. Gold nanoparticles (NPs) with a mean diameter of 1.3 nm were synthesized in very good yields using a stabilizing dendrimer based on benzylic thioether subunits. The extended dendritic ligand covers the NP surface and contains a peripheral protected acetylene, providing coated and monofunctionalized NPs. These NPs themselves can be considered as large molecules, and thus, applying a wet-chemical deprotection/oxidative acetylene coupling protocol exclusively provides dimers of NPs interlinked by a diethynyl bridge. The concept not only enables access to novel organic/inorganic hybrid architectures but also promises new approaches in labeling technology.

Gold nanoparticles (Au NPs) are promising model compounds for nanoelectronic devices,<sup>1,2</sup> sensor applications<sup>3</sup> and catalysis.<sup>4,5</sup> Au NPs are also intensively used for labeling, as represented in numerous review articles addressing this topic.<sup>6–9</sup> In many cases, Au NPs are functionalized with DNA or peptides as recognition sites for labeling purposes. These protocols are limited to aqueous or polar organic conditions and are usually statistical reactions with low yields of monofunctionalized Au NPs. To date, monofunctionalization of Au NPs in apolar organic media has been achieved only by the use of a solid support as a protecting group<sup>10,11</sup> or by ligand polymerization on the NP surface.<sup>12</sup> In addition, single polymer strands were reported to stabilize one NP on average.<sup>13</sup> The strategy presented here involves the design of an organic ligand that (i) controls the particle formation by coating and passivating the NP surface and (ii) allows the introduction of a controlled number of functional groups at the NP periphery. Such NPs exposing a restricted number of functional groups can be considered as molecules with nanoscale dimensions and can be addressed by wet-chemical protocols. While di- and monofunctionalized NPs are promising building blocks of well-defined organic–inorganic hybrid architectures, the latter ones are in addition particularly appealing as potential labels.

It was recently shown that benzylic thioether oligomers have promising stabilizing features as multidentate ligands during the synthesis of Au NPs.<sup>14</sup> In the presence of larger thioether

oligomers, NPs with narrow dispersity are obtained in excellent yields. Furthermore, these NPs are decorated with only two ligands, allowing the introduction of a controlled number of peripheral functional groups dictating their chemical behavior. Thus, these functionalized NPs can be considered as large artificial molecules; as a first example, Au NPs containing two peripheral ethynyl groups were interlinked to form oligomers by a wet-chemical oxidative acetylene coupling protocol.<sup>15</sup> By expanding the benzylic thioether motif to dendritic structures, we recently synthesized unfunctionalized dendrimers, and one second-generation representative was able to stabilize exactly one Au NP.<sup>16</sup> The observed 1/1 ligand/Au NP ratio might make available monofunctionalized NPs, which are much better suited both for labeling and as building blocks for discrete organic–inorganic hybrid architectures. The acetylene homocoupling of functionalized NPs is a new approach for covalent assembly of NP architectures in nonpolar organic media (the concept is illustrated in Figure 1). Other approaches for the direct assembly of NP dumbbells have been reported,<sup>10–12,17–20</sup> and recent review articles have presented the formation of various NP architectures and their interparticle forces.<sup>21–24</sup>

The thioether dendrimer design presented here is based on a structural motif that recently demonstrated its potential as a coating and surface-passivating ligand during the synthesis of Au NPs. Important design aspects are the dilution of the branching points and the steric surface protection using bulky *tert*-butyl groups in the “diluting” subunits. The reduced branching was chosen to favor enwrapping by the dendritic ligand rather than a scenario where the NPs grow inside a ball-shaped dendrimer.<sup>25,26</sup> Our dendritic ligands were further functionalized by introducing a central oligo(phenylene ethynylene) (OPE) rod comprising a central pyridine unit and a triisopropylsilyl (TIPS)-protected acetylene (Figure 1). The pyridine nitrogen not only provides an additional coordination site for the Au NP but was recently also shown to result in a perpendicular arrangement of the rod on the NP surface.<sup>27,28</sup> The masked acetylene is introduced as a peripheral functionality, providing an integer number of wet-chemically addressable functional groups in each obtained Au NP. The thioether dendrimers G1 and G2 were synthesized by  $S_N2$  reactions of already reported compounds (Scheme 1). The

Received: June 27, 2012

Published: August 23, 2012



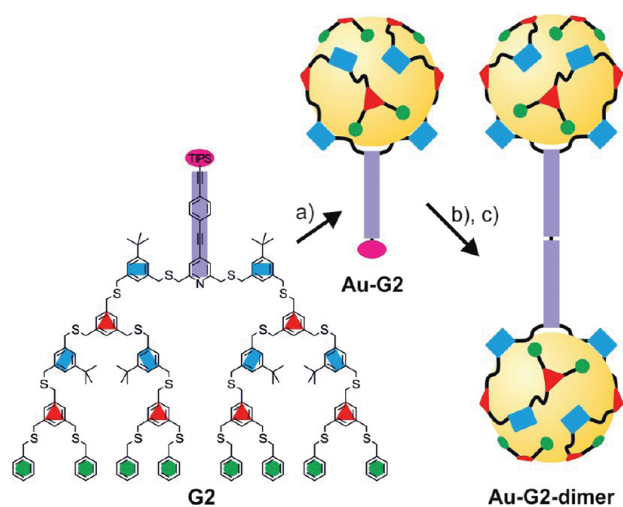
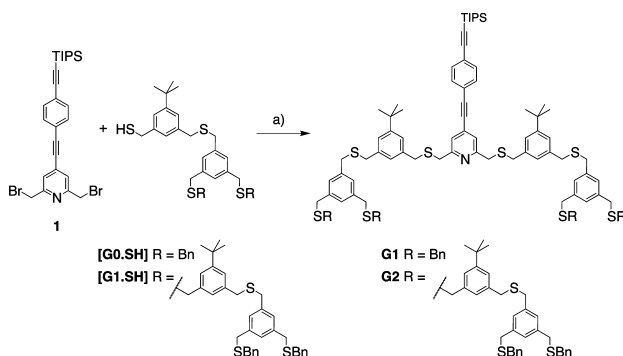


**Figure 1.** General concept of forming ligand-stabilized Au NPs and NP dimers. (a) NP synthesis: HAuCl<sub>4</sub>, TOAB, NaBH<sub>4</sub>, H<sub>2</sub>O/CH<sub>2</sub>Cl<sub>2</sub>. (b) Deprotection: TBAF, CH<sub>2</sub>Cl<sub>2</sub>. (c) Oxidative coupling: CuCl, TMEDA, O<sub>2</sub> (ambient air). For a space-filling representation, see Figure S4.

thiol dendrons<sup>16</sup> [G0.SH] and [G1.SH] have substituted the benzylic bromines of the OPE rod **1**.<sup>27</sup> The monofunctionalized ligands were obtained in good to excellent yields.

#### Scheme 1. Synthesis of Monofunctionalized Thioether Dendrimers G1 and G2 as Stabilizing Ligands for Au NPs<sup>a</sup>



<sup>a</sup>(a) NaH, THF, rt; 85–95%.

The Au NP-stabilizing features of thioether dendrimers **G1** and **G2** were investigated using techniques that have been successfully applied in earlier studies.<sup>15,16,27</sup> The formation of functionalized Au NPs was performed in a H<sub>2</sub>O/CH<sub>2</sub>Cl<sub>2</sub> solvent mixture following a protocol developed by Brust et al.<sup>29</sup> The dendritic ligands **G1** and **G2** dissolved in CH<sub>2</sub>Cl<sub>2</sub> were added to an aqueous solution of tetrachloroauric acid and the phase-transfer agent tetraoctylammonium bromide (TOAB) in CH<sub>2</sub>Cl<sub>2</sub>. Au NPs **Au-G1** and **Au-G2** were obtained after the addition of sodium borohydride in water. After aqueous workup and removal of TOAB with a precipitation/centrifugation protocol, the excess ligand was removed by gel-permeation chromatography (GPC). See the Supporting Information (SI) for a more detailed protocol. The purified NPs were obtained in yields exceeding 80% and were initially analyzed by UV/vis spectroscopy. The UV/vis spectra obtained (Figure S1 in the SI) showed the presence of Au NPs without a strong plasmon band of gold at 520 nm, indicating that the NPs had diameters below 2 nm.<sup>30,31</sup> The presence of the delocalized OPE structure in the

periphery of the NPs was manifested by a broad peak at ~300 nm. Single drops of the solutions used for UV/vis spectroscopy were transferred to carbon-coated copper grids (CCCGs) for transmission electron microscopy (TEM) investigations. The micrographs (Figure 2 and Figures S5 and S6) showed small Au

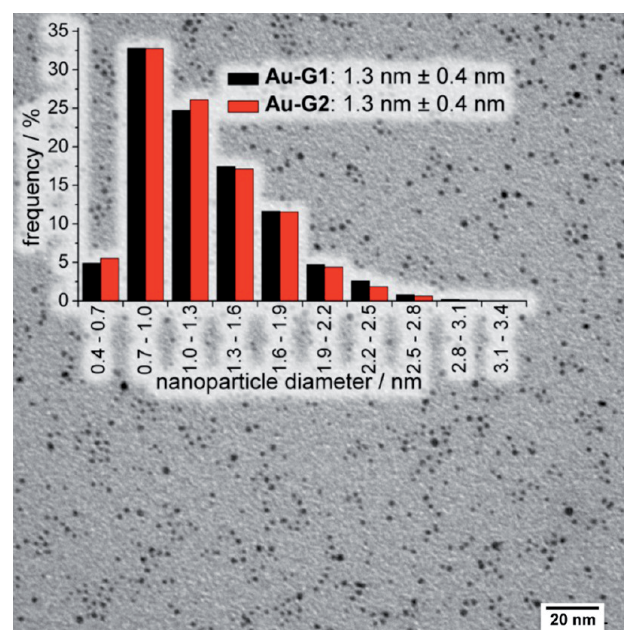


**Figure 2.** Representative dense TEM image of Au-G1 NPs. Inset: size distributions for Au-G1 (black) and Au-G2 (red) NPs.

NPs with a narrow size distribution. An automatic investigation method using ImageJ<sup>32</sup> was applied to measure the size (diameter) of the NPs formed (see the SI for the analysis protocol). More than 5000 NPs from more than 10 dense TEM images were analyzed. Similar size distributions were obtained for **Au-G1** and **Au-G2**, with mean diameters of 1.3 ± 0.4 nm (Figure 2 inset). These diameters are similar to those recently measured for Au NPs stabilized by the parent unfunctionalized dendrimers.<sup>16</sup> For **Au-G2**, small-angle X-ray scattering (SAXS) was employed as a second tool to determine the NP size. The measured 2D scattering signal was integrated to obtain an intensity plot (Figure S2) that suggested form factors of spheres. The plot was fitted with a model for polydisperse, spherical NPs, and a mean NP diameter of 1.3 nm with a standard deviation of 0.5 nm was obtained, corroborating the values obtained by TEM. To analyze the coating ligand/Au NP ratio, thermogravimetric analysis (TGA) of **Au-G1** and **Au-G2** was performed. To remove the organic shell in the TGA experiments, the dry NPs were heated to 950 °C. The weight loss curves were similar for the two samples (Figure S3). The amounts of weight loss were 21% in the case of **Au-G1** and 26% for **Au-G2**. These values were used to calculate the average number of gold atoms stabilized per dendrimer (see the SI for details). We found that on average one **G1** dendrimer stabilizes 30 Au atoms, while **G2** coats 50 atoms. The dimensions of the **Au-G1** and **Au-G2** NPs determined by TEM and SAXS suggest an average number of ~55 gold atoms per NP. In analogy to the parent ligand structure,<sup>16,28</sup> a single **G2** dendrimer or a pair of **G1** dendrimers are required to stabilize one Au NP.

The discrete number of coating ligands also results in an equally well-defined number of peripheral masked acetylene

functions per Au NP, and thus, the extent of surface functionalization per NP must be reflected in the connectivity of the NP subunits in the hybrid architectures obtained upon exposing them to acetylene coupling chemistry. While chains of NPs would be expected for the bifunctional **Au-G1**, similar to another example of bifunctional NPs,<sup>33</sup> the monofunctionalized analogue **Au-G2** should form dimers exclusively. Samples of both Au NPs (**Au-G1** and **Au-G2**) were exposed to a Glaser–Hay<sup>34</sup> wet-chemical oxidative acetylene coupling protocol. In brief, tetrabutylammoniumfluoride (TBAF) was first added to liberate the masked acetylene, and then tetramethylethylenediamine (TMEDA) and CuCl were added under ambient atmosphere to provide molecular oxygen. After 20 min, precipitation was observed only for the reaction mixture containing **Au-G1**, while the one containing **Au-G2** remained as a dark solution. The precipitation of bifunctional Au NPs due to the formation of too-long oligomeric chains was previously found for comparable systems.<sup>15,27</sup> To keep the oligomers short and dissolved, a small sample of the reaction mixture containing **Au-G1** was worked up after 10 min. After further dilution to avoid accidental proximities of NPs that were not covalently bound, samples were deposited on CCGs and investigated by TEM. The micrographs showed the presence of single NPs, dimers, and higher oligomeric assemblies of NPs. These oligomers were predominantly found as chains of NPs, and typical representatives of these **Au-G1** superstructures are displayed in Figure 3. A more comprehensive

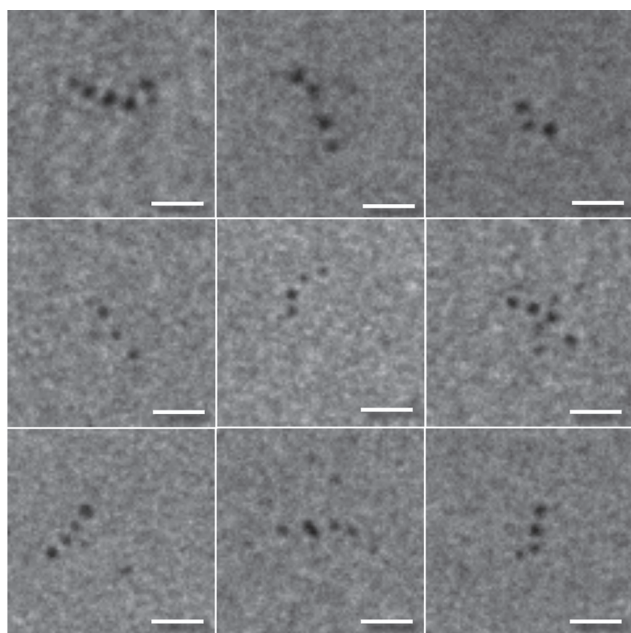


**Figure 3.** Representative TEM images of diluted solutions of **Au-G1** superstructures. The scale bars represent 10 nm.

overview of the micrographs is displayed in Figures S7 and S8. The chainlike arrangement of the NPs in these micrographs not only corroborates the wet-chemical coupling chemistry as the origin of the interlinked NPs but also supports the picture of having two functional groups per **Au-G1** NP on opposite sides. Strong similarities between **G1** and linear thioether ligands that were investigated in earlier studies<sup>14,15,27,35</sup> are obvious. Dendrimer **G1** and the linear ligands have similar sizes and consist of eight thioether moieties. NPs stabilized by these two ligands have comparable sizes with two coating ligands per NP.

When the ligands bear an acetylene, chains are formed upon oxidative acetylene coupling and precipitate if their lengths exceed a certain threshold value.<sup>15,27</sup>

In contrast to these bifunctional NPs, the monofunctionalized **Au-G2** NPs were expected to form dimers only, and indeed, even after prolonged reaction times or with excessive amounts of coupling chemicals, precipitation was not observed. The protected **Au-G2** NP monomers were first deprotected with a large excess of TBAF in  $\text{CH}_2\text{Cl}_2$ . After aqueous workup, the solution was concentrated to dryness using a stream of nitrogen. The homocoupling was then conducted in small amounts of  $\text{CH}_2\text{Cl}_2$  in an open reaction vessel for 3 h using excesses of CuCl and TMEDA (see the SI for a detailed protocol). Samples of the reaction mixture containing the NP hybrid architectures were deposited as highly diluted solutions on CCGs for TEM investigations. Thus, only a few NPs were present in each TEM image and showed sizes similar to the protected **Au-G2** monomers (Figure 4 and Figures S9 and S10). In these

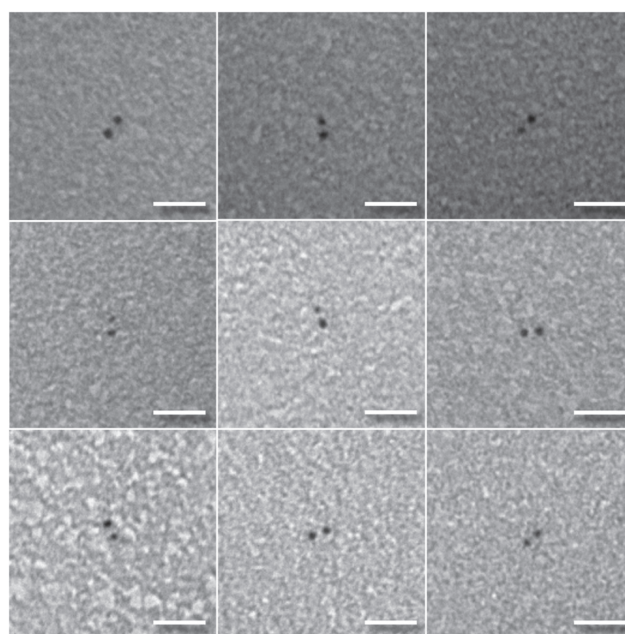


**Figure 4.** Representative TEM images of diluted solutions of **Au-G2** dimers. The scale bars represent 10 nm.

micrographs of diluted samples, the yield of NP dimers was analyzed. On 20 TEM images, ~400 NPs were counted, and almost half of them were dimers (47% yield); 46% of the NPs found were still present as monomers, and only 7% NPs existed in trimeric structures. The yield of dimers represents a 2–3-fold increase compared with the yield of superstructures formed with bifunctional NPs stabilized with linear thioether ligands (16–20%).<sup>27</sup> At first glance, the formation of trimeric structures from monofunctionalized NPs was surprising, and only a more detailed analysis of the interparticle spacing shed light on this unexpected observation.

From the TEM images of the diluted samples, the distance between the NPs in the dimers was analyzed, and the interparticle distance distribution displayed in Figure 5 was obtained. A bimodal distribution was found, with one maximum matching the expected distance of the straight spacer at 2.5 nm. This distance results from a perpendicular arrangement of the rod on the gold surface<sup>27</sup> triggered by the coordination of the

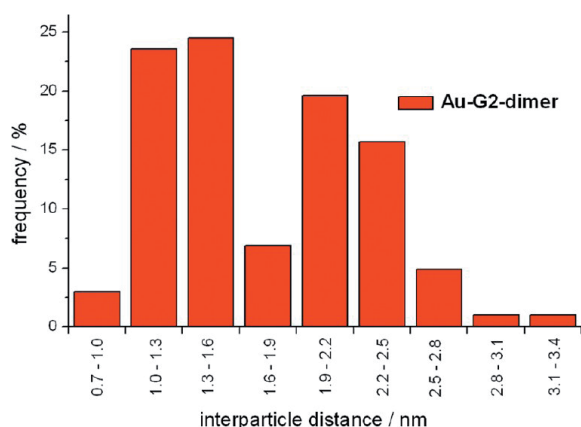


**Figure 5.** Interparticle distance distribution for Au-G2 dimers measured from TEM images of very dilute solutions.

nitrogen lone pair of the central pyridine subunit.<sup>28</sup> An unexpected second maximum of the interparticle distance distribution at 1.3 nm was observed, probably indicating coordination of the free acetylene to the gold surface of a neighboring NP. A careful inspection of the interparticle distances in the trimeric structures supported this hypothesis, since in all of the trimeric structures at least one short distance was found. This result also provides a rationale for their formation, namely, the coordination of an acetylene-functionalized NP to the surface of an NP that was already engaged in a dimer structure.

In summary, the concept of controlling the size and surface functionalization of NPs with dendritic multidentate ligands has been demonstrated. The obtained mono- and difunctionalized NPs can be considered as nanoscale molecules that can be interlinked to form organic–inorganic hybrid architectures by wet-chemical reactions. Our current interest is geared toward increasing the size and stability of the functionalized NPs and exploring the potential of the approach for NP materials other than gold.

## ■ ASSOCIATED CONTENT

### ● Supporting Information

Descriptions of dendrimer synthesis, NP synthesis, NP coupling, and NP analysis by UV/vis, TGA, TEM, and SAXS as well as representative TEM images of NP monomers, dimers, and oligomers. This material is available free of charge via the Internet at <http://pubs.acs.org>.

## ■ AUTHOR INFORMATION

### Corresponding Author

marcel.mayor@unibas.ch

### Present Address

<sup>1</sup>Evonik Industries AG, Untere Kanalstraße 3, D-79618 Rheinfelden, Germany

### Notes

The authors declare no competing financial interest.

## ■ ACKNOWLEDGMENTS

We gratefully acknowledge financial support by the EU through the project FUNMOL (no. 213382 of the call FP7-NMP-2007-SMALL-1), the Swiss National Science Foundation, the Swiss Nanoscience Institute, and National Research Project No. 62 “Smart Materials”.

## ■ REFERENCES

- (1) Homberger, M.; Simon, U. *Philos. Trans. R. Soc., A* **2010**, *368*, 1405.
- (2) Schmid, G. *Chem. Soc. Rev.* **2008**, *37*, 1909.
- (3) Zhang, X.; Guo, Q.; Cui, D. *Sensors* **2009**, *9*, 1033.
- (4) Corma, A.; Garcia, H. *Chem. Soc. Rev.* **2008**, *37*, 2096.
- (5) Della Pina, C.; Falletta, E.; Prati, L.; Rossi, M. *Chem. Soc. Rev.* **2008**, *37*, 2077.
- (6) Willner, I.; Willner, B. *Nano Lett.* **2010**, *10*, 3805.
- (7) Powell, R. D.; Hainfeld, J. F. *Micron* **2011**, *42*, 163.
- (8) Cutler, J. I.; Auyeung, E.; Mirkin, C. A. *J. Am. Chem. Soc.* **2012**, *134*, 1376.
- (9) Dykman, L.; Khlebtsov, N. *Chem. Soc. Rev.* **2012**, *41*, 2256.
- (10) Sung, K.-M.; Mosley, D. W.; Peelle, B. R.; Zhang, S.; Jacobson, J. M. *J. Am. Chem. Soc.* **2004**, *126*, 5064.
- (11) Worden, J. G.; Shaffer, A. W.; Huo, Q. *Chem. Commun.* **2004**, 518.
- (12) Krüger, C.; Agarwal, S.; Greiner, A. *J. Am. Chem. Soc.* **2008**, *130*, 2710.
- (13) Wilson, R.; Chen, Y.; Aveyard, J. *Chem. Commun.* **2004**, 1156.
- (14) Peterle, T.; Leifert, A.; Timper, J.; Sologubenko, A.; Simon, U.; Mayor, M. *Chem. Commun.* **2008**, 3438.
- (15) Peterle, T.; Ringler, P.; Mayor, M. *Adv. Funct. Mater.* **2009**, *19*, 3497.
- (16) Hermes, J. P.; Sander, F.; Peterle, T.; Urbani, R.; Pfohl, T.; Thompson, D.; Mayor, M. *Chem.—Eur. J.* **2011**, *17*, 13473.
- (17) Brousseau, L. C., III; Novak, J. P.; Marinakos, S. M.; Feldheim, D. L. *Adv. Mater.* **1999**, *11*, 447.
- (18) Dadosh, T.; Gordin, Y.; Krahn, R.; Khivrich, I.; Mahalu, D.; Frydman, V.; Sperling, J.; Yacoby, A.; Bar-Joseph, I. *Nature* **2005**, *436*, 677.
- (19) Claridge, S. A.; Mastroianni, A. J.; Au, Y. B.; Liang, H. W.; Micheel, C. M.; Fréchet, J. M. J.; Alivisatos, A. P. *J. Am. Chem. Soc.* **2008**, *130*, 9598.
- (20) Olson, M. A.; Coskun, A.; Klajn, R.; Fang, L.; Dey, S. K.; Browne, K. P.; Grzybowski, B. A.; Stoddart, J. F. *Nano Lett.* **2009**, *9*, 3185.
- (21) Westerlund, F.; Bjørnholm, T. *Curr. Opin. Colloid Interface Sci.* **2009**, *14*, 126.
- (22) Choi, C. L.; Alivisatos, A. P. *Annu. Rev. Phys. Chem.* **2010**, *61*, 369.
- (23) Bishop, K. J. M.; Wilmer, C. E.; Soh, S.; Grzybowski, B. A. *Small* **2009**, *5*, 1600.
- (24) Grzelczak, M.; Vermant, J.; Furst, E. M.; Liz-Marzán, L. M. *ACS Nano* **2010**, *4*, 3591.
- (25) Crooks, R. M.; Zhao, M.; Sun, L.; Chechik, V.; Yeung, L. K. *Acc. Chem. Res.* **2001**, *34*, 181.
- (26) Esumi, K.; Kameo, A.; Suzuki, A.; Torigoe, K. *Colloids Surf., A* **2001**, *189*, 155.
- (27) Hermes, J. P.; Sander, F.; Peterle, T.; Cioffi, C.; Ringler, P.; Pfohl, T.; Mayor, M. *Small* **2011**, *7*, 920.
- (28) Thompson, D.; Hermes, J. P.; Quinn, A. J.; Mayor, M. *ACS Nano* **2012**, *6*, 3007.
- (29) Brust, M.; Walker, M.; Bethell, D.; Schiffrin, D. J.; Whyman, R. *J. Chem. Soc., Chem. Commun.* **1994**, 801.
- (30) Alvarez, M. M.; Khoury, J. T.; Schaaff, T. G.; Shafiqullin, M. N.; Vezmar, I.; Whetten, R. L. *J. Phys. Chem. B* **1997**, *101*, 3706.
- (31) Hostetler, M. J.; Wingate, J. E.; Zhong, C.-J.; Harris, J. E.; Vachet, R. W.; Clark, M. R.; Londono, J. D.; Green, S. J.; Stokes, J. J.; Wignall, G. D.; Glish, G. L.; Porter, M. D.; Evans, N. D.; Murray, R. W. *Langmuir* **1998**, *14*, 17.
- (32) Magelhaes, P. J.; Ram, S. J.; Abramoff, M. D. *Biophotonics Int.* **2004**, *11*, 36.
- (33) DeVries, G. A.; Brunnbauer, M.; Hu, Y.; Jackson, A. M.; Long, B.; Neltner, B. T.; Uzun, O.; Wunsch, B. H.; Stellacci, F. *Science* **2007**, *315*, 358.
- (34) Hay, A. S. *J. Org. Chem.* **1962**, *27*, 3320.
- (35) Hermes, J. P.; Sander, F.; Peterle, T.; Mayor, M. *Chimia* **2011**, *65*, 219.

Supporting Information for the manuscript

## **Monofunctionalized Gold Nanoparticles stabilized by a Single Dendrimer form Dumbbell Structures upon Homocoupling**

*By Jens Peter Hermes, Fabian Sander, Ulrike Fluch, Torsten Peterle, Damien Thompson, Raphael Urbani, Thomas Pfohl and Marcel Mayor\**

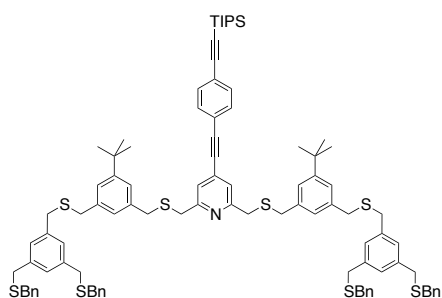
General methods . . . . .	S2
Experimental procedures for the synthesis of functional dendrimers . . . . .	S2
Gold Nanoparticle formation . . . . .	S4
Formation of nanoparticle dimers . . . . .	S4
Nanoparticle analysis . . . . .	S5
Representative TEM images . . . . .	S8
References . . . . .	S14

### General methods

All commercially available starting materials were of reagent grade and used as received. Absolute tetrahydrofuran (THF) was purchased from *Fluka*, stored over 4 Å molecular sieves, and handled under Argon. Methyl *tert*-butyl ether (MTBE), hexane and dichloromethane were of technical grade and distilled prior to use. Column chromatography purifications were carried out on *silica gel 60* (particle size 40-63 μm) from *Fluka*. Deuterated solvents were purchased from *Cambridge Isotope Laboratories*. <sup>1</sup>H and <sup>13</sup>C NMR spectra were recorded with a *Bruker DMX 400* instrument (<sup>1</sup>H resonance 400 MHz) or a *Bruker DRX 500* instrument (<sup>1</sup>H resonance 500 MHz) at 298 K. Matrix Assisted Laser Desorption Ionisation Time of Flight (MALDI-ToF) mass spectra were performed on a *Bruker microflex LRF* mass spectrometer in linear positive mode with 1.8.9-anthracenetriol as matrix. Elemental analyses were performed by W. Kirsch on a *Perkin-Elmer Analysator 240*. Gel Permeations Chromatography (GPC) was performed on a *Shimadzu Prominence* System with *SDV* preparative columns from *Polymer Standards Service* (two columns in series, 60 cm each, operating range: 100 – 30,000 g mol<sup>-1</sup>) using chloroform as eluent. Size exclusion chromatography (SEC) was performed using *Bio-Rad Bio-Beads S-XI Beads* (operating range 600 – 14000 g mol<sup>-1</sup>) with toluene as eluent.

## Experimental procedures for the synthesis of functional dendrimers

### G1 dendrimer

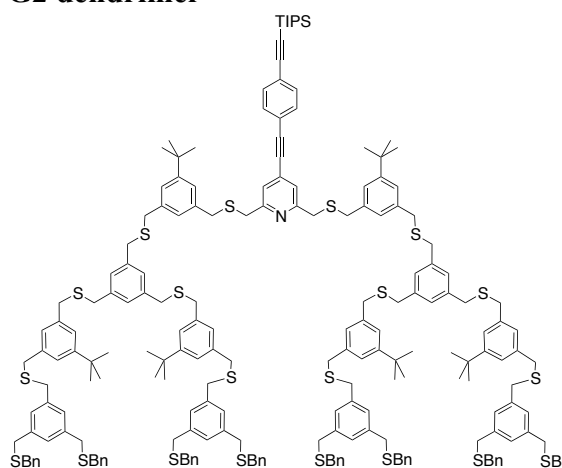


The free thiol dendron **[G0.SH]**<sup>1</sup> (94.0 mg, 0.16 mmol, 2.1 eq) and 2,6-bis(bromomethyl)-4-((4-((triisopropylsilyl)ethynyl)phenyl)ethynyl)pyridine<sup>2</sup> (41.5 mg, 0.076 mmol, 1 eq) were dissolved in dry tetrahydrofuran (5 ml) under an atmosphere of argon. The mixture was degassed by bubbling argon through the solution to avoid disulfide formation during the reaction. After this procedure, sodium hydride (60 % in mineral oil, 9 mg, 0.23 mmol, 3 eq) was added and the mixture was left stirring at room temperature for 1 h. The reaction was

quenched with water and extracted with MTBE three times. The combined organic fractions were washed with brine, dried over magnesium sulfate and evaporated to dryness. Purification of the crude product was achieved by column chromatography (hexane/dichloromethane 2:3, then 1:2, then 1:2 with 2% triethylamine) to yield **G1** (100.2 mg, 0.065 mmol, 85%) as slightly yellow oil.

<sup>1</sup>H-NMR (400 MHz, CDCl<sub>3</sub>): δ = 7.46 (*m*, 4H, ar-*H*), 7.31 – 7.21 (*m*, 24H, ar-*H*), 7.17 (*br*, 2H, ar-*H*), 7.12 (*br*, 2H, ar-*H*), 7.08 (*br*, 4H, ar-*H*), 7.05 (*br*, 2H, ar-*H*), 3.72 (*s*, 4H, CH<sub>2</sub>), 3.69 (*s*, 4H, CH<sub>2</sub>), 3.60 – 3.55 (*m*, 24H, CH<sub>2</sub>), 1.29 (*m*, 18H, butyl*H*), 1.14 (*s*, 21H, *i*Pr-*H*); MS (MALDI-TOF, *m/z*): broad peak around 1559 [M<sup>+</sup>]; Anal. calcd. for C<sub>96</sub>H<sub>109</sub>NS<sub>8</sub>Si: C 73.84, H 7.04, N 0.90; found: C 73.88, H 7.20, N 0.97.

## G2 dendrimer



[**G1.SH**]<sup>1</sup> (1036 mg, 0.709 mmol, 2.25 eq) and 2,6-bis(bromomethyl)-4-((4-((triisopropylsilyl)ethynyl)phenyl)ethynyl)pyridine<sup>2</sup> (172 mg, 0.315 mmol, 1 eq) were dissolved in dry tetrahydrofuran (15 ml) under an atmosphere of argon. The mixture was degassed by bubbling argon through the solution to avoid disulfide formation during the reaction. After this procedure, sodium hydride (60 % in mineral oil, 51 mg, 1.26 mmol, 4 eq) was added and the mixture was left stirring at room temperature for 3 h. The reaction was quenched with water and extracted with MTBE three times. The combined organic fractions were washed with brine, dried over magnesium sulfate and evaporated to dryness. Purification of the crude product was achieved by column chromatography (cyclohexane:dichloromethane 1:4 with 1% triethylamine) followed by recycling GPC (8 cycles) to yield **G2** (987 mg, 0.298 mmol, 95%) as light orange very viscous oil.

<sup>1</sup>H-NMR (400 MHz, CDCl<sub>3</sub>): δ = 7.45 (*m*, 4H, aryl-*H*), 7.32 – 7.03 (*m*, 78H, aryl-*H*), 3.71 (*s*, 4H, CH<sub>2</sub>), 3.67 (*s*, 4H, CH<sub>2</sub>), 3.59 – 3.54 (*m*, 72H, CH<sub>2</sub>), 1.28 (*s*, 54H, C(CH<sub>3</sub>)<sub>3</sub>), 1.14 (*s*, 21H, *i*Pr-*H*); <sup>13</sup>C-NMR (125 MHz, CDCl<sub>3</sub>): δ = 158.6, 151.6, 151.5, 138.7, 138.4, 138.0, 137.9,

137.8, 137.7, 132.1 (2×), 131.7, 131.6, 129.0, 128.5, 128.3, 127.0, 126.9, 126.8, 125.1, 124.9, 124.8, 124.3, 123.0, 121.9, 93.6, 93.3, 88.6, 37.3, 36.1, 35.9, 35.7, 35.6, 35.4, 34.6, 31.4, 16.7, 11.3; **MS** (MALDI-TOF, *m/z*): broad peak around 3416 [ $M^+$ ]; Anal. calcd. for  $C_{208}H_{237}NS_{20}Si$ : C 73.04, H 6.98, N 0.41; found: C 72.49, H 7.00, N 0.68.

### **Gold nanoparticle formation and purification, general procedure:**

Gold nanoparticle (Au NP) syntheses were carried out on a 2.5–3.5 mmol scale with respect to the thioether dendrimers **G1** or **G2**. Tetrachloroauric acid (8 eq for **G1** and 20 eq for **G2**) was dissolved in deionized water (2.5 mL). One equivalent of gold precursor was used per thioether moiety of the respective dendrimer. A solution of TOAB (16 eq for **G1** and 32 eq for **G2**) in  $CH_2Cl_2$  (2.5 mL) was added, and the two-phase mixture stirred until the aqueous phase became colorless. The respective ligand **G1** or **G2** (1 equivalent) was dissolved in dichloromethane (2.5 mL) and then added to the reaction mixture, followed by a freshly prepared solution of sodium borohydride (64 eq for **G1** and 132 eq for **G2**) in water (2.5 mL). After 15–20 min stirring, the resulting strongly colored  $CH_2Cl_2$  phase was separated, and the aqueous phase was washed twice with  $CH_2Cl_2$ . The combined organic fractions were dried over magnesium sulfate, filtered, and concentrated to a volume of ca. 2 mL. Ethanol (20 mL) was added to precipitate the NPs, which were then centrifuged. The supernatant was discarded, and the procedure was repeated twice. After this procedure, the NPs were subjected to SEC or GPC. The colored, NP-containing fractions were collected, the removal of excess ligand checked by UV/vis and the solvent was removed using a rotary evaporator without heating or by a  $N_2$ -stream.

### **Formation of gold nanoparticle dimers, general procedure:**

The formation of Au NP aggregates and dimers was done on a 1 mg scale regarding **Au-Gx**. The acetylene functionalized Au NPs were dispersed in dichloromethane (200  $\mu$ l) and tetra-*n*-butylammonium fluoride (1M in tetrahydrofuran, 50  $\mu$ l) was added. The mixture was left stirring for 1 hour, and quenched with water, extracted with dichloromethane and dried with  $MgSO_4$ . After filtration the solution was concentrated and *N,N,N',N'*-tetramethylethylenediamine (50  $\mu$ l) and copper(I) chloride (3 mg) were added. After 15 minutes all NPs **Au-G1** were precipitated as oligomers **(Au-G1)<sub>>4</sub>**, while **Au-G2-dimers** were still reacting. The dimerization reaction was left stirring for 3 hours and then quenched with a saturated solution of ammonium chloride, extracted with dichloromethane and dried with  $MgSO_4$ . After filtration the solution was concentrated and investigated by TEM on carbon coated copper

grids. Highly diluted solutions were used for deposition on the grids to avoid accidental proximity of not covalently linked NPs. Interparticle distances were measured manually on the TEM micrographs mainly from dimers and some trimers.

## Nanoparticle analysis

### *UV/vis spectroscopy*

UV/vis spectra were recorded on a *Shimadzu UV 1800* spectrophotometer in  $\text{CH}_2\text{Cl}_2$ . Figure S1a shows the UV/vis spectra of Au NPs **Au-G1** and **Au-G2**, respectively. We identify the delocalized OPE system as peak around 300 nm and the small plasmon resonance band of Au NPs at 520 nm. The NP should be below 2 nm, as there is no distinct peak at 520 nm.<sup>3,4</sup> Both spectra are very similar indicating similar sizes of Au NPs. The difference in height of the OPE peak might be explained by an excess ligand that was present in the sample of **Au-G2**.

Figure S1b shows the representative UV/vis spectra of the NPs **Au-G2** before and after the coupling. The shoulder at 520 nm stayed the same while the OPE band shows a bathochromic shift due to the elongation of the delocalized OPE system. The plasmon resonance probably did not shift because the ratio of interparticle distance and NP diameter does not favor a plasmonic coupling.

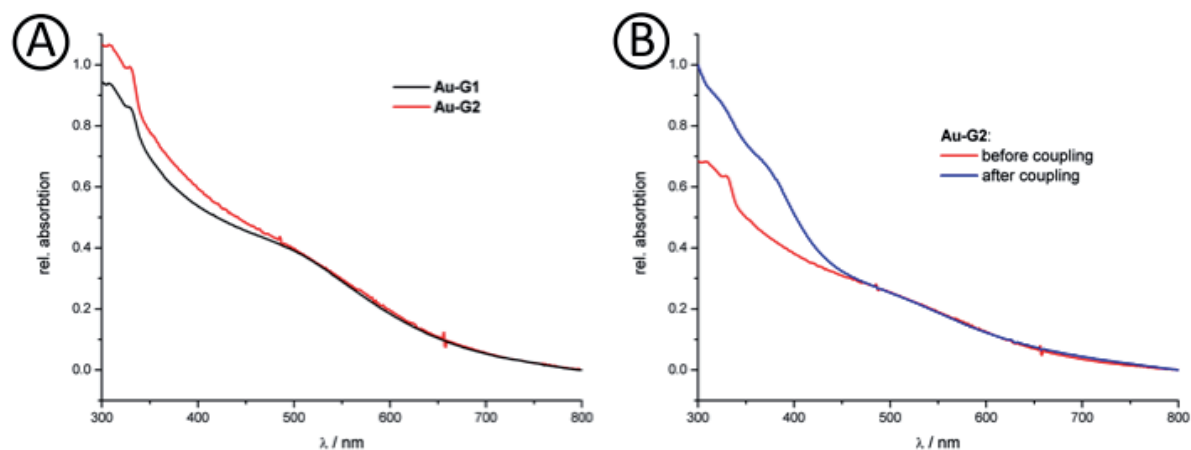


Figure S1. UV/vis spectra of Au NPs: a) **Au-G1** (black) and **Au-G2** (red); b) **Au-G2** before (red) and after the acetylene coupling (blue). All spectra are normalized to fit at 520 nm.

### *Transmission Electron Microscopy (TEM)*

TEM was performed on a *Philips CM100* transmission electron microscope at 80 kV. Electron micrographs were recorded on a 2000 by 2000 pixel charge-coupled device camera



*Veleta* from *Olympus*. The micrographs were recorded with a magnification of 180kx leading to micrographs with 520 nm by 520 nm and a size of 0.26 nm per pixel. Therefore the column width of the histograms was chosen to be 0.3 nm. One NP has a diameter of four pixels and an area of ten to twelve pixels.

The NPs were deposited by carefully putting a drop of the NP dispersion on top of a thin carbon film that spanned a perforated holey carbon support film covering a gold-plated copper microscopy grid. The remaining solvent was directly blotted with filter paper and the grid air dried.

#### *Nanoparticle diameter*

The NP diameters were measured automatically using the program *imageJ*.<sup>5</sup> The rather dense images (see micrographs: Figure S4-S5) were first transferred into 8-bit greyscale and then into black and white using the function “Threshold” and the setting “intermodes”. The area of the NPs was measured with “Analyze particles”. The particles on edges were excluded and holes included. Au NPs were measured with areas from 0.4 nm<sup>2</sup> till infinity and with circularities from 0.9-1. We did not consider particles with an area less than 0.4 nm<sup>2</sup> because otherwise the general noise would be counted as particles. As the final diameters were calculated from the measured areas we needed to focus on perfectly spherical NPs to avoid mistakes upon calculation. More than 80 % percent of NPs had circularities above 0.9. NP sizes were measured from more than ten dense micrographs (around 5,000 counts of NPs).

#### *(Small) Angle X-Ray Scattering, SAXS*

A Bruker AXS Nanostar setup, including an Incoatec Cu-I $\mu$ S microfocused X-ray source ( $\lambda = 0.154$  nm) with Montel multilayer optics at a generator power of 40W (45kV, 650 $\mu$ A) and a virtually noise-free, real-time Vântec 2D-detector with photon counting ability, was used to perform X-ray measurements in the range of scattering vectors from 0.5 - 7.5 nm<sup>-1</sup>. The 2D detector image of the NPs dissolved in benzene and transferred in glass capillaries (diameter 1.5 mm) were taken under vacuum at ambient temperatures with exposure times of 4 h per sample and azimuthally-averaged using SAXS v.4.1.36 software from Bruker to produce 1D intensity profiles (Figure S2a). The software GNOM<sup>6</sup> was used to transform the 2D scattering signals by applying an inverse Fourier transformation. A distance distribution of the scattering electrons was obtained, which should have its maximum at the NP radius (Figure S2b). The maximum of the distribution matches with 6.57 Å perfectly the radius calculated by the initial fit.

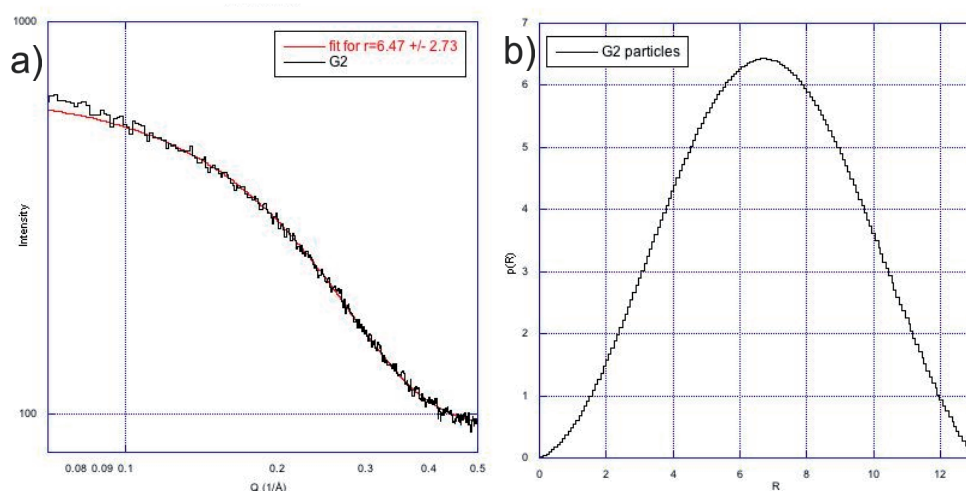


Figure S2. a) SAXS intensity plot in a log-log representation and best fit for **Au-G2**; b) distance distribution of the scattering electrons (Å) of **Au-G2** calculated by the software GNOM;<sup>6</sup> as expected the maximum matches the NP radius.

#### *Thermogravimetric analysis (TGA)*

Thermogravimetric analyses were performed on a *Mettler Toledo TGA/SDTA851<sup>e</sup>*. The samples were heated from 35°C to 950°C with an increase of 10°C/min. Samples **Au-G1** and **Au-G2** show similar weight loss curves (Figure S3). Decomposition starts at around 200 °C and reaches a plateau between 600 and 700 °C. The weight loss is attributed to the decomposition and removal of the organic shell from the NP surface and the plateau is interpreted as the end of this process, when all the organic coating has been removed. Comparable weight losses of 21 % and 26 % were measured for **Au-G1** and **Au-G2**, respectively.

The mass of gold per organic ligand was calculated from the ratio

$$\text{mass}(\text{Au per ligand}) = \frac{\text{mass}\%(\text{Au})}{\text{mass}\%(\text{ligand})} \cdot \text{mass}(\text{ligand}) \quad (1)$$

The number of gold atoms per ligand is calculated from

$$\text{Au atoms per ligand} = \frac{\text{mass}(\text{Au per ligand})}{\text{molecular weight}(\text{Au})} \quad (2)$$

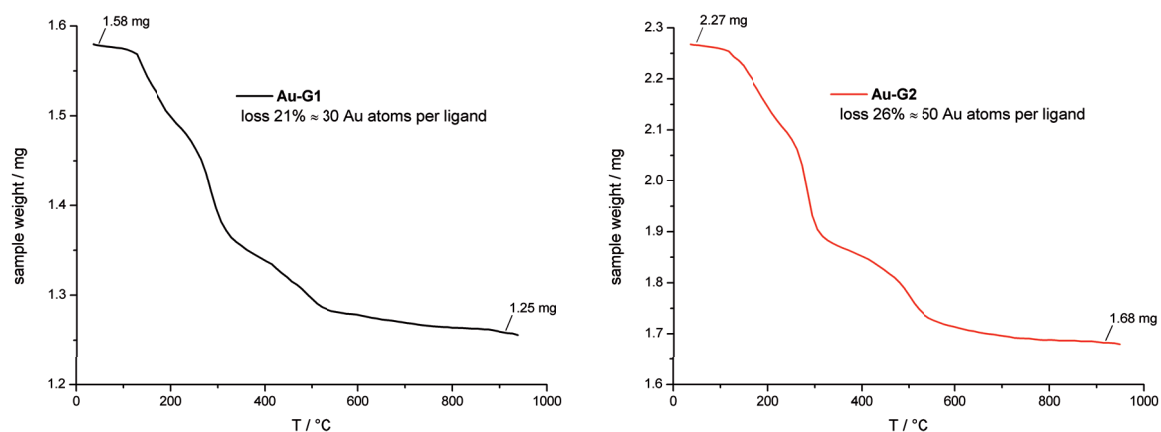


Figure S3. Thermogravimetric analyses of **Au-G1** (black) and **Au-G2** (red).

### Space filling model

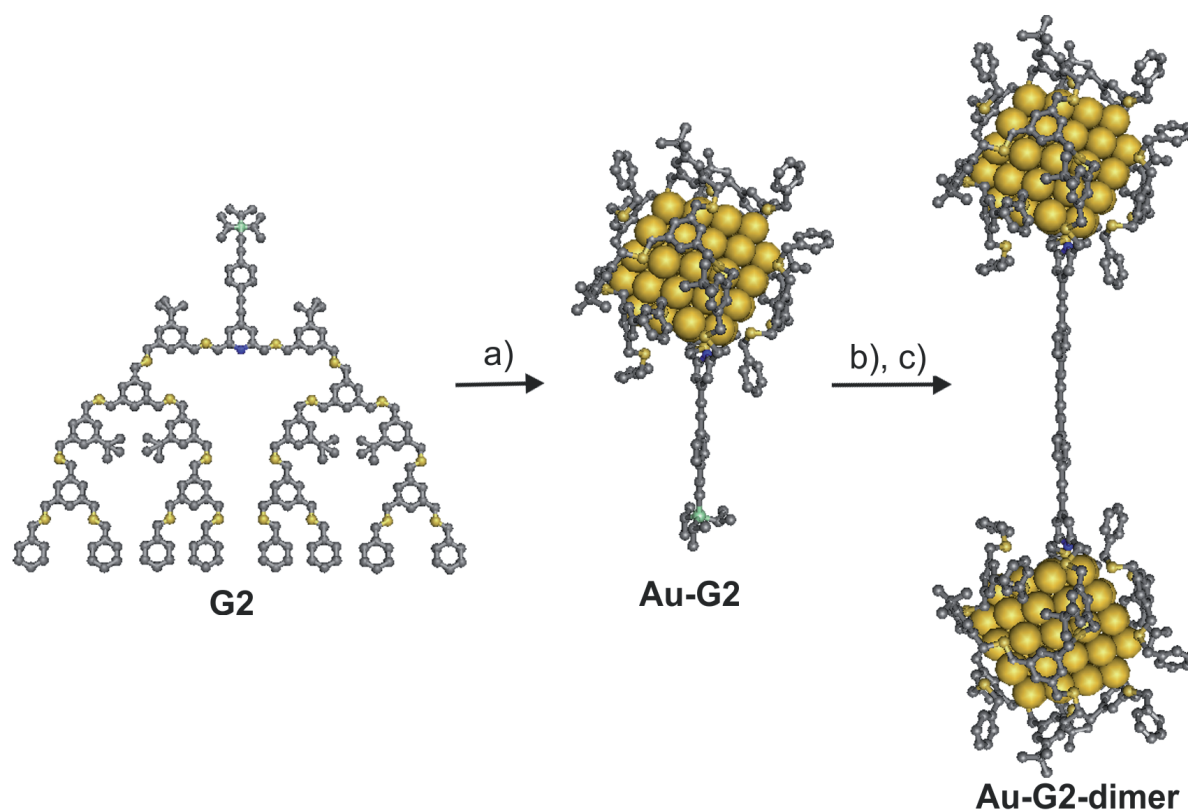


Figure S4. Space filling representation of the general concept; a) NP synthesis:  $\text{HAuCl}_4$ , TOAB,  $\text{NaBH}_4$ ,  $\text{H}_2\text{O}/\text{CH}_2\text{Cl}_2$ ; b) deprotection: TBAF,  $\text{CH}_2\text{Cl}_2$ ; c) oxidative coupling:  $\text{CuCl}$ , TMEDA,  $\text{O}_2$  (ambient air).

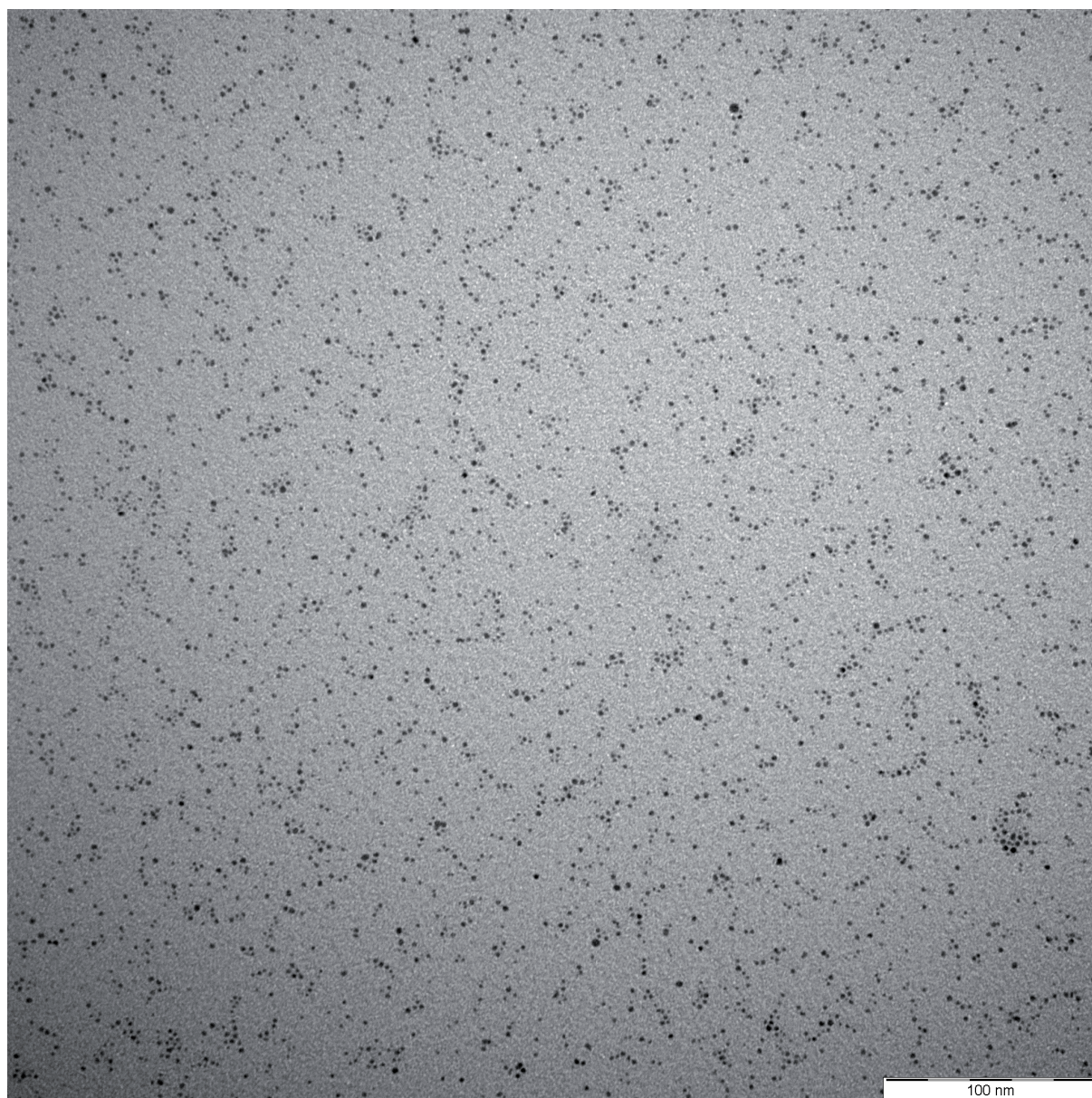
**Representative TEM images of ligand-stabilized gold nanoparticles**

Figure S5. TEM image of a concentrated solution of Au NPs **Au-G1**.

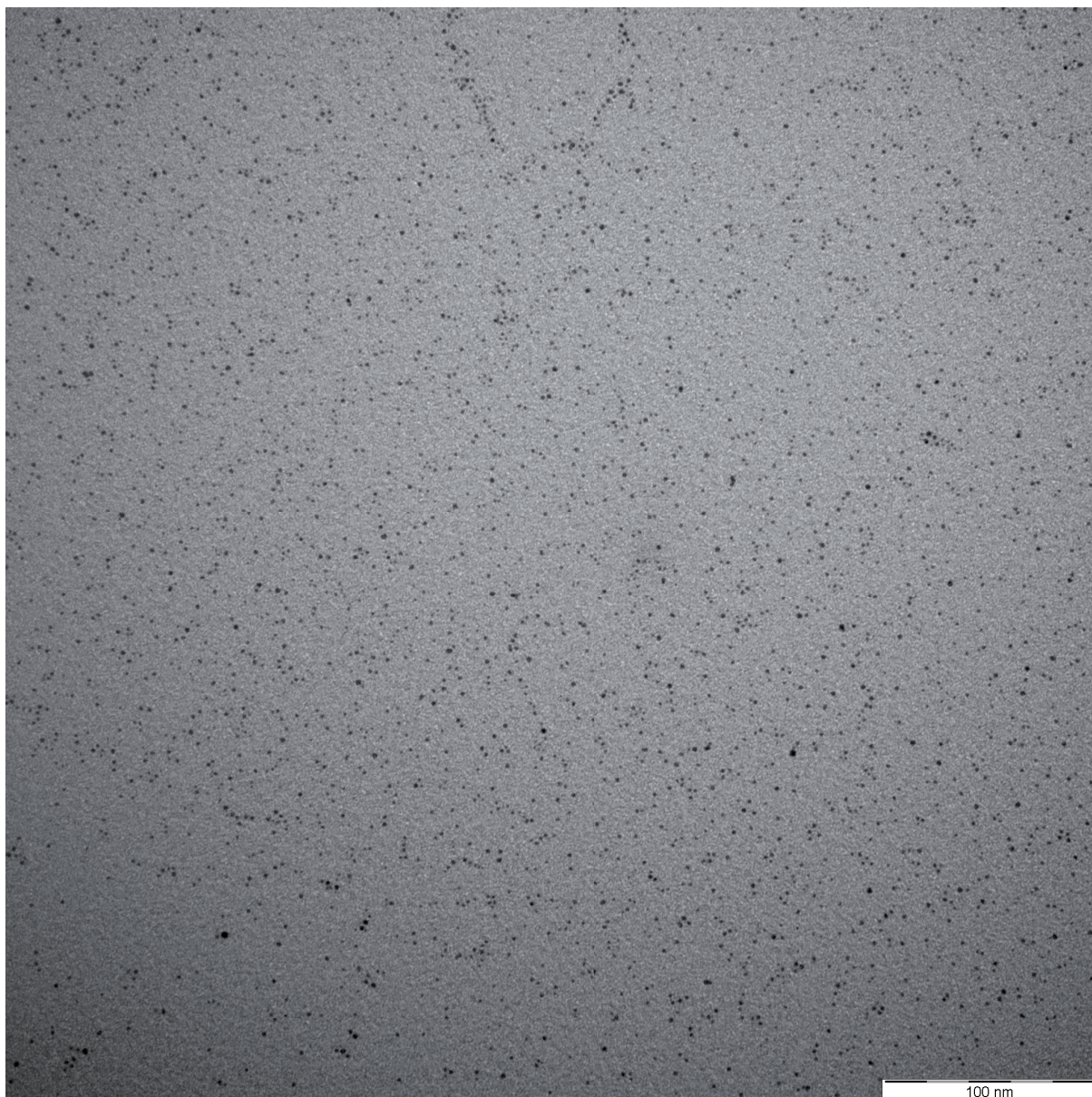


Figure S6. TEM image of a concentrated solution of Au NPs **Au-G2**.

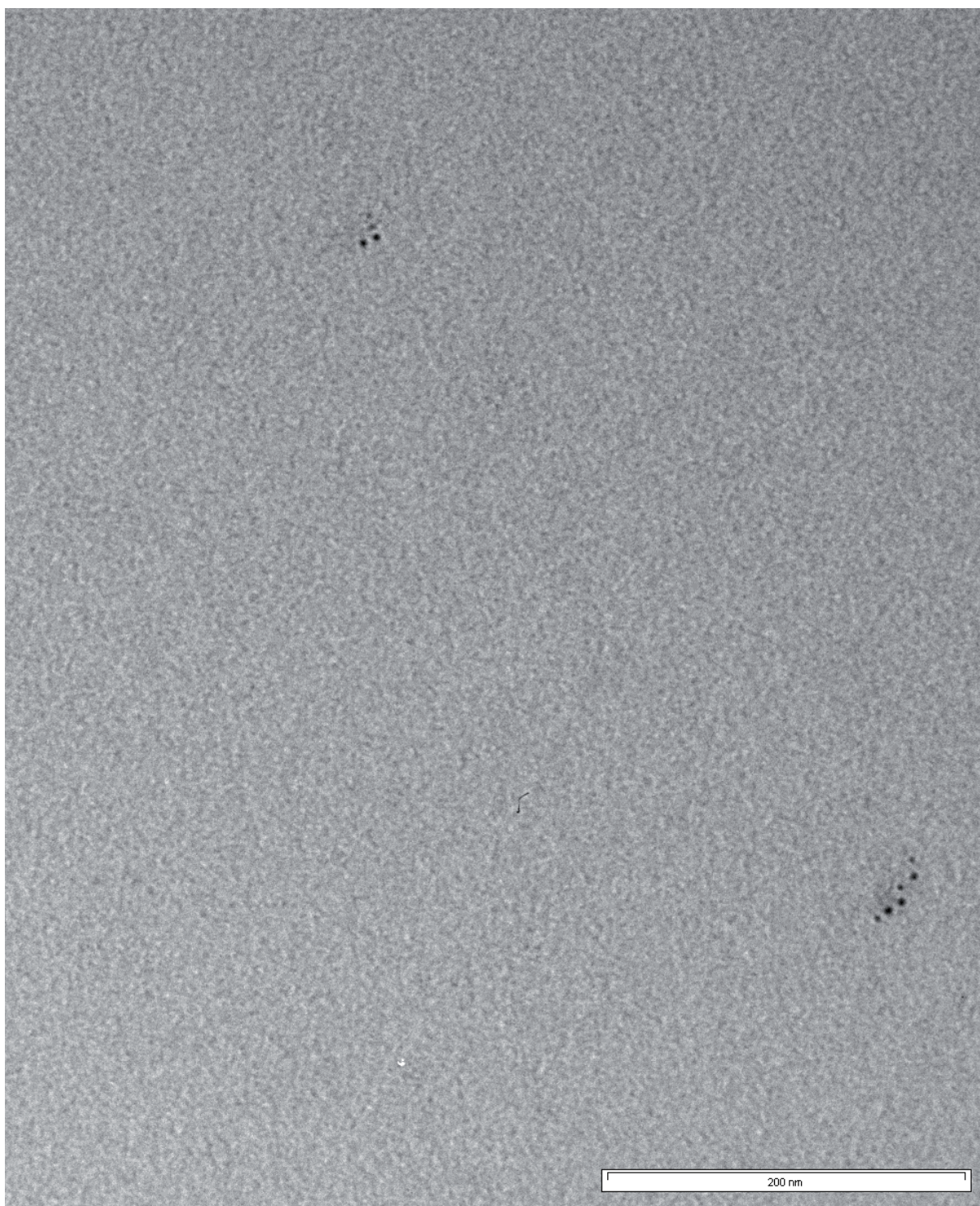


Figure S7. TEM image of a diluted solution of **Au-G1-oligomers**.

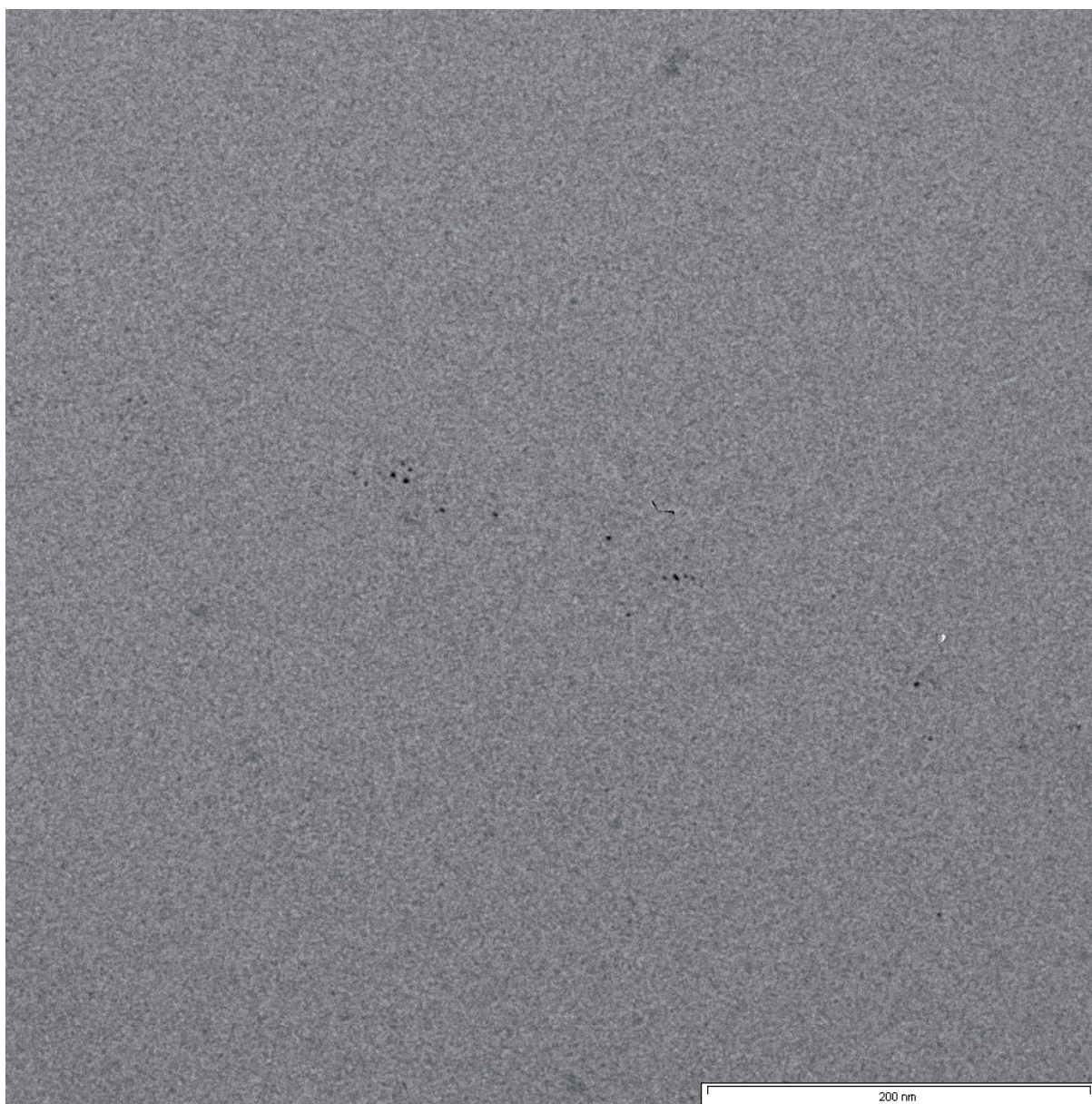


Figure S8. TEM image of a diluted solution of **Au-G1-oligomers**.

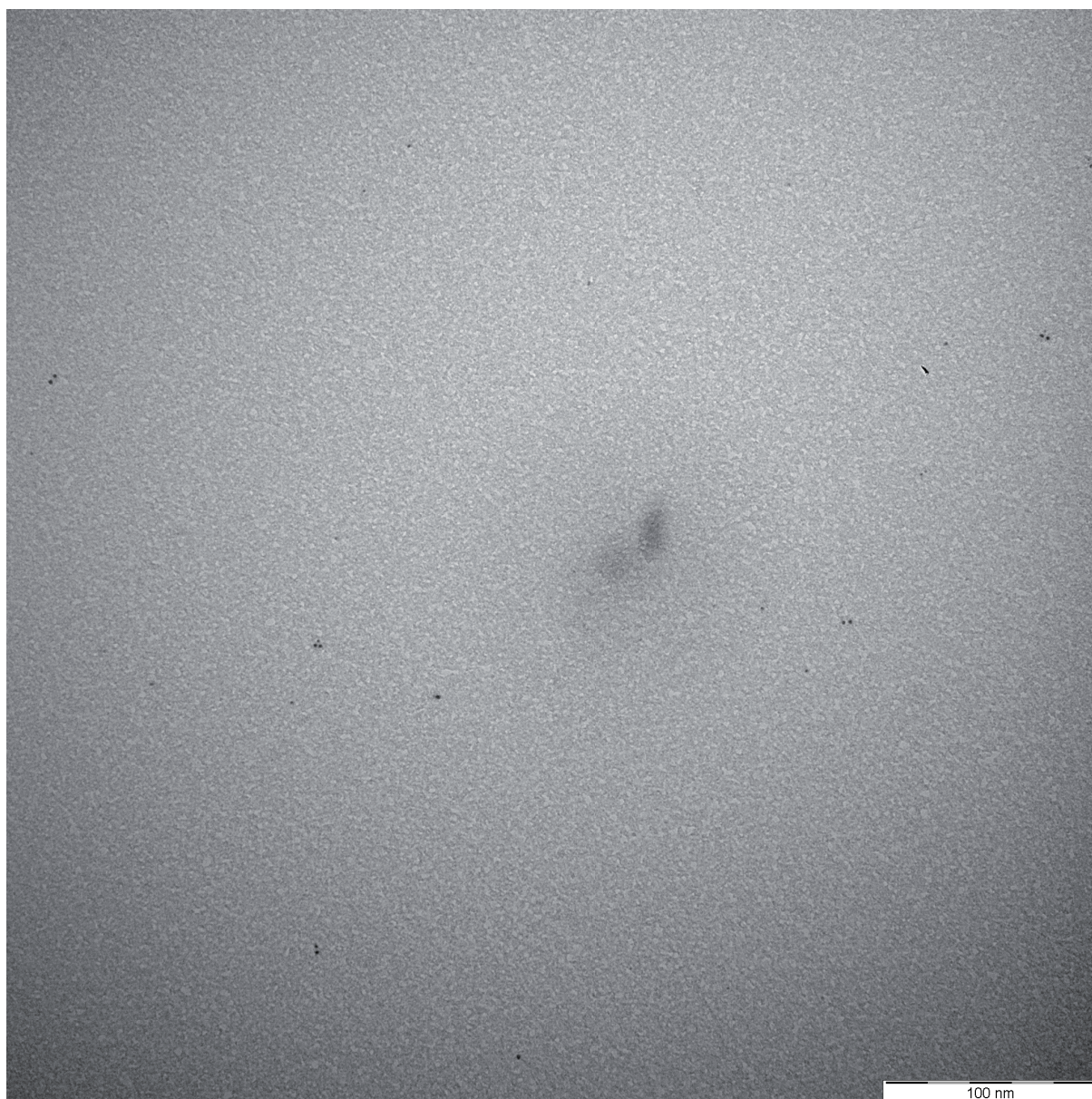


Figure S9. TEM image of a diluted solution of **Au-G2-dimers**.



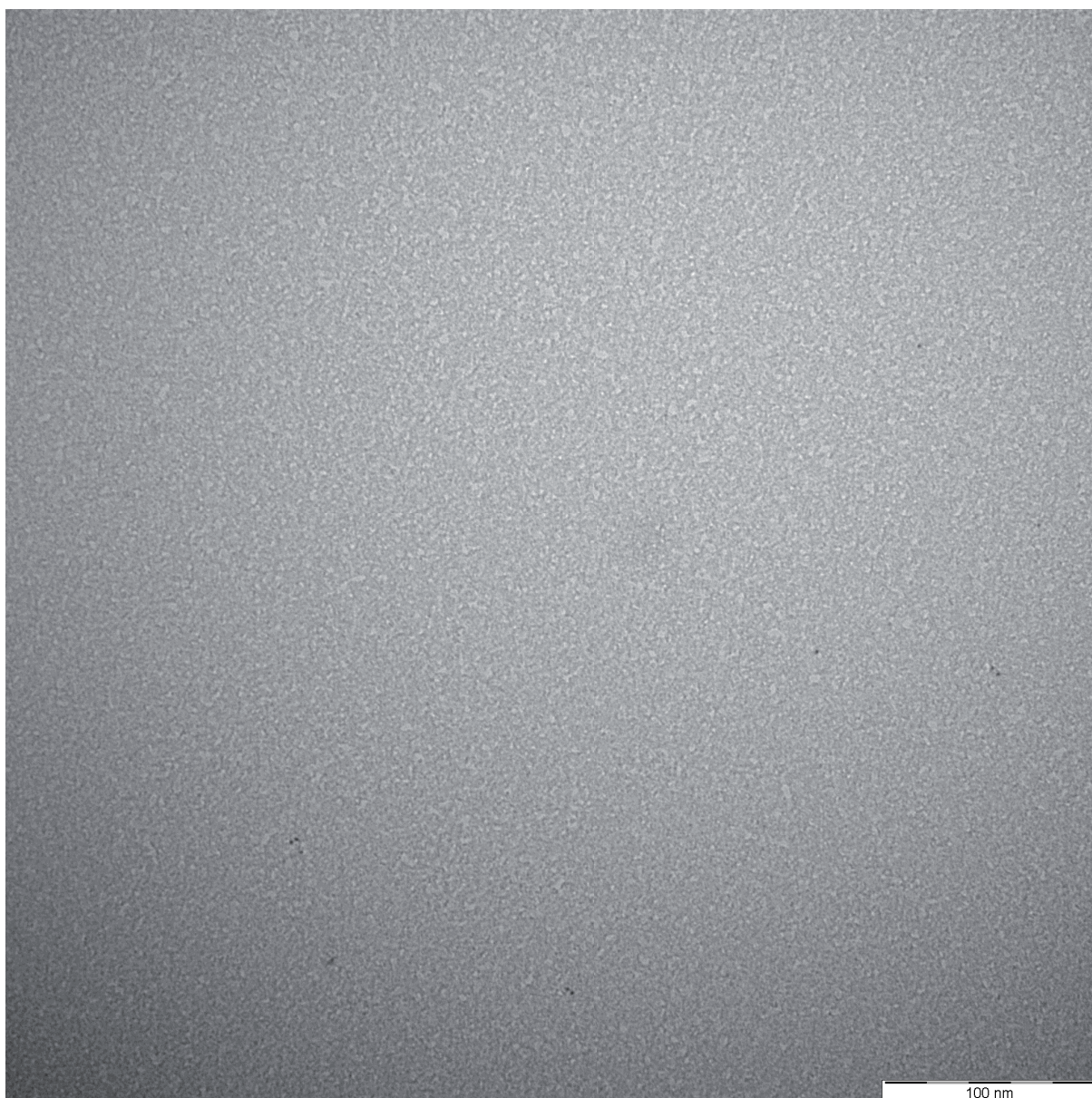


Figure S10. TEM image of a diluted solution of **Au-G2-dimers**.

**References**

- (1) Hermes, J. P.; Sander, F.; Peterle, T.; Urbani, R.; Pfohl, T.; Thompson, D.; Mayor, M. *Chem. Eur. J.* **2011**, *17*, 13473–13481.
- (2) Hermes, J. P.; Sander, F.; Peterle, T.; Cioffi, C.; Ringler, P.; Pfohl, T.; Mayor, M. *Small* **2011**, *7*, 920–929.
- (3) Alvarez, M. M.; Khoury, J. T.; Schaaff, T. G.; Shafiqullin, M. N.; Vezmar, I.; Whetten, R. L. *J. Phys. Chem. B* **1997**, *101*, 3706–3712.
- (4) Hostetler, M. J.; Wingate, J. E.; Zhong, C.-J.; Harris, J. E.; Vachet, R. W.; Clark, M. R.; Londono, J. D.; Green, S. J.; Stokes, J. J.; Wignall, G. D.; Glish, G. L.; Porter, M. D.; Evans, N. D.; Murray, R. W. *Langmuir* **1998**, *14*, 17–30.
- (5) Magelhaes, P. J.; Ram, S. J.; Abramoff, M. D. *Biophotonics Int.* **2004**, *11*, 36–42.
- (6) Svergun, D. I. *J. Appl. Crystallogr.* **1992**, *25*, 495–503.



## Controlled Formation of Bi- and Monofunctionalized Gold Nanoparticles

Jens Peter Hermes and Marcel Mayor\*

*Manuscript prepared for submission*

### Introduction

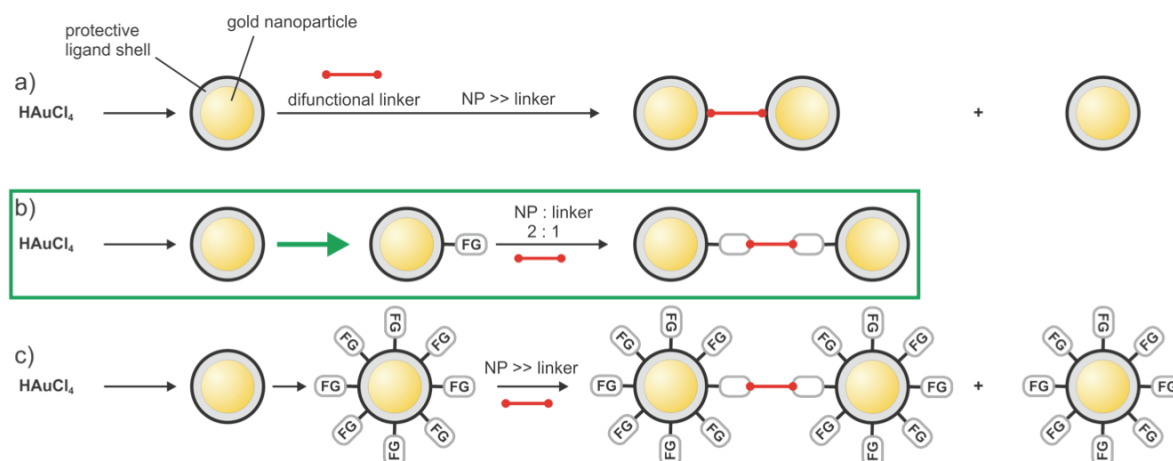
Gold nanoparticles (Au NPs) are attracting renewed interest due to their usefulness in chemistry, electronics, catalysis and medicine.[1–3] However, the formation and utilization of Au NPs dates back far before their current vogue, with dying of glass by freshly precipitated colloidal gold solutions already known in late Greco-Roman times.[4] A famous example is the 4<sup>th</sup> Century Lycurgus cup, which appears red when lit from behind and green when lit from the front, as light is absorbed and scattered by nanocrystals of a gold–silver alloy. In 1857, Faraday was the first to connect the color with the size of Au NPs and was the first to investigate their deliberate synthesis.[5] The next milestone was the formation and analysis of citrate-stabilized NPs by Turkevich et al. in 1951.[6] More recent breakthroughs demonstrated ultrahigh precision in the formation of passivated Au NPs. [7–10] Schmid et al. presented the gold cluster  $\text{Au}_{55}(\text{PPh}_3)\text{Cl}_6$ , [7] which has become known as the ‘Schmid-cluster’, having stimulated the areas of quantum electronics[8] and labeling.[11] Brust et al. introduced a two-phase protocol that allowed aqueous tetrachloroauric(III) acid ( $\text{HAuCl}_4$ ) to be transferred into the organic phase (toluene) using tetraoctylammonium bromide (TOAB). The gold salt was then reduced with aqueous sodium borohydride in the presence of an alkanethiol yielding stable Au NPs with diameters below 3 nm and narrow size distributions.[9]

Since then the number of studies dedicated to Au NPs increased significantly over the past two decades, exploiting the unmatched stability of Au NPs among metal nanoparticles. They also show fascinating size and shape dependent properties[12] and have various applications. They are used as plasmonic devices, for example as a plasmonic ruler to measure the distance between two NPs attached to linkers of unknown length.[13,14] Extended research is conducted on Au NPs in nanoelectronics[2,15] such as information storages devices.[16] As Au NPs of different sizes are easily visualized by electron microscopy they are the label of choice for visualizing and investigating bio- and macromolecules.[17–20] Au NPs

also have numerous current and future applications as sensors[21–23] and as catalysts.[24,25]. More background information is available within extended review articles[1,2,26] and in a special issue of *Chem. Soc. Rev.* entitled “Gold - Chemistry, Materials and Catalysis”.

## Towards Applications

As mentioned above, Au NPs have a broad variety of current and future applications. One very important application is their use in home pregnancy tests where NPs are coated with a certain antibody and their coagulation occurs if the specific antigen is present in the urine, triggering a plasmonic response that can be detected by the naked eye as the clumps of coagulated NPs are trapped in a filter.[27] If the specific antigen is not present the NPs will remain separated and the coloring of the filter will not occur. In order for this pregnancy test to work certain conditions need to be fulfilled (Figure 1). 1) The NPs need to be formed in a certain size and they need to be stable. 2) The surface of the NP needs to be functionalized with the antibody and 3) the specific antigen must be present. These steps are vital for the controlled assembly of Au NPs, and one can choose between two alternative strategies. One can either i) form unfunctionalized NPs (Figure 1a) or NPs bearing many functionalities (Figure 1c) and use linker molecules and experimental conditions that favor formation of discrete NP architectures (Figure 1a,c) or ii) one can try to control the number of functional groups on the NP surface for the subsequent assembly (Figure 1b, green arrow in green box). Examples of the first approach may be found in the studies of Dadosh et al. and Brousseau III et al., who formed NP dimers of citrate-stabilized NP using a carefully chosen ratio of unfunctional NPs to dithiol linker molecules (Figure 1a).[28,29] Simon and coworkers used an excess of multifunctional NPs to click them to a DNA template and obtained ordered chain-like architectures.[30] There are many other examples that utilize similar approaches and some are presented in recent reviews that show the richness of NP assemblies.[31–35] However, within this review we focus on the controlled functionalization (green arrow in Figure 1b) of Au NPs with one or two functional groups (FG) on the NP surface and present some examples for their further utilization.



## Controlled Functionalization of Gold Nanoparticles

There are various approaches to introduce functionalities onto a NP surface. One way is to form NPs stabilized by weak ligands like citrate or amines first. Afterwards the ligand is replaced by a stronger-binding alkanethiol molecule[38] followed by exchange with a functional thiol, e.g. OPE-dithiol.[36] This approach is very convenient if many functional groups are envisaged or if the concentration of linker molecules used for the subsequent NP assembly may be controlled. It is also possible to exchange the weak ligand with a mixture of functional and unfunctional thiols at the same time for an increased control over the number of functionalities on the NP surface. Stoddart and coworkers used a molar ratio of 3000:1 of alkanethiol and functional thiol to obtain mono-functionalized NPs in a large excess of nonfunctionalized NPs.[39] The subsequent assembly of dimers and trimers was achieved without removing the unfunctional NPs.

Controlled assemblies are needed for applications in labeling and medical diagnostics, and are the key remaining bottleneck for the development of

reproducible nanoelectronics components based on NP superstructures, such as dimers, chains and 3D architectures. A very promising route to controlled assembly (Figure 1b) requires simply pure samples of monofunctionalized NPs (suitable linkers and linking chemistries may be selected from textbook organic synthesis). To our knowledge only a few review articles focus on the controlled functionalization of Au NPs.[34,35,40–42] One way to obtain NPs with a controlled low number of functionalities is by separating NPs using chromatography. The first report of monovalent Au NPs was presented in the 1980s where a undecagold cluster ( $\text{Au}_{11}$ ) was stabilized by seven phosphine ligands, with just one of the phosphines carrying a functionality (Figure 2a).[43,44] The clusters were purified by repeated ion-exchange chromatography and their monofunctionality was inferred from photometry and their chemical behavior. Monovalent undecagold (0.8 nm diameter) was then further labeled with an antibody by Hainfeld.[45] The unlabeled NPs were removed by ion-exchange chromatography and the presence of mono-labeled NPs was confirmed by electron microscopy. This approach was later extended to synthesize a monovalent 1.4 nm gold cluster that is commercially available since 1992 as Nanogold by Nanoprobes (Figure 2b).[11] Therefore we will not present Au NP assemblies using these commercial NPs.

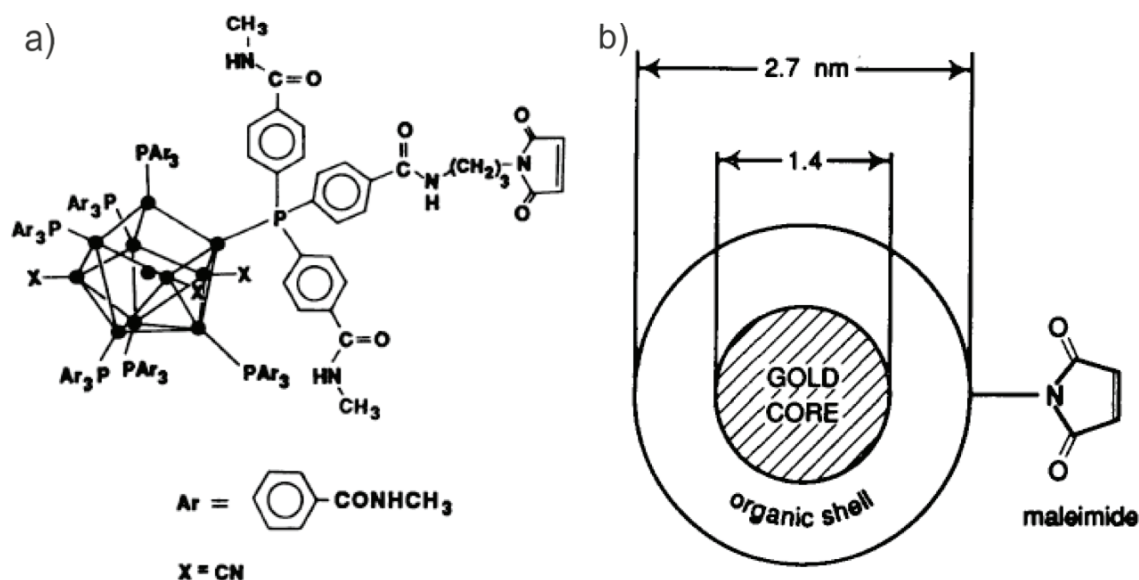


Figure 2. a) The proposed molecular structure of monofunctionalized undecagold (0.8 nm diameter), from Reference [45]; b) A schematic drawing of commercially available monofunctionalized gold cluster called Nanogold, from Reference [11].

Au NPs functionalized with different amounts of DNA strands were successfully separated by gel electrophoresis (Figure 3a).[46] Mono- to penta-functionalized NPs

were isolated by Alivisatos and coworkers with DNA strands consisting of at least 100 base pairs. The pure mono-DNA-labeled NPs were later covalently dimerized by enzyme ligation supported by a reversible duplex formation with a template DNA[47] in a neat combination of covalent chemistry plus non-covalent self-assembly. In earlier studies the same group had already used gel electrophoresis to isolate NP dimers and trimers.[48] Monofunctional NPs purified by gel electrophoresis were also used to form cyclic hexameric structures[49] and highly ordered two-dimensional NP arrays on DNA tiles.[50–52] NPs with multiple functionalities were also used to form 2D arrays resulting in more defects and lesser control of the final assembly.[53]

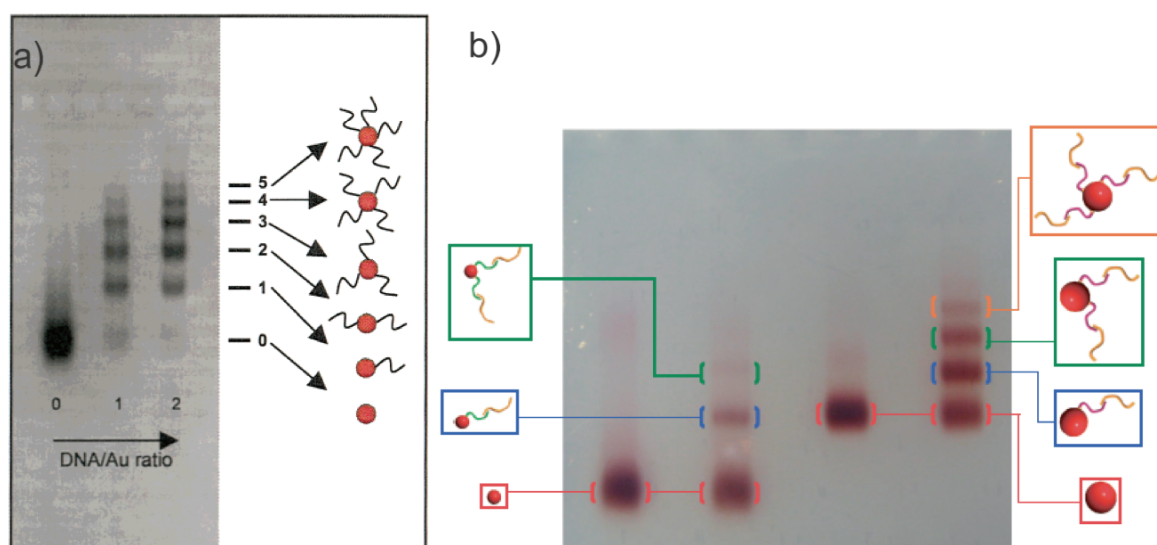


Figure 3. Successful separation of Au NPs bearing different numbers of DNA strands: a) at least 100 base pairs are required in order to achieve sufficient separation, from Reference [46]; b) shorter DNA markers are used by reversibly extending to a double strand for the purification, from Reference [54].

The long DNA strands used for the purification have a drawback: they require higher efforts and costs for their production and can also be an obstacle for the tailored NP assembly. Aldaye and Sleiman, and Ohya and coworkers, were able to reduce the size of the DNA marker by a reversible elongation with a second DNA strand and isolated the mono-DNA-labeled NPs by gel electrophoresis (Figure 3b).[54,55] After removal of the elongation strands the NPs were assembled into 1D- and 2D-architectures, such as chains, triangles and squares. NPs with two DNA markers were also isolated by gel electrophoresis and used to build up trimers with two monofunctionalized NPs.[47,54] If these trimeric structures were connected by single stranded DNA, two complementary trimers were synthesized and hybridized to form hexameric structures.[47] Most superstructures aligned in linear structures reflecting



the steric benefit of binding the two functionalities on opposite sides of the NP. Suzuki and coworkers preassembled two single stranded DNA markers to a template in order to attach two functional units to the NP surface at the same time in close proximity.[56] They subsequently attached two smaller functional NPs to the bifunctional NPs and obtained triangular architectures clearly showing the close proximity of the two initial DNA labels.

Immobilized metal ion affinity chromatography (IMAC) was used to purify mono-peptide labeled NPs.[57] Coordinating a peptide tag to an immobilized metal ion enabled the separation of functional and unfunctional NPs. In this case, a sequence of six histidines was used as a tag (His<sub>6</sub>-tag) and Nickel(II) as the immobilized metal ion. This Nickel-mediated NP-protein binding was introduced earlier by Hainfeld and coworkers.[40,58] After forming the Nickel-His-tag complexes in a chromatography column the unfunctional NPs were washed off and the mono-labeled NPs were eluted with imidazole (Figure 4a). However, in order to obtain only mono-functionalized Au NPs the concentration of peptide marker had to be very low (10fold excess of NPs) so that the NPs bear either one or no functionality leading to a low yield of monofunctional NPs. The same approach was chosen to synthesize Au NPs with the Nickel(II) complex[59] on their surface in order to bind these labeled NP to His<sub>6</sub>-tag functionalized proteins[59] and nanofibres.[60]

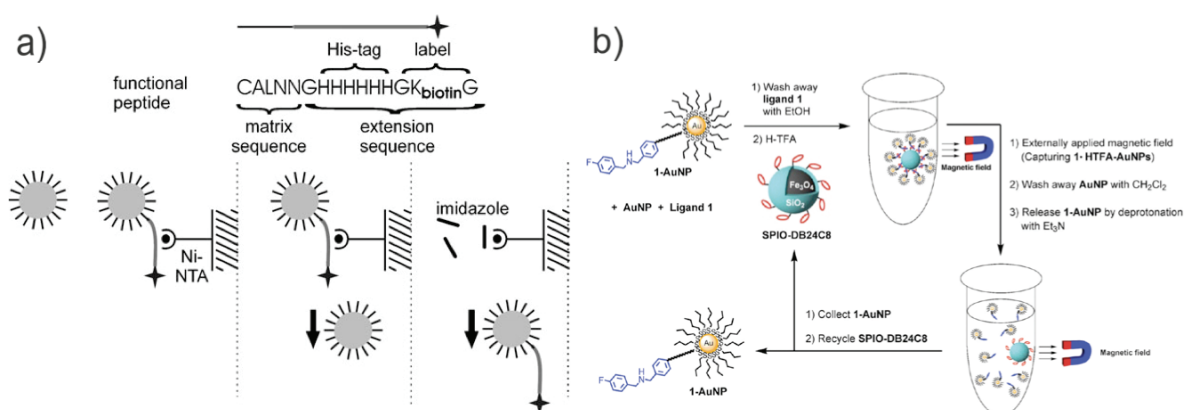


Figure 4. Concept used to separate a mixture of NPs having either one or no functional group attached to their surface. Functionalized NP were selectively trapped in a column (left) or on magnetic particles (right), while unfunctional NPs were removed. Finally pure samples of monofunctionalized NPs were released and collected, from References [57,61].

Leung and coworkers were able to remove unfunctional NPs with a similar protocol (Figure 4b).[61] A mixture of monofunctionalized and unfunctionalized Au NPs was

separated using crownether functionalized magnetic particles that noncovalently bound the NP functional group, a protonated secondary amine. The unfunctionalized NPs were washed away with dichloromethane, while the amines of the functional NPs were deprotonated, allowing the functional NPs to be separated from the magnetic particles by applying an external magnetic field.

All attempts presented so far require expensive and time-consuming purification steps. Reactions on solid supports provide an alternative route to obtain monofunctional NPs without the need for chromatographic purification. A polymer resin was functionalized with an alkyl chain bearing a terminal thiol, which was allowed to undergo exchange with the surface of an alkanethiol stabilized Au NP (Figure 5a). Unreacted NPs were washed off before the cleavage from the resin was performed under acidic conditions and monofunctional NPs with a diameter of around 2.8 nm were obtained.[62] This research published by Huo and coworkers was the first example of asymmetric functionalization, which means that just one part of the NP surface is functionalized while the rest of the surface is blocked. Shortly after that Sung et al. published a similar example[63] and within both studies the monofunctionalized NPs were assembled to dimeric structures with TEM investigations clearly confirming their identity.[62,63] The usefulness of solid supports was further improved by introducing noncovalent attachment to the polymer resins (Figure 5b) permitting the use of milder, less acidic conditions for the final cleavage.[64]

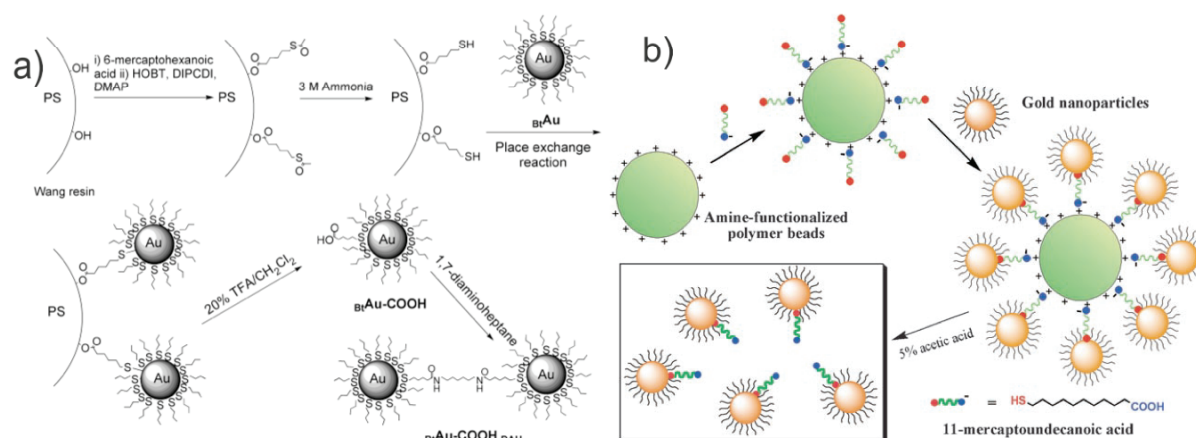


Figure 5. Schematic of the stepwise formation of monofunctionalized Au NPs using molecular exchange with a polymer resin: a) the alkanethiol is covalently attached to the resin, from Reference [62]; b) the alkanethiol is immobilized on the polymer beads using noncovalent interaction, from Reference [64].

Shumaker-Parry and coworkers used a glass surface as solid support for the asymmetric functionalization of Au NPs with a diameter of 41 nm.[65] This allowed the introduction of different functionalities upon removal from the glass surface. A drawback of this technique was the presence of an unknown number of functional ligands. However, this unknown number seemed to be low and concentrated to just one area of the surface. These NPs, each bearing either a carboxylic acid or an amine, were coupled with each other to form mostly dimers and therefore could be described as quasi monofunctionalized.[65] This means that the NPs behave in monofunctional nature although multiple functionalities are present. The versatility of this protocol was later proven using smaller 18 nm diameter NPs and other binding motifs for the formation of dimeric structures, while the stabilization was improved by using trivalent thiols.[66]

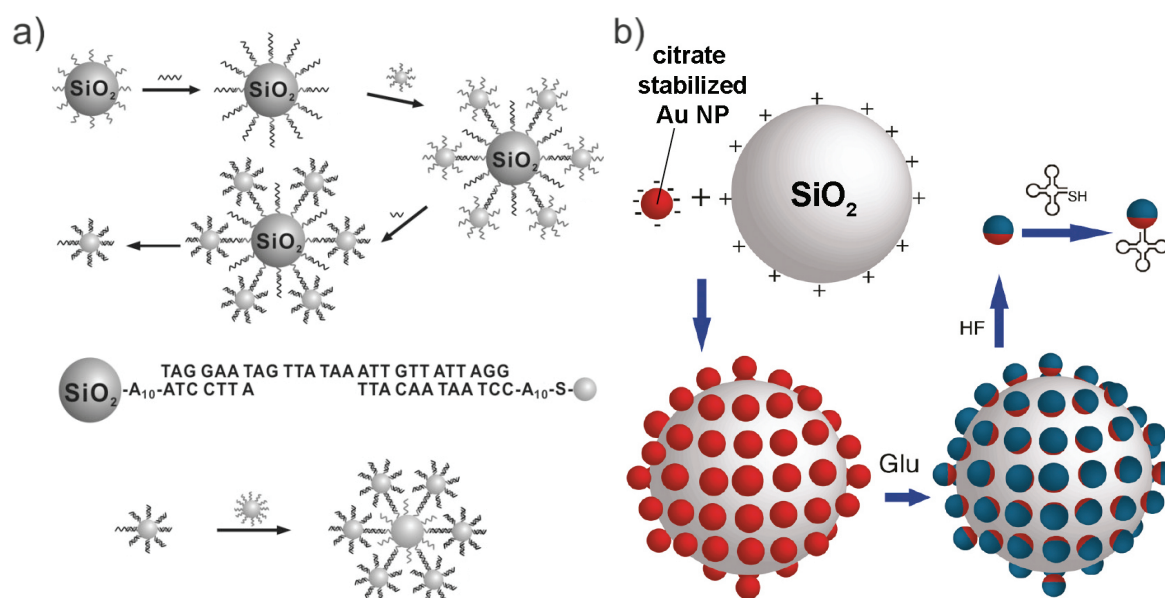


Figure 6. The concept of asymmetric functionalization to obtain a) quasi-monofunctionalized and b) truly monofunctionalized Au NPs. Initially Au NPs are bound to a larger SiO<sub>2</sub> particle and their free surface is blocked against further functionalization. Upon cleavage from the larger particle either quasi-monofunctionalized NPs are obtained with just a small surface area available for functionalization. If the functional group of choice is relatively large monofunctionalized Au NPs are obtained; adapted from References [67,68].

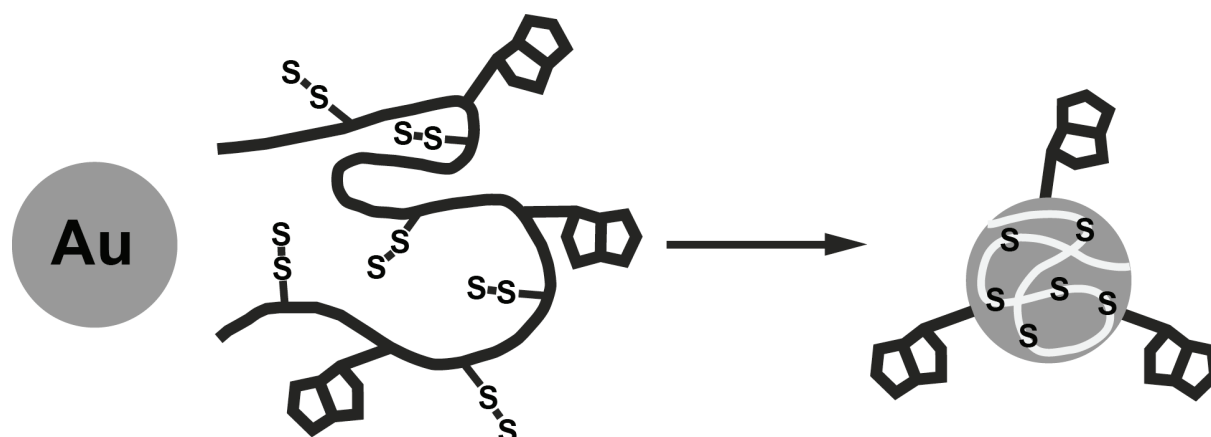
Mirkin and coworkers used SiO<sub>2</sub> particles (much larger than the Au NPs) as a basis for this asymmetric functionalization.[67] Au NPs stabilized with multiple DNA strands were hybridized onto the SiO<sub>2</sub> particle and the free DNA strands were blocked. After tailored melting of the first duplex quasi monofunctionalized Au NPs were obtained and successfully assembled around a larger multifunctionalized NP to obtain a

satellite structure (Figure 6a).[67] This concept was further improved by Li et al. who obtained truly mono-DNA-functionalized Au NPs.[68] They also used relatively large SiO<sub>2</sub> particles and introduced a bulky DNA functionality after removal from the solid support to block the attachment of a second functionality (Figure 6b). In general, the utilization of solid supports is an elegant way for controlled functionalization of Au NPs. One drawback is that an excess of NPs is required in order to favor monofunctionalization, which leads to lower yields. While there are several examples of the solid support approach for DNA or peptide labeled NPs, our impression is that commercial 'Nanogold' and NPs purified by gel electrophoresis are the two most common approaches to obtain monofunctionalized NPs in aqueous media. As the controlled functionalization in aqueous solvents was studied to a greater extent, solid supports seem to be more convenient for nonpolar organic media. Therefore, the following examples will mostly focus on controlled functionalization in organic solvents.

Ligand polymerization on the NP surface was another successful attempt to synthesize monofunctional NPs [69]. 4-Vinylthiophenol was used as a stabilizing ligand for Au NPs (diameter between 2 nm and 5 nm) and was polymerized on the NP surface. A controlled free radical polymerization was performed under high dilution conditions and with small amounts of starter molecules that contained a carboxylic acid group. This led to the introduction of just one carboxylic acid group on the NP surface. The NPs were dimerized and attached onto polypeptide chains, confirming the monofunctionalization.

The approaches described so far mostly produced NPs bearing one functionality while unfunctional ligands are still present on the NP surface. All approaches needed further purification steps or additional reactions of the initial NP in order to obtain monofunctional NPs. On the other hand, a macromolecular stabilizing ligand able to cover the entire or most of the NP surface could provide a more efficient route to monofunctional NPs. Wilson and coworkers first reported this concept in 2004.[70] They prepared dextran polymers that contained many disulfide bonds and were big enough to enwrap an entire Au NP, 15 nm in diameter. On average, one NP was stabilized by one polymer molecule (Scheme 1). To our knowledge this was the first report of a one-to-one ratio of NP and stabilizing ligand. While in this case the

polymer carried several functionalities, a new concept was introduced towards monofunctionalization.



Scheme 1. The concept of enwrapping of a 15 nm gold nanoparticle with a single polymer molecule, adapted from Reference [70].

In 2006 Kiedrowski and coworkers presented the successful formation of a monofunctional Au cluster stabilized by a single ligand.[71] In 2001 they initially presented the stabilization of the Au<sub>55</sub> Schmid-cluster with four tridentate benzylic thioether ligands.[72] The ligands were based on 1,3,5-trimethylbenzene structures and substituted the twelve phosphine ligands around the cluster by a phase transfer reaction into a buffered aqueous solution. The four tridentate ligands were fused to form a dodecadentate ligand which was then functionalized. The dodecadentate ligand provided monofunctionalized gold clusters that were stabilized by a single ligand. These NPs were attached to a single stranded DNA and used to perform temperature dependent studies on the DNA duplex formation.[71] This DNA melting was performed in order to study the thermostability of the label.

We recently used the concept of introducing the desired functionality into a macromolecular ligand in our research group. Flexible benzylic thioether moieties were assembled in a dendritic structure to form multidentate ligands with 1,3,5-trisubstituted benzenes as branching units.[73] These dendritic ligands were present during the Brust-Schiffrin method[9] and stable NPs were formed. We found that the second generation dendrimers consisting of 20 thioether moieties were able to stabilize an entire Au NP of 1.2 nm diameter. These ligands were further equipped with an oligo phenylene ethynylene (OPE) rod, which carried a protected terminal acetylene (Figure 7).[74] In the presence of the functional second generation

dendrimers monofunctional NPs were formed, which were subsequently assembled to give dumbbell structures with yields close to 50%.

NPs stabilized with the octadentate first generation dendrimers were on average bifunctional, carrying two terminal protected acetylenes. This finding was consistent with earlier studies of our group where linear thioether oligomers (also eight thioether moieties) required two ligands for stabilizing Au NPs.[75–78]

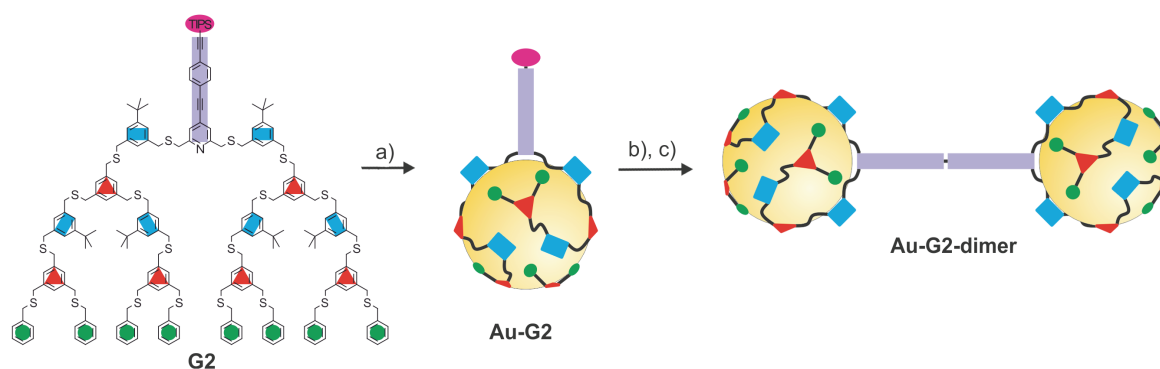


Figure 7. Concept of using pre-functionalized macromolecular ligands to introduce the desired functionality already within the NP formation, adapted from [74].

Stellacci and coworkers also formed divalent NPs.[79] They selectively functionalized Au NPs by ligand exchange. This place exchange was found to be favored at diametrically opposed positions due to polar defects occurring when a curved NP surface is coated with an ordered monolayer. The divalent NPs were used to form 1D-chains with different NP distances depending on the diamine linker used for the assembly.[79]

### Conclusion and Perspective

The approaches to obtain bi- and monofunctionalized Au NPs are versatile and can be divided into three main groups: chromatographic purification, asymmetric functionalization and use of macromolecular functional ligands. While the first two concepts require post-processing of the prepared NPs, the latter necessitates additional synthetic modification prior to NP formation. As organic chemists we prefer working with modified precursors as this allows diverse tailoring of functional groups and a subtle tuning of the desired NP properties. We can easily analyze and finely control our macromolecular ligands before using them as stabilizing agents, while the spectroscopy of the post-processing is more difficult to perform and analyze. As we recently obtained NPs stabilized by a single functional ligand we will now use this

single-molecule nanostructure as a building block to assemble 2D architectures and investigate their potential use as labels and components in nanoelectronics devices.

### References

- [1] M.-C. Daniel, D. Astruc, *Chem. Rev.* **2004**, *104*, 293–346.
- [2] M. Homberger, U. Simon, *Phil. Trans. R. Soc. A* **2010**, *368*, 1405–1453.
- [3] R. Sardar, A. M. Funston, P. Mulvaney, R. W. Murray, *Langmuir* **2009**, *25*, 13840–13851.
- [4] H. Goesmann, C. Feldmann, *Angew. Chem. Int. Ed.* **2010**, *49*, 1362–1395.
- [5] M. Faraday, *Phil. Trans. R. Soc. Lond.* **1857**, *147*, 145–181.
- [6] J. Turkevich, P. C. Stevenson, J. Hillier, *Discuss. Faraday Soc.* **1951**, *11*, 55.
- [7] G. Schmid, R. Pfeil, R. Boese, F. Bandermann, S. Meyer, G. H. M. Calis, J. W. A. van der Velden, *Chem. Ber.* **1981**, *114*, 3634–3642.
- [8] G. Schmid, *Chem. Rev.* **1992**, *92*, 1709–1727.
- [9] M. Brust, M. Walker, D. Bethell, D. J. Schiffrin, R. Whyman, *J. Chem. Soc., Chem. Commun.* **1994**, 801–802.
- [10] M. Brust, D. J. Schiffrin, D. Bethell, C. J. Kiely, *Adv. Mater.* **1995**, *7*, 795–797.
- [11] J. F. Hainfeld, F. R. Furuya, *J Histochem Cytochem* **1992**, *40*, 177–184.
- [12] H. Häkkinen, *Chem. Soc. Rev.* **2008**, *37*, 1847–1859.
- [13] J. M. Romo-Herrera, R. A. Alvarez-Puebla, L. M. Liz-Marzán, *Nanoscale* **2011**, *3*, 1304.
- [14] P. K. Jain, M. A. El-Sayed, *Chem. Phys. Lett.* **2010**, *487*, 153–164.
- [15] G. Schmid, *Chem. Soc. Rev.* **2008**, *37*, 1909–1930.
- [16] S.-J. Kim, J.-S. Lee, *Nano Lett.* **2010**, *10*, 2884–2890.
- [17] I. Willner, B. Willner, *Nano Lett.* **2010**, *10*, 3805–3815.
- [18] R. D. Powell, J. F. Hainfeld, *Micron* **2011**, *42*, 163–174.
- [19] J. I. Cutler, E. Auyeung, C. A. Mirkin, *J. Am. Chem. Soc.* **2012**, *134*, 1376–1391.
- [20] L. Dykman, N. Khlebtsov, *Chem. Soc. Rev.* **2012**, *41*, 2256.
- [21] R. Wilson, *Chem. Soc. Rev.* **2008**, *37*, 2028–2045.
- [22] Z. Wang, Y. Lu, *J. Mater. Chem.* **2009**, *19*, 1788.
- [23] X. Zhang, Q. Guo, D. Cui, *Sensors* **2009**, *9*, 1033–1053.
- [24] C. Della Pina, E. Falletta, L. Prati, M. Rossi, *Chem. Soc. Rev.* **2008**, *37*, 2077–2095.

- [25] A. Corma, H. Garcia, *Chem. Soc. Rev.* **2008**, *37*, 2096–2126.
- [26] R. A. Sperling, W. J. Parak, *Phil. Trans. R. Soc. A* **2010**, *368*, 1333–1383.
- [27] L. B. Bangs, *Pure Appl. Chem.* **1996**, *68*, 1873–1879.
- [28] L. C. Brousseau III, J. P. Novak, S. M. Marinakos, D. L. Feldheim, *Adv. Mater.* **1999**, *11*, 447–449.
- [29] T. Dadosh, Y. Gordin, R. Krahne, I. Khivrich, D. Mahalu, V. Frydman, J. Sperling, A. Yacoby, I. Bar-Joseph, *Nature* **2005**, *436*, 677–680.
- [30] M. Fischler, A. Sologubenko, J. Mayer, G. Clever, G. Burley, J. Gierlich, T. Carell, U. Simon, *Chem. Commun.* **2008**, 169–171.
- [31] F. Westerlund, T. Bjørnholm, *Curr. Opin. Colloid In.* **2009**, *14*, 126–134.
- [32] C. L. Choi, A. P. Alivisatos, *Annu. Rev. Phys. Chem.* **2010**, *61*, 369–389.
- [33] M. Grzelczak, J. Vermant, E. M. Furst, L. M. Liz-Marzán, *ACS Nano* **2010**, *4*, 3591–3605.
- [34] C. P. Shaw, D. G. Fernig, R. Lévy, *J. Mater. Chem.* **2011**, *21*, 12181.
- [35] T. Zhang, Z. Yang, D. Liu, *Nanoscale* **2011**, *3*, 4015.
- [36] J. Liao, L. Bernard, M. Langer, C. Schönenberger, M. Calame, *Adv. Mater.* **2006**, *18*, 2444–2447.
- [37] M. Sikora, P. Szymczak, D. Thompson, M. Cieplak, *Nanotechnology* **2011**, *22*, 445601.
- [38] H. Häkkinen, *Nat. Chem.* **2012**, *4*, 443–455.
- [39] M. A. Olson, A. Coskun, R. Klajn, L. Fang, S. K. Dey, K. P. Browne, B. A. Grzybowski, J. F. Stoddart, *Nano Lett.* **2009**, *9*, 3185–3190.
- [40] J. F. Hainfeld, R. D. Powell, *J. Histochem. Cytochem* **2000**, *48*, 471–480.
- [41] Q. Huo, J. G. Worden, *J Nanopart Res* **2006**, *9*, 1013–1025.
- [42] Zou Jianhua, Dai Qiu, Guda Ramakrishna, Liu Xiong, Worden James G., Goodson Theodore, Huo Qun, in *Nanoparticles: Synthesis, Stabilization, Passivation, and Functionalization*, American Chemical Society, **2008**, pp. 31–40.
- [43] J. E. Reardon, P. A. Frey, *Biochemistry* **1984**, *23*, 3849–3856.
- [44] D. Safer, L. Bolinger, J. S. Leigh Jr., *J. Inorg. Biochem.* **1986**, *26*, 77–91.
- [45] J. F. Hainfeld, *Science* **1987**, *236*, 450–453.
- [46] D. Zanchet, C. M. Micheel, W. J. Parak, D. Gerion, A. P. Alivisatos, *Nano Lett.* **2001**, *1*, 32–35.



- [47] S. A. Claridge, A. J. Mastroianni, Y. B. Au, H. W. Liang, C. M. Micheel, J. M. J. Fréchet, A. P. Alivisatos, *J. Am. Chem. Soc.* **2008**, *130*, 9598–9605.
- [48] C. J. Loweth, W. B. Caldwell, X. Peng, A. P. Alivisatos, P. G. Schultz, *Angew. Chem. Int. Ed.* **1999**, *38*, 1808–1812.
- [49] F. A. Aldaye, H. F. Sleiman, *Angew. Chem. Int. Ed.* **2006**, *45*, 2204–2209.
- [50] J. Zheng, P. E. Constantinou, C. Micheel, A. P. Alivisatos, R. A. Kiehl, N. C. Seeman, *Nano Lett.* **2006**, *6*, 1502–1504.
- [51] J. Sharma, R. Chhabra, Y. Liu, Y. Ke, H. Yan, *Angew. Chem. Int. Ed.* **2006**, *45*, 730–735.
- [52] J. Sharma, R. Chhabra, C. S. Andersen, K. V. Gothelf, H. Yan, Y. Liu, *J. Am. Chem. Soc.* **2008**, *130*, 7820–7821.
- [53] J. D. Le, Y. Pinto, N. C. Seeman, K. Musier-Forsyth, T. A. Taton, R. A. Kiehl, *Nano Lett.* **2004**, *4*, 2343–2347.
- [54] T. Tamaki, N. Miyoshi, T. Uehara, Y. Ohya, *Chemistry Letters* **2010**, *39*, 1084–1085.
- [55] F. A. Aldaye, H. F. Sleiman, *J. Am. Chem. Soc.* **2007**, *129*, 4130–4131.
- [56] K. Suzuki, K. Hosokawa, M. Maeda, *J. Am. Chem. Soc.* **2009**, *131*, 7518–7519.
- [57] R. Lévy, Z. Wang, L. Duchesne, R. C. Doty, A. I. Cooper, M. Brust, D. G. Fernig, *ChemBioChem* **2006**, *7*, 592–594.
- [58] J. F. Hainfeld, W. Liu, C. M. R. Halsey, P. Freimuth, R. D. Powell, *J. Struct. Biol.* **1999**, *127*, 185–198.
- [59] L. Duchesne, D. Gentili, M. Comes-Franchini, D. G. Fernig, *Langmuir* **2008**, *24*, 13572–13580.
- [60] M. Bruning, L. Kreplak, S. Leopoldseder, S. A. Müller, P. Ringler, L. Duchesne, D. G. Fernig, A. Engel, Z. Ucurum-Fotiadis, O. Mayans, *Nano Lett.* **2010**, *10*, 4533–4537.
- [61] C.-P. Chak, S. Xuan, P. M. Mendes, J. C. Yu, C. H. K. Cheng, K. C.-F. Leung, *ACS Nano* **2009**, *3*, 2129–2138.
- [62] J. G. Worden, A. W. Shaffer, Q. Huo, *Chem. Commun.* **2004**, 518–519.
- [63] K.-M. Sung, D. W. Mosley, B. R. Peelle, S. Zhang, J. M. Jacobson, *J. Am. Chem. Soc.* **2004**, *126*, 5064–5065.
- [64] X. Liu, J. G. Worden, Q. Dai, J. Zou, J. Wang, Q. Huo, *Small* **2006**, *2*, 1126–1129.

- [65] R. Sardar, T. B. Heap, J. S. Shumaker-Parry, *J. Am. Chem. Soc.* **2007**, *129*, 5356–5357.
- [66] A. Hofmann, P. Schmiel, B. Stein, C. Graf, *Langmuir* **2011**, *27*, 15165–15175.
- [67] F. Huo, A. K. R. Lytton-Jean, C. A. Mirkin, *Adv. Mater.* **2006**, *18*, 2304–2306.
- [68] Z. Li, E. Cheng, W. Huang, T. Zhang, Z. Yang, D. Liu, Z. Tang, *J. Am. Chem. Soc.* **2011**, *133*, 15284–15287.
- [69] C. Krüger, S. Agarwal, A. Greiner, *J. Am. Chem. Soc.* **2008**, *130*, 2710–2711.
- [70] R. Wilson, Y. Chen, J. Aveyard, *Chem. Commun.* **2004**, 1156.
- [71] W. M. Pankau, S. Mönninghoff, G. von Kiedrowski, *Angew. Chem. Int. Ed.* **2006**, *45*, 1889–1891.
- [72] W. M. Pankau, G. von Kiedrowski, K. Verbist, *Chem. Commun.* **2001**, 519–520.
- [73] J. P. Hermes, F. Sander, T. Peterle, R. Urbani, T. Pfohl, D. Thompson, M. Mayor, *Chem. Eur. J.* **2011**, *17*, 13473–13481.
- [74] J. P. Hermes, F. Sander, U. Fluch, T. Peterle, D. Thompson, R. Urbani, T. Pfohl, M. Mayor, *J. Am. Chem. Soc.* **2012**, accepted.
- [75] T. Peterle, A. Leifert, J. Timper, A. Sologubenko, U. Simon, M. Mayor, *Chem. Commun.* **2008**, 3438–3440.
- [76] T. Peterle, P. Ringler, M. Mayor, *Adv. Funct. Mater.* **2009**, *19*, 3497–3506.
- [77] J. P. Hermes, F. Sander, T. Peterle, M. Mayor, *CHIMIA* **2011**, *65*, 219–222.
- [78] J. P. Hermes, F. Sander, T. Peterle, C. Cioffi, P. Ringler, T. Pfohl, M. Mayor, *Small* **2011**, *7*, 920–929.
- [79] G. A. DeVries, M. Brunnbauer, Y. Hu, A. M. Jackson, B. Long, B. T. Neltner, O. Uzun, B. H. Wunsch, F. Stellacci, *Science* **2007**, *315*, 358–361.

## Controlled Formation of Bi- and Monofunctionalized Gold Nanoparticles

Jens Peter Hermes and Marcel Mayor\*

*Manuscript prepared for submission*

### Introduction

Gold nanoparticles (Au NPs) are attracting renewed interest due to their usefulness in chemistry, electronics, catalysis and medicine.[1–3] However, the formation and utilization of Au NPs dates back far before their current vogue, with dying of glass by freshly precipitated colloidal gold solutions already known in late Greco-Roman times.[4] A famous example is the 4<sup>th</sup> Century Lycurgus cup, which appears red when lit from behind and green when lit from the front, as light is absorbed and scattered by nanocrystals of a gold–silver alloy. In 1857, Faraday was the first to connect the color with the size of Au NPs and was the first to investigate their deliberate synthesis.[5] The next milestone was the formation and analysis of citrate-stabilized NPs by Turkevich et al. in 1951.[6] More recent breakthroughs demonstrated ultrahigh precision in the formation of passivated Au NPs. [7–10] Schmid et al. presented the gold cluster  $\text{Au}_{55}(\text{PPh}_3)\text{Cl}_6$ ,[7] which has become known as the ‘Schmid-cluster’, having stimulated the areas of quantum electronics[8] and labeling.[11] Brust et al. introduced a two-phase protocol that allowed aqueous tetrachloroauric(III) acid ( $\text{HAuCl}_4$ ) to be transferred into the organic phase (toluene) using tetraoctylammonium bromide (TOAB). The gold salt was then reduced with aqueous sodium borohydride in the presence of an alkanethiol yielding stable Au NPs with diameters below 3 nm and narrow size distributions.[9]

Since then the number of studies dedicated to Au NPs increased significantly over the past two decades, exploiting the unmatched stability of Au NPs among metal nanoparticles. They also show fascinating size and shape dependent properties[12] and have various applications. They are used as plasmonic devices, for example as a plasmonic ruler to measure the distance between two NPs attached to linkers of unknown length.[13,14] Extended research is conducted on Au NPs in nanoelectronics[2,15] such as information storages devices.[16] As Au NPs of different sizes are easily visualized by electron microscopy they are the label of choice for visualizing and investigating bio- and macromolecules.[17–20] Au NPs

## 4 Conclusion and Outlook

Macromolecular multidentate thioether ligands were synthesized and used for the stabilization of Au NPs with diameters around 1.2 nm and narrow size distributions. Bifunctional NPs were formed in the presence of linear octadentate ligands and their functionality, an OPE rod with a protected terminal acetylene, was used to form NP superstructures upon homocoupling. Switching from benzene to pyridine as anchor of the functionality induced a perpendicular arrangement of the rod on the NP surface. Theoretical calculations suggested that this controlled orientation was directed by coordination of the nitrogen's lonepair to the gold surface. Thioether dendrimers were used to enlarge the ligand structure and thus its denticity. Their stabilizing ability strongly depended on the size of the protective ligand shell showing the importance of the *tert*-butyl functionalized benzene units. By using icosadentate dendrimers (20 thioether moieties) we were able to form monofunctionalized NPs. These artificial molecules were used to form dumbbell structures with satisfying yields and controlled interparticle distances.

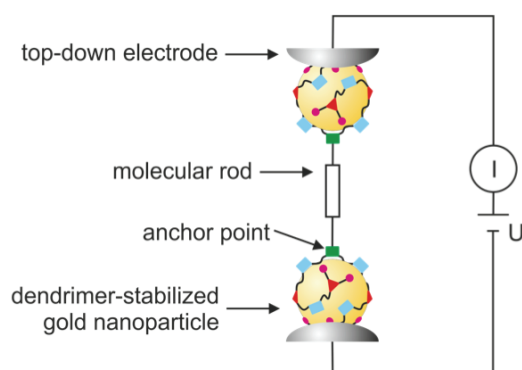


Figure 18. Au NP dumbbells might be suitable model compounds for single molecule conduction measurements.

We found that the free acetylenes used for the homocoupling also attack directly the NP surface leading to shorter NP distances. This could be avoided by using pre-dimerized dendrimer ligands during the NP formation in order to obtain directly NP dumbbells. These organic-inorganic superstructures are interesting model compounds for investigations in the research field of molecular electronics. The dumbbells could be trapped between two top-down electrodes in order to perform single molecule conduction measurements of various molecular rods (Figure 18). The monofunctional NPs have a variety of potential utilizations. They could be used

as TEM labels for visualizing carbon nanotubes and assembled into 2D-networks by 'clicking' them to multifunctional linkers or templates containing azide groups.

The applied conditions of the NP formation could be further investigated in order to tailor the NP diameter and dispersity. The temperature and the speed of  $\text{NaBH}_4$  addition could be altered systematically to gain further insights, as tuning the excess of gold compared to thioether moieties (up to threefold) had no influence on the NP diameter. The controlled formation of larger NPs would be interesting in fundamental aspects as well as for some potential applications as plasmonic devices.

Further research can be conducted towards other metal nanoparticles. While gold NP are strongly stabilized by thiols or thioethers a new ligand series based on oxygen instead of sulfur might be suited to stabilize silver, platinum, palladium or other metal nanoparticles. While adjusting the ligand design the ligand-NP coordination might be increased by substituting most or all benzenes with pyridines providing an additional binding site. In addition the macromolecular ligand could be equipped with protected thiols. In a post-processing step these thiols might be liberated in close proximity to the NP surface in order to form covalent bonds and increase the overall NP stability. The monofunctionalized NPs enable several further utilizations and the research field still offers a broad scope for further system adjustment and development of a new variety of intriguing new concepts.





**Personal Data**

Name Jens Peter Hermes  
Date/place of Birth 09.03.1983, Bremen (D)  
Nationality German  
Email jens.hermes@gmail.com

**Education**

1995 - 2002 Gymnasium Syke  
2003 - 2008 Diploma studies in Chemistry, Westfälische Wilhelms-Universität Münster, Diploma thesis under the supervision of Prof. Dr. M. Knoll: „Dotierungsfrontmigration in polymerelektronischen Systemen mit unterschiedlichen Migrationsschichsystemen“  
2008 - 2012 PhD thesis, University of Basel, under the supervision of Prof. Dr. M. Mayor

**Additional work**

2008 - 2012 Organization of Practical Course in Organic Chemistry for Students of Nanosciences



